Structural and functional studies of a chimeric $GABA_A$ receptor

Duncan Laverty

A thesis submitted to University College London for the Degree of Doctor of Philosophy

April 2016

Department of Neuroscience, Physiology and Pharmacology

University College London

Gower Street

WC1E 6BT

Declaration

I, Duncan Laverty, confirm that the work presented in this thesis is my own. Where information has been derived from other sources, I can confirm that this has been indicated in the thesis.

Abstract

$GABA_A$ receptors are ligand-gated ion channels principally responsible for inhibitory neurotransmission in the mammalian CNS. GABA binding initiates a series of conformational changes causing the receptor to transition from inactive (shut/closed) to active (open) ion channel states; and during prolonged agonist exposure, to a desensitized (closed) state. Critical to the fine-tuning of inhibitory responses *in vivo* is the allosteric modulation of $GABA_A$ receptors by an array of compounds, many of which impart their effect through binding within the receptor's transmembrane domain.

Beyond the importance of GABA-mediated inhibition in maintaining nervous system function, $GABA_A$ receptors are established therapeutic targets for psychiatric and neurodevelopmental disorders. Despite this, an understanding of the structure of these receptors at atomic resolution is crucially lacking; particularly with regards to the structural elements underpinning channel gating and allosteric modulation. Therefore, $GABA_A$ receptor ion channels were subjected to atomic-resolution structural analyses using chimeric receptors, in addition to comparative studies with bacterial ion channel homologues.

A functional receptor was formed from chimeras between the extracellular domain of the prokaryotic ion channel GLIC and the transmembrane domain of $GABA_A$ receptor α1 subunits. These receptors exhibited $GABA_A$ receptor-like properties with respect to their response to brain neurosteroids. The amenability of this receptor to high-level expression and purification was assessed. The baculovirus-insect cell expression system was identified as an appropriate system for generating receptor of sufficient quantity and purity to generate diffracting protein crystals.

Additional studies of $GABA_A$ receptor modulators at the bacterial homologs GLIC and ELIC identified previously unreported effects prompting further structural investigation using X-ray crystallography, cryo-electron microscopy and native mass spectrometry.

In conclusion, these studies reveal a new system for atomic structural resolution investigation of $GABA_A$ receptor subunits, likely to be applicable to other receptors. These receptors are potentially powerful tools for understanding the mechanism of $GABA_A$ receptor allosteric modulation.

Acknowledgements

Firstly, thanks to my supervisor Prof. Trevor Smart for his support throughout this project. I would also like to thank Marc Gielen for his guidance and advice at the start of the project. Thanks also go to the rest of the lab, past and present, and Phil Thomas in particular, for the day to day support and entertainment. I must also thank the MRC (LMCB Studentship) for financial support.

Outside of the lab there are many people that must be thanked for their technical advice and assistance; Matt Gold (and lab) for protein purification assistance, advice and discussions; Pierre-Jean Corringer, who provided invaluable advice regarding protein purification; Marc Delarue, now collaborating on the GLIC-Pentobarbital project; Ambrose Cole and users of the Birkbeck X-Ray Lab for advice and assistance with protein crystallization, diffraction data collection and analysis; Dan Kofi-Clare, who carried out the electron microscopy presented in this thesis; Kostas Thallasinos, Adam Cryar and Kitty Hendricks, who carried out mass spectrometry experiments; the Membrane Protein Laboratory at Harwell for assistance with CPM and FSEC experiments and general advice on membrane protein purification; Gillian Dornan (Passmore group, MRC LMB) for advice on Baculovirus-insect cell expression.

My biggest thanks go to my family, with whom we've had many relaxing weekend trips out of the city.

Finally, Melissa has gone through all of this with me and words don't do justice to how amazing her support has been.

Contents

List of Figures

List of Tables

List of Equations

List of Abbreviations

ACh	Acetylcholine
AMPA	2-amino-3-(3-hydroxy-5-methyl-isoxazol-4-yl)propanoic acid
α -Bgtx	α-Bungarotoxin
BBS	α-Bungarotoxin Binding Site
CHS	Cholesterol Hemisuccinate
CNS	Central Nervous System
CPM	N-[4(7-dimethyamino-4-methyl-3 coumarinyl)phenyl]maleimide
Cryo-EM	Electron Cryo-Micrsocopy
DDD	Direct Electron Detector Device
DDM	Dodecyl-β-D-Maltopyranoside
DEER	Double electron-electron resonance
DMNG	Decyl Maltose Neopentyl Glycol
DPPC	Dipalmitoylphosphatidylcholine
eGFP	Enhanced Green Fluorescent Protein
ECD	Extracellular domain
ELIC	Pentameric-ligand gated ion channel from *E. chrysanthemi*
EM	Electron Microscopy
EPR	Electron Paramagnetic Resonance
EC_{50}	The concentration of a substance eliciting 50% of the maximal response
ER	Endoplasmic reticulum
FSEC	Fluorescence size exclusion chromatography
GABA	γ-aminobutyric acid
GLIC	Pentameric-ligand gated ion channel from *G. violaceus*
GluCl	Glutamate-gated chloride channel
Gly	Glycine
$5\text{-}HT_3$	$5\text{-hydroxytryptamine}_3$
ICD	Intracellular domain
iGluR	Ionotropic Glutamate Receptor
IC_{50}	The concentration of antagonist producing a 50% maximal inhibition
IMAC	Immobilized Metal Affinity Chromatography
IM-MS	Ion mobility mass spectrometry
IVM	Ivermectin
LC	Locally-closed
LGIC	Ligand gated ion channel
MS	Mass spectrometry
nAChR	Nicotinic Acetylcholine Receptor

NMDA	N-Methyl-D-aspartate
NMR	Nuclear Magnetic Resonance
nMS	Native Mass Spectrometry
pH_{50}	The pH (or concentration of protons) eliciting 50% of the maximal response
PDB	Protein Data Bank
PEG	Polyethylene glycol
pLGIC	Pentameric-ligand gated ion channel
PNS	Peripheral Nervous System
POPC	1-palmitoyl-2-oleoyl-sn-glycero-3-phosphocholine
PS	Pregnenolone Sulphate
PTX	Picrotoxin
RMSD	Root-Mean-Square Deviation
SA	Spontaneous activity
SDS PAGE	Sodium dodecyl sulphate polyacrylamide gel electrophoresis
SEC	Size exclusion chromatography
TEVC	Two-electrode voltage-clamp
THDOC	Tetrahydrodeoxycorticosterone
TMD	Transmembrane Domain
TRP	Transient Receptor Potential channel
UDM	n-Undecyl-β-D-Maltopyranoside
WT	Wild-type

Chapter 1: Introduction

1.1. Pentameric-ligand gated ion channels

Underpinning neuronal activity in the central and peripheral nervous systems (CNS and PNS) are neurotransmitter-gated ion channels and metabotropic receptors. Amongst these neurotransmitter receptors is the pentameric-ligand gated ion channel (pLGIC) superfamily, comprised of anionic Type-A γ-aminobutyric acid receptors ($GABA_AR$) and glycine receptors (GlyR); cationic nicotinic acetylcholine receptors (nAChR) and type 3 5-hydroxytryptamine receptors ($5\text{-}HT_3$; serotonin); and additionally zinc-activated cation channels (ZAC; Smart and Paoletti, 2012). Upon the release of neurotransmitter, these receptors rapidly respond to enable ion flow across the plasma membrane and effect neuronal cell excitation (mediated by acetylcholine and serotonin) and inhibition (mediated by GABA and glycine). Formerly defined as "Cys-loop" receptors (owing to a highly conserved Cys-containing structural loop), the pLGIC superfamily extends to anionic-invertebrate receptors activated by glutamate and serotonin (as well as cationic-GABA gated invertebrate receptors) and the recently identified bacterial homologs from *Gloeobacter violaceus* (GLIC) and *Erwinia chrysanthemi* (ELIC; Miller and Smart, 2010; Corringer et al., 2012; Smart and Paoletti, 2012). In order to understand the normal functional role of these receptors, their pharmacology and how dysfunction confers disease states; substantial efforts have been made to obtain high-resolution three-dimensional structures of pLGICs. From the ensemble of available structures X-ray structures of GLIC, ELIC, Glutamate-gated chloride channel (GluCl) from *C. elegans*, human homomeric $GABA_A$ β3, human α3 GlyR and mouse $5\text{-}HT_3$ receptors, plus electron microscope (EM) structures of *torpedo* nAChR and zebrafish α1 GlyR one can begin to appreciate the concerted rearrangement of atoms that occur at pLGICs following transmitter release and binding to their orthosteric sites (Unwin, 2005; Hilf and Dutzler, 2008; Bocquet et al., 2009; Hilf and Dutzler, 2009; Hibbs and Gouaux, 2011; Althoff et al., 2014; Hassaine et al., 2014; Miller and Aricescu, 2014; Du et al., 2015; Huang et al., 2015).

The main focus of this thesis is the mechanistic details of ionotropic $GABA_A$ receptor activation, and how this is allosterically modulated. The structural elements underlying these events are likely conserved across pLGIC family members. In light of this, the $GABA_A$ receptor family is introduced first, emphasizing its physiological function and pharmacology. Given the limited structural information for $GABA_A$ receptors, the mechanistic details of ligand binding, channel gating and allosteric modulation in the framework of the currently available structural and functional information across the pLGIC family is also considered.

1.2. $GABA_A$ receptors

The complex interplay of excitatory and inhibitory LGICs is crucial for maintaining normal neural network activity. In the mammalian CNS the neurotransmitter GABA is the predominant mediator of inhibition (Moss and Smart, 2001). GABA release activates ionotropic ($GABA_A$) and metabotropic ($GABA_B$) receptors. In the context of the mature neuronal network, activating $GABA_A$ receptors causes fast inhibition, resulting from an increased transmembrane flux of anions, membrane hyperpolarization (usually) and an electrical shunt of the neuronal membrane (Nicoll et al., 1990; Staley and Mody, 1992).

This, however, is an oversimplification of GABAergic transmission. During development, $GABA_A$ receptor activation plays a pivotal role in synapse formation and refinement of neuronal networks. In the immature nervous system, where neuronal transmembrane chloride levels form a depolarising electrochemical gradient, activation of $GABA_A$ receptors results in a membrane-depolarizing effect (Ben-Ari et al., 2012; Hubner and Holtoff, 2012). Thus early in development, these receptors mediate the main excitatory drive in neuronal networks. Moreover, this depolarizing GABA-mediated response can be sufficient to trigger calcium influx, which has been implicated in modulating neuronal cell migration and growth as well as synapse formation (Ben-Ari, 2002; Farrant and Nusser, 2005). As the nervous system matures,

and concurrent with a change in intracellular chloride levels to lower concentrations, there is a shift in the typical functional response to GABA release, which now drives neural inhibition (Farrant and Kaila, 2007).

1.2.1. $GABA_A$ receptor structure

As for other pLGIC-family members, $GABA_A$ receptors are characterized by the pentameric arrangement of subunits around a central pore that constitutes the integral ion channel (*Fig 1.1 A*). The $GABA_A$ receptor family is highly diverse with eight subunit families, yielding 19 subunits, identified in the genome. These consist of α1-6, β1-3, γ1-3, δ, ε, π, θ and ρ1-3 (Olsen and Sieghart, 2008; Olsen and Sieghart, 2009). Moreover, alternative splicing of RNA of certain subunits (e.g. splicing of the γ2 subunit producing short and long variants) ensures even greater receptor subunit diversity (Möhler, 2006; Farrant and Nusser, 2005). Between subunits of the same family there is ~70% sequence identity, whilst between members of the different families, ~20-40 % sequence identity (or 50% sequence similarity) is observed (Sigel and Steinmann, 2012).

Despite this diversity, $GABA_A$ receptor subunits share a common core of structurally defined domains (*Fig 1.1*). Indeed, this core is observed across all pLGIC family members (and is described later in greater detail), emphasizing the modular nature of these receptors. The large N-terminal domain is normally exposed to the extracellular space and consequently is referred to as the extracellular domain (ECD; *Fig 1.1 B*). Extensive studies reveal that this domain houses the orthosteric agonist (GABA) binding site (formed at the β-α subunit interface), as well as binding constituents for allosteric modulators including for example, the benzodiazepines (at the α-γ subunit interface). Additionally, the ECD is the location of the characteristic Cys-loop (formed by a disulphide bond between Cys-residues) which is juxtaposed to the cell membrane. Spanning the cell membrane are four (α-helical) transmembrane segments (M1-M4), which are arranged within a single subunit to form a four α-helical bundle and are referred to as the transmembrane domain (TMD; *Fig 1.1 A*). In the pentameric assembly the M2 domains combine to form the channel pore, which allows for

selective permeation of anions across the membrane (principally chloride and additionally bicarbonate ions). Extending from the base of M3 and M4 helices in to the intracellular space is a large stretch of amino acids which form a presumably unstructured loop and is now defined as the intracellular domain (ICD; *Fig 1.1 B*). As the most variable feature across $GABA_A$ receptor subunits (and indeed pLGICs), this domain can vary substantially in length (in excess of 100 amino acid residues for some subunits). Though without appreciable secondary structure (on the basis of structural predictions), this domain forms the binding locations of interacting and accessory proteins, as well as influencing receptor activity through modulation via post translational modification, such as phosphorylation and ubiquitination (Moss and Smart, 2001; Lüscher et al., 2011).

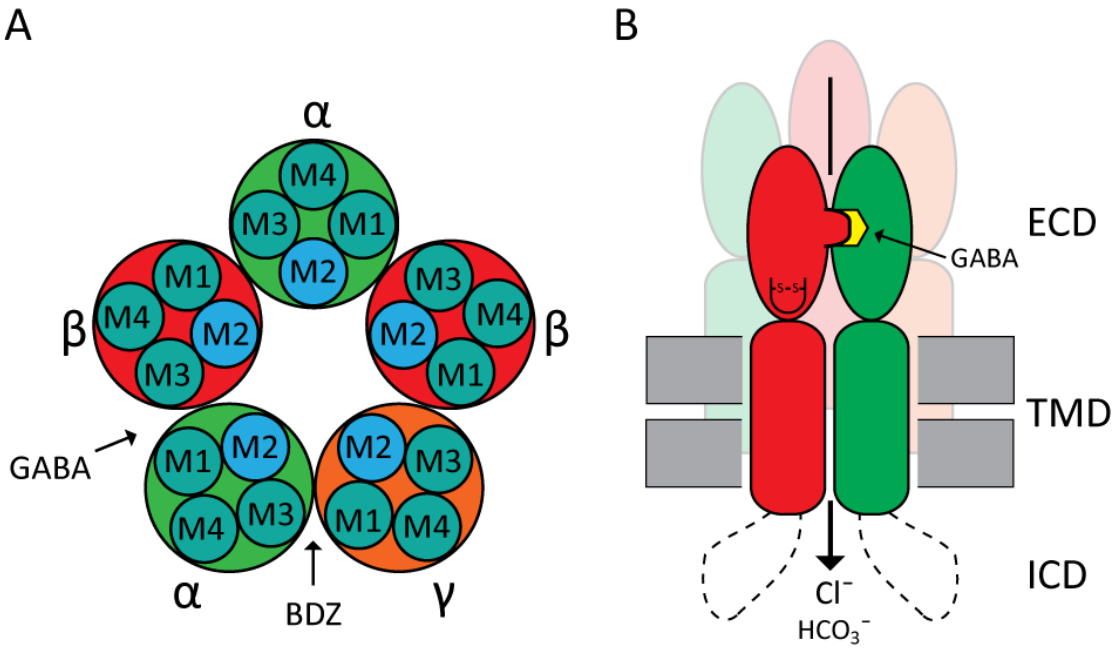

Figure 1.1 – $GABA_A$ receptor structure

A. Native α1β2γ2 $GABA_A$ receptor assembly in a 2:2:1 subunit stoichiometry with an "anticlockwise" arrangement of βαβαγ (as viewed from the extracellular space). The arrangement of M1-M4 helices is shown, with the M2 helix lining the channel. Binding of GABA and benzodiazepines occurs in the ECD at β-α and α-γ subunit interfaces respectively. **B.** Global architecture and arrangement of subunits shows approximate location of orthosteric agonist binding site (at β-α interface), "Cys-loop" (loop 7) and ICD. Upon channel gating, Cl^- (and HCO_3^-) flow passively across the cell membrane.

1.2.2. $GABA_A$ receptor composition and assembly

While these core domains are observed across all subunit families, energetic interactions at subunit interfaces dictate the allowed composition and arrangement of subunits in the pentameric assembly. Ultimately the final composition of a receptor critically influences receptor function and pharmacology, as well as regional and subcellular expression profiles in the brain. Despite the multiplicity of subunit isoforms and possible combinations, *in vivo* studies suggest probably less than ~20 $GABA_A$ receptor native subtype combinations exist with αβγ (in a 2α:2β:1γ stoichiometry; *Fig1.1*) and αβδ amongst the prominent combinations (Möhler, 2006; Olsen and Sieghart, 2008). The majority of native $GABA_A$ receptors are composed of α1β2γ2, accounting for ~40 – 60% of all expressed receptors (Sieghart and Sperk, 2002; Möhler, 2006).

In vitro, $GABA_A$ receptors can assemble in to considerably more diverse combinations comprising homopentamers of a single subunit (e.g. ρ or β subunits) and heteropentamers of two or three subunit classes. It is notable that α subunits are presumably unable to assemble as homopentameric receptors, even in recombinant expression systems, though a functional chimeric receptor between the ECD of ρ1 and the TMD of α1 has been reported (Martínez-Torres et al., 2000; Gielen et al., 2015). This emphasizes the importance of specific, energetically favoured interactions that govern receptor assembly. Indeed receptor imaging studies reveal that native (single) α-subunits are expressed and retained in the ER, requiring association with β subunits (and normally β and γ subunits) as the minimal subunit assembly cohort for trafficking to the cell surface (Connolly et al., 1996; Kittler et al., 2000). The formation of αβ heterodimers is reported to precede the formation of the receptor heteropentamer, and is determined by specific interactions in the N-termini of receptor subunits (Lüscher et al., 2011). Studies of heterologously-expressed β3 homomers reveal the role of N-terminal amino acids (G171, K173, E179 and R180) in mediating functional homomeric receptor expression (but not of αβ heteromers; Taylor et al., 1999). Studies of α1-subunits further suggest a role for two invariant tryptophan residues (W69 and W94 residues located in the N-terminus; Srinivasan et al., 1999) in forming the α-β

subunit interface and of an N-terminal residue "cassette" (residues 58-67) in formation of α1 and α6 containing receptors (in combination with β and γ subunits; Taylor et al., 2000). Currently, it is unclear as to what interactions prevent receptor (homo-) oligomerization and subsequent trafficking to the cell surface.

1.2.3. Phasic and tonic inhibition

In addition to setting the pharmacological profile of a receptor, subunit composition plays an important role in defining $GABA_A$ receptor populations at the levels of brain region, neuronal cell type and subcellular localisation. In concert with the specific functional properties of different receptor composition, this allows for differential responses dependent on local GABA and modulator concentrations. This is most noteworthy for receptors targeted to the synapse, and those excluded from this region, termed extrasynaptic (*Fig 1.2*). The former, composed principally of α(1-3)βγ subunits, respond to the transiently high synaptic concentrations of GABA (in the mM range) in the synaptic cleft, mediating phasic (fast synaptic) inhibition (Jones and Westbrook, 1995; Rudolph and Möhler, 2004). The latter, extrasynaptic, receptor populations (including αβ, α5βγ, α4βδ and α6βδ compositions; notably δ-containing receptors are apparently exclusively extrasynaptic) respond to low ambient GABA levels (in the low nM to μM range) outside of the synaptic cleft. The results of this response is to provide low intensity, persistent inhibition, termed tonic inhibition (Farrant and Nusser, 2005; Brickley and Mody, 2012). Additionally presynaptic $GABA_A$ receptors have been reported, though with less clearly defined pharmacological properties and physiological role (Draguhn et al., 2008; Ruiz et al., 2010).

The functional response to GABA is distinct amongst receptors mediating phasic and tonic inhibition, in terms of receptor kinetics (Fisher and Macdonald, 1997), and likely sets the tone for the inhibitory response. It should also be noted that distinct sensitivities to endogenous (e.g. neurosteroids) and exogenous (e.g. anaesthetics) allosteric modulators are observed at synaptic and extrasynaptic receptors (*Fig 1.2*; Brickley and Mody, 2012). Maintaining a fine balance between the two major forms of inhibition is critical in regulating neural network activity.

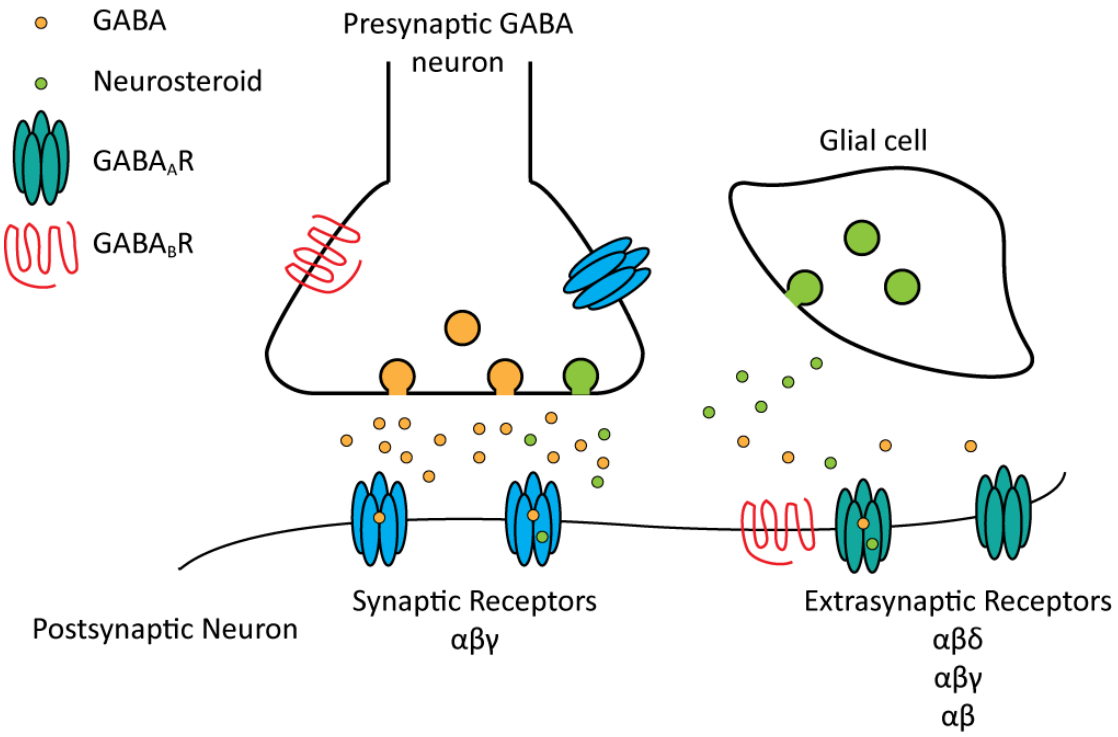

Figure 1.2 - GABAergic transmission and neurosteroid modulation in the CNS

Presynaptic GABA release activates synaptic and extrasynaptic populations of $GABA_A$ receptors and $GABA_B$ receptors on postsynaptic neurons. Activation of synaptic $GABA_A$ receptors results in phasic inhibition of postsynaptic nerve cells, while continuous activation of extrasynaptic receptors contributes to tonic inhibition. The role of pre-synaptic $GABA_A$ receptor activation is not clearly defined. Release of endogenous neurosteroids from neurons and glial cells and binding to $GABA_A$ receptors positively modulates receptor function (prolonging the decay of the inhibitory response).

1.2.4. $GABA_A$ receptor trafficking

Underlying the precise control of inhibitory GABAergic transmission is tight regulation of the number of $GABA_A$ receptors trafficked to and clustered at the synapse. Mechanisms that influence trafficking of receptors to and from the cell surface involves a variety of receptor associated molecules and their respective post-translational modifications (Moss and Smart, 2001; Jacob et al., 2008). The binding sites for many of these accessory proteins, as well phosphorylation consensus

sequences are found within the large subunit ICD between M3 and M4 (Lüscher and Keller, 2004; Lüscher et al., 2011).

$GABA_A$ receptors are anchored at the inhibitory synapse by gephyrin and dystroglycan, whilst binding with GABARAP (GABA receptor associated protein), Plic-1 and Huntingtin-Associated Protein 1 is believed to affect surface stability and receptor trafficking (Kittler et al., 2004; Lüscher and Keller, 2004; Jacob et al., 2008; Lüscher et al., 2011). Additionally, phosphorylation of receptors and receptor binding proteins influences trafficking (Smart and Paoletti, 2012). Phosphorylation consensus sequences have been identified for α4, β(1-3) and γ2 subunits (within the ICD), where they act as substrates for serine-threonine and tyrosine kinases, and modulate cell surface receptor expression (Comenencia-Ortiz et al., 2014). Moreover receptor phosphorylation has been shown to alter the functional (e.g. β subunit phosphorylation alters receptor desensitization and deactivation) and pharmacological (e.g. neurosteroid binding enhances phosphorylation of α4-containing receptors) profile of $GABA_A$ receptors (Hinkle and Macdonald, 2003; Comenencia-Ortiz et al., 2014; Adams et al., 2015). Notably, receptors are dynamic entities within the plasma membrane and are able to exchange with extrasynaptic/perisynaptic receptors, transferring via lateral mobility in the cell membrane (Thomas et al., 2005; Bogdanov et al., 2006). As with the previous mechanisms, this assists in maintaining receptor number at the synapse

1.2.5. $GABA_A$ receptor pharmacology

A defining feature of the $GABA_A$ receptor is the diverse pharmacological profile displayed across receptor subunit subtypes. Unsurprisingly, this profile is dramatically altered by the differential arrangement of subunits, rendering receptors sensitive or insensitive to a range of endogenous and synthetic compounds. Moreover, the receptor pharmacology allows for clear identification of the functional effects of specific $GABA_A$ receptors over other ionotropic and metabotropic (notably $GABA_B$) receptors of the CNS.

Crucial to the definition of receptor pharmacology is an understanding of the mechanism of binding and action. One can also differentiate between pharmacological agents solely on the basis of where they bind; either at sites within the receptor ECD or TMD, and their functional effect; to directly activate the receptor or modulate receptor function in a positive or negative manner.

1.2.6. $GABA_A$ receptor ECD pharmacology

The ECD houses the orthosteric agonist (GABA) binding site, formed at the interface of β-α subunits of native α1β2γ2 $GABA_A$ receptor (forming two sites per receptor; *Fig 1.1*). Homopentameric ρ1 receptors are similarly GABA-gated, bearing five analogous agonist binding-sites at all subunit interfaces (Smart and Paoletti, 2012). The structure of this site, largely conserved across pLGICs, is discussed in greater detail in *Section 1.4*. Other key receptor agonists, binding at the GABA-binding, site are the high-affinity agonist muscimol and partial agonist 4,5,6,7-Tetrahydroisoxaolo[5,4-c]pyridine-3-ol (THIP). Selective receptor antagonism is imparted by the binding of bicuculline and gabazine at the orthosteric site (Johnston, 2013).

Of the compounds that bind at sites homologous to the orthosteric site (i.e. at non-agonist binding subunit interfaces), the best characterised (in terms of binding and functional effect) are the benzodiazepine class of drug (*Fig 1.1 A*). These drugs have high clinical significance and are widely prescribed owing to their profound effects in treating insomnia, anxiety, and convulsions (Rudolph and Knoflach, 2011). Benzodiazepines (e.g. diazepam) are positive allosteric modulators of $GABA_A$ receptors and act to potentiate submaximal GABA responses through increasing the apparent affinity of a receptor to GABA (Rudolph and Knoflach, 2011). Binding is mediated by residues at the interface of α and γ subunits and is proposed to promote the formation of a pre-activation state prior to channel gating (presumably through global rearrangement of receptor structure; Gielen et al., 2012). Although there is a requirement of an α-γ subunit interface, benzodiazepines are selective to the extent that modulation is restricted to α1,2,3,or 5-containing receptors, excluding modulation of δ-containing receptors, which nominally replaces the γ2 subunit in

heteropentameric $GABA_A$ receptors. Moreover the relationship between binding and receptor potentiation can be further refined (from knock-in mouse studies)by the requirement of a critical histidine residue in α subunits (α1H101, α2H101, α3H126 and α5H105; Wieland et al., 1992; Benson et al., 1998), the absence of which in α4 and α6 subunits renders them insensitive to benzodiazepines. Further expansion of the structure of the benzodiazepine-binding pocket (principally by homology modelling, molecular docking and mutagenesis studies) will ultimately assist in the generation of specific α-selective compounds with fewer side effects (Richter et al., 2012)

1.2.7. $GABA_A$ receptor TMD pharmacology

The TMD contains the pore-forming and lipid-bilayer interacting elements of the $GABA_A$ receptor and, unsurprisingly, the binding sites for a wide range of endogenous and synthetic compounds that can directly activate or modulate channel function. The list contains compounds exhibiting great diversity in chemical structure, and includes volatile and intravenous anaesthetics (including etomidate, propofol and barbiturates), Zn^{2+}, protons, and neuroactive steroids (Wilkins et al., 2002; Franks, 2008; Hosie et al., 2009; Hosie et al., 2003).

Many of these compounds, particularly anaesthetics, impart their effect through binding to the β subunit in heteromeric receptors, and more precisely at a site proximal to the 15' M2 residue (Miller and Smart, 2010). Though introduced in greater depth in *Section 1.3* the prime numbering system has been established to identify residues in M2 (the pore lining α-helices); starting at 0' (at the cytoplasmic side, a conserved arginine) to 20' (at the extracellular end). This 15' residue is ideally situated to translate binding and/or transduction of a binding signal to the M2 helix and affect channel conformation. Evidence for the former (coordination of binding) is provided from studies comparing the sensitivity of β1 versus β2/3 containing $GABA_A$ receptors to modulation by anticonvulsants, a non-steroidal anti-inflammatory agent (mefenamic acid) and the anaesthetic etomidate (Miller and Smart, 2010). The equivalent 15' residue of the α-subunit (Ser260) is widely recognised as a major

determinant of general anaesthetic and alcohol action in $GABA_A$ receptors and Gly receptors (Mihic et al., 1997).

While the aforementioned compounds typically enhance receptor function, acting as allosteric agonists or positive allosteric modulators (PAMs), inhibition of the $GABA_A$ receptor at the level of the TMD is provided by distinct classes of compounds, termed negative allosteric modulators (NAMs). Channel blocking agents, including picrotoxin and t-butyl-bicyclophosphoro-thionate (TBPS) bind within the channel pore and prevent ion flow (Van Renterghem et al., 1987; Bali and Akabas, 2007; Gielen et al., 2015) (*Fig 1.3 A*). Block by these compounds can subsequently be relieved at high GABA concentrations.

While the channel-block effects of picrotoxin are clearly defined, allosteric inhibition of $GABA_A$ receptors by a class of endogenous (inhibitory) neurosteroids (including pregnenolone sulphate (PS), dehydroepiandrosterone sulphate (DHEAS)) is apparently more complex and consequently poorly understood. In contrast to the potentiating neurosteroids (discussed below), inhibitory steroids are less potent effectors at $GABA_A$ receptors and inhibit receptor function in a complex kinetic manner (Seljeset et al., 2015). Extensive electrophysiological studies of receptors expressed in recombinant systems have yet to provide a unanimous description of preferential binding for PS to a distinct activation state of the receptor (with binding observed for receptors in both inactive and active states; Akk et al., 2001; Eisenman et al., 2003). Moreover apparent promotion of the desensitized form of the receptor upon binding adds further complexity to the kinetic profile of these steroidal compounds (Wang et al., 2002; Eisenman et al., 2003). While efforts have been made to ascertain a mechanism of binding for inhibitory steroids, the location of a site remains elusive. A point of note, however, being that a transmembrane-located intrasubunit site mediating the effects of positive modulatory steroids (introduced below) does not overlap with a site responsible for coordinating the binding of inhibitory steroids (Akk et al., 2008).

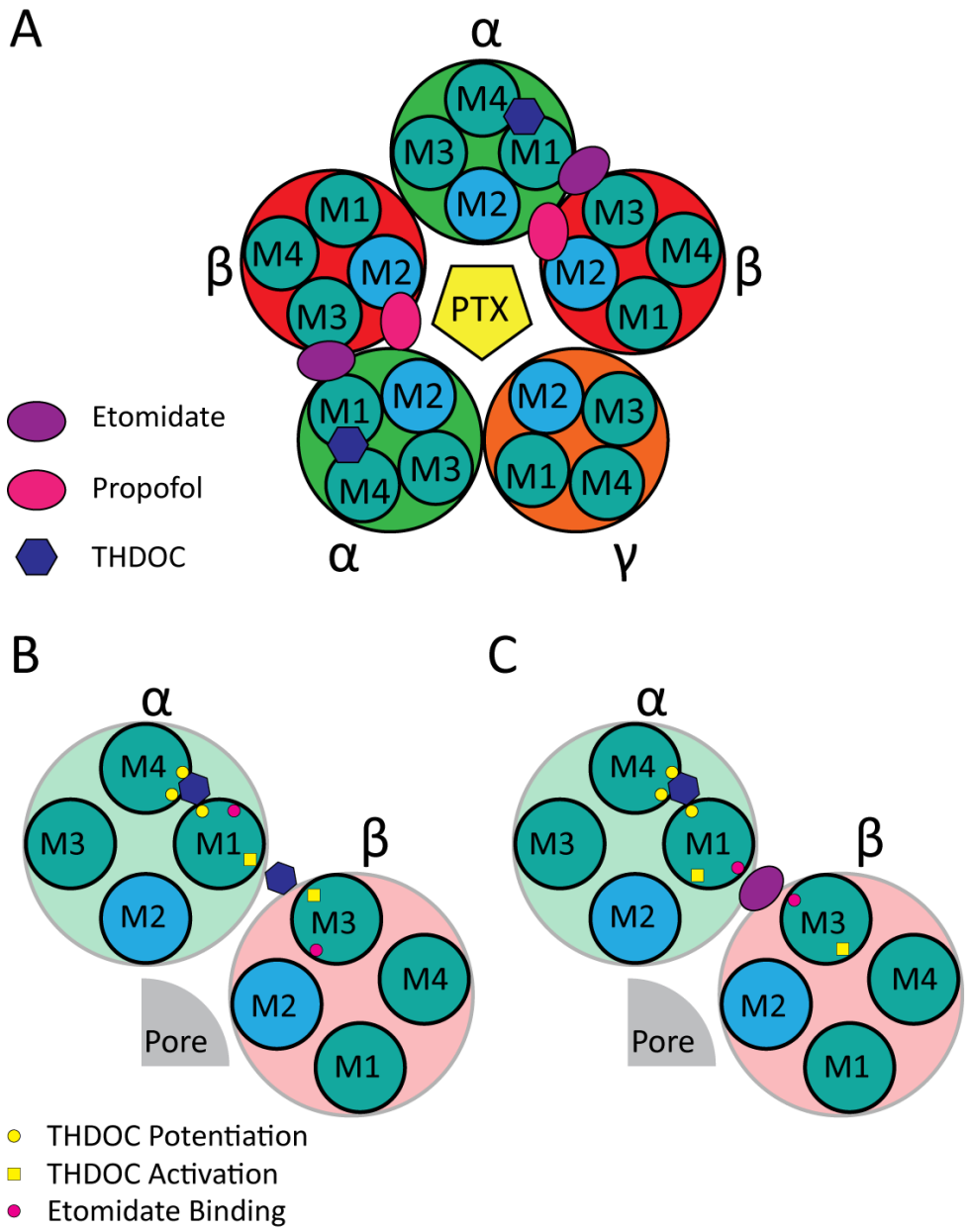

Figure 1.3 - $GABA_A$ receptor transmembrane domain pharmacology

A. Picrotoxin acts in a non-competitive manner by blocking the pore and preventing the flow of ions (Bali and Akabas., 2007; Hibbs and Gouaux., 2011). Anaesthetics bind at the interface formed with β subunits; propofol at α-β, β-α and γ-β and etomidate at β-α (Chiara et al., 2012). Endogenous positive neurosteroids, e.g. THDOC binds at an intrasubunit site within α-subunits and potentiates receptor function. **B.** Mutagenesis studies suggest THDOC potentiation is coordinated by α1 M1 (Q241) and M4 (N407 and Y410) residues and activation by different α1 M1 (T236) and β2 M3 (Y284) residues (Hosie et al., 2006) **C.** Photo-affinity labelling studies suggest that residues forming the presumed neurosteroid activation site are unlikely to be positioned at the β-α interface when etomidate is bound. Azi-etomidate photo-labelled residues at the interface are found at α1 M1 Met236 and β3 M3 Met286 (Li et al., 2009).

1.2.8. Neurosteroid modulation of $GABA_A$ receptors

An important class of endogenous $GABA_A$ receptor allosteric modulators is the potentiating neurosteroids, e.g. allopregnanolone and tetrahydrodeoxycorticosterone (THDOC). These are metabolites of progesterone and deoxycorticosterone, which directly bind to and enhance the GABA response at $GABA_A$Rs(Belelli and Lambert, 2005; Lambert et al., 2009). Experiments in the 1940's characterized the sedative and anaesthetic effect of pregnane steroids (reviewed by Lambert et al., 2009). Their mechanism and site of action however remained unknown for many years until Harrison and Simmonds (in the 1980's) used the synthetic steroidal anaesthetic alphaxalone and demonstrated that, as for other sedatives such as barbiturates and benzodiazepines, the site of steroid action was the $GABA_A$ receptor (Harrison and Simmonds, 1984; Reddy, 2010). This was confirmed by studies of endogenously synthesized steroids (in electrophysiological recordings and $^{36}Cl^-$ flux into synaptosomes), showing that they were potent modulators of $GABA_A$ receptors (Lambert et al., 2009).

Neurosteroids modulate $GABA_A$ receptors in a biphasic manner. At low nanomolar concentrations they potentiate the GABA response, whilst at higher submicromolar-to-micromolar concentrations they directly activate the receptor (Hosie et al., 2006; 2009). Interaction studies with the barbiturate pentobarbital suggested that neurosteroids bind at a distinct site (Lambert et al., 2009). This led to the postulate that these low and high concentration effects for neurosteroids were mediated by two distinct binding sites on the $GABA_A$R. Electrophysiological studies of recombinant $GABA_A$Rs using point mutations (guided by homology modelling and receptor chimeras) provided initial insight into the location of these two sites (Hosie et al., 2006). An intrasubunit potentiation (low steroid concentration) site, conserved amongst the α-subunit family, lies within a cavity of the TMD (normally occupied by membrane lipids) where steroid binding is coordinated by residues in M1 and M4 (*Fig 1.*3 *B*). At higher neurosteroid concentrations an additional site was proposed; an interfacial-binding pocket (between α subunit M1 and β subunit of M3) to initiate direct activation of the receptor (*Fig 1.3 B*). Subsequent studies on the binding of the

general anaesthetic etomidate have however questioned the precise location of the activation site, with the residues identified as forming an activation site no longer ideally located at the subunit interface for neurosteroid binding when a photoactive derivative of etomidate (azietomidate) is also bound to the receptor (Li et al., 2009) (*Fig 1.3C*). Further analysis is evidently required to probe the location of an activation site.

The need to better define the specific sites of neurosteroid action comes from the experimental and clinical evidence that suggest an endogenous role for neurosteroids in neurological and psychiatric conditions. During stress, pregnancy and following ethanol consumption there is an up regulation in steroid synthesis, and the resulting (local) nanomolar levels of steroid are able to potentiate the GABA response(Belelli and Lambert, 2005). Disruption of this endogenous neurosteroid response potentially results in a number of disorders including depression, anxiety, alcoholism and epilepsy (Reddy, 2010; Wang, 2011).The treatment of these conditions therefore represents an area for the development (and then clinical application) of synthetic neurosteroid analogs with improved pharmacokinetics and efficacy. Our ability to generate potential new candidates will benefit from a clearer understanding of the molecular mechanisms of steroid mediated responses.

In the framework of recently solved receptor structures, and on the basis of structure-function studies, we will further discuss the determinants of binding for a number of these modulators in *Section 1.6*.

1.2.9. $GABA_A$ receptors as therapeutic targets in disease states

$GABA_A$ receptors have been implicated directly in the etiology of many disorders of the brain, including: anxiety disorders, cognitive disorders, epilepsies, mood disorders, schizophrenia and sleep disorders (Johnston, 2005; Möhler, 2006; Smart and Paoletti, 2012; Rudolph and Möhler, 2014; Braat and Kooy, 2015). It is beyond the scope of this thesis to introduce all these disorders in detail. It is of little surprise that $GABA_A$

receptors form the target for a variety of pharmacological and therapeutic agents, as introduced above, which act to modify receptor activity in a manner often dependent on specific receptor subunit combinations (Rudolph and Möhler, 2014). Although a number of drugs in widespread clinical use are effective for the provision of anaesthesia and sedation, as well as in treating anxiety and insomnia (Rudolph and Knoflach, 2011), it might be reasoned that detrimental drug side-effects could be better understood by establishing how these agents act at the atomistic level. Ultimately, this will only be possible with further high-resolution structural studies, which might form the template for rationale design of compounds exhibiting greater subunit specificity.

1.3. Structural basis for pLGIC activation and allosteric modulation

As established pLGICs play a pivotal role in responding to the major neurotransmitters in the brain and mediating intracellular communication between nerve cells (Katz and Miledi, 1966). Neurotransmitter release stimulates ion flux through either cation-selective channels (principally nACh and 5-HT_3 receptors), inducing an excitatory (membrane depolarizing) response, or anion-selective (principally $GABA_A$ or Gly receptors), inducing an inhibitory (hyperpolarizing) response (Miller and Smart, 2010). Common to all these receptors is the pentameric assembly of receptor subunits around a central ion channel. Moreover, and as introduced for the $GABA_A$ receptor family, a common feature of complexity and diversity results from the multiple subunit isoforms observed across pLGICs. For $GABA_A$Rs, eight subunit families have been identified; GlyRs have two subunit families (α and β); nAChRs are formed from five subunit families (yielding 19 subunit isoforms); and 5-HT_3 are typically formed from two subunits (albeit with a total of five subunits identified thus far; Smart and Paoletti, 2012).

pLGICS are typically found as heteromeric arrangements under physiological conditions (Unwin, 1995), displaying distinct functional and pharmacological profiles dependent on the specific subunit isoforms present. Ultimately this complexity and the consequential difficulty in obtaining high yields of purified protein has precluded many of these receptors from being subjected to extensive high-resolution structural studies. The identification of receptor orthologs across wider metazoan life (from invertebrates to fish; as well as humans and mammals), and in the genomes of a few bacterial species, has ultimately provided a greater source of receptors from which to build a repertoire of pLGIC structures (Tasneem et al., 2005; Corringer et al., 2012). Indeed the first crystal structures of full-length pLGICs were from bacterial sources; *Erwinia chrysanthemi* (ELIC) and *Gloeobacter violaceus* (GLIC) (Hilf and Dutzler, 2008; Bocquet et al., 2009; Hilf and Dutzler, 2009). Unsurprisingly, given their early appearance in evolution, these bacterial receptors exhibit a simplified subunit composition, being formed of a single subunit type in a homopentameric arrangement, while exhibiting the common core of structural elements observed across the pLGIC family. More recently, and in line with advances in biochemical techniques and structure determination methods, there has been an influx of full-length (or minimally modified) receptor structures of eukaryotic lineage, including: X-ray structures of a glutamate-gated chloride channel from *C. Elegans* (GluClα), human homomeric $GABA_A$ β3, human α3 GlyR and mouse 5-HT_3 receptors; and cryo-EM structures of zebrafish α1 GlyR (Hibbs and Gouaux, 2011; Althoff et al., 2014; Hassaine et al., 2014; Miller and Aricescu, 2014; Du et al., 2015, Huang et al., 2015). From this ensemble of structures, common principles of signal transduction and receptor modulation can be identified, and the mechanisms underlying this characterised at the atomic level.

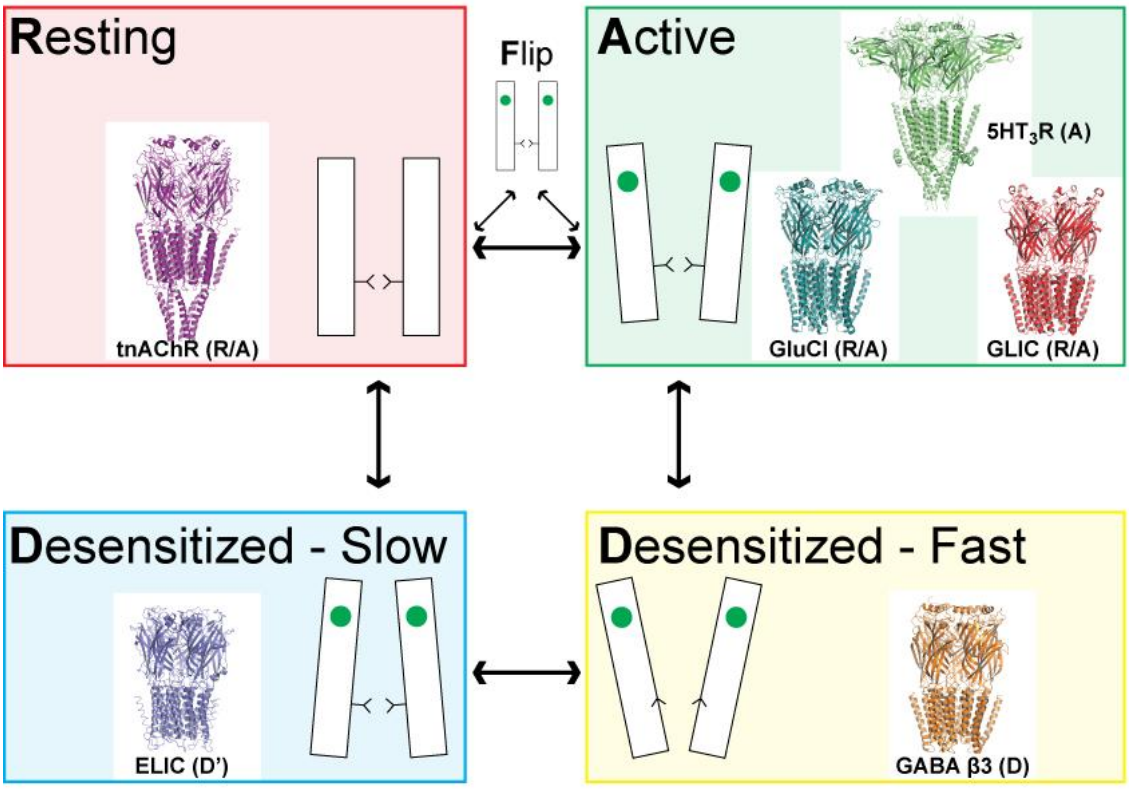

Figure 1.4 - Overview of allosteric transitions from structures of pLGICs

A simplified conformational model of signal transduction is shown in this schematic diagram derived from a summary of crystal and EM structures of receptors solved in distinct conformational states. These are based on four states: Resting, Active, Desensitized (Fast) and Desensitized (Slow), with the position of a pre-activation or "flip" state also shown. The structures are complemented by a simplified pair of subunits (rectangles) showing the ion channel gate, with (green circles) or without agonist binding. For simplicity, direct isomerisation between non-adjacent states is not shown. The position of various pLGICs shows the likely conformational state in which these were first solved. Structures of *Torpedo n*AChR, GLIC and GluClα have been generated in resting and active conditions. The 5-HT_3receptor is very similar to other published open channel structures, though with a more constricted pore conformation. ELIC and GABA β3 receptor structures are proposed to represent pLGICs in distinct desensitized states.

1.3.2. Conformational transitions in pLGIC gating

Despite the evolutionary distance between neurotransmitter-gated channels (mediating fast synaptic neurotransmission) and their bacterial orthologs (for whom physiological roles are still poorly understood), there appears to be a common allosteric scheme for receptor function (Cecchini and Changeux, 2014). At rest the ion channel is closed, preventing the flow of ions. Upon agonist binding, the receptor undergoes rapid conformational changes, resulting in channel opening allowing the passive flow of ions across the membrane (Colquhoun, 2006) (*Fig 1.4*). Typically during prolonged agonist exposure, the flow of ions diminishes as the receptor enters desensitized state(s) (in which the channel transitions to a closed state despite the presence of bound agonist; Katz and Thesleff, 1957). Eventually the receptor returns to an agonist unbound-resting form (*Fig 1.4*). Ultimately this is an over-simplified picture of events, and the allosteric transition between states is characterised by the presence of receptor intermediates. These states and the intermediates have been extensively studied by electrophysiological and computational methods and can be distinguished by their life times (Auerbach, 2015). Ultimately, obtaining high-resolution crystallographic structural information of a single receptor in all states has not yet been possible; unsurprising given that some intermediates are likely short-lived and thermodynamically unstable (and consequently refractory to crystallization).

Given the apparent conservation of three-dimensional structure across the pLGIC superfamily we can assign individual receptor structures to distinct allosteric states (*Fig 1.*4) allowing for an ensemble interpretation of receptor activation and modulation (in light of complementary functional studies). In introducing a mechanism for pLGIC activation and modulation, we have focused principally on GluClα and GLIC, which provide the most extensive repertoire of crystallographic structures for single receptors in distinct states and in complex with orthosteric agonist and allosteric modulators (Hibbs and Gouaux, 2011; Althoff et al., 2014; Sauguet et al., 2014a; 2014b). We also introduce a recent development in high-resolution structural studies of allosteric transitions of a single pLGIC (of the zebrafish α1 GlyR), made possible by

recent developments in electron cryo-microscopy (cryo-EM) (Cheng et al., 2015; Du et al., 2015).

1.3.3. General architecture of pLGICs

As epitomized by early electron micrographs of *Torpedo* nAChR (at 4Å) and latterly of GluClα (at 3.3Å, in complex with stabilizing Fab antibody fragments and ivermectin), we can define a general architecture for pLGICs (Unwin, 2005; Hibbs and Gouaux, 2011). While (pentameric) receptors can vary in molecular mass from 150 – 300 kDa (Corringer et al., 2012), the receptor is formed of five subunits, with each subunit bearing a core "modular" structure comprised of an ECD, TMD and ICD (the latter exhibiting greatest structural variability). The resulting receptor is typically 110Å in length (excluding the ICD) and 60Å wide (*Fig 1.5*).

1.3.4. The extracellular domain

The ECD of GluClα, in agreement with earlier structures of isolated-soluble pentameric ECDs of the acetylcholine-binding protein from molluscs (Brejc et al., 2001; Celie et al., 2004), is folded in an antiparallel-arrangement of β-sheets (*Fig 1.5*). The inner hydrophobic residues stabilize this immunoglobulin-like β-sandwich. While this arrangement is a common feature across prokaryotic and eukaryotic pLGIC structures, there is notable variation in the length of the connecting loops between the sets of β sheets and also in the presence of one or more N-terminal α-helices in eukaryotic receptors (that are absent in prokaryotic structures; Hibbs and Gouaux, 2011; Hassaine et al., 2014; Miller and Aricescu, 2014; Du et al., 2015, Huang et al., 2015). These connecting loops form critical intra- and intersubunit contacts involved in determining receptor assembly, the formation of an agonist binding site and in generating signal transduction elements (Taylor et al., 1999; Corringer et al., 2000). Additionally, a role for the N-terminal α-helices in receptor assembly has been proposed (from a crystal structure of the homopentameric $GABA_A$ β3 subunit) through formation of

intersubunit electrostatic interactions (Miller and Aricescu, 2014). Though discussed in greater detail in *Section 1.4*, the ECD is the site of the orthosteric agonist binding site which forms at the interface between principal (P, +) and complementary (C, -) subunits (Corringer et al., 2000) (*Fig 1.5 A*). Facing the extracellular solution, the ECD forms the access point for ions, which are able to enter a wide water-filled vestibule before reaching the ion channel (*Fig 1.5 B & C*). Within this structure lie negatively-charged residues (in cationic nAChRs) and positively-charged residues (in anionic channels), likely to be involved in ion selectivity and permeation (Hansen et al., 2008; Smart and Paoletti, 2012)

1.3.5. The ECD-TMD (coupling) interface

At the point at which the ECD is juxtaposed to the plasma membrane, connecting loops form a network of critical interactions between the receptor ECD and TMD and couple agonist binding to channel gating (discussed in Section 1.4; *Fig 1.5 A*). At the base of the ECD, sits the highly conserved Cys-loop, or loop 7, which is a loop of residues between β6-β7 strands contained within a disulphide-bridge formed between two Cys residues (Bouzat et al., 2004). While this Cys-bridge is not observed in prokaryotic pLGICs, a critical role for Loop 7 in receptor gating is still retained (Sauguet et al., 2014b). Loop 7 forms the main contributor to the ECD-TMD interface, and carries a canonical ΦPΦD (where Φ is typically an aromatic residue; Cecchini and Changeux, 2014). Additionally the pre-M1 linker (M1 being the first transmembrane spanning α-helix), loop 2 (between β1-β2), loop 9 and M2-M3 loop form the remainder of the ECD-TMD interface (Lyford et al., 2003; Newell et al., 2004). It is noteworthy that while primary sequence might differ in this region, the three-dimensional structure of this interface is strongly conserved across all pLGICs and is critical to the mechanisms of receptor signal transduction. This concept is supported by the generation of a range of functional pLGIC ECD-TMD chimeras, most notably of a prokaryotic-eukaryotic chimera between the ECD of GLIC and the TMD of the α1GlyR subunit (Duret et al., 2011; Moraga-Cid et al., 2015).

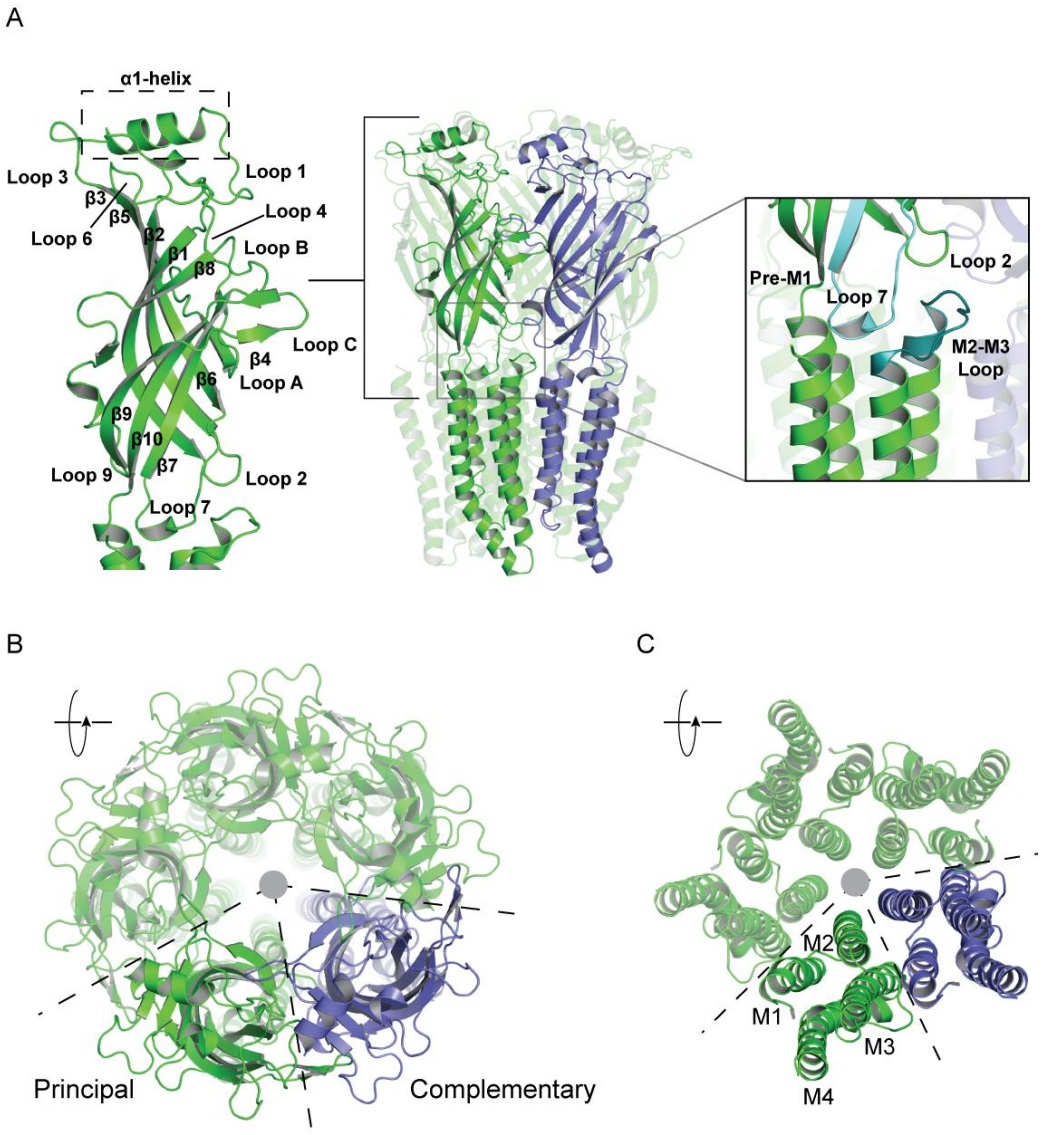

Figure 1.5 - General architecture of a pLGIC: GluClα from C. elegans

A. GluClα from *C. elegans* solved in complex with L-glutamate, ivermectin and Fab antibody fragments is shown viewed parallel to the membrane. Fab fragments have been removed in this representation. The principal subunit is displayed in green and complementary subunit is in blue. The left panel shows the structure of the extracellular domain of the principal subunit. The position of the binding loops and the N-terminal α-helix is shown. The inner and outer β-sheets of the ECD are indicated. Right panel shows the ECD-TMD interface, involved in coupling agonist binding to channel gating. Crucial structures are highlighted: Loop 2 formed by β1-β2, Loop 7 ("Cys-loop", light blue) formed by β6-β7, the pre-M1 region and the M2-M3 loop (teal). Interactions in this region underlie the "coupling" process **B.** The arrangement of subunit ECDs when viewed from the extracellular space down the five-fold pseudo-symmetry axis (pore position shown by the grey circle). Colouring as in A. **C.** Pentameric arrangement of TMDs around the pore (grey circle) and relative position of M1 – M4 helices and M2-M3 loop**.** Colouring as in A.

1.3.6. The transmembrane domain

As observed in early EM structures of *tn*AChR, and in all subsequent high resolution (full-length) pLGIC structures, each subunit exhibits four transmembrane spanning segments that fold into the α-helices M1-M4 (*Fig 1.5 C*; Miyazawa et al., 2003). These four helices are arranged to form a bundle distinct to that observed in ionotropic glutamate receptors and inverted potassium channels (Zhou et al., 2001; Kumar and Mayer, 2013; Karakas and Furukawa, 2014; Lee et al., 2014). The second M2 α-helices form the channel pore, which are stabilised through interactions with neighbouring M2 helices and buttressed by M1 and M3 helices of the same subunit (Miyazawa et al., 2003; Corringer et al., 2012). The identity of M2 residues lining the pore is similar or identical across members of the pLGIC family, including hydrophobic residues at the mid-point of M2 forming a channel gate (at 9') and charged residues (conserved amongst cationic or anionic channels) forming the selectivity filter (Miller and Smart, 2010; Smart and Paoletti, 2012). The orientation of the M2 helices is dependent on the receptor's activation state. Conformational changes in M2 occur as a result of both rigid-body motions and bending or "kinking" of the M2 helix, which must therefore exhibit a degree of inherent flexibility (Miller and Smart, 2010; Prevost et al., 2012; Sauguet et al., 2014b; Bera and Akabas, 2005). Positioned at the periphery of the four helix-bundle lies the M4 α-helices. These face the lipid bilayer, and forms crucial interactions with membrane lipids to modulate receptor function (Barrantes, 2015; Carswell et al., 2015).

1.3.7. The intracellular domain

Extending into the intracellular space of the cell is the large and variable M3-M4 loop, or intracellular domain (ICD). Though not conserved in prokaryotic pLGICs (where short linkers are observed), the M3-M4 loop can be in excess of 100 residues in eukaryotic pLGICs and forms the binding site for receptor accessory and trafficking proteins (Moss and Smart, 2001; Smart and Paoletti, 2012; Stokes et al., 2015). While much of this

forms an unstructured mass, EM-structures of *tn*AChR and crystal-structure of mouse 5-HT_3 receptor reveal an additional intracellular MA helix (and also shorter MX helix for 5-HT_3 receptor; Unwin, 2005; Hassaine et al., 2014). The MA helix extends the ion permeation pathway beyond the channel formed by the TMD M2 helices, and likely plays additional roles in ion conductance (Kelley et al., 2003). While missing from anionic-receptor crystal and EM structures; GluClα, $GABA_A$ β3, $GlyR_{EM}$ (noting that the native ICD was replaced with shorter linkers), the existence of such secondary structure in anionic pLGICs is less clear.

1.4. Mechanism for agonist binding and channel gating (from GluClα and GLIC)

Within the general framework of crystal structures of GluClα, it is possible to formulate a mechanism of how agonist binding at a site in the ECD is able to gate the ion channel.

1.4.1. Orthosteric agonist binding

The first step in channel activation is the binding of agonist. Early studies revealed that agonist binding occurs at an interfacial site between neighbouring subunits, with contributions from three binding loops on the "principal" subunit (Loops A, B and C) and three loops (Loops D, E and F) on the "complementary" subunit (Corringer et al., 2000; Brejc et al., 2001).

Largely conserved across all pLGICs, the rules governing the formation of an agonist binding interface is dependent on subunit composition and stoichiometry. For example, in heteromeric α1β2γ2 $GABA_A$ receptors binding strictly occurs at the two the β-α interfacial positions (Smart and Paoletti, 2012), while binding at all five equivalent positions is possible in homomeric arrangements, as observed in $GABA_A$ ρ1, Gly α1 and nAChR α7 receptors (Amin and Weiss, 1996; Beato et al., 2004).

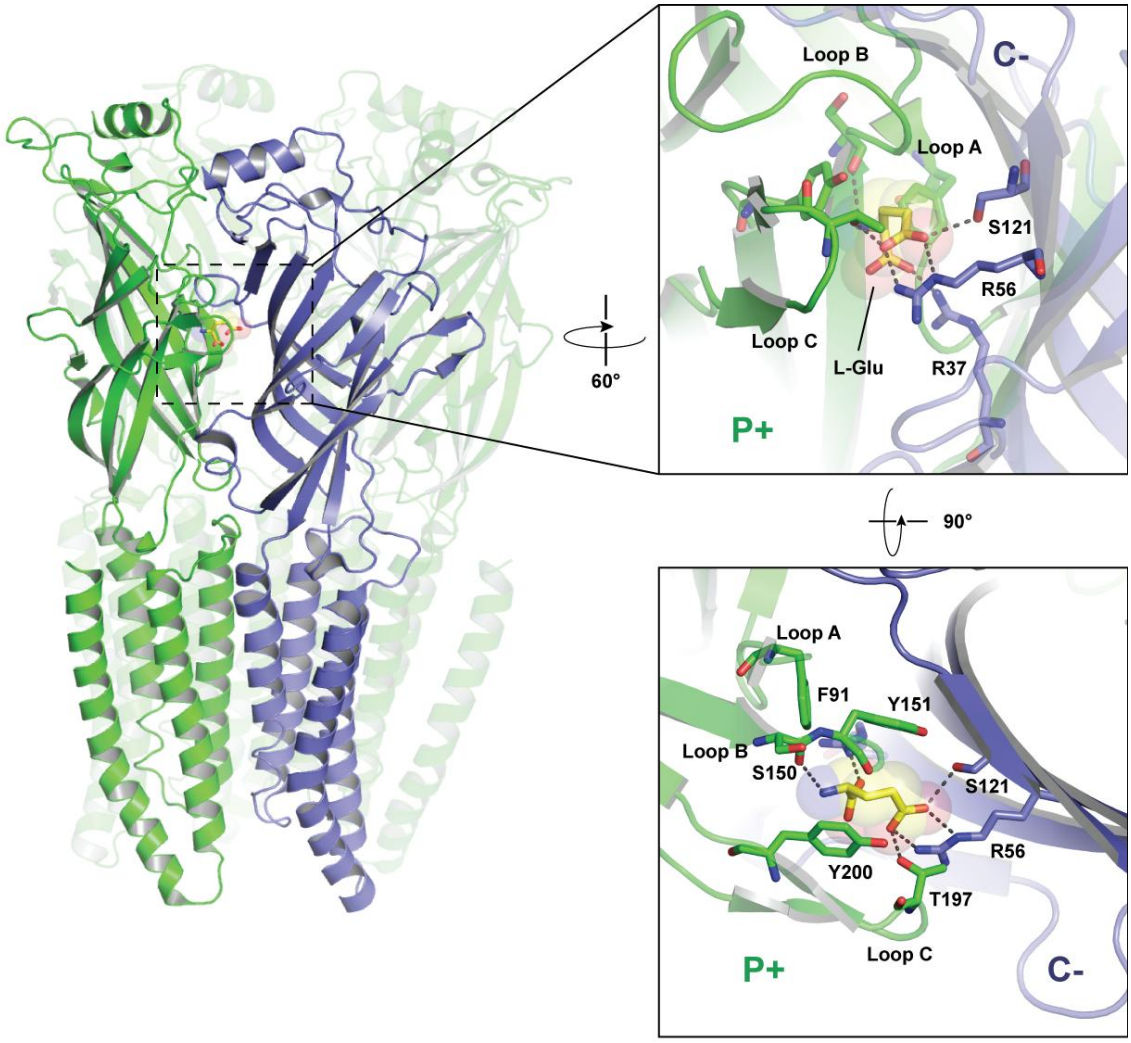

Figure 1.6 - The orthosteric agonist binding site: Glutamate bound GluClα

The principal and complementary subunit interface of GluClα with bound L-glutamate shown in stick and sphere representation. L-glutamate binds at the orthosteric agonist binding site formed by Loops A, B and C of the principal subunit (green) and Loops D, E and F of the complementary subunit (blue). Panel top right; view of the binding site parallel to the membrane following rotation of the structure in the main figure. Dashed lines indicate hydrogen bonding between residues of the binding pocket and L-glutamate. Panel bottom right; a view of the binding site from the extracellular space following rotation of the structure shown in the top panel. The network of interactions orientating the agonist in the binding pocket can be clearly observed. Cation-π interaction between α-amino nitrogen of glutamate and Tyr 200 on loop C also contributes to agonist binding.

Crystallographic structures of the soluble Acetylcholine-binding protein (AChBP) confirmed the position of the agonist binding site and provided the first high-resolution details of ligand recognition(Brejc et al., 2001; Celie et al., 2004). An "aromatic box" of residues (contributed by the binding loops) stabilized the agonist molecule (ACh) through cation-π interactions(Thompson et al., 2010); in AChBP these are Loop A – Tyr, Loop B -Trp, Loop C - two Tyr and Loop D – Trp. This arrangement is essentially observed in full-length agonist bound receptor structures. In GluClα, L-glutamate (the endogenous agonist) is coordinated by aromatic residues on Loops A, B and C, though Arg (and Lys) residues on loops D and E of the complementary subunit also coordinate agonist binding through electrostatic interactions with the glutamate carboxylate moiety (*Fig 1.6*; Hibbs and Gouaux, 2011).

Surprisingly, the general mode of agonist binding is conserved even in receptors separated considerably in evolution. ELIC, from the plant pathogen *E. chrystanthemi*, is gated by primary amines and the neurotransmitter GABA (Spurny et al., 2012). Co-crystallization studies have revealed that binding occurs at the orthosteric site, with GABA caged by aromatic residues of binding loops from the principal and complementary subunits. Moreover, a crystal structure of the GABA β3 homopentameric receptor reveals further details of the agonist-binding pocket.

Though not gated by the orthosteric agonist GABA, this receptor was crystallized in the presence of a novel agonist, benzamidine (which functionally gates the channel; Miller and Aricescu, 2014). In agreement with the consensus model, the agonist was coordinated at the neurotransmitter binding pocket by stacking interactions between the benzyl ring (of benzamidine) and aromatic residues of the binding loops, and further coordinated by putative polar, electrostatic and cation-π interactions (Miller and Aricescu, 2014).

It is notable that this aromatic support is broken in the prokaryotic pLGIC homolog GLIC (Bocquet et al., 2009; Hilf and Dutzler, 2009; Nury et al., 2010). In contrast to other members of the pLGIC family, the orthosteric agonist of GLIC is protons (Bocquet et al., 2007). These do not bind at a site overlapping with Loops B and C, and are likely to bind at one or more sites elsewhere in the ECD (Duret et al., 2011; Gonzalez-Gutierrez et al., 2013). Despite this, antagonism of the proton-elicited current of GLIC

has been observed by cinnamic acid derivatives, with molecular docking studies suggesting that binding (via interactions with the carboxylate moiety of the acid) occurs at a interfacial site in the ECD slightly below the orthosteric site (Prevost et al., 2013).

1.4.2. Loop C capping

Following agonist binding but prior to the global reorganization of the receptor resulting in channel opening, it is postulated that the receptor occupies an intermediate preactivation or "flip" state (*Fig 1.4;* Lape et al., 2008). In this state the channel remains closed, and apparently stabilized by the occupancy of (full) agonists (but incompletely by partial agonists). It is proposed that the C-loop, and more specifically a capping motion (i.e. repositioning itself closer to the agonist molecule), might stabilize this intermediate (Miller and Smart, 2010). Ultimately without further structural information it is difficult to determine whether this "flip" state forms a discrete structural state or series of states prior to full activation (Mukhtasimova et al., 2009).

1.4.3. Rigid body motions of the ECD of GluClα

Following agonist binding (and passage through an intermediate pre-activation or "flip" state) a wave of conformational transitions occurs resulting in channel opening. In light of crystal structures for GluClα and GLIC in ascribed resting and active states we can begin to understand the concerted motions that occur during this process.

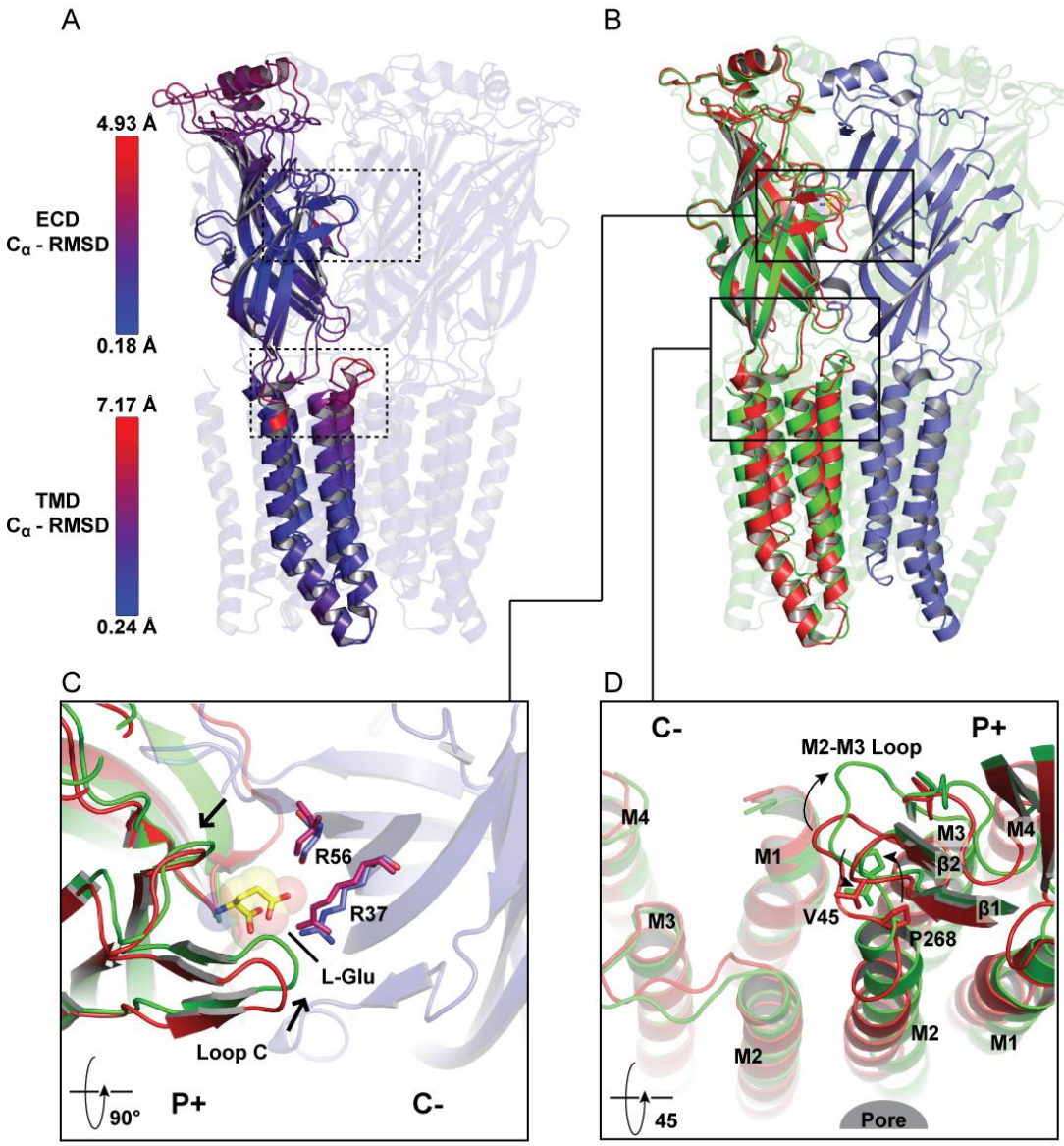

Figure 1.7 - Loop C closure and ECD-TMD transitions during activation of GluClα

A. Superposition of principal subunits (viewed parallel to the membrane) of apo- and ivermectin-GluCl. Subunits are colour-coded to show distances between equivalent $C_\alpha$atoms in transition from closed to open and from open to closed states (using the colorbyrmsd.py script in Pymol). The ECD and TMD of a complete pentamer were aligned individually. Residues 103-105 were missing in the apo-GluCl structure and were excluded from these calculations. Notable regions of low (e.g. binding pocket) and high (e.g. top of TMD) movement are indicated. **B.** Superposition of a single subunit of apo- and L-glutamate/ivermectin-GluCl (PDB 3RIF) shows global movement on transition from the closed to agonist-bound open state. **C.** Binding site closes after agonist binding through rigid body motions. Movement of arginine residues on the complementary face are shown (Apo-magenta) and (L-Glut-Blue) **D.** Superposition of TMD of complementary subunit shows movement at the ECD-TMD interface in the principal subunit, as viewed across the channel pore. For clarity only the TMD of the complementary subunit is shown.

Superposition of the principal subunits of GluCl in the apo (resting) and ivermectin/glutamate-bound (active) states reveal that the ECD and TMD move largely as rigid bodies (*Fig 1.7 & 1.8;* Hibbs and Gouaux, 2011; Althoff et al., 2014). Notable hotspots of movement (following agonist binding) are seen at the top of the pore lining M2 helix and the M2-M3 loop (as defined by fluctuations in C_α-Root Mean Square Deviation (RMSD) between open and closed states; *Fig 1.7 A*). Movement of the β-sandwich of the ECD reveals a twisting of the entire subunit around the pore axis and simultaneous tilting towards the centre of the pore. This consequently results in a compaction of the subunit interface. At the level of the agonist binding site loops A, B and, most notably, loop C close the binding pocket around glutamate as a result of (rigid body) twisting of the extracellular domain (*Fig 1.7B & C*). Notably Loop C does not appear to move as an independent entity, as had been proposed from agonist bound structures of AChBP (Celie et al., 2004; Hansen et al., 2005). In closing the binding pocket, glutamate is stabilized through the interactions described previously. Additional displacement of arginine residues on the complementary face allows for accommodation of glutamate in the compacted binding pocket (*Fig 1.7 C*), and subsequently reinforces binding through hydrogen bonding (Althoff et al., 2014).

1.4.4. Coupling at the ECD-TMD interface of GluClα

The coupling interface, formed by connections between the ECD and TMD, undergoes significant reorganization during channel activation, consistent with extensive functional data (Reeves et al., 2005; Lee et al., 2008). Interactions are observed between the (inner) β1-β2 loop (Loop 2) and M2-M3 loop, as well as the Cys-loop (loop 7) and extracellular ends of the transmembrane spanning helices (*Fig 1.7 D*). In transitioning from the resting to active state of GluClα, loop 2 moves towards the M2-M3 loop, which in turn is displaced away from the channel pore (towards the receptor's periphery).The result of this is a tilting of the M2 helix away from the ion channel.

1.4.5. GluClα activation opens the ion channel

Superposition of the transmembrane domains further reveals how these conformational rearrangements result in channel opening. In the apo state M2 helices lining the channel are orientated perpendicular to the plane of the membrane (Fig 1.7, 1.8 and 1.9). A hydrophobic gate is formed by the side chains of 9' Leu (L254) residues, restricting the pore radius to ~1.4 Å and occluding the channel (*Fig 1.9)*.As chloride ions having a Pauling radius of 1.8 Å ion flow is restricted in this state (Hibbs and Gouaux, 2011)**.** Upon activation, the TMD expands at the extracellular side following clockwise rotation of M3 and M4 (around the centre of the helical bundle) and tilting of the M2 helix away for the pore (*Fig 1.8*). The channel gate formed by side chains of 9' Leu residues is now removed, moving out of the channel pore and allowing for the passage of chloride ions. Notably the channel remains constricted at the intracellular side (at the level of the -2' proline), though with a diameter of 4.6 Å still able to allow the passage of chloride ions (*Fig 1.9*).

It should be noted in interpreting structures of GluClα that active-open channel forms of the receptor were determined in the presence of the allosteric modulator ivermectin. Ivermectin, as discussed below, wedges itself between M1 and M3 helices of adjacent subunits to stabilize an open channel. The open channel structure is essentially identical in both the absence and presence of orthosteric agonist L-glutamate (Hibbs and Gouaux, 2011). Moreover the orthosteric agonist-binding site is near identical regardless of whether glutamate is bound or not. To corroborate the interpretations of GluCl structures, one can compare the global architecture and relative re-arrangements to those observed for the prokaryotic homolog GLIC, solved under resting (neutral pH) and active (acidic/low pH) conditions. These structures are free of the constraints that ivermectin and/or antibody fragments (used as crystallization aids) may have imposed on GluClα structures (Hibbs and Gouaux, 2011; Sauguet et al., 2013b; 2014b).

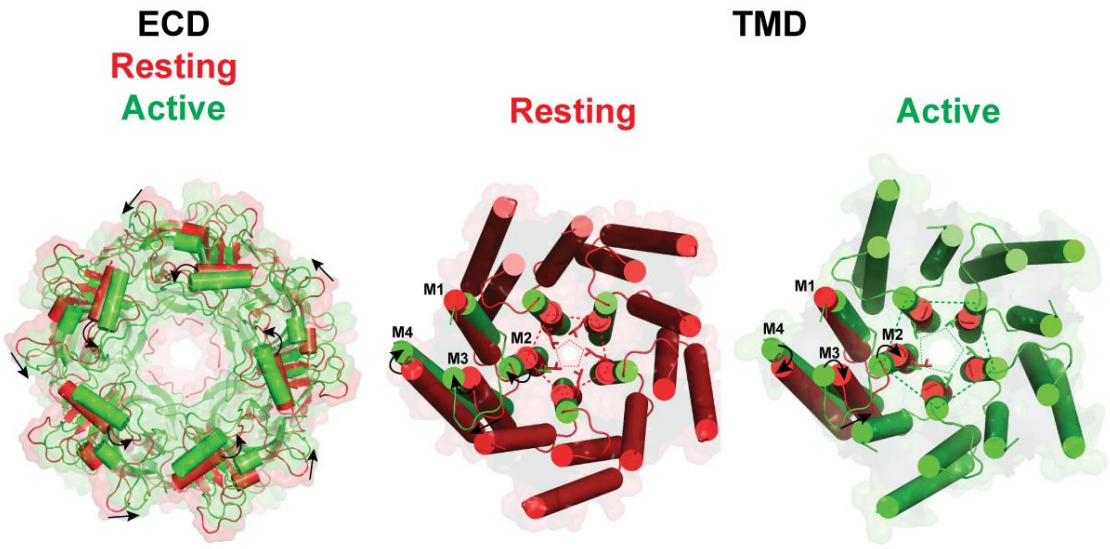

Figure 1.8 - ECD and Ion channel conformational changes during GluClα activation

Apo-GluCl (red) and Ivermectin-GluCl (green) were globally aligned (using the entire pentamer) to show overall changes in conformation in the ECD and TMD. There is a counter-clockwise twist of ECDs, resulting in compaction of the subunit interface. N-terminal α-helices move towards the five-fold symmetry axis upon activation (though there is an overall expansion of the extracellular access pore). In the TMD there is an apparent clockwise rotation of the entire domain (around the pore axis) and within the helical bundle. Upon activation M2, M3 and M4 helices rotate in clockwise manner around the centre of the bundle. The M2 α-helices are in a straight conformation (in the apo-state) and are tilted away from the pore axis (at the extracellular end) in the active state. Constriction and expansion at the extracellular end of M2, and at the hydrophobic gate formed by M2 9' Leu residues is shown by dotted lines between subunits.

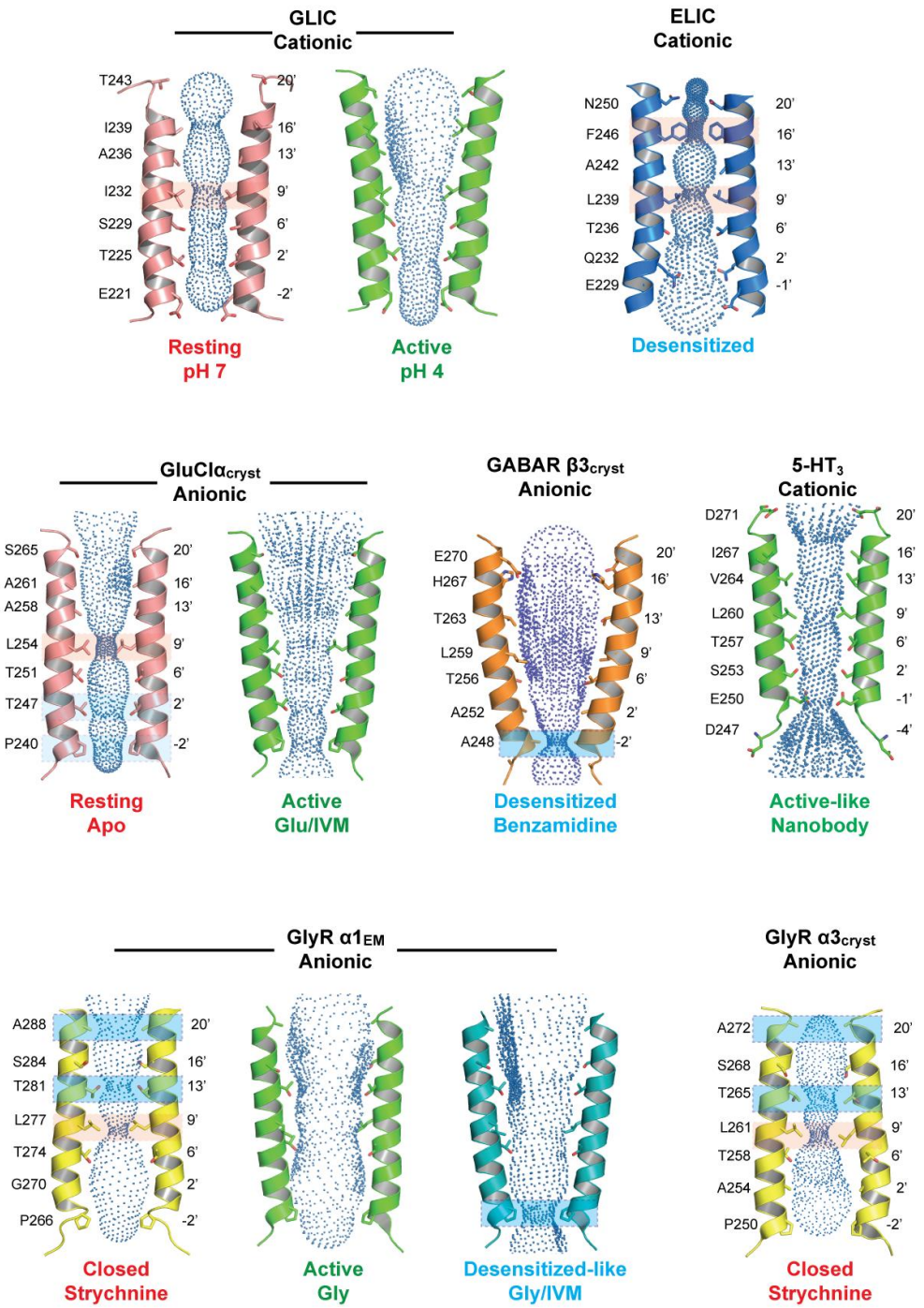

Figure 1.9 - Ion channel profile across pLGIC activation states

Side view of M2 helices for indicated states of various pLGICs (Hilf and Dutzler., 2008; Bocquet et al., 2009; Hibbs and Gouaux, 2011; Althoff et al., 2014; Hassaine et al., 2014; Miller and Aricescu, 2014; Sauguet et al., 2014b; Du et al., 2015, Huang et al., 2015). M2 residues are shown in stick formation. Volume accessible to solvent is shown as spheres (analysed using Caver software with probe radii of 0.9 Å (Petrek et al., 2006)). Red shaded boxes show constriction of <1.8Å radii and blue boxes of 1.8 – 3.3 Å radii.

1.4.6. Mechanism for activation from GLIC

By superposing the principal subunits of GLIC solved in a resting state at neutral pH 7, and in an active state (PDB 4HFI) at acidic pH 4, reveals distinct similarities and differences to GluClα with regards to the global domain reorganization associated with channel gating (*Fig 1.10*). The ECD, as in GluClα, behaves as an approximate rigid body, whilst the TMD in contrast displays reduced global reorganization compared to GluClα, but with a pronounced movement of the M2 helix.

1.4.7. Rigid body movements of the ECD close the orthosteric binding site

The ECD domain under resting conditions adopts an extended conformation, with each subunit's β-sandwich positioned away from the five-fold symmetry axis. In contrast to GluClα, this positions the ECD in a relatively loose arrangement, with each subunit distal to neighbouring subunits and the orthosteric binding site expanded in volume. Upon activation, after exposure to low pH, the entire ECD undergoes global anticlockwise twisting and "un-blooming" motions (*Fig 1.10 A and B*). This brings the ECD in to a less extended configuration, with the β-sandwich positioned closer to the central axis of the receptor. Through these twisting and "un-blooming" motions the subunit interface becomes compacted, and there is apparent closure of the orthosteric binding site loops B and C (which follows the global rotation of the ECD; *Fig 1.10 A*).

In the context of pLGICs which display agonist binding at the orthosteric site, closure of loop C would act to facilitate agonist binding and stabilization, whilst movements in loop B likely serve to transmit structural information to initiate channel opening (Sauguet et al., 2014b; Auerbach, 2015). This might explain the observation that substitution of residues in loop B of $GABA_A$ receptors is capable of initiating spontaneous channel opening (Newell et al., 2004). Whilst the global closure of the binding pocket of GLIC (upon proton activation) is consistent with the wealth of knowledge for agonist binding in AChBP structures, as observed for structures of

GluClα, it reveals a contraction based upon quaternary rearrangements, rather than flexing of loop C.

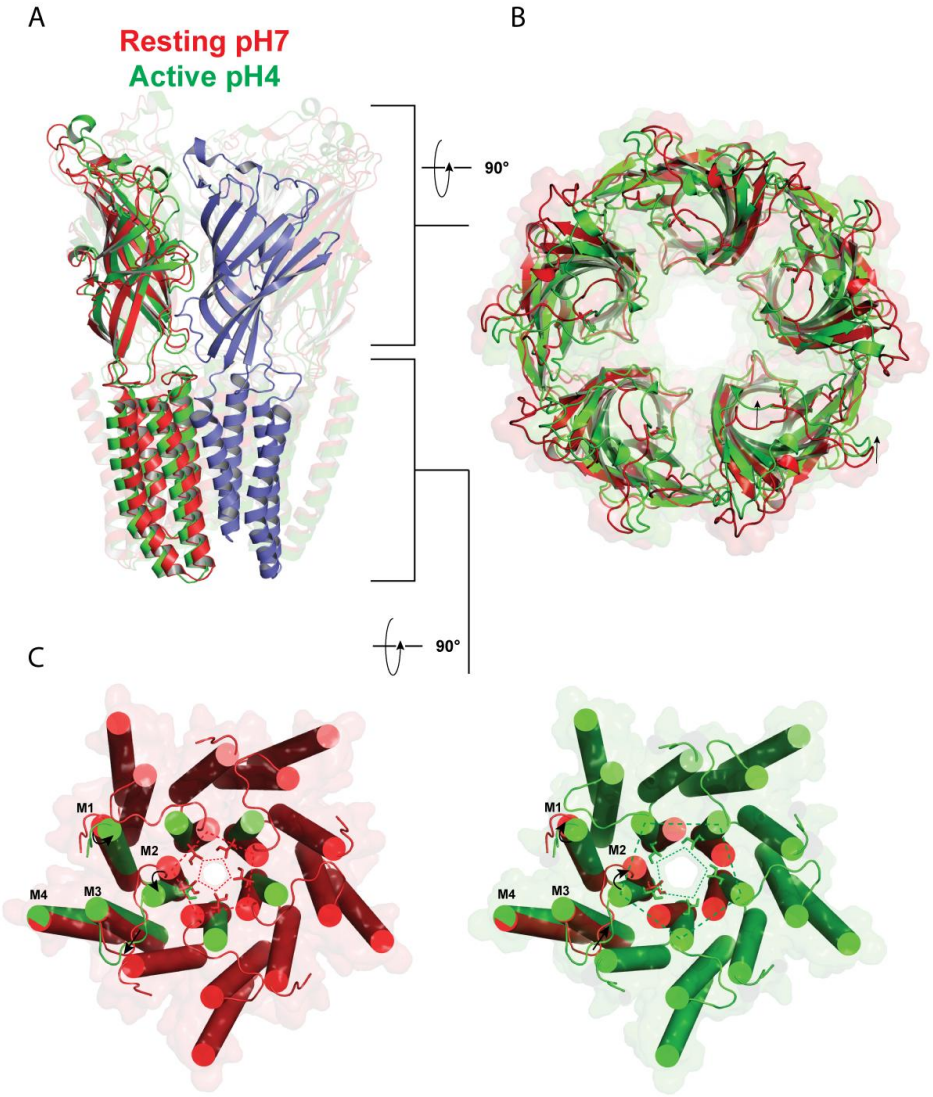

Figure 1.10 - ECD and Ion channel conformational changes during GLIC activation

A. Superposition of single subunits for resting (neutral pH 7, red) and active (pH 4, green) GLIC shows global movement on transitioning from closed to an agonist-bound open state. In the resting state the ECD forms an extended conformation, increasing the interface volume between neighbouring domains. B. Superposition of the ECD (pentamer) reveals twisting of the β-sandwich upon channel activation and radial movement towards the pore-axis thereby reducing the volume of ECD-ECD interface. C. Rearrangement of the TMD during activation (closed – red to open – green). M1 and M2 helices rotate in clockwise manner, while M3 and M4 are largely immobile. The upper end of M2 tilts away from the pore axis revealing a global iris-like opening of the channel. Constriction and expansion at the extracellular end of M2 and at the hydrophobic gate formed by M2 9' Leu residues is shown by dotted lines between subunits.

It is notable that the binding site for protons in GLIC has yet to be identified. While it is thought to reside in the ECD (though at a site not overlapping the orthosteric agonist binding pocket), there is also an argument that protonation of an M2 Histidine (H235) is sufficient to stabilize the open channel, which closes upon deprotonation in molecular dynamic simulations (Duret et al., 2011; Wang et al., 2012; Prevost et al., 2013). Of similar note, it is significant that in structures of GluClα in the absence of orthosteric agonist (glutamate), but presence of allosteric agonist (ivermectin) a compaction of the orthosteric binding pocket is still observed. Regardless of the location of proton binding, it is maybe not surprising that the orthosteric site undergoes rearrangement in GLIC. This might be considered to be a structural consequence of the quaternary rearrangement of the ECD upon activation and is inherently required for the transfer of information across the receptor(i.e. from the ECD to the TMD; Auerbach, 2015).

1.4.8. Coupling at the ECD-TMD interface of GLIC

At the coupling interface between ECD and TMD there is transition of key structural elements which underpin signal transduction. During the transition from resting to active states there is a redistribution of hydrophobic interactions between loop 2, pre-M1 and loop 7, which serves to increase connectivity to the TMD via the M2-M3 loop. At the global level the M2-M3 loop moves (horizontally) away from the pore axis, towards the receptor periphery (*Fig 1.10 C*). This position (in the open form) is stabilized by a steric block of a conserved proline (23') in the M2-M3 loop by residues at the tip of loop 2 (as also proposed for GluClα; Calimet et al., 2013).

1.4.9. Proton activation of GLIC opens the ion channel

In contrast to the global rotational rearrangement of all helices in the TMD of GluClα (on transition from closed to open state), activation of GLIC at the level of the TMD is characterized by localized rearrangements. As in the apo-structure of GluClα, under

resting conditions M2 helices lining the channel are orientated perpendicular to the plane of the membrane, forming a constriction of the channel at the level of the 9' Ile residue (the hydrophobic channel gate; *Fig 1.9 and Fig 1.10*). This constriction, though less narrow than that observed in GluClα, is not compatible with hydrated ion flow, thus delineating a non-conductive state. Upon activation, M3 and M4 helices remain largely stationary, while M1 tilts in the uppermost half, towards the pore. The channel lining M2 helices tilt at the extracellular end, opening the channel with an iris-like motion (*Fig 1.10*). The direction of this flexure follows the line of horizontal movement of the M2-M3 loop, and is tangential to the channel axis (rather than the radial movement of M2 helices observed in GluClα). As a result of M2 tilting, the extracellular side of the channel expands, with Ile 9' residues moving out of the pore, and the channel adopting an open conformation (*Fig 1.9 & Fig 1.10*). As in structures of GluClα, the intracellular end of M2 is largely immobile during this process.

In summary, the mechanism of channel gating (at least in transition from closed to open conformations) appears largely conserved, and is consistent with EM-structures of tnAChR captured by plunge-freezing methods (Unwin and Fujiyoshi, 2012). Underlying this is the re-configuration of M2 helices from a straightened conformation, in the closed form, to a locally tilted or flexed conformation, in the open form, and consequential displacement of hydrophobic 9' residues forming the channel gate. Indeed an array of functional studies across the pLGIC superfamily emphasise the importance of this 9' position in gating, and more specifically in stabilizing the channel in a closed state under resting conditions (Revah et al., 1991; Chang and Weiss, 1998; 1999; Bocquet et al., 2007). Mutation of the hydrophobic 9' residue to polar residues induces gain-of-function, stabilizing the channel in the active state and characterised by spontaneous channel activity (than can be antagonized by channel blocking agents).

1.5. A mechanism for pLGIC desensitization

While structures of GLIC and GluClα provide means for high-resolution structural analysis of receptors in closed and open states, they do not suggest a mechanism for

the structural re-configuration that occurs upon transition through to a desensitized state. At the functional level, neither GLIC nor GluClα_{cryst} exhibit properties (in macroscopic electrophysiological recordings) to suggest that these receptors undergo pronounced desensitization during prolonged “crystallization” agonist exposure (e.g. pH 4 and ivermectin; Etter et al., 1996; Bocquet et al., 2007; Hibbs and Gouaux, 2011; Laha et al., 2013). This possibly provides a reason as to why these receptors are stabilized in the open channel conformations in the crystal form. Unravelling the structural re-arrangements underpinning desensitization has ultimately proved to be more elusive.

Desensitization represents a reduction in receptor response during prolonged agonist exposure, and is a conserved property amongst most pLGICs (Katz and Thesleff, 1957). At the level of the ion channel this state reflects the transitions from an active-open channel to desensitized closed-channel conformation (where agonist is bound continuously), and a consequential reduction in ion flow (Papke et al., 2011). At the physiological level, desensitization is likely to play roles in reducing postsynaptic currents, and thereby protecting nerves cells to repetitive transmitter release. Moreover, desensitization can serve to modulate the time-course of decay of the post-synaptic currents and additionally play a role in tuning the (tonic) response of extrasynaptic receptors to low, ambient concentrations of agonist (Jones and Westbrook, 1995; Bianchi and Macdonald, 2002).

Single-channel electrophysiological recordings of nAChRs suggest that there are at least two distinct kinetic components to the desensitization response (Sakmann et al., 1980). Receptors transition to a fast desensitized state, with a lifespan of the order of 10-100 ms, and subsequently into a slow desensitized state, in which the receptor can reside over a timescale of seconds. Elucidating the likely structures of these states proved difficult for a long period of time. However, on the basis of recent functional and structural evidence we can begin to understand the potential re-arrangements that occur during desensitization and the profile of the channel lining helices.

1.5.1. Re-arrangement of the ECD-TMD occurs during desensitization

Previous functional data has suggested structural elements in the ECD and at the ECD-TMD are responsible for setting receptor desensitization(Bouzat et al., 2008; Wang and Lynch, 2011). In the latter case, and on the basis of voltage fluorimetry experiments of the α1-GlyR, conformational changes are observed in pre-M1, loop 2 and M1 α-helix(Wang and Lynch, 2011). While these changes were reported to be specific to desensitization, it is pertinent to note that these regions are also important in setting the efficacy of channel gating, which might obscure whether observed changes relate to the macroscopic or microscopic rates of desensitization (Pless and Lynch, 2009b; Gielen et al., 2015). Though macroscopic electrophysiological recordings of GLIC do not reveal receptor desensitization, double electron-electron resonance (DEER) experiments of GLIC reconstituted into liposome reveals a proton-induced desensitized state (Velisetty and Chakrapani, 2012; Dellisanti et al., 2013). This response is apparently mediated by rearrangement of interfacial loops; loop 2, M2-M3 loop and loop 9. During the transition from closed to desensitized state loop 2 becomes less mobile and loop 9 shows considerable mobility (Dellisanti et al., 2013). Moreover, DEER experiments confirm that the GLIC pH 4 structure does not correspond to a desensitized state (Dellisanti et al., 2013).

1.5.2. A desensitization gate is located in the ion channel

While it is likely that the ECD-TMD undergoes substantial rearrangement during desensitization, functional studies have pointed towards a second model for receptor desensitization. This model proposes that receptor desensitization proceeds from the open state of the channel and suggests the involvement of a “desensitization” gate located within the channel (Auerbach and Akk, 1998). This gate would be distinct to the “activation gate” formed by the ring of hydrophobic residues at the 9’ M2 position. Affinity labelling studies of nAChR with a hydrophobic probe 3-(trifluoromethy)-3-(m-iodophenyl) diazirine (TID) revealed a decrease in labelling at the level of the M2 9’ residue during the transition from open to fast desensitized states, suggesting local

conformational change in the channel (Yamodo et al., 2010). Moreover electron paramagnetic resonance (EPR) spectroscopy experiments (to measure distance between spin–labelled Cys residues) of GLIC reconstituted into liposomes proposes that desensitization involves a distinct gate between 2' and 9' M2 residues (albeit with experimental caveats that should be accounted for**,** including the size of the introduced spin labels and restrictions on motion; Velisetty and Chakrapani, 2012).

These studies all point towards the existence of a distinct desensitization gate, the location of which being mid-way up the channel pore. Recent studies of a desensitization gate in α1β2γ2 $GABA_A$ and α1 Gly receptors suggest a distinct pore location (Gielen et al., 2015). Given that open channel structures (GLIC and GluClα) reveal a narrowing of M2 helices down to the (intracellular) -2'residues and that at a functional level desensitization likely proceeds from an open channel state, it was postulated that desensitization might result from an 'extension' of the activation process. The likely location of a 'desensitzation gate' would by this principal be proximal to the cytoplasmic portion of the channel. Indeed mutagenesis of residues along the cytoplasmic end of M2/M3 interface had a pronounced effect on receptor desensitization. Additionally, the channel blocker picrotoxin (which binds at the level of 2' Thr and -2' Pro residues in crystal structures of GluClα) was shown to prevent desensitization, in accord with an overlap of a picrotoxin binding site and 'desensitization gate' (Hibbs and Gouaux, 2011). Moreover, the model proposed would be consistent with experimental data to suggest that picrotoxin is trapped in the resting, but not desensitized, state of the $GABA_A$ receptor(Bali and Akabas, 2007)**.**

Capturing a single receptor in a number of gating states (with different life spans and thermodynamics) provides a significant challenge. With regards to receptor structure during desensitization, we can however use existing experimental data to assist in interpretation of crystallographic (and more recently cryo-EM) structures of receptors in distinct states.

While nearly 20 crystal structures of the prokaryotic pLGIC ELIC have been solved, and in the presence of orthosteric agonists including GABA, cysteamine and (bromo)propylamine, the conformation of the channel always delineates a closed non-conductive state (Zimmermann and Dutzler, 2011; Gonzalez-Gutierrez et al., 2012;

Spurny et al., 2012). Structures of ELIC are characterized by a hydrophobic constriction of the channel at the M2 9' Leu and 16' Phe residues (*Fig 1.9*). Whilst this was initially interpreted as a resting form of the receptor, DEER spectroscopy studies have subsequently suggested that ELIC is not an appropriate model of a resting pLGIC (Dellisanti et al., 2013). Given that co-crystallization of ELIC with orthosteric agonists exhibits a closed channel structure, it is speculated that this conformation may correspond to that observed during slow receptor desensitization (Cecchini and Changeux, 2014).

1.5.3. An intracellular desensitization gate in inhibitory pLGICs

Notably, the recent crystal structure of the GABA β3 homopentamer (solved in the presence of the novel agonist benzamidine) revealed a unique pore structure, with respects to the configuration of M2 helices (Miller and Aricescu, 2014; *Fig 1.9 & 1.11 A-D*). The channel is expanded at the extracellular side and M2 helices taper down as they approach the intracellular side of the plasma membrane (*Fig 1.11 A*). The "hydrophobic gate" at the 9' M2 Leu residue reveals a similar diameter to that observed in open channel structures, though curiously with Leu side-chains rotated out of the pore (when compared to the configuration in GluClα (*Fig 1.11 B* Hibbs and Gouaux, 2011). At the -2' M2 residue the channel forms its narrowest constriction of 3.15 Å. In this state chloride ions would not be passed, with the channel in a closed configuration (distinct to that observed in ELIC, GLIC-pH 7, apo-GluClα and *tn*AChR; *Fig 1.9*). Given that agonist was bound in the structure, this was proposed to represent a receptor in a desensitized form. The location of this constriction is in strong agreement with location of a "desensitization gate" proposed by mutagenesis studies of the $GABA_A$ (and Gly) receptor (Gielen et al., 2015). Indeed mapping critical desensitisation residues of the M2/M3 interface on the crystal structure reveals a strong network of interactions, with residues lodged along this interface perfectly positioned to induce rearrangement of the channel lining M2 helix (*Fig 1.11 C*). Moreover this network is well positioned to interact with and cradle the side chain of a conserved aromatic residue at the base of M3 (Tyr 299 in GABA $\beta3_{cryst}$) that was proposed to induce

localized desensitization through a side chain conformational switch (Miller and Aricescu, 2014).

The local constriction of the GABA β3 channel represents an "extension" of the intracellular narrowing observed for pore lining helices in active-receptor structures (GluClα-IVM and GLIC-pH 4; notably minimal rearrangement is observed for the M1, M3, M4 helices and M2-M3 loop when superposed with GluClα-IVM *Fig 1.11 D*). Therefore we might speculate that the intracellular desensitization gate is responsible for initiating transition through the fast-desensitized state (Cecchini and Changeux, 2014).

In corroboration of this, recent nuclear magnetic resonance (NMR) and EPR spectroscopy studies of reconstituted-ELIC revealed that in the transition from a resting to a desensitized state, an expansion of extracellular and contraction of intracellular portals of the channel pore occurs (Kinde et al., 2015). While in agreement with the proposed desensitized structure of GABA β3 receptor, and functional studies of $GABA_A$ and α1 Gly receptors, this is in stark contrast to crystal structures of agonist bound ELIC. This would add weight to the argument that agonist-bound structures of ELIC are a reasonable model for the slow-desensitized receptor.

While there is now a strong agreement between functional desensitization data (for ELIC, $GABA_A$ and Gly receptors) and the crystal structure of the GABA β3 receptor, it should be noted that the crystallized form of the GABA β3 receptor is not one of physiological relevance (given that it not activated by GABA). Moreover the observed response to the novel agonist, benzamidine, has not yet been fully characterised. Additional caveats regard the reported spontaneous activity previously reported for GABAA β3 homopentamers and the potential effects this might have on channel structure (Wooltorton et al., 1997). Of similar note, it is also unclear what effect truncation of the receptor ICD, and replacement with shorter linkers, has on constraining receptor structure (Papke and Grosman, 2014). Finally, and as apparent from studies of ELIC, it is notable that crystal packing may (artificially) affect the conformation that a (normally dynamic) receptor adopts.

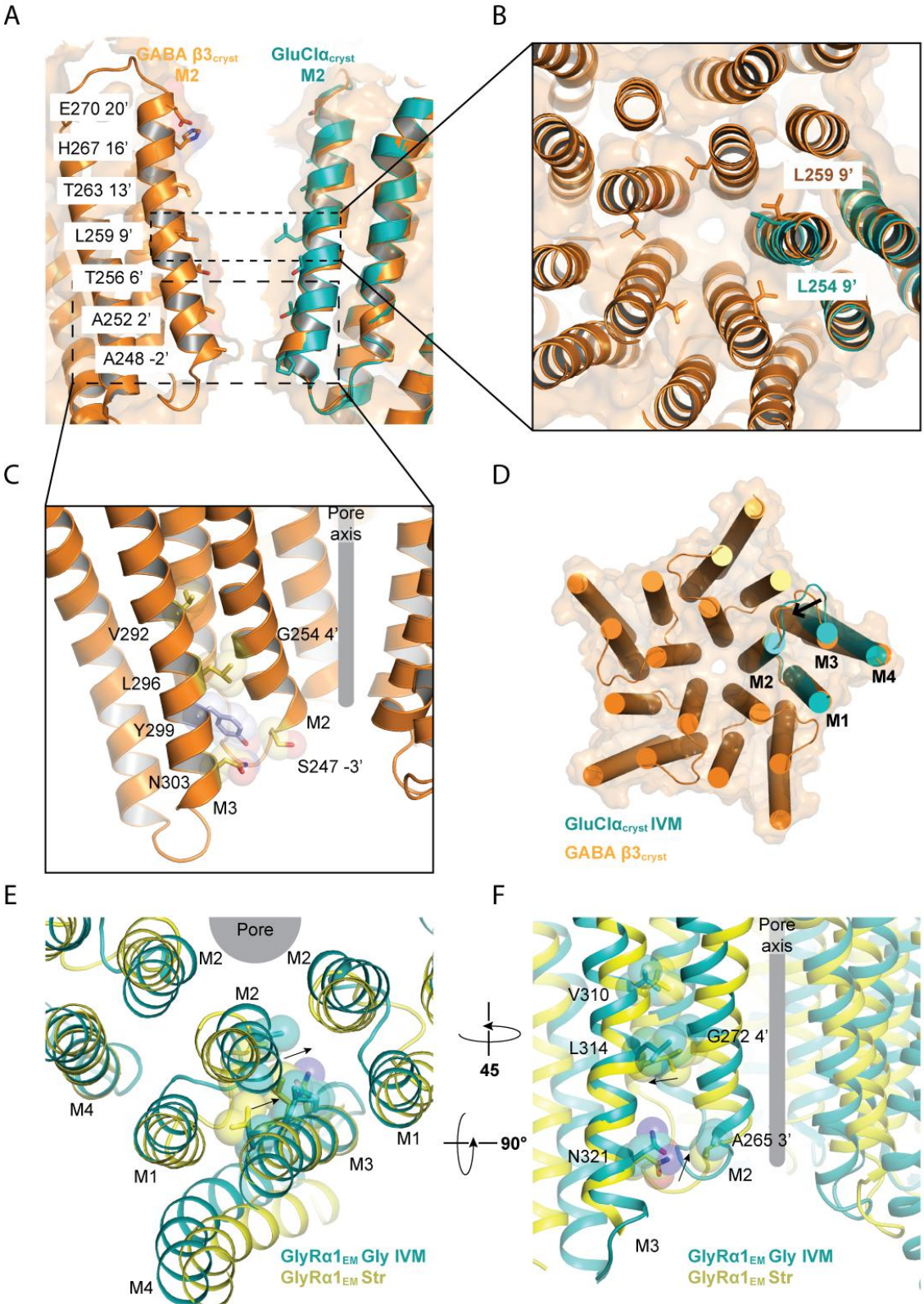
A
GABA β3cryst M2
GluClαcryst M2
E270 20'
H267 16'
T263 13'
L259 9'
T256 6'
A252 2'
A248 -2'
B
L259 9'
L254 9'
C
Pore axis
V292
G254 4'
L296
Y299
M2
S247 -3'
N303
M3
D
M3
M4
M2
M1
GluClαcryst IVM
GABA β3cryst
E
Pore
M2
M2
M2
M4
M1
M3
M1
M4
GlyRα1EM Gly IVM
GlyRα1EM Str
45
90°
F
Pore axis
V310
L314
G272 4'
A265 3'
N321
M2
M3
GlyRα1EM Gly IVM
GlyRα1EM Str

Figure 1.11 - Desensitization gate at the intracellular end of the ion channel in pLGICs

A. Surface profile and orientation of pore lining M2 residues (stick representation) in GABA β3 (orange) and GluCl-ivermectin (blue). The constriction formed by the extended confirmation of M2 helices at the intracellular end of GABA β3 TMD is apparent from superposition of individual TMDs. This surface profile clearly shows the channel constriction at -2'. **B.** Rotation of M2 helices in GABA β3 receptor moves 9' residues out of pore, resulting in an expanded global channel profile below 16'. **C.** Location of critical desensitization residues identified in a study of native α1β2γ2 $GABA_A$Rs (Gielen et al. 2015) and a conserved aromatic residue (Ty299 in GABA β3) in stick and sphere representation. The nearest subunit is removed for clarity**. D.** Superposition of single TMD of GluCl-ivermectin reveals minimal movement of helical bundle in GABA β3. The M2-M3 loop moves towards the pore axis and extension of the lower end of M2 closes the channel. **E.** and **F.** Location of critical desensitization residues identified in study α1 GlyR (Gielen et al., 2015) mapped on to the α1 GlyR cryo EM structures (strychnine (Str) – closed and glycine/ivermectin (IVM) – desensitized-like) as viewed from the extracellular space **(E)** and perpendicular **(F)** to the membrane plane at the base of the TMD. The near subunit is removed for clarity. Individual subunits of the pentamer were superpositioned.

1.5.4. An allosteric modulator induces a 'desensitized-like' channel structure

Despite the aforementioned caveats, the structure of a Zebrafish α1 Gly receptor in the presence of orthosteric agonist glycine (Gly) and allosteric modulator ivermectin (IVM) determined by cryo-EM would suggest a potential mechanism for (fast) desensitization consistent with that proposed for the GABA β3 receptor(Du et al., 2015). Free from the constraints of crystal packing, solubilized receptors are now directly imaged in the electron microscope, in a near native state. This approach reveals that the α1 GlyR-Gly-IVM structure has a tighter constriction of the intracellular portal of the pore, when compared to α1 GlyR-glycine structure (which reveals a fully-open active form, *Fig 1.9 and Fig 1.11 E & F*). With a radius of 2.5Å this is too narrow to permit passage of a hydrated chloride ion (Du et al., 2015). In electrophysiological recordings the glycine/ivermectin bound receptors exhibit reduced susceptibility to picrotoxin block (consistent with the findings from functional studies of native α1

GlyRs (Gielen et al., 2015)). Given that the pore-profile of this receptor resembles those of the GABA β3 receptor (and in light of the functional data), the α1-GlyR-Gly-IVM complex would apparently reflect an agonist-allosteric modulator-bound desensitized state of a pLGIC.

Superpositioning the EM structures for a closed-strychnine bound and Gly-IVM bound α1 Gly receptor further reveals the tight-knit network of interactions formed by residues lining the M2/M3 interface (as identified by mutagenesis studies). In transitioning from a closed to partially open/desensitized channel configuration, there is a displacement of residues at the intracellular-most end of the interface (*Fig 1.11 E & F)*. The Gly-IVM cryo-EM structure reveals a mechanism whereby allosteric modulators (e.g. ivermectin) binding at an intersubunit cavity are able to promote desensitization. Conversely, modulators binding at intrasubunit cavities (formed by M1, M2 and M3) in nAChRs are able to prevent desensitization (Dacosta et al., 2011; Gill et al., 2011).

While recent crystal and EM structures, as well as functional data, shed new light on the structures underpinning desensitization, a clear consensus regarding receptor desensitization has yet to be reached. Ultimately high-resolution structural studies of a single receptor in both the fast and slow desensitized states will likely assist in interpretation of the existing data.

1.5.5. What role does the ICD play in channel gating?

From the ensemble of available structures we can build a plausible mechanism for agonist activation. However a significant caveat is that, with the exception of the 5-HT_3 receptor (and nAChR), high-resolution structures have only been obtained for receptors lacking the large M3-M4 loop (Unwin, 2005; Hassaine et al., 2014). Typically truncated and replaced with a short linker sequence, it is far from clear as to the role that this loop may play in channel gating, and particularly its involvement in the conformational re-arrangements of the TMD.

1.6. Allosteric modulation at the TMD

Clinical and endogenous compounds are able to modulate pLGIC function through binding at allosteric sites distinct to the orthosteric binding pocket. These compounds display a range of properties; from intrinsic (agonist) activity to potentiation or inhibition of receptor function. The TMD of pLGICs, and the $GABA_A$ receptor in particular, appears to be the likely target for a wide variety of modulators including general anaesthetics, neurosteroids, channel block agents and lipids (Hosie et al., 2006; Franks, 2008; Hosie et al., 2009; Barrantes, 2015; Gielen et al., 2015). In the framework of recent high-resolution crystal structures we can begin to further understand how some of these might bind and impart their effects.

1.6.1. The channel block sites

Channel blocking agents are non-competitive inhibitors that occlude the aqueous pore of the ion channel and thereby prevent the flow of ions. The functional effects of the pore-blocker picrotoxin (PTX) have been extensively studied across pLGIC, and in the case of $GABA_A$ receptors block the active state of the receptor, though are also trapped in a resting receptor conformation (Bali and Akabas, 2007; Gielen et al., 2015). Co-crystallization of GluClα with PTX reveals a binding site deep in the channel pore, at the level M2 2' Thr and -2' Pro residues(Hibbs and Gouaux, 2011; *Fig 1.12 D*). This binding site likely overlaps with the location of a desensitization gate in $GABA_A$ and Gly receptors. Anaesthetic barbiturates though typically thought to bind outside of the channel pore in anionic-$GABA_A$ receptors have been shown to inhibit cationic-nAChRs through preferential binding within the channel of a desensitized receptor (Hamouda et al., 2014a; Sauguet et al., 2014a; Hamouda et al., 2014b). Moreover in the cation selection ELIC, the anaesthetic bromoform was found to bind within the channel pore (in addition to an interfacial site in the TMD; Spurny et al., 2013).

1.6.2. Anaesthetic binding sites

The wealth of functional and structural evidence points towards anaesthetic binding sites located outside of the channel pore for both anionic and cationic pLGICs. At cationic nAChRs anaesthetics typically display inhibitory properties (Sauguet et al., 2014a). Photo-affinity labelling studies of *tn*AChR with a photoactivatable propofol analog reveal binding at a channel site and an intrasubunit site within the helical bundle of the δ-subunit (Jayakar et al., 2013). Curiously the latter site partially overlaps with a crystallographically identified binding site for propofol at GLIC, where propofol acts as an inhibitor (Weng et al., 2010; Nury et al., 2011).

It is unlikely that an equivalent site exists in $GABA_A$ receptors, at which propofol potentiates channel function. Indeed photo-affinity labelling studies have identified binding sites for photo-reactive propofol and etomidate analogs at interfacial transmembrane sites in $GABA_A$ receptors (Li et al., 2009; Yip et al., 2013). In studies of α1β3γ2 it was found that etomidate binds selectively at the β-α subunit interface, with propofol binding at β-a, α-β and β-γ sites with apparently equal affinity(Chiara et al., 2012; Olsen et al., 2013). It was subsequently found that propofol binds at a site located within the $GABA_A$ receptor β-subunit, but positioned at the interface of subunit TMDs (Yip et al., 2013). This was proposed following photo-labelling of an apparently critical His (267) residue in β3 homopentamers and α1β3 heteropentamers. The location of the proposed site does not overlap with the intrasubunit anaesthetic site identified for propofol in GLIC, but does however partially overlap with an intersubunit anaesthetic site identified crystallographically for bromoform binding at a ethanol-sensitized mutant GLIC receptor(Nury et al., 2011; Sauguet et al., 2013a). The crystal structure of the homopentameric GABA β3 receptor (though not bound in situ with anaesthetics) reveals putative binding pockets for etomidate and propofol in close proximity to residues previously identified by photo-affinity labelling studies (*Fig 1.12 B*; Miller and Aricescu, 2014). It has subsequently been suggested for propofol that high- and low-affinity binding sites reside in vicinity of this pocket (in GABA β3 receptors), and that they would both be inaccessible in the closed channel state (Eaton et al., 2015; Franks, 2015).

1.6.3. Intersubunit binding sites

Structures of GluClα and more recently α1 GlyR (by crystallography and cryo-EM respectively) in complex with the insecticide ivermectin reveal a mechanism of pLGIC modulation through binding at an intersubunit TMD site (Hibbs and Gouaux, 2011; Du et al., 2015). Ivermectin typically acts in an irreversible manner to potentiate or inhibit channel function (depending on the type of pLGIC; Corringer et al., 2012). At GluClα it acts as an allosteric agonist, while at α1 GlyRs it potentiates agonist activity (Etter et al., 1996; Hibbs and Gouaux, 2011; Du et al., 2015). Ivermectin binds similarly in both structures, wedging between the interface of M3 and M1 helices for principal and complementary subunits respectively (*Fig 1.12 C*). It forms multiple contacts with residues of M2, notably polar interactions with the M2 15' Ser residue, M3 (principal), M1 (complementary) and in the case of the α1 GlyR with the M2-M3 loop. Of particular note is that the homologous M2 15' residue in $GABA_A$ and Gly receptors has been shown be a key determinant of general anaesthetic and alcohol modulation (Mihic et al., 1997; Miller and Smart, 2010). It appears in the case of ivermectin that binding at this site (which is located proximal to the M2) is capable of stabilizing the active state of the channel for GluClα, while in the GlyR it apparently stabilizes a low conductance or possibly desensitized state(Hibbs and Gouaux, 2011; Du et al., 2015).

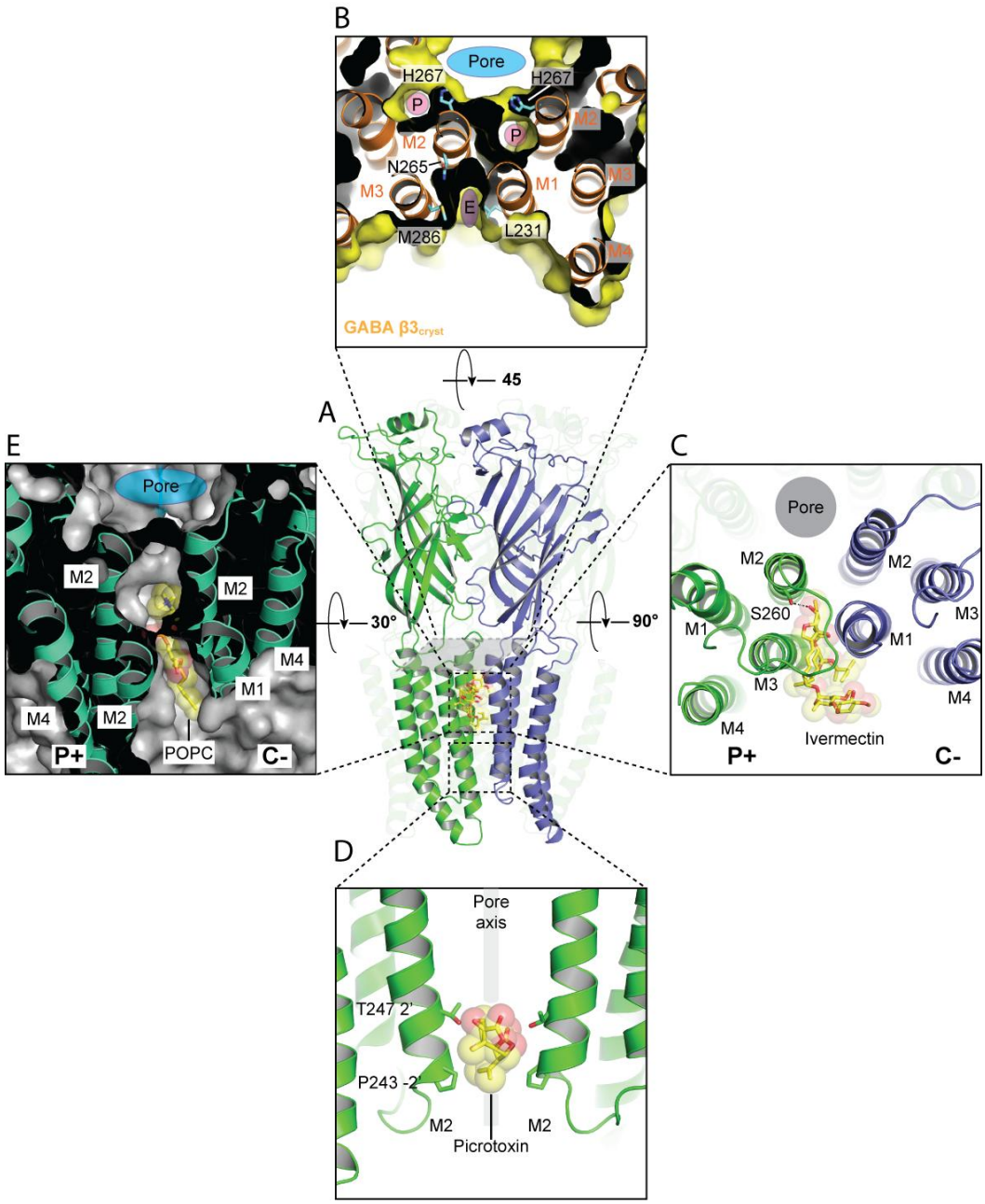

Figure 1.12 - Allosteric modulation in the TMD of pLGICs: GluClα and GABA β3

A. Central panel shows two subunits of GluClα with ivermectin bound at the interface of subunit TMDs. **B.** Top centre: Binding cavities for propofol and etomidate as observed in the GABA β3 structure. The propofol cavity (P) is lined by M2 His267 and formed within a subunit TMD facing the interface. The etomidate cavity (E) is at the subunit interface and lined by M2 (15' N265) and M3 residues of one subunit and M1 of the facing subunit. **C.** Right panel; view of the ivermectin binding site from the extracellular side of the membrane. Polar interactions with M2 15' Ser residue is shown by dotted lines. **D.** Bottom centre; Picrotoxin (stick and sphere representation) binding deep in the pore of GluClα at the level of 2' Thr and -2' residues **E.** Left panel; POPC-lipid binding cavity in GluClα, analogous to the ivermectin binding site, viewed approximately parallel (tilted slightly) to the plane of the membrane.

1.6.4. Lipophilic modulators

Given that this site is freely accessible from the lipid bilayer it opens new avenues for potential mechanisms of allosteric modulation of pLGICs, for example, by lipophilic modulators. At the $GABA_A$ receptor one such class of endogenous lipophilic modulators, introduced previously, are the neurosteroids. These compounds act in a biphasic manner; potentiating at low nanomolar concentrations and acting as allosteric agonists at high micromolar concentrations (Hosie et al., 2006). In contrast to ivermectin and other synthetic compounds, neurosteroid binding is not mediated by the M2 15' residue. Neurosteroid potentiation is likely to occur upon binding at an intrasubunit site within the TMD of α-subunits. Mutagenesis studies reveal that a conserved α-subunit Gln residue is critical, which from homology models, can be mapped to the base of M1 facing M4 of the same subunit. This aqueous cavity can accommodate a neurosteroid molecule, when it is orientated perpendicularly to the plane of the membrane. By this approximation, the steroid molecule forms other binding site contacts with residues in the upper part of M4 (Hosie et al., 2006).

By contrast, the location of a site mediating the direct activating effects of neurosteroids remains unclear, though it is likely to be formed by TMD residues at the subunit interface(Hosie et al., 2006). Given the allosteric agonist properties displayed by ivermectin and its binding location in GluClα, it will be of interest to determine whether neurosteroids (both potentiating and inhibitory) can interact at $GABA_A$ receptors via a similar site. Ultimately, structure determination (by crystallography or cryo-EM) of a steroid-bound receptor will provide further mechanistic insight.

Endogenous molecules in the lipid bilayer may also use this 'interfacial avenue' to interact with and allosterically modulate pLGIC function (Barrantes, 2015). Indeed cholesterol and anionic lipids have been shown to impart stabilizing and modulatory effects on nAChRs (Labriola et al., 2013). Though $GABA_A$R-active endogenous neurosteroids are synthesized from cholesterol, it is unclear as to what effect the parental sterol has on $GABA_A$ receptors (Sooksawate and Simmonds, 2001). Molecular dynamic simulations suggest that cholesterol may stably bind at a site analogous to the GluCl-ivermectin-binding site (Hénin et al., 2014). During these simulations cholesterol

is able to promote channel opening. Ultimately, direct experimental evidence will be needed to corroborate these findings.

While crystal structures of GLIC reveal bound membrane lipids (in a crevice formed by the upper parts of M1 and M4), functional-reconstitution reveals that GLIC is inherently insensitive to its lipid environment when compared to its eukaryotic counterparts (Bocquet et al., 2009; Nury et al., 2011; Labriola et al., 2013). Further structural evidence for lipid-modulation of pLGICs comes from a crystal structure of GluClα with bound 1-palmitoyl-2-oleoyl-sn-glycero-3-phosphocholine (POPC) molecules (Althoff et al., 2014). POPC occupies a site overlapping the ivermectin binding site, and is able to penetrate the helix interface with phosphocholine head groups juxtaposed to M2 helices (*Fig 1.12 E*). Surprisingly, this interaction alone is sufficient to induce a distinct expanded, open-like channel confirmation. It will be of interest to determine whether this site displays specific lipid selectivity and whether a common mode of allosteric modulation is observed across different classes of lipids.

1.7. Overcoming the barriers to pLGIC structure determination

An array of high-resolution structures for full length pLGICs in various conformational states have been determined, with some bound to agonists and allosteric modulators. Despite this, the amount of structural data for $GABA_A$ receptors is still very limited. This is largely due to the inherent difficulty in purifying and crystallizing eukaryotic membrane proteins. Developments in pre-crystallization screening (to optimize detergent extraction and purification of receptors), crystal optimization and structure solution techniques will ultimately assist in the generation of further high-resolution X-ray pLGIC models. Of equal interest will be the application of alternative approaches, including cryo-EM and native mass spectrometry for characterising protein in its native state. In the case of cryo-EM, direct imaging of purified protein can now (with the advent of developments in direct electron detection cameras and image processing) allow high-resolution structure determination. In comparison, native mass spectrometry can reveal different modes of lipid and small molecule binding to

membrane proteins in their native states. In addition to crystallography, these two approaches have been applied during this study. Short “primers” can be found in the Appendix, which summarise the steps involved in structure determination by cryo-EM (*Appendix Primer 1*) and the structural questions that can be addressed by mass spectrometry (*Appendix Primer 2*).

1.8. Thesis Aims

While significant progress has been made in advancing our understanding of the structural mechanisms underpinning $GABA_A$ receptor activation and modulation, to date there is only one high-resolution structure of a $GABA_A$ receptor in the Protein Data Bank (PDB), the homopentameric β3 receptor (Miller and Aricescu, 2014). Indeed at the start of this study, this was not even the case, with high resolution structures available only for the receptor homologs GLIC, ELIC and GluClα (as introduced in *Chapter 1*). While these form useful templates for homology modelling to guide structure function studies, there will likely be grey areas in the 'structural' interpretation of data. Ultimately, the generation of more high-resolution data for $GABA_A$Rs will provide the greatest detail regarding receptor function and modulation.

The ability to generate high-resolution structures for pLGICs is inherently dependent on the ability to express and purify the full length receptor at both high yield and purity, and then grow strongly diffracting protein crystals for structural determination. For eukaryotic pLGICs, such as $GABA_A$Rs, this is far from trivial.

As emphasized in *Chapter 1*, pLGICs are modular receptors, comprised of an ECD, TMD and ICD. Owing to this property, it has been possible to generate receptor chimeras, whereby domains of distally related receptors have been fused to form functional proteins, e.g. a chimera between the ECD of the prokaryotic GLIC and TMD of the human α1 GlyR subunit (Duret et al., 2011). The question was therefore raised; can we use the domains of previously crystallized receptors, e.g. the ECD of GLIC, as a surrogate host for other eukaryotic receptor domains, e.g. the TMD of the $GABA_A$R? Given the evident amenability of the 'surrogate host' to high-level purification and crystallization, one might postulate that this could coerce the eukaryotic domain to pack in the crystal form for high-resolution structural analyses. In doing so, fundamental questions regarding domain structure, role in receptor function and allosteric modulation could be assessed.

We therefore choose to explore the potential for generating chimeric $GABA_A$ receptors, principally targeting the TMD of the $GABA_AR$ α1 subunit for fusion with the ECD of GLIC. This $GABA_AR$ subunit was chosen due to a current lack of high-resolution structural information and its apparent role in setting critical receptor properties, such as desensitization, and allosteric modulation by neurosteroids. We reason that 'breaking' the $GABA_A$ receptor subunit into its individual core components, such as the TMD, would improve the potential for successful purification and crystallization (that might otherwise be hindered in studies of the full-length, glycosylated receptor complex).

We set about designing chimeric $GABA_A$ receptors and assessed functionality and allosteric modulation of receptors expressed in *Xenopus* oocytes for electrophysiological recordings (*Chapter 3*). In order to generate sufficient yield of a chimeric receptor for crystallization, a number of purification strategies were assessed on their ability to stabilize GLIC-$GABA_AR$ α1 chimeras in detergent micelles (*Chapter 4*). Additionally, we probed the different pharmacological properties of native $GABA_ARs$, their prokaryotic homologs and receptor chimeras. These revealed previously unreported allosteric modulator responses at GLIC (to the barbiturate, pentobarbital; *Chapter 5*) and ELIC (to the inhibitory neurosteroid, pregnenolone sulphare; *Chapter 6*), which we have assessed in further structural studies to ascertain binding sites. Finally, as the field of membrane protein structural biology develops, we have begun to assess the use of non-crystallographic techniques, cryo-EM and mass spectrometry in structural studies of pLGICs (*Chapter 6*).

Chapter 2: Material and Methods

2.1. Reagents

Sources for the reagents used in this study are provided throughout the materials and methods along with relevant experimental details.

2.2. Molecular Biology

Extended details of the constructs generated and used in this study are given in *Appendix Tables 1-3*.

GLIC, ELIC, $GluCl_{cryst,}$ $GABA_AR$ and chimeric subunits were subcloned in to pRK5 for mammalian expression, with a Kozak consensus sequence inserted upstream of the native signal peptide sequence. The mature GLIC and ELIC protein-encoding sequences were flanked by the signal peptide from the α7 nAChR. The plasmid containing the gene for $GluCl_{cryst}$ (originally in pGEM)was a gift from Eric Gouaux (Addgene plasmid number 31488) and that containing GLIC (originally in pMT3) was a gift from Pierre-Jean Corringer.

2.2.1. PCR amplification and analysis

Chimeric subunits were generated by an overlap PCR protocol and subcloned in to pRK5 for expression. The procedure consists of four-steps, with PCR products purified following gel extraction at each relevant step:

1. PCR amplification of the amino-terminal end of the receptor was generated using the forward primer SP6 and a reverse primer (*Table 2.1*) that overlapped the junction between the parental receptor DNAs.
2. PCR amplification of the carboxyl-terminus end of the receptor was generated using the reverse primer P5 and a forward primer (*Table 2.1*) that overlapped the junction between the parental receptor DNAs.
3. The PCR products from steps 1 and 2 were assembled following a PCR amplification using SP6 and P5 primers.
4. The PCR product of step 3 was sublconed into pRK5 using the restriction enzymes ClaI and EcoRI and T4 DNA ligase.

Table 2.1 PCR primers for $GABA_A$ receptor chimeras with GLIC and GluClα

Primer	Sequence 5'- 3'	Template
GLIC-GABA α1 F	GATTTCTCGTCAATATGGCTACTTTGTTATTCAAACATATC	$GABA_A$ α1
GLIC-GABA α1 R	TAACAAAGTAGCCATATTGACGAGAAATCCGCAA	GLIC
GLIC-GABA β2 F	GGATTTCTCGTCAATATGGCTACTTCATCCTGCAGAC	$GABA_A$ β2
GLIC-GABA β2 R	GCAGGATGAAGTAGCCATATTGACGAGAAATCCGCAAC	GLIC
GluClα-GABA α1 F	CAGCTCAAAAGAGAATTCGGCTACTTTGTTATTCAAACATATC	$GABA_A$ α1
GluClα-GABA α1 R	TTGAATAACAAAGTAGCCGAATTCTCTTTTGAGCTGGATCGTG	GluClα

Primers are shown for the receptor chimeras where F = Forward primer (used in combination with P5 primer for pRK5 vector) and R=reverse primer (used in combination with SP6 primer for pRK5 vector).

Receptor fragments and full-length genes were generated by PCR using Phusion DNA Polymerase (Thermo Fischer, Rockford, Illinois, USA). PCR was performed using a G-StormThermal Cycler (Somerton, Somerset, UK) using the following generic protocol, for which settings were adapted depending on the experiment.

1. Activation: 98°C for 30s
2. DNA Denaturation: 98°C for 10s
3. Annealing: Variable temperature (typically 55-72°C) for 30s
4. Extension: 72°C for variable time of 15-30s/kb
5. Return to step 2, 25-40x (dependent on reaction)
6. Final extension: 72°C or 10 min

For all reactions; PCR products were run on an agarose gel (0.8-2% depending on the fragment size to be isolated) for reaction analysis. Bands equating to PCR products of the expected size were excised and DNA was isolated using a QIAquick Gel Extraction Kit (Qiagen).

Single-point mutations of receptor subunits and affinity tag-insertions were generated by inverse PCR using Phusion DNA polymerase. The PCR product of this amplification reaction was isolated following gel extraction and purification; (5') phosphorylated using a T4 polynucleotide kinase (New England Biolabs, UK) and ligated using a T4 DNA ligase (New England Biolabs, UK or Roche, Basel, Switzerland). All plasmids were transformed in to DH5α *E. coli* cells (New England Biolabs, UK) unless otherwise stated and plated on to Luria Broth (LB) agar plates supplemented with the appropriate antibiotic (see *Table 2.2* and *Appendix Table 1-3*); ampicillin at 100 µg/ml or kanamycin at 30-50 µg/ml) and incubated overnight at 37°C. Colonies were picked and incubated in 3-5 ml of LB supplemented with antibiotic with shaking (overnight at 37°C). Plasmid DNA was purified using QIAprep Spin Miniprep kit (Qiagen). The concentration of DNA was determined using a spectrophotometer (BioPhotometer; Eppendorf, Hamburg, Germany) or Nanodrop (Thermo Fischer). Where necessary, the volume of bacterial culture for DNA purification was scaled up in order to carry out Midi scale plasmid preparation (HiSpeed Plasmid Midi Kit (Qiagen)). Coding regions of all construct genes were verified by DNA sequencing (Source BioScience, Nottingham).

Table 2.2 Antibiotics and reagents for bacterial culture and selection

Reagent	Source	Solvent	[Stock]	[Final]
Ampicillin	Melford	Water	100 mg ml^{-1}	100 µg ml^{-1}
Kanamycin sulphate	MP Biochemicals	Water	50 mg ml^{-1}	50 µg ml^{-1}
Gentamicin sulphate	Sigma	Water	7 mg ml^{-1}	7 µg ml^{-1}
Tetracycline	Sigma	Ethanol	10 mg ml^{-1}	10 µg ml^{-1}
Bluogal	MP Biochemicals	DMSO	100 mg ml^{-1}	100 µg ml^{-1}
Isopropyl β-D-1-thiogalactopyranoside (IPTG)	Melford	Water	100 mM	0.1-0.2 mM

Melford: Melford Laboratories (Ipswich, UK). Sigma: Sigma-Aldrich (Steinheim, Germany). MP Biochemicals (UK)

2.2.2. Bungarotoxin-tagged construct design and generation

For live-cell imaging of surface-expressed receptors, the nucleotide sequence encoding a 13 amino acid α-bungarotoxin binding site (BBS) mimotope was introduced into the receptor subunit gene; WRYYESSLEPYPD (Wilkins et al., 2008). This sequence was positioned such that the site would be introduced 7 amino acid residues from the start of the mature protein. Complementary DNA fragments for the 13 residues BBS were incorporated into oligonucleotides, such that the site could be introduced into the gene-of-interest by inverse PCR. See *Table 2.3* for PCR primers.

Table 2.3 PCR primers for inserting α-bungarotoxin binding site

Primer	Sequence (x=Gene of interest)
BBS Forward	5′-GTTTAGAACCATATCCAGATx-3′
BBS Reverse	5′-TACTTTCATAATATCTCCAx-3′

2.2.3. Bacterial expression constructs

Chimeric subunits were subcloned into a modified pET26 vector for bacterial expression under the T7 promoter as a fusion protein with the maltose-binding protein (*Fig 2.1*). The final construct encoded the pelB signal sequence followed by a $(His)_{10}$ tag, maltose binding protein (MBP), a *Herpes simplex* (HRV) 3C protease site and the chimeric subunit sequence. The genes encoding GLIC and ELIC as MBP-fusion proteins (in the pET26 vector described above) were gifts from Raimund Dutzler (Addgene plasmid 39239).

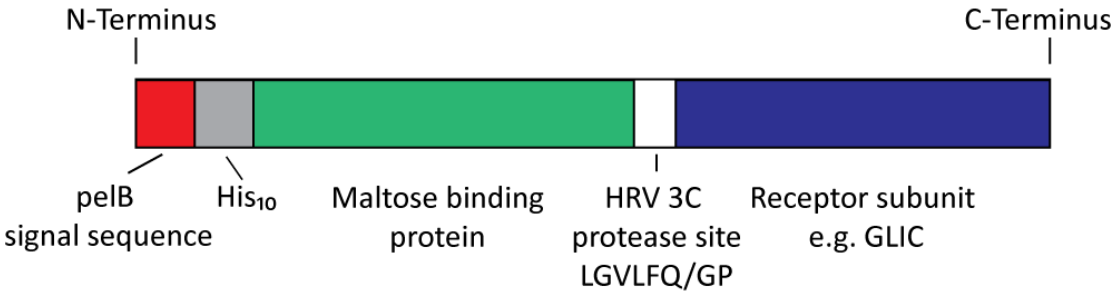

Figure 2.1 – Schematic of MBP-fusion protein for bacterial expression and purification

Schematic representation of the MBP-fusion protein construct used for bacterial expression and purification of GLIC, ELIC and GLIC-$GABA_AR$ chimeras. A pelB signal peptide sequences targets the protein to the inner membrane of bacteria. The His-MBP fusion tag is inserted at the N-terminus of the full-length fusion protein, which can be cleaved at a HRV 3C site to yield the mature untagged receptor.

2.2.4. Baculovirus-Insect cell expression constructs

The gene encoding chimeric subunits and a C-terminal $(His)_8$ tag was subcloned in to pFastBac1 vector for baculovirus-driven expression in insect cells. Transposition of the gene of interest into recombinant bacmid DNA was carried out using DH10 Bac cells (following manufacturers guidelines, with minor modifications. Invitrogen/Life Technologies Ltd). Cells were plated on kanamycin/gentamicin/tetracycline/Bluogal /IPTG LB agar plates (*Table 2.2*) for blue/white colony selection (allowing up to 48 hrs for colour selection). White colonies containing the recombinant bacmid were selected for isolation of recombinant bacmid DNA.

Briefly, single white colonies were picked and inoculated in 2YT broth supplemented with kanamycin/gentamicin/tetracycline and grown at 37°C (overnight with shaking). Cells were harvested by centrifugation, lysed and bacmid DNA isolated by isopropanol precipitation. Due to the large size of recombinant bacmid DNA (>135 kb), it was therefore analysed by PCR using a combination of M13 Forward or Reverse primers (as detailed in the Bac-to-Bac Handbook, Invitrogen**,** *Table 2.4***)** and by using a primer specific to the gene of interest (to confirm successful transposition). PCR products were analysed by gel electrophoresis. Recombinant bacmids (exhibiting successful transposition) were stored at 4°C prior to use.

Table 2.4 PCR primers for analysis of recombinant bacmid DNA

Primer	Sequence
M13 Forward	5′-CCCAGTCACGACGTTGTAAAACG-3′
M13 Reverse	5′-AGCGGATAACAATTTCACACAGG-3′

2.3. Electrophysiology

2.3.1. Preparation of Xenopus oocytes

Xenopus laevis were housed in the Biological Services Unit or at Royal Free College Hospital (UCL). Segments of ovaries were taken using a Schedule 1 procedure (following terminal anaesthesia with tricane methane sulphonate MS 222) and prepared for electrophysiological recordings as previously described (Gielen et al., 2012). Briefly, segments of the ovaries were incubated in a (Calcium-free) collagenase-type 1 solution (OR2 + collagenase) for approximately 2-4 hrs (OR2; 85mM NaCl, 5mM HEPES, 1mM $MgCl_2$, pH 7.6 with 1M KOH). Oocytes were washed several times in OR2 (without collagenase), followed by washing in Barth's solution (88mM NaCl, 1mM KCl, 0.33mM $Ca(NO_3)_2$, 0.41mM $CaCl_2$, 0.82mM $MgSO_4$, 2.4mM $NaHCO_3$, 10mM HEPES pH 7.6 with NaOH). Defolliculated oocytes were stored in Barth's solution supplemented with gentamicin at 16-18°C.

For receptor expression in oocytes, plasmid DNA was diluted to 1-30 ng/μl in TE buffer. Single oocytes were subsequently injected with 27.6 nl of receptor subunit cDNA into the nucleus. Oocytes were incubated at 17°C in Barth's solution for 1-4 days prior to recordings (depending on the receptor subunits to be expressed).

Oocytes expressing homomeric wild-type (WT), mutant or chimeric subunits were used between 1-4 days after injection. Wild-type homomeric receptors typically showed robust expression after 1 day, whist chimeric receptors typically showed robust currents after 2-4 days. Injected oocytes were transferred to an in-house designed and fabricated recording chamber and viewed and positioned under optical magnification (*Fig 2.2*). During recordings oocytes were continuously superfused with the following recording solutionfor proton-gated receptors: 100 mM NaCl, 2mM KCl, 2mM $CaCl_2$, 1mM $MgCl_2$, 10 mM MES, 10 μM EDTA; and for GABA and glutamate-gated receptors: 100 mM NaCl, 2mM KCl, 2mM $CaCl_2$, 1 mM $MgCl_2$, 5 mM HEPES, adjusted to pH 7.4 with 1M NaOH). Recording pipettes (borosilicate glass) were fabricated using a two-

stage vertical puller (resistance 0.8-2 MOhms) and filled with 3M KCl. Oocytes were voltage clamped at -60 mV, and experiments carried out at room temperature. Receptor activated currents were induced by application of the appropriate agonist using a gravity flow perfusion system for fast-application. For pH sensitivity experiments, 10 mM MES buffered recording solution was adjusted to the appropriate pH with 1M NaOH. Currents were recorded using an Axoclamp 2B amplifier, a Digidata 1322A interface and pCLAMP (Version 8) and recorded to disk (Dell Computers). Currents were digitized at 500 Hz and filtered at 50 Hz**.**

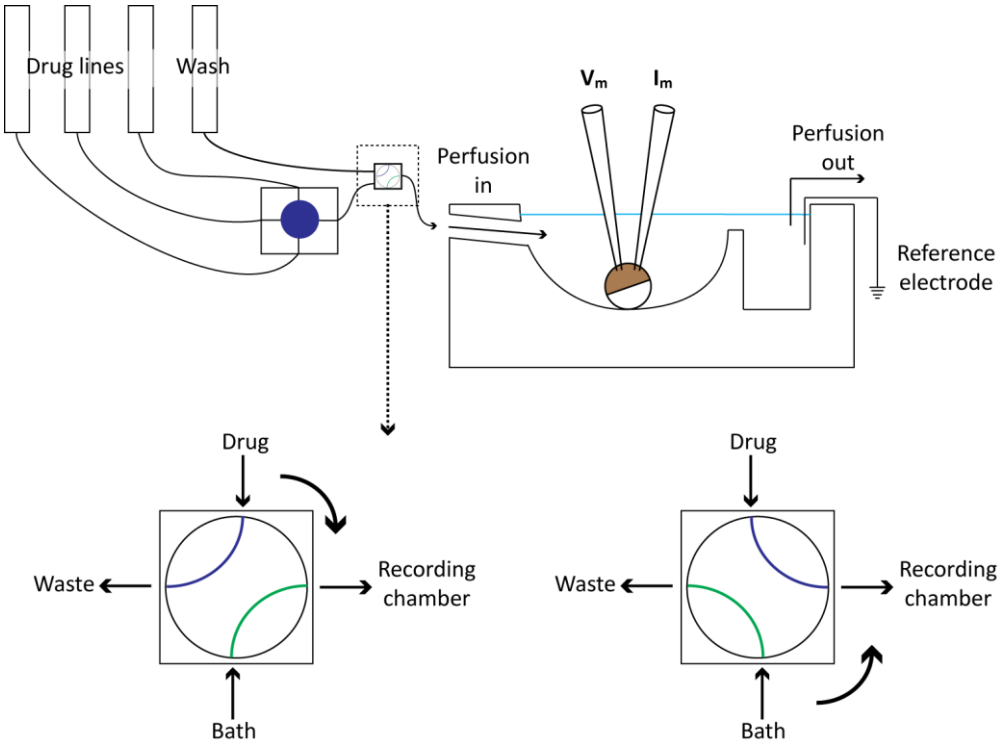

Figure 2.2 - Schematic of Two-Electrode Voltage Clamp recording set up and application system

Oocytes were continuously perfused using a gravity flow system and vacuum pump (for perfusion out of bath). Drugs were applied by gravity flow and a two-way manually operated switch. Under normal conditions the wash/bath line (e.g. recording solution) is channelled in to the recording chamber (and drug to the waste line). For drug application, rapid rotation of the switch through 90° directs the drug solution to the recording chamber and wash solution to the waste line.

Table 2.5 Drug solutions used for electrophysiology

Drug	Source	[Stock]	Stock solvent
GABA	Sigma	1M	Water
Ivermectin	Sigma	1mM	DMSO
Pentobarbital	Sigma	100mM	DMSO/Water
Picrotoxin	Sigma	10 mM	DMSO
Pregnenolone sulphate	Sigma	10 mM	DMSO/Water
S97617	Sigma	Up to 100mM	DMSO/Water
THDOC	Sigma	10mM	DMSO

Drugs were sourced from Sigma-Aldrich (Steinheim, Germany) and prepared as described. Where DMSO was used as solvent, the final concentration of DMSO in recording solution did not exceed 0.1% (v/v). In the cases where DMSO concentration was > 0.5%, recordings in the presence of an equivalent concentration of vehicle alone were carried out to ensure specific effects of the drug (over DMSO). Pentobarbital was a sodium salt.

Drug application was dependent the type of experiment. For peak recordings, agonist (GABA/glutamate/protons) was applied in combination with other drugs (either co-applied, or pre-applied, or applied following receptor-activation. Drug details in *Table 2.5*). In constructing concentration-response relationships, a normalising concentration of agonist was frequently applied (to assess run-up or run-down of membrane currents). For assessment of receptor activation and desensitization rates, the response to prolonged agonist exposure (40-60 s) was recorded.

2.3.2. Electrophysiology data analysis

Concentration response data were typically generated from 6 to 8 data points. The amplitudes of peak currents were measured and then normalised to the response amplitudes evoked by a normalising agonist concentration (in Clampfit, Molecular Device, USA). If agonist-induced currents resulted in a loss of voltage clamp (and hence underestimation of actual membrane current) this was accounted for prior to analysis.

Individual data sets were fitted with the Hill equation (see below), and a variation was also used that enabled two-component fits and inhibition-response relationships to be described using Origin 6.0. The concentrations causing half-maximal effects (EC_{50}/IC_{50}) and Hill slope (n_H) values were generated from individual data fits. For mean fits; pending on feasibility, relative membrane currents were normalised to either an experimentally- or theoretically-derived maxima, and then fitted with the Hill Equation.

Equation 2.1 Hill Equation

$$\frac{I_{proton}}{I_{Max,proton}} = \sum_{i=1}^{i=j} \frac{1}{1+(EC_{50}/[A])^{n_H}}$$

Where $I_{max,\ proton}$ is the maximum response to a saturating concentration of protons, EC_{50} is the concentration of protons ([A]) inducing a half-maximal current, n_H is the Hill coefficient and i is the number of components where j typically = 1-3.

Equation 2.2 Inhibition equation

$$\frac{I}{I_{Max}} = \sum_{i=1}^{i=j} 1 - \left[\frac{1}{1+(IC_{50}/[B])^{n_H}} \right]$$

Antagonism was evaluated through constructing inhibition-concentration relationship curves and a data fit generated using the equation above. IC_{50} is the concentration of antagonist ([B]) inducing a half-maximal reduction in the agonist current and n_H is the Hill coefficient.

2.3.3. Activation and Decay Analysis

Agonist current rise times were determined as the time for the current amplitude to increase from 20% to 80% of the maximal response. For analysis of receptor decay kinetics, oocytes were exposed to agonist for prolonged period (ideally 45-60, but due to an endogenous oocyte response to protons this was not always possible and data sets exhibiting considerable “noise” in the decaying phase were discarded). Weighted decay time constants for desensitization were determined by fitting the decaying phase with 2 or 3 exponential components (in Clampfit version 8) and using the equation below (an example data fit is shown in *Fig 2*.3).

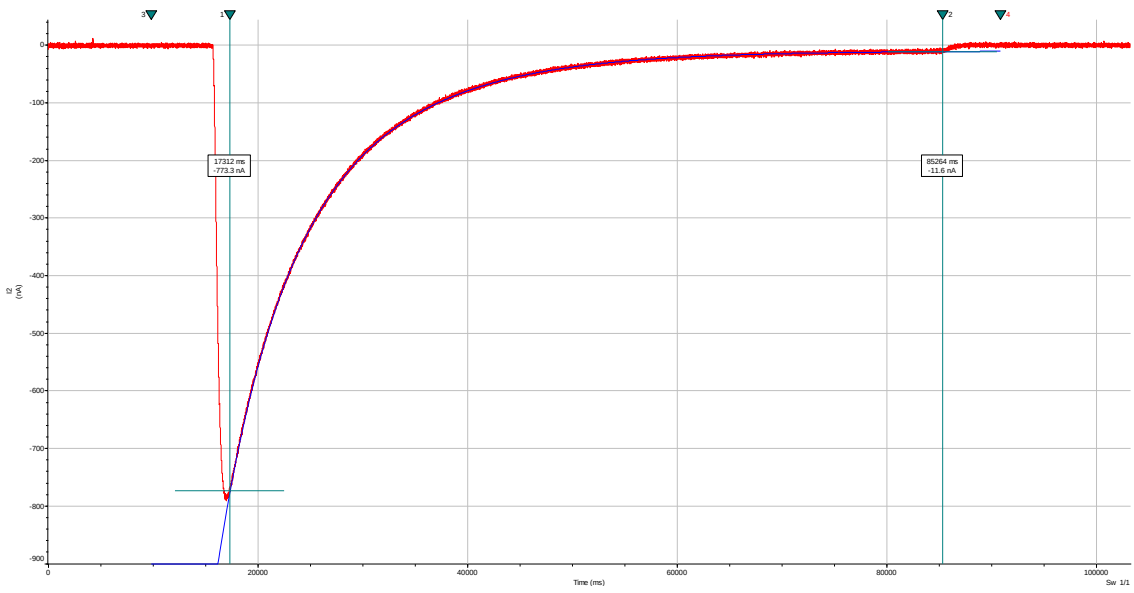

Figure 2.3- Agonist-evoked response with a bi-exponential decay function

Current (red trace) recorded from an oocyte expressing GluCl-$GABA_A$ upon application of a saturating concentration of agonist, glutamate. Cursors (vertical teal lines) were placed at the approximate start and end of the decaying phase and fitted with a bi-exponential decaying function. Function parameters from this fit were used to generate a weighted decay time constant for desensitization (τ_ω).

Equation 2.3 Weighted time decay constant

$$\tau_w = (A_1.\tau_1 + A_2.\tau_2) / (A_1 + A_2);$$

Where τ_1 and τ_2 represent the time constants for a bi-exponential decay (see above figure for example of fit to data), and A_1 and A_2 are relative amplitude contributions of τ_1 and τ_2.

2.3.4. Spontaneous Channel Activity Analysis

Given that picrotoxin block could not be measured for some receptors, in order to compare relative spontaneous channel activity between mutant receptors, activity was measured as a percentage of the maximum current induced by high agonist concentration.

Equation 2.4 Percent spontaneous activity

$$SA(\%) = \frac{I_{Holding}}{I_{Holding+Max,proton}}$$

Where $I_{Holding}$ is the stable standing current (e.g. spontaneous activity; SA) observed immediately following oocyte voltage clamp (at resting pH) and I_{max}, proton is the max current size induced by a high (maximal) proton concentration.

2.4. HEK Cell Electrophysiology and Imaging

2.4.1. HEK Cell Culture and transfection

HEK293 cells were maintained in Dulbecco's modified Eagle's media supplemented with 10% v/v fetal bovine serum, penicillin-streptomycin (100 units/100 μg/ml) and 2 mM glutamine (all from Gibco, Invitrogen Ltd.) at 37°C in humidified 95 % air and 5 % CO_2. For imaging and electrophysiology experiments cells were plated on to 18 mm glass coverslips (VWR International) coated with poly-L-lysine (Sigma), and in 10 cm culture dishes (Greiner-Bio-One GmbH, Frickenhausen, Germany) for routine culture or cell lysate preparations. For passaging, cells were washed with Hank's Balanced salt solution (HBSS: Gibco), detached from the dish with trypsin-EDTA (Gibco) before quenching the trypsin in culture media and replating. HEK293 cells were transfected using a calcium phosphate protocol at ~4-18 hrs post plating (depending on the application). For imaging and electrophysiology experiments cDNAs encoding receptor subunits was mixed with eGFP (except in the case of eGFP-tagged receptor constructs, which were mixed with monomeric DsRed). DNA mixtures (~2-4 μg total cDNA) were diluted in 340 mM CaCl2 (20 μl/coverslip) and 2x HBSS (24μl/coverslip), and the suspension applied to cells. Cells were used 18-48 hrs post transfection. For cell lysate preparations, the above protocol was scaled-up for the addition of 10-20 μg cDNA per 10 cm culture dish.

2.4.2. HEK Cell Imaging

For (live-cell) imaging of surface-expression of receptors, a BBS was introduced in to receptor subunit gene as described previously. To image α-bungarotoxin labelling of live transfected HEK293 cells (co-transfected with eGFP), cells were washed in Krebs Ringer buffer (140mM NaCl, 4.7mM KCl, 1.2mM $MgCl_2$, 2.52mM $CaCl_2$, 11mM Glucose and 5mM HEPES, adjusted to pH 7.4 with 1M NaOH), followed by application of Alexa555-conjugated α-bungarotoxin (Molecular Probes, ThermoFisher, Waltham, MA, USA) for 5 min. Cells were washed (briefly) in Krebs and then imaged immediately

using a Zeiss LSM 510 Meta confocal microscope (Carl Zeiss Ltd., Welwyn, Garden City, Hertfordshire, UK) equipped with a 488 nM argon and 543 nM He-Ne laser line and a 40x water-immersion objective. Images were later analysed with ImageJ (Fiji). An example of such images and their interpretation is shown in *Fig 2.4*.

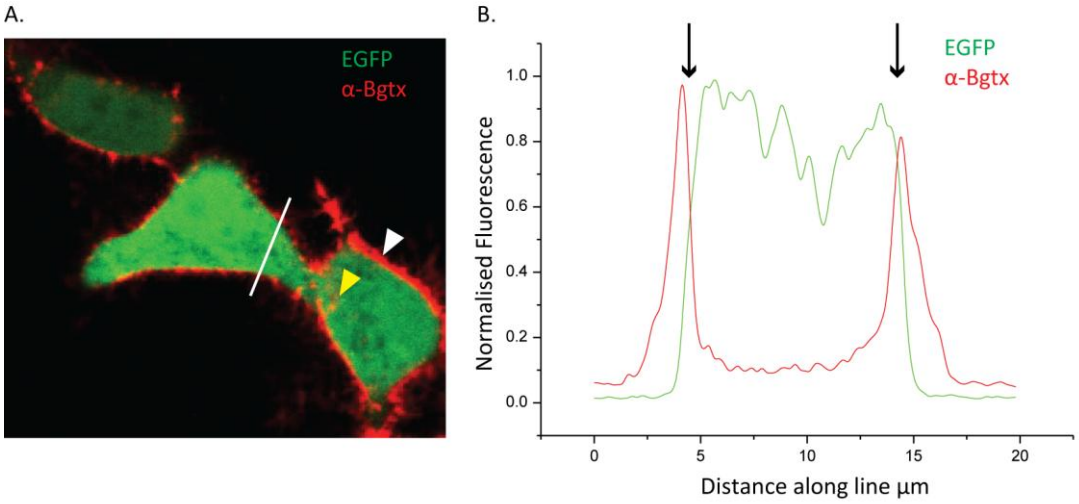

Figure 2.4 - Cell surface labelling of BBS-tagged receptors with α-Bungarotoxin (conjugated to Alexa555)

A. Example of cell surface labelling of HEK293 cells expressing BBS-tagged GLIC-$GABA_AR$ α1 chimeric receptor as revealed following incubation with α-Bungarotoxin (Bgtx) conjugated to Alexafluor 555. Transfected cells were identified by co-transfection with eGFP. Cell surface expression is clearly visible as a fluorescent signal around the edge of cells (i.e. the plasma membrane). A strong band of labelling is shown by the white arrowhead. Apparent intracellular labelling (as indicated by the yellow arrowhead) is likely to be contributed by labelled-receptors embedded in the membrane but outside of the image focal plane. We do not expect to observe receptor internalization under the imaging conditions used in this study. **B.** Analysis of the profile of the fluorescent signal along a line (white line in A) reveals clear demarcation between intracellular expression of soluble eGFP and plasma membrane embedded bungarotoxin-labelled receptors. The position of the plasma membrane is shown by arrows. Note: BBS is inserted into the receptor's N-terminus at a position exposed to the extracellular space. Fluorescent signals for eGFP and α-Bgtx was normalised to maximum arbitrary fluorescent units.

2.4.3. HEK Cell Electrophysiology: Whole-cell patch clamp

Transfected HEK293 cells (on glass coverslips) were placed in a recording chamber, and visualized using phase-contrast optics. Transfected cells were identified using eGFP signal (visualized under epifluorescence optics). During recordings cells were continuously perfused at room temperature with a Krebs recording solution (in mM; 140 NaCl, 4.7 KCl, 1.2 $MgCl_2$, 2.52 $CaCl_2$, 11 glucose and 5 HEPES, adjusted to pH 7.4 with 1M NaOH). Whole-cell currents were recorded from cells voltage-clamped at -20 mV. Whole-cell currents were filtered at 5 kHz and digitized at 50 kHz via a Digidata 1332A (Molecular Device, USA) and recorded to disk (Dell Computers). Patch pipettes (borosilicate glass) were fire polished to 2-4 mOhms and filled with an intracellular solution (in mM; 120 KCl, 1 $MgCl_2$, 11 EGTA, 10 HEPES, 1 $CaCl_2$, 2 ATP, adjusted to pH 7.2 with 1M NaOH). The osmolarity of intracellular solution was typically 300 mOsm/l.

2.5. Expression and purification of receptor in bacterial cells

2.5.1. Expression and purification of GLIC and chimeric receptors in E. coli

For expression of GLIC and chimeric receptors in *E. coli*, receptors were expressed as a fusion protein with Maltose Binding Protein as previously described (Nury et al., 2011). Proteins were overexpressed in *E. coli* C43 cells (Lucigen, Middleton, WI, USA). For a typical large-scale expression: An overnight culture in LB_{Kan30} (50-100 ml) was used to inoculate 5l of 2YT media (~8.5 ml of 850 ml 2YT in 2.5l Erlenmeyer flasks) and grown with shaking (180-220 rpm) at 37°C. Expression was induced by addition of 0.1 mM IPTG (Sigma-Aldrich) once cell density reached an absorbance (OD_{600}) of ~1.0. Cells were cooled to 20°C and expression was carried out overnight at 20°C (shaking at 180 rpm). Cells were harvested and resuspended in Buffer A (300 mM NaCl, 20 mM Tris-HCl pH7.6) supplemented with EDTA-free Inhibitor Cocktail Complete (Roche). Cells were disrupted by sonication (Soniprep 150 – 9mm probe) and unlysed cells and debris cleared by centrifugation at 15,000g for 30 min at 4°C (JA20 rotor. Beckman Coulter,

High Wycombe, UK). The membrane fraction was isolated by centrifugation of the cleared lysate at 200,00g (45Ti or 70Ti rotor) for 2 h at 4°C. Membrane pellets were resuspended in Buffer A and proteins extracted with 40 mM n-Dodecyl-β-D-Maltopyranoside (DDM) (Affymetrix-Anatrace, Generon Ltd, UK) overnight under gentle agitation. Insoluble material was removed by centrifugation at 200,000g and solubilized protein purified by affinity chromatography with amylose resin (New England Biolabs) or by immobilized metal affinity chromatography (IMAC) with TALON Co^{2+} resin (ClonTech, Takara Bio, France). Initial screens of chimeric receptor expression in bacteria used purification on amylose resin.

For purification on an amylose resin, the resin was pre-equilibrated in Buffer A supplemented with 0.02% DDM (w/v) prior to binding of the fusion protein. Protein was batch bound to the resin for 2-4 hrs at 4°C and then packed in to an Econo-Pac column (Bio-Rad, Hercules, CA, USA). Unbound material was collected in the flow-through, and resin washed thoroughly with 0.1% and 0.02% DDM (w/v) in Buffer A. Fusion protein was eluted in 0.02% DDM in Buffer A with 20 mM maltose. Eluted proteins were concentrated and further purified by gel filtration on a Superose 6 10/300 GL column (GE Healthcare, Bucks, UK), equilibrated in Buffer A supplemented with 0.02% DDM, attached to an AKTA FPLC (at 4°C; GE Healthcare, Bucks, UK) operating under Unicorn Control Software. Sample was run over the column at a constant flow rate of 0.3 ml/min and the A_{280nm} of the eluent monitored by an in-line UV detector. Fractions of the peak corresponding to the pentameric fusion-protein were pooled and the fusion tag cleaved in solution with PreScission Protease (purified "in-house" and kindly provided by Dr Matthew Gold, Dept of NPP UCL, cleaving at an LQVLPQ/GP consensus sequence). His-tagged MBP and a contaminating (amylose-binding) protein were removed by running the sample over TALON Co^{2+} resin (Clontech, Takara Bio, France) and amylose columns respectively. The cleaved native pentameric protein was purified by a final gel filtration step, concentrated with a 100kDa MWCO Amicon-Ultra centrifugal filter unit (EMD-Millipore) and flash-frozen in liquid nitrogen for storage.

For purification of GLIC on TALON Co^{2+} resin a modified protocol was used to that in (Gonzalez-Gutierrez et al., 2013). Resin was pre-equilibrated in Buffer A supplemented with 0.5 mM DDM prior to binding of fusion protein. Protein was batch bound to resin for 2-4 hrs at 4°C in the presence of 10 mM Imidazole, and then packed in to a Bio-Rad Econo-Pac column. Unbound material was collected in the flow through, and resin subsequently washed with Buffer A supplemented with 0.5 mM DDM and 30 mM Imidazole. Fusion protein was eluted in a single step with 300 mM Imidazole (in Buffer A supplemented with 0.5 mM DDM). Eluted proteins were concentrated and imidazole removed using a PD10 Desalting column (GE Healthcare) before overnight cleavage of the fusion tag using dual tagged His/GST-PreScission Protease (Pierce/Life Technologies). His-tagged MBP was removed by binding to amylose resin for an hour and cleaved GLIC collected in the flow through. Cleaved GLIC and PreScission protease were further separated by gel filtration on a Superose 6 10/300 GL column (GE Healthcare) equilibrated in Buffer A supplemented with 0.5 mM DDM attached to an AKTA FPLC. Peak fractions corresponding to cleaved pentameric GLIC were pooled and concentrated to 10 mg/ml for crystallization trials. Fractions at all stages were analysed by SDS-PAGE and western blot (as described below).

2.5.2. Expression and purification of ELIC in E. coli

For expression of ELIC in *E. coli*, receptors were expressed as a fusion protein with Maltose Binding Protein largely as previously described (Hilf and Dutzler, 2008). Purification additionally used a modified version of the protocol described in (Gonzalez-Gutierrez et al., 2012). Proteins were overexpressed in *E. coli* C43 cells growing in 2YT media at 37° C, as carried out for GLIC, and expression was induced by addition of 0.2 mM IPTG once the cell suspensions reached an absorbance (OD_{600}) of ~1.6-1.8. Cells were cooled to 20°C and expression carried out overnight at 20°C shaking at 180 rpm. Cells were harvested by centrifugation and resuspended in ELIC Buffer A (150 mM NaCl, 50 mM Sodium Phosphate pH 7.9) supplemented with EDTA-free Inhibitor Cocktail Complete (Roche). Cells were disrupted by sonication and unlysed cells and debris cleared by centrifugation at 15,000g for 30 min at 4°C. The

membrane fraction was isolated by centrifugation of the cleared lysate at 200,00g (45Ti or 70Ti Rotor) for 2 h at 4°C. Membrane pellets were resuspended in ELIC Buffer A and proteins extracted with 40 mM n-Undecyl-β-D-Maltopyranoside (UDM) (Affymetrix-Anatrace, Generon Ltd, UK) overnight under gentle agitation. Insoluble material was removed by centrifugation at 200,000g and solubilized protein purified by immobilized metal affinity chromatography with Ni-NTA. Solubilized membranes were passed through a 0.45 µm filter before loading on to a 1ml HisTrap HP (GE Healthcare) column using a peristaltic pump P-1 (GE Healthcare) at 4°C in the presence of 10 mM imidazole. Flow through was recycled at least one further time over the column. The column was washed with ~20 column volumes of ELIC Buffer A supplemented with 3 mM UDM and 30 mM imidazole. Bound proteins were eluted in a single step with 300 mM imidazole. 1 ml fractions were collected and protein-containing fractions pooled, concentrated and desalted using a PD-10 column to remove imidazole. Fusion-protein was digested overnight at 4°C using His/GST-HRV 3C protease (Pierce/Life Technologies). A second round of affinity chromatography (by TALON Co^{2+} resin) was used to remove His-tagged MBP and protease. The flow through from this step contained cleaved ELIC. ELIC was concentrated and further purified on gel filtration column (Superose 6 10/300) equilibrated in ELIC Buffer B (150 mM NaCl, 10 mM Sodium Phosphate pH 7.9) supplemented with 1.2 mM UDM. Peak fractions corresponding to the pentameric protein were pooled and concentrated (for crystallization typically at 9-11 mg/ml). See further details regarding the preparation of ELIC for EM experiments.

2.6. Expression and purification of chimeric receptors in Sf9 insect cells

2.6.1. Insect cell culture

Sf9 insect cells (Invitrogen/Gibco) were cultured using standard methods. In brief, cells were cultured in suspension in Erlenmeyer flasks at 27°C shaking at 130 rpm in an Inova 42R shaking incubator (New Brunswick/Eppendorf), under no further atmospheric control, in two types of media: Sf900 SFM (Invitrogen/Gibco) or

InsectXpress with L-glutamine (Lonza/SLS, UK). After screening the effect of media on protein expression, InsectXpress media was used for scale-up experiments.

2.6.2. Transfection and Baculovirus-generation

Transfections were carried out on adherent cells, cultured in 6-well plates. Cells were seeded at ~1x10^6 cells/well and transfected using PEI Max (MW 40,000. Polysciences). Briefly, for each well 12 μg PEI in PBS was mixed with 4 μg of bacmid DNA, incubated at room temperature for 20 min and then added to the cells. Cells were incubated for 5-7 days at 27°C without shaking prior to harvest of the P1 virus. Culture media containing recombinant virus particles was collected and clarified by centrifugation. P1 virus was either used immediately for 'P2 viral' amplification or stored at 4°C in the dark. P2 virus was generated through infection of cells in suspension at a density of 1-2x10^6 cells/ml. Cells were infected with P1 virus at a dilution of 1:100 (v/v). Cells were incubated at 27°C shaking at 130 rpm for 72 hrs prior to harvesting P2 virus. Cell suspensions were centrifuged and supernatant containing P2 virus collected. Protein expression in transfected and infected cells was analysed by SDS-PAGE and western blot.

For protein expression experiments cells were grown in suspension to 1-2 x 10^6 cells/ml in 850 cm^2 roller bottles (400 ml cells/ bottle). Cells were infected with P2 virus at a dilution of 1:100 (v:v) and incubated at 27°C (unless otherwise stated) shaking at 130 rpm for 48-72 hrs.

2.6.3. Small-scale expression and detergent screening

In order to screen a number of constructs for expression, or a panel of detergents for their efficiency of extraction, a small-scale purification scheme was implemented. Starting material for purification was typically the biomass of 3-10 ml of insect cells (from a 30 ml culture infected with P2 virus). The following protocol was adapted from

one developed by the Joint Center for Innovative Membrane Protein Technologies (JCIMPT) for small scale screening of GPCRs and other membrane protein complexes. It should be noted that in this study, the procedure was used primarily to monitor construct expression and provide preliminary results for detergent extraction efficiency. It should also be noted that the effect of preparing cell membranes using the "high-salt/hypertonic wash" procedure prior to detergent extraction of receptors has not, at this stage, been explored in scale up studies in this study.

Insect cells were harvested by centrifugation and one time washed with cold PBS. Cell pellets were resuspended in Lysis Bufer (20 mM HEPES pH7.5, 20 mM KCl, 10 mM $MgCl_2$) and homogenized on ice (20 strokes of a dounce homogenizer). The amount of cell biomass and volume of lysis buffer used typically depended on the number of variables to be screened (e.g. screening of one construct against 10 detergents; 30 ml cells biomass resuspended in 3 ml of lysis buffer, homogenized and split between 10 1.5 ml eppendorf tubes ~0.3 ml/tube). Cell suspensions were centrifuged at 16,000-18,000 g for 30 min at 4°C. The supernatant was discarded and the pellet resuspended in buffer A (50 mM HEPES pH7.5, 500 mM NaCl, 10% glycerol) before centrifugation at 16,000 g for 30 min at 4°C. This step was subsequently repeated at least 3 more times. Cell pellets (crude membrane preparation) were resuspended in detergent extraction buffer and mixed at 4° C for 1-2 hrs. Detergents (see *Table 2.7*) were used at a final concentration of 1% final and cholesterol hemisuccinate (CHS) at 0.1% (w/v). Insoluble material was removed by centrifugation at 16,000 g for 30 min at 4°C, and solubilized proteins purified by TALON Co^{2+} resin (in the presence of 20 mM imidazole) at 4°C for at least 2 hrs. 25 µl of TALON resin (equilibrated in buffer A supplemented with 20 mM imidazole) was used per sample. Following incubation, TALON resin (and bound protein) was pelleted at 700 g for 5 min at 4°C, and washed three times in Buffer A supplemented with 0.05% detergent (and 0.005% CHS) and 20 mM imidazole. Bound protein was eluted in a single step with 200 mM imidazole (typically 60 µl of elution buffer supplemented with detergent/CHS was used to elute protein from 25 µl of TALON resin). Eluted proteins were analysed by SDS PAGE and coomassie blue stain. Given that an equal mass of starting material was used per sample, we could assess and compare on a semi-quantitative level the extent to which various detergents

extracted a single protein of interest. Constructs (and individual virus stocks) could be rapidly assessed on the strength of their expression using this small-scale purification approach.

2.6.4. Large-scale expression and purification

Strong candidate receptors for structural studies identified from small-scale screens (and detergents potentially capable of extracting an appreciable yield of protein) were introduced in to scale-up expression studies.

Cells were harvested for purification after 72 hrs and collected by centrifugation at 3,220 g and washed once with cold PBS. Cell pellets were either used immediately or flash-frozen in liquid nitrogen and stored at -80°C. Pellets were resuspended in Buffer TBS (20 mM Tris pH 8, 300 mM NaCl) and EDTA-free protease inhibitor cocktail complete. Cells were disrupted by sonication on ice (10x using 15 s on/off cycles) with a Soniprep 150 equipped with a 9 mm probe. The homogenate was clarified by centrifugation at 8,000 g for 20 min at 4°C (JA-12 rotor) and the supernatant transferred to a chilled ultracentrifuge tube. The membrane fraction was isolated by centrifugation at 125,000 g for 1.5 hrs at 4°C (45Ti or 70Ti rotor). Membranes were resuspended in a volume of TBS corresponding to one volume per mass of the membrane pellet and homogenized with a dounce homogenizer on ice, and transferred to a chilled glass beaker. DDM was added at 0.1 g/g membrane and CHS at 0.1% final, and membranes solubilized (under gentle agitation by stirring) at 4°C for 2 hours. Insoluble material was removed by centrifugation at 125,000 g for 1 hr at 4°C (various rotors). Solubilized protein was bound in batch to TALON Co^{2+}-affinity resin overnight at 4°C in the presence of 10 mM imidazole. TALON resin was pre-equilibrated in Buffer TBS supplemented with 0.03% DDM. Resin bound protein was subsequently exchanged in to TBS containing DMNG/CHS in two-steps. Resin was first washed with 10 CVs of TBS supplemented with 0.04% DMNG, 0.002% CHS and 25 mM Imidazole, followed by washing with 20 column volumes (CV) of TBS supplemented with 0.02% DMNG, 0.001% CHS and 25 mM imidazole. Protein was eluted by a single-

step with 250 mM Imidazole (0.02% DMNG, 0.001% CHS). Eluted proteins were concentrated using an Amicon centrifugal filtration device exhibiting a 100 kDa cut-off membrane. Precipitated material was removed by centrifugation (16,000 g, 10 min, 4°C) and proteins further purified by gel filtration on a Superose 6 10/300 GL column equilibrated in Buffer TBS with 0.02% DMNG and 0.001% CHS. Peak fractions were analysed by SDS PAGE, and fractions corresponding to the pentameric protein pooled and further concentrated to ~3-7 mg/ml, and either used immediately for crystallization trials or flash frozen in liquid nitrogen and stored at -80°C.

2.6.5. SDS PAGE and Western Blotting

Protein samples were prepared in Laemmli buffer or LDS sample buffer and incubated briefly at room temperature. Samples were separated by SDS PAGE (Tris-Glycine gels) and either stained immediately with Coomassie Brilliant Blue (Sigma Aldrich) or transferred to a nitrocellulose membrane (0.45 μM pore) for western blot analysis. For western blot analysis membranes were initially blocked in 5% milk in PBS-T (PBS supplemented with 0.1% Tween-20), followed by incubation overnight at 4°C in primary antibody (in PBS-T + 5% (w/v) milk, *Table 2.6*). Blots were washed in PBS-T and then incubated in secondary antibody (in PBS-T + 5% milk). Blots were once again washed in PBS-T and then exposed to ECL reagent (Pierce Protein Biology, Thermo Fisher). Bands were detected using an ImageQuant LAS4000 Analyser (GE Healthcare).

Table 2.6 Antibodies used for western blot (WB) analysis

Antibody	Source (Cat. No)	Description	Application	Dilution (v/v)
Anti-6X His tag	Abcam ab18184	Mouse monoclonal	WB	1:4000
Anti-MBP	NEB	Rabbit antiserum	WB	1:5000

Table 2.7 Detergent and lipid solutions used for purifications and crystallography

Detergent/Lipid	Abbrev.	FW (Da)	CMC (mM)	CMC (%)
n-Decyl-β-D-Maltopyranoside	DM	482.6	~1.8	0.087
n-Undecyl-β-D-Maltopyranoside	UDM	496.6	~0.59	0.029
n-Dodecyl- β-D-Maltopyranoside	DDM	510.6	~0.17	0.0087
n-Octyl- β-D-Maltopyranoside	OM	545.4	~19.5	0.89
Octyl Glucose Neopentyl Glycol	OGNG	568.7	1.02	0.058
Decyl Maltose Neopentyl Glycol	DMNG	949.1	0.036	0.0034
Lauryl Maltose Neopentyl Glycol	LMNG	1005.2	0.001	0.01
Lauryldimethylamine N-oxide	LDAO	229.4	~1-2	0.023
Sodium lauryl sulphate	SDS	288.4	8.2	0.23
Anapoe-C10E6	C10E6	Avg. 423	~0.9	0.038
Anapoe-C12E8	C12E8	Avg. 539	~0.09	0.0048
Anapoe-C12E9	C12E9	Avg. 583	~0.05	0.003
Fos-Choline-12	FC12	351.5	~1.5	0.047
6-Cyclohexyl-1-Hexyl-β-D-Maltoside	Cymal 6	508.5	~0.56	0.028
7-Cyclohexyl-1-Hexyl-β-D-Maltoside	Cymal 7	522.5	~0.19	0.0099
Digitonin	-	1229.3	< 0.5mM	
Cholesteryl Hemisuccinate	CHS	486.73	-	-
Cholesteryl Hemisuccinate Tris Salt	CHS	607.9	-	-
1-Palmitoyl-2-Oleoyl-sn-Glycero-3-Phosphocholine	POPC	760.08	-	-
1,2-Dihexadecanoyl-sn-Glycero-3-Phosphocholine	DPPC	734.04	-	-
Amphipol A8-35	A8-35	~8 kDa	-	-

All detergents were sourced from Anatrace (Generon, Maidenhead, Berkshire, UK), with the exception of SDS (Sigma-Aldrich Steinheim, Germany), Digitonin (Calbiochem, Merck-Millipore, Darmstad, Germany), Cholesteryl Hemisuccinate (Sigma-Aldrich). CMC is the Critical Micelle Concentration, and values are for detergent in water (as provided by the supplier). Lipid (POPC and DPPC) solutions were typically prepared in 80% gel filtration buffer and 20% DMSO.

2.6.6. CPM Fluorescence Thermal Stability Assay

CPM assays were carried out at the Membrane Protein Laboratory, Harwell Research Campus (Didcot, UK)

Purified receptor protein (GLIC-$GABA_AR$ α1 chimeras in DMNG and CHS and ELIC in UDM) was mixed with a panel of detergents to assess thermal stability using an unfolding assay, (Alexandrov et al., 2008). Thermal stability was quantitatively characterised by changes in fluorescence output of the thiol specific fluorochrome N-[4(7-dimethyamino-4-methyl-3-coumarinyl)phenyl]maleimide (CPM).

Detergents were prepared in assay buffer (20 mM Tris pH 7.5, 150 mM NaCl) at a final concentration equivalent to 3x CMC (as detailed in *Table 2.7*). For example, DDM has a CMC of 0.0087%, and was used at 0.026% (i.e. 3x CMC) in CPM assays. CPM dye ((Sigma-Aldrich) was prepared as a 4 mg/ml stock in DMSO, and then further diluted 1:20 in assay buffer (supplemented with DDM) before dilution to a final working concentration as detailed below. Protein samples were typically diluted to ~4 mg/ml. For CPM assays the "reaction" was composed as follows (per well of a 96 well PCR plate):

Reaction Buffer	47 µl
Protein	1 µl
CPM Dye	2 µl
Total Volume	50 µl

The reaction mixture was mixed and briefly incubated at room temperature before transfer to a qPCR machine (Agilent Mx3005P, Agilent Technologies, Santa Clara, CA, USA) equipped with excitation/emission filter sets to monitor CPM fluorescence (Ex 384 nm/Em 470 nm). The experimental protocol consisted of a temperature ramp (in 1°C increments) from 25°C to 95°C. At each temperature step three fluorescence readings were recorded (and averaged).

For qualitative purposes raw data was plotted as temperature versus fluorescence readout. For quantitative purposes an inflection point of the melting curve, which is assumed to equal the melting temperature (T_m) was calculated. In order to calculate the T_m, a Boltzmann sigmoidal function was used to fit the experimental data. Data analysis was guided (and constrained) by visual inspection of the data, especially where fluorescent signals show considerable variability at high temperature.

2.7. Protein Crystallography

Protein crystallization was dependent on the purified receptor sample, e.g. GLIC-$GABA_AR$ α1 chimera, GLIC or ELIC and on the experiment type, e.g. co-crystallization, seeding, etc. General protocols for crystallization plate setup were followed for all purified receptors. Any variations in protocol have been detailed. Briefly, GLIC-$GABA_AR$ α1 chimeras were screened for crystal growth using sparse matrix screens and conditions previously reported for GLIC. WT GLIC was crystallized in previously reported conditions (Nury et al., 2011) and WT ELIC was also co-crystallized in previously reported conditions (Hilf and Dutzler., 2008), and under new crystallization conditions identified using sparse matrix screens.

2.7.1. General crystallization notes

Crystallization was carried out by vapour diffusion in either the sitting drop (e.g. 96 well MRC 2 drop plates/Swissci; Molecular Dimension, Suffolk, UK) or hanging drop configuration (e.g. 24 well plates and silicon coverslips). Plates were maintained at 4°C, 16°C or 22°C. Protein samples were concentrated with centrifugal filter devices (with molecular weight cut-offs of 50 or 100 kDa) either as the last step of purification or immediately prior to crystallization. Bacterial receptors, GLIC and ELIC, were typically concentrated to 6-10 mg/ml for crystallization trials, while GLIC-$GABA_AR$ α1 chimeras

were used in crystallization trials at 1-7 mg/ml. Prior to crystallization protein samples were centrifuged for 10 mins at >16, 000 g to remove any precipitated material.

Crystallization sitting drops in 96 well plates were set up using a TTP Labtech Mosquito robot. 80 µl of reservoir solution was transferred from a 96 well deep block (containing either "Sparse matrix" or optimization screen, as detailed below) to the reservoir well of a 96 well MRC 2 drop plate (*Fig 2.5*) using a Liquidator Pipetting System (Mettler Toledo, Leicester, UK). The plate was transferred to the plate position of the Mosquito robot and protein sample dispensed manually in to an 8 well disposable strip for automated transfer. A protocol was run which allowed for automated dispensing of crystallization drops (typically 100 nl of protein plus 100 nl of reservoir or 150 nl protein plus 75 nl reservoir).

Crystallization hanging drops (*Fig 2.5 A*) on siliconized circle coverslips (18 x 0.22 mm; Hampton Research, CA, USA) in 24 well plates were set manually. 500 µl of reservoir solution was dispensed in to the well of a 24 well plate. Drops (total volume of 1-2 µl) were composed of protein and reservoir mixed in 1:1 ratio. Coverslips were inverted over the reservoir solution and sealed with grease (see *Fig 2.5 A*).

2.7.2. Sparse matrix and additive screens

In initial crystal growth screening of chimeric receptors and ELIC, commercially available "sparse matrix" screens were used. These screens are generated from a range of crystallization conditions that have previously supported successful crystal growth (for subsequent X-ray diffraction studies). These conditions can be sampled for new proteins, if no previous information about crystallization exists. Sparse matrix screens specific to α-helical type transmembrane proteins have been designed, covering a range of pH conditions, precipitants, e.g. polyethylene glycols (PEG) and salts.

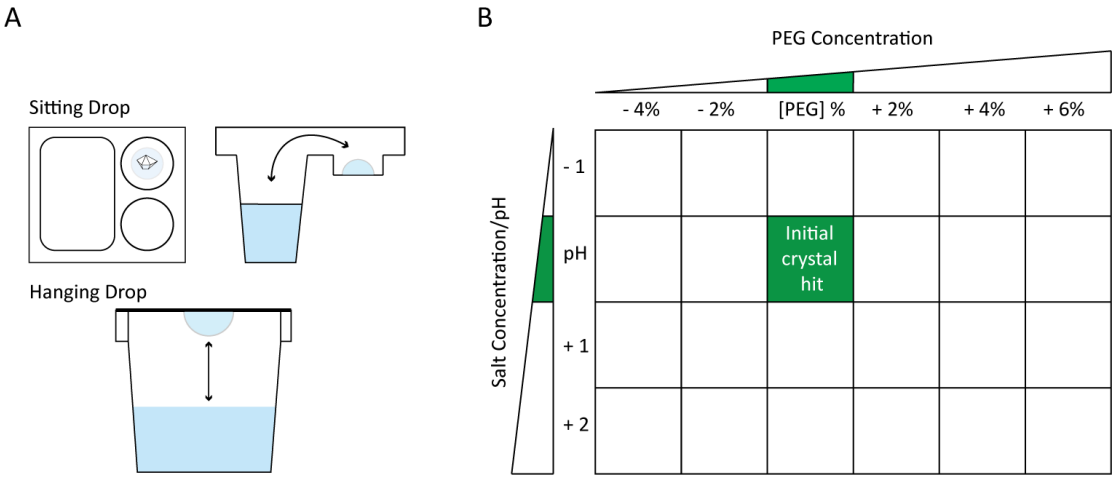

Figure 2.5 - Crystallization optimization set up and schematic of (vapour diffusion) sitting and hanging drop configurations

A. Sitting drop well configuration in MRC 2 Well plates (arrow represents vapour diffusion event) and hanging drops set on a coverslip. **B.** A broad screen around an initial crystallization condition hit (green box) is shown, in which [PEG %] and buffer pH has been varied. Variations of this configuration can be used to vary salt concentration.

Additionally additive and detergent screens can be used in optimizing crystal growth. These are used after identification of crystal "hits", i.e. a condition which supports crystal growth, and following initial rounds of optimization. Their use can prove helpful in improving crystal quality, e.g. size, shape and diffraction limit. Additive screens typically include ligands, detergents, multivalent salts, volatile and non-volatile organics as identified from data mining (of crystallization conditions in the PDB). Successful hits from additive and detergent screens can be used to design further optimization experiments. Indeed in the case of newly identified detergents, these might also be implemented during the final stages of purification. The commercially available screens used (in the 96 well sitting drop format) during this study are detailed in *Table 2.8*. For additive screens, the reservoir solution was composed of 72 µl "initial/optimized crystal hit" solution and 8 µl additive/detergent screen.

Table 2.8 Sparse matrix, detergent and additive screens

Screen Name	Screen Type	Supplier	Ref.
MemStart-Sys	Sparse matrix	Molecular Dimensions	Iwata., 2003
MemGold	Sparse matrix	Molecular Dimensions	(Newstead et al., 2008)
MemGold2	Sparse matrix	Molecular Dimensions	(Newstead et al., 2008; Parker and Newstead, 2012)
MemAdvantage	Additive	Molecular Dimensions	(Parker and Newstead, 2012)
Detergent Screen HT	Detergent	Hampton Research	Michel., 1991

2.7.3. Optimization screens

After identification of conditions yielding "crystal hits, optimization screens (*Fig 2.5 B*), or grid screens, are set up around the conditions yielding the crystal hits. In optimization screens of a condition containing a precipitant (e.g. PEG), salt and buffer, two of the components are varied while one is kept constant. An example of a broad screen (in 24 well format) around an initial hit, in which PEG concentration and pH have been varied is shown in *Fig 2.5 B*. Broad screens are often used to try to reproduce the initial hit, and if successful the range of concentrations or pH is further narrowed down (e.g. varying [PEG] in increments of 0.5% rather than 2%). Ideally, optimization trays should refine crystallization conditions to those which minimize crystal nucleation and maximise crystal size and quality.

During this study we carried out optimization screens in both 24 well and 94 well plate formats (i.e. crystal hits identified in sitting drops were also assessed by hanging drop). Initial hits were positioned close to the centre of a screen (*Fig 2.5 B*). Optimization

screens in the 24 well plate format were manually prepared from reagent stock solutions. Reagents were either prepared in house or obtained from the supplier of initial sparse matrix screens. For optimization screens in the 96 well format, a Perkin Elmer Multiprobe II Robotic liquid handling system was used. Solutions for the four corner points of a screen were prepared (e.g. comprising all components of the crystallization conditions in the minimal and maximal concentrations and pH to be used in the screen). These solutions were used (in varying ratios) to form the entire 96 well screen (which was prepared in a 96 deep well block). Screens were kept at 4°C for long term storage.

2.7.4. Co-crystallization

For co-crystallization experiments protein was mixed with drug or lipid solutions (at twice the final concentration) and incubated on ice prior to crystallization. Once mixed with reservoir solution at a 1:1 ratio the desired final concentration of drug was achieved. Crystallization experiments were then set up as normal (with the exception of some seeding experiments).

GLIC Co-crystallization

GLIC was incubated on ice with pentobarbital or a brominated derivative, 5-(2-Bromo-ethyl)-5-ethyl-pyrimidine-2,4,6-trione (S97617; both prepared in DMSO at 100 mM stocks). The concentration of drug solution was 5 mM once the protein sample was mixed with the reservoir solution at 1:1. No precipitation of protein was observed during incubation with the drug.

ELIC Co-crystallization

ELIC was incubated with either DPPC or POPC lipids (with gentle mixing). Lipids were prepared as 2% stocks in gel filtration buffer (with UDM) and added to a final concentration of 0.02%. The agonists GABA or propylamine (250 mM stock in gel

filtration buffer; Sigma-Aldrich) were then added at 30 mM or 5mM respectively. The antagonist pregnenolone sulphate was added at 250 µM (from a 10 mM stock).

2.7.5. Micro-seeding strategies

Where crystallization trials yielded crystals with unfavourable properties (small, ill-defined shapes and weakly diffracting), a seeding strategy was used. This technique has been used in a number of membrane protein crystallization studies to improve crystal size and reproducibility, and eventually yield high quality diffracting crystals (Dürr et al., 2014; Sauguet et al., 2014b).

Under normal crystallization conditions, the sample (e.g. pLGIC in buffer, salt and detergent) starts in a stable, undersaturated state. In this state crystals cannot nucleate. Upon addition of a crystallization reagent the relative supersaturation of the sample increases, and can result in three events (defined as zones of the crystal phase diagram; *Fig 2.6*). In the metastable zone nuclei cannot form but crystals can grow; in the labile zone crystals can both form and grow; and in the precipitation zone the sample precipitates and crystal formation is not possible. Using a seed stock formed from a crushed small crystal or crystal fragment, one can control the extent of crystal nucleation (bypassing the need for spontaneous nucleation) and in doing so grow crystals of increased size and with greater reproducibility. The seed stock is added to a fresh protein sample and reservoir solution, in varying ratios, at the point of setting new crystallization drops. As under normal conditions, the addition of seeds in an unsaturated solution, or in the precipitation zone, does not support crystal growth. However addition of seeds to a drop saturated to the metastable phase can support crystal growth (where originally spontaneous nucleation could not occur, *Figure 2.4*). By serially diluting the seed stock the number of crystals that grow in this zone can be manipulated, ideally supporting the growth of fewer large crystals. Similar results can be achieved by streaking a crystalline material (dislodged from an existing crystal by means of seeding tool, e.g. cat whisker) drawn across a recipient drop. Ideally the recipient drop should be in the metastable zone.

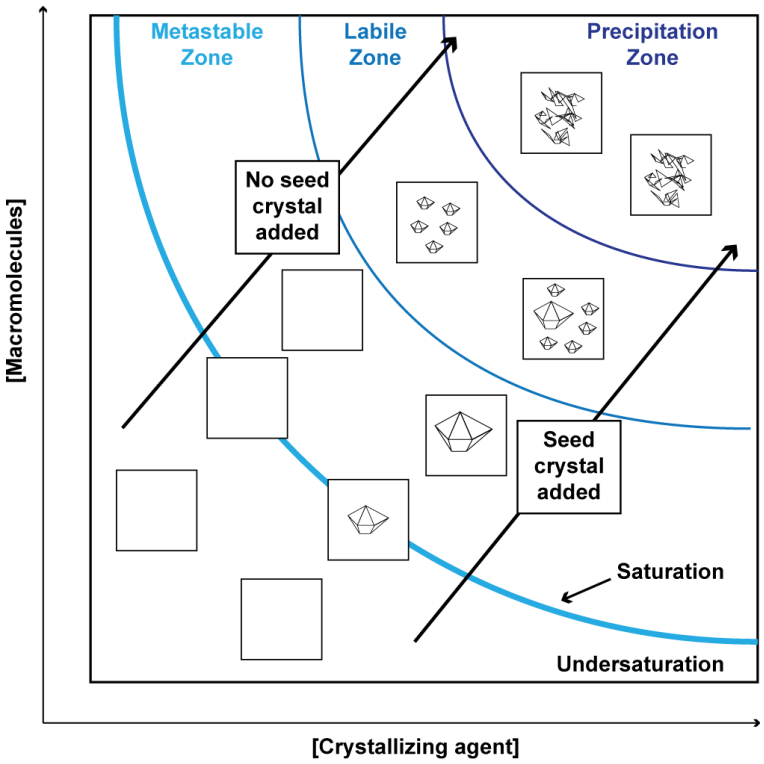

Figure 2.6- The crystallization phase diagram and the effect of crystal seeding

The crystal phase diagram is shown (adapted from Luft & De Titta, Acta Cryst. 1999). The solubility of a protein (macromolecule) in solution is shown as a function of the concentration of the precipitant (crystallization reagent) present. The metastable, labile and precipitation zone all represent states of supersaturation. Crystal nucleation can only occur from the labile zone, however growth is supported in the metastable zone. Addition of crystal seeds (ideally to a crystallization drop in the metastable zone) bypasses the need for spontaneous nucleation of crystals.

2.7.6. Seeding strategies applied to GLIC (co-)crystallization

In “normal” crystallization experiments, GLIC had a tendency to form plate-shaped crystals, lacking substantial size in all dimensions. Plate-shaped crystals were used to generate a seed stock for seeding experiments. Crystallization drops containing plate crystals were opened, and crystals crushed using a glass probe. Then, 5 µl of the crystallization reagent was added to the well containing crushed crystal slurry and transferred to an eppendorf tube on ice containing a bead. A further 5 µl of crystallization reagent was added to the well and transferred to the tube. This process

was repeated until all crystal fragments had been transferred (~40-50 µl). The tube containing the bead and crystal seed slurry was then vortexed for 3 min, periodically stopping and returning the tube to ice. The final slurry formed the seed stock. Seed solutions were typically used in an undiluted form (a process termed Microseed Matrix Screening) to set new crystallization drops. Seeding experiments were carried out in 24 well optimization screens. Drops were manually set and were composed of 1.2 µl protein, 0.8 µl reservoir solution and 0.4 µl seed stock (equivalent ratios were also maintained in different drop volumes). Seeds prepared from apo-GLIC were also used as seed stocks for drops set with GLIC incubated with drug.

Streak seeding was also carried out for GLIC, using a seeding tool (composed of a natural fibre). Donor crystals were touched with the seeding tool, and seeds deposited in a recipient drop by running the seeding tool in a straight line across the middle of the drop. Recipient drops were composed of GLIC protein and crystallization reagent in which crystal nucleation or precipitation had not been observed (i.e. well below supersaturation).

2.7.7. Cryo-crystallography

Throughout this study X-ray diffraction data was collected at cryogenic temperatures (-173°C). Crystals were therefore rapidly cooled by plunging in to liquid nitrogen (and stored) prior to diffraction data collection. Crystals were typically transferred using a nylon loop (Hampton Research) or micro-loop (Mitegen, Ithaca, NY, USA) to a solution composed of the mother liquor supplemented with 20% glycerol, and allowed to briefly equilibrate. During this period, crystals were monitored for visible changes in their physical properties, e.g. cracking. For ELIC 30% glycerol or ethylene glycol was also used as cryoprotectant. Crystals of GLIC-$GABA_AR$ α1 chimeras, GLIC and ELIC were also assessed for diffraction without cryoprotectant, but the lack of cryoprotectant having detrimental effects in all cases. After incubation in cryoprotectant, crystals were rapidly plunged into liquid nitrogen and stored in vials under liquid nitrogen prior to X-ray diffraction experiments.

2.7.8. Diffraction Data Collection Strategies

X-ray diffraction of crystals was screened by a synchrotron radiation source. Diffraction data were collected at Diamond Light Source (Harwell, UK) on beamlines I03, I04 and I24 (microfocus); the French National Synchrotron Facility – Soleil (Gif-sur-Yvette, France) on beamline Proxima 2 (microfocus); and the European Synchrotron Radiation Facility (ESRF, Grenoble, France) on beamlines ID23-1 and ID23-2 (microfocus). Microfocus beamlines allow for the beam size to be focused down to 5 µm x 5 µm. This allows for precise characterisation of the diffraction properties of small crystals and at various regions of larger crystals (which would not necessarily be possible with a beam of larger dimensions).

For crystal characterisation, short exposure times at 50% beam transmission were used, e.g. 0.1-0.5 s exposure times at 50% beam transmission. Typically 3 diffraction images separated by 45° were collected (total rotation of crystal of 90°). During image acquisition oscillation angles of 0.1-1° were used. Where crystals could not easily be identified or to align best diffracting portion of a large crystal, grid scans of crystals were used to assist crystal alignment (this is not available on all beamlines used during this study). Briefly, a grid is drawn over a region of interest and X-ray diffraction pattern recorded for each sector. The strongest diffracting region is aligned to the beam centre and crystal rotated through 90°. A second grid scan is carried out and, the crystal aligned to the strongest diffracting region. In doing, so the crystal can be precisely aligned relative to the beam centre.

Crystal characterisation and (where possible) data collection strategy calculations were carried out using automated software pipelines associated with the beamlines (as part of the acquisition software). The characterization and strategy program EDNA was run for collections of 2-4 images. This program is run automatically with diffraction images used as input files to be run in the program Mosflm (Powell et al., 2013). Mosflm carries out indexing of reflections and allows for crystal orientation, unit cell parameters and a possible crystal space group to be determined. Following complete data set collection, Mosflm is used to intergrate images and generate an output (MTZ)

file of reflection indices with their intensities and standard deviations. The MTZ file format can be used in programs of the CCP4 program suite (Collaborative Computational Project No. 4 suite of software for macromolecular X-ray crystallography (Winn et al., 2011)).

2.7.9. Data Processing and Model Building and Refinement for GLIC

During this study a data set (from a single crystal) of GLIC (grown in the presence of a pentobarbital-derivative) at a resolution of 3.2 Å was collected at 0.954 Å on beam ID23-1 at ESRF (Data set: 1225 images of 0.2° oscillation, 100% beam transmission, 0.04 s exposure; *Table 2.9*). The model presented in Chapter 5 was generated from an MTZ output file from the automatic software pipeline applied to data collections at ESRF. Data is indexed and integrated in XDS (X-ray Detector Software, MPI for Medical Research, Heidelberg, Germany (Kabsch, 2010)), and fed (via the program Pointless, which also checks the assigned symmetry space group) into Aimless for data reduction. The resulting MTZ file was used for structure determination by molecular replacement. Molecular replacement uses known structures to phase experimental data and provide an initial model for structure refinement. This is achieved through rotation and translation of the known structure in the unit cell of the collected diffraction data.

Additionally the raw image files were processed manually in Mosflm (following the principles described for initial crystal characterisation). As for autoprocessed data, indexed and integrated data was reduced using the Aimless program in CCP4 (Winn et al., 2011). The resulting MTZ file was also used for structure solution by molecular replacement in Phaser (as described below). Results from manually and auto-processed data were identical.

The structure of GLIC in this study was solved by molecular replacement in Phaser (McCoy et al., 2007) using GLIC at 2.4 Å (PDB 4HFI) as a search probe (in which detergent and water molecules were removed). The translation function Z-score (TFZ) in Phaser show that the solution is correct; TFZ = 13.8. As a rule of thumb, a TFZ value

>8 shows correct structure solution. For data presented in Chapter 5, an initial round of automated model building, structure refinement and density modification was carried out using Phenix Autobuild. Given that the space group and unit cell dimensions were isomorphous to the apo-GLIC, which was used as a search probe, we assessed initial density maps for their quality but also ambiguous peaks in electron density and difference maps (an example of "ideal" density maps generated by refinement and their interpretation is shown in *Fig 2.7*).

Table 2.9 Crystallographic Statistics (values in parentheses are for the highest resolution shell)

Data Collection Beamline	**ID23-1**
Space Group	C2
Cell Dimension a, b, c (Å)	180.7, 132.8, 159.2
Cell Angles α, β, γ (°)	90, 102, 90
Wavelength (Å)	0.9537
Resolution (Å)	49.47 – 3.19 (3.28-3.19)
Completeness (%)	91.0 (55.1)
Multiplicity	4.3 (2.8)
I/σI	7.2 (1.3)
R_{meas}	0.189
R_{merge}	0.147 (0.051)
$CC_{1/2}$	0.944 (0.567)

Coordinate files, electron density and difference maps were opened in Coot (a molecular graphics application for model building) for visual inspection (Emsley et al., 2010). Where side chains could not be fit to density or showed poor stereochemistry (as assessed by the Ramachandran plot function in Coot), only the Cα-backbone was built. Clear electron density was visible for 6 detergent molecules in the channel pore (consistent with published GLIC structures), and also visible as positive density in the difference map. The position of this density allowed for superposition of detergent molecules modelled for GLIC (PDB 4HFI; for purposes of visualization). Initial maps revealed positive peaks in the difference map (when contoured at >5 σ) at subunit

interfaces. In light of previous observations we modelled these as chloride or acetate ions (in Coot). Indeed many of the clear peaks in electron density and difference maps (that were not contributed by the protein model) could be interpreted based upon previous observations made for GLIC crystal structures. Electron density and difference maps were prepared for molecular graphics with FFT program in CCP4 and opened in Pymol for image preparation. B-factors stated in the text are those generated in Phenix program "auto.refine". All images and alignments were prepared in Pymol (DeLano Scientific, 2002; except for images of α1 GlyR in Chapter 1 which were prepared in Chimera, USCF).

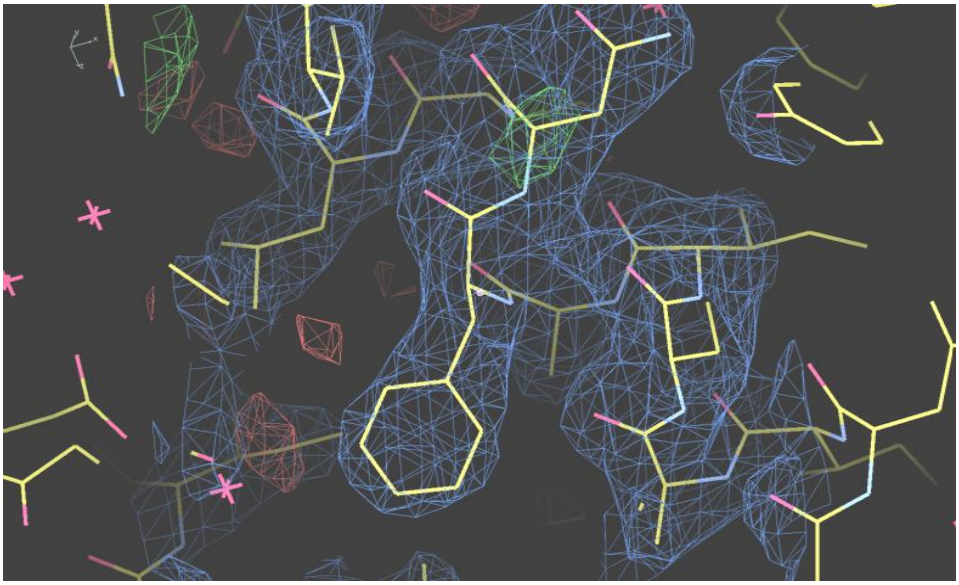

Figure 2.7-An example of a 2mFo-DFc density map (blue) and mFo-DFc difference map (green/red) for published structure of GLIC (PDB 4HFI).

The 2mFo-DFc map is generated during refinement and is the primary map used for manual inspection and model building. Fo and Fc are the experimentally measured and model-based amplitudes for the structure. The map shown is a portion of the structure of GLIC (PDB 4HFI; maps obtained from the Electron Density Servers (EDS)). The 2mFo-DFc map is coloured blue and contoured at 1.5 σ, i.e. 1.5 standard deviations above the mean electron density, and shows where we expect most of the model to be (excluding hydrogen atoms). The mFo-DFc (difference) map is coloured green (positive contours at +3 σ) and red (negative contours at -3σ). The positive density (green) indicates features present in the data not accounted for the model (e.g. a drug molecule). The negative density (red) indicates parts of the model that are not supported by the data (e.g. an incorrectly modelled residue side chain). This model of GLIC (after multiple rounds of model building and refinement) fits well with the density maps. In this case positive peaks in the difference map likely represent unmodeled interatomic scattering.

2.8. Electron Microscopy

Electron microscopy was carried out at Birkbeck EM Laboratory. Duncan Laverty prepared protein samples, assisted with image collection and project design. Dan Clare (Birkbeck) prepared EM grids, collected and analysed images and assisted project design. ELIC (negative stain and cryo-EM) and GLIC-$GABA_AR$ α1 chimeras (negative stain-EM) were used in these experiments.

2.8.1. Sample preparation for EM (exchange in to Tris Buffer or Amphipol)

Where protein samples were not in Tris-buffered solution, a final buffer-exchange step was included in the previously described purification procedure. 300-500 µl of purified cleaved-pentameric ELIC was injected on to a Superose 6 10/300 GL column equilibrated in 20 mM Tris pH7.6, 150 mM NaCl and 1.2 mM UDM and run at a flow rate of 0.3 ml/min. The elution profile was identical to that of ELIC purified in sodium phosphate buffer. Peak fractions were analysed by SDS PAGE and coomassie stain, pooled and concentrated initially to 3 mg/ml for EM.

For the exchange of ELIC in to Amphipol A8-35; 500 µl of purified pentameric ELIC (in SEC buffer + 1.2 mM UDM at 1mg/ml, as described in *Section 2.5.2*) was mixed with Amphipol A8-35. A 50 mg/ml stock of A8-35 was prepared in ELIC SEC buffer (10 mM Sodium Phosphate, pH 7.9 and 150 mM NaCl) without detergent. Amphipol A8-35 was added to the protein in varying ratios of 1:3, 1:6, etc (protein: A8-35, w/w). The protein-amphipol solution was mixed overnight at 4°C. Following incubation, the protein-amphipol solution was added to a tube containing 60 mg of Biobeads (Biorad). Biobeads adsorb free detergent and amphipol molecules (removing them from aqueous solution). This was mixed for a further 1-2 hrs at 4°C. Biobeads were separated from ELIC in A8-35 by passing over a small EconPac column (; the ELIC/A8-35 complex was collected in the flow through). The flow through was injected on to a Superose 6 10/300 GL column equilibrated in 20 mM Tris pH7.6 and 150 mM NaCl. Peaks corresponding to pentameric ELIC-amphiol A8-35 and free amphipol molecules

were observed. Peak fractions for the former were pooled and concentrated 1-2 mg/ml for EM.

2.8.2. Sample preparation for Negative Stain EM

Protein sample in detergent or amphipol was used for negative stain EM at 0.01-1mg/ml. 3.5 µl of purified protein sample was applied to glow-discharged EM grids (6mm) covered with a continuous coating of carbon. Glow discharging renders the normally hydrophobic carbon surface more hydrophilic. This was left for 30-60 sand then blotted, before staining with 5 µl of 2% uranyl acetate for 1-2 min. The protein was removed by blotting and imaged in the electron microscope. EM girds were stored at room temperature prior to imaging. Additionally, for certain experiments EM grid were pre-treated with poly-lysine (Sigma Aldrich) to positively charge the surface. Staining was carried out as normal.

2.8.3. Sample preparation for Cryo-EM

For cryo-EM sample preparation the concentration of purified ELIC (in detergent, UDM, or amphipol, A8-35) was adjusted to 0.5-3 mg/ml. 3.5 µl of protein was applied to glow discharged holey or lacey carbon coated (copper) grids. An additional treatment of with poly-lysine was also used for some grids. After approximately 30 s grids were blotted to remove the protein solution and rapidly plunged in to liquid ethane for vitrification.

2.8.4. Sample imaging and data analysis

Negative stain EM images were collected on a Tecnai T10 (FEI, Oregon, USA) operated at 100 keV, at a magnification of 44,000 x and Tecnai T12, operated at 120 keV, at a

magnification of 67,000 x. Cryo-EM images were collected on a Tecnai Polara EM (FEI) operated at 200 keV with a K2 direct electron detector (Gatan, Pleasanton, CA, USA) at 27,000 x magnification. Particles (~4,500) were aligned and classified in RELION (Scheres, 2012).

2.9. Mass Spectrometry

Mass spectrometry was carried out in the laboratory of Konstantinos Thalassinos (Structural and Molecular Biology, UCL). Duncan Laverty prepared samples for mass spectrometry. Data acquisition and analysis was carried out by Adam Cryar (Peptide Fragment Mapping) and Kitty Hendricks (Native Mass Spectrometry)

2.9.1. Tryptic Digest of In-gel Proteins and Mass Spectrometric Analysis

Tryptic Digest

Identification of purified proteins was confirmed using mass spectrometry. Protein samples were separated by SDS PAGE and stained by coomassie. Target protein bands were excised and destained with a mixture of acetonitrile and 50 mM ammonium bicarbonate pH8 (40% and 60% v/v respectively). Native proteins were subsequently reduced with 10 mM DTT at 80°C for 30 min, followed by alkylation with 55 mM Iodoacetamide for 20 min at RT in the dark. Gel pieces were washed by swelling and shrinking with sequential washes with 50 mM ammonium bicarbonate and acetonitrile. Proteins were digested overnight with Trypsin (at 10 ng/μl in 50 mM Ammonium bicarbonate) at 37°C. Peptides were extracted in a mixture of formic acid (1%) and acetonitrile (2%) (prepared in water) and dried under vacuum. Samples were stored frozen at -20°C prior to analysis.

Peptide Fragment Data Acquisition

Nano-Reversed Phase Liquid Chromatography (RPLC) separation of each tryptic digest sample prior to analysis by mass spectrometry was performed using a nano-ACQUITY UPLC system (Waters Corporation) with the use of a 5 µm SYMMETRY C18, 180 µm x 200 mm trap column and a 1.7 µm BEH130 C18, 75 µm x250 mM analytical column. A two-phase linear gradient was performed where solvent A was 0.1 % formic acid in water and solvent B was 0.1 % formic acid in acetonitrile. Sample was applied to the trapping column at mobile phase composition of 3 % solvent B with a flow rate of 5.0 µl/min. The column was then desalted for 2 min at the same conditions. A linear gradient was then applied at a flow rate of 0.3 µl/min whereby the concentration of solvent B was increased from 3 to 40 % over 29 min. Analysis by mass spectrometry was acquired using a Synapt HDMS (Waters Corporation) coupled to the nano-ACQUITY system. The Synapt time-of-flight mass analyser was calibrated over a mass/charge (*m/z*)range of 175.11 Da to 1285.54 Da using the fragment ions of the peptide [Glu1]-Fibrinopeptide B (GFP). The double charged precursor monoistopic peak of GFP was fragmented with a collision energy of 30 eV. During analysis a solution of GFP at 500 fmol/µl was delivered at a flow rate of 0.3 µl/min via a NanoLockSpray source. This faciltated the post acquisition lockmass correction of data using the monoisotopic mass of the doubly charged precursor of GFP. The reference sprayer was sampled every 60s. Accurate mass measurements were made using a data independent mode (LC-MS^E) of acquisition. Briefly, energy in the collision cell was alternated from low energy (6 eV) to high energy (energy ramp from 15-35 eV) whilst continuously acquiring MS data. Measurements were made over a *m/z* range of 100-2000 Da and the time of flight mass analyser was operated in V mode with a scan time of 1s.

Peptide Fragment Mapping Data Processing

All data processing was carried out using PLGS v2.5 (Waters Corporation). The computational methods used to process the data are explained in detail in (Geromanos et al., 2009). Data was searched against a Swissprot specific protein

database (generated for *Spodoptera frugiperda*Sf9 insect cells) appended with the sequence of the chimeric receptor to be identified. Carbamidomethyl-C was specified as a fixed modification. Oxidation (M), was specified as variable modifications. A maximum of two missed cleavages of the protease were allowed for semi-tryptic peptide identification. For peptide identification two corresponding fragment ions were set as a minimum criterion whereas for protein identification a minimum of one corresponding peptide identification and seven fragment ions were required.

2.9.2. Native Mass Spectrometry (nMS) and Ion-Mobility Mass Spectrometry (IM-MS) Spectrometry

nMS and nIM-MS experiments were carried out on a Synapt G1 Mass Spectrometer (Waters, Herts, UK). Ionization of samples was carried by nano-Electrospray Ionization (ESI) in IM-nMS experiments. For ionization, samples were loaded in to the mass spectrometer using gold-coated glass capillaries (manufactured in-house). Spectra were recorded in positive ion mode and time-of-flight mass analyser in V-mode. Data were analysed using MassLynx software version 4.1 (Waters) all spectra smoothed using a mean function. Calculation of masses from the mass spectra was carried out using a script developed by K. Thalassinos. In brief the script takes observed mass/charge (*m/z*) values and calculates their corresponding mass when given a charge state (of 1 to 100). A charge series is made, for which an average mass and standard is calculated. Charge states with the lowest standard deviation are taken to generate the final experimental mass.

2.10. Homology Modelling

A 3D homology model of the GLIC-$GABA_AR$ α1 chimera was generated using Modeller (Version 9.7; Eswar et al., 2008) and the crystal structure of GLIC (PDB 3EAM; Bocquet et al., 2009) as a template. 50 models were generated and ranked by DOPE score.

Chapter 3: Generation of functional chimeric $GABA_A$ receptors; electrophysiological and pharmacological characterisation

3.1. Introduction

To increase our understanding of the structural mechanisms underlying Cys-loop receptor operation, specifically $GABA_AR$ gating and allosteric modulation at the level of the ion channel, we based our experimental approach on the design and generation of a functional chimeric $GABA_A$ receptor. The rationale for this is based on recent work demonstrating that structural and functional studies are possible when using a prokaryotic-eukaryotic receptor chimera model, which has recently been created between the extracellular domain (ECD) of GLIC and the glycine receptor α1 subunit transmembrane domain (TMD) (Duret et al., 2011; Moraga-Cid et al., 2015).

We took a similar approach, exploring the potential use of the ECD of previously crystallized receptors, for example the prokaryotic proton-gated receptor GLIC, to act as a surrogate host for $GABA_AR$ subunit TMDs. While "GLIC-based" chimeras will represent our primary focus, we will also use alternative ECD surrogate hosts for $GABA_A$ receptor TMDs. By taking this approach we might be able generate a functional receptor, which is amenable to both high level expression and crystallization, particularly where known crystal-packing contacts exist and might be expected. For example, interactions between neighbouring ECDs are shown to form principal contact points in the crystal packing of GLIC (Bocquet et al., 2009).

Given that we propose to utilise a chimeric receptor system in this study (rather than full-length receptor subunits), it is crucial that the receptors generated represent a suitable model for study of native $GABA_ARs$ by retention of appropriate functional characteristics. Therefore, prior to assessment of high-level expression (and purification), receptors were characterised at a functional and pharmacological level. Those exhibiting characteristic "$GABA_AR$-like" traits would serve as candidate receptors to advance forward to further structural studies (in Chapter 4).

Upon generation of receptor chimeras, we took advantage of two recombinant expression systems, HEK293 cells and *Xenopus* oocytes, for screening receptor assembly, trafficking, ion channel function and pharmacology. Whilst ion channels that are over-expressed and purified from bacteria and insect cells typically form the starting material for structural studies (e.g. X-ray crystallography and electron microscopy), the construct used in purification protocols is often tested for functionality in alternative more amenable recombinant expression systems (Hibbs and Gouaux, 2011; Lee et al., 2014). Ion channels expressed and characterised electrophysiologically in *Xenopus* oocytes and HEK293 cells likely represent what might be expected to exist in a water-soluble protein-detergent lipid complex following extraction from the host plasma membrane. As a result electrophysiological studies and purification rarely use the same expression system. Despite this, recent developments in mammalian expression systems for high-level protein expression, particularly HEK293 cells (and to a lesser extent insect cells), are notable in that they allow for robust functional characterisation and purification of the protein of interest from the same membranous environment (Miller and Aricescu, 2014)(Cao et al., 2013a; Moraga-Cid et al., 2015). In acknowledging these caveats, we have used HEK293 primarily to assess trafficking of receptors to the cell surface (using fluorescence microscopy) and ion channel expression in *Xenopus* oocytes with two-electrode voltage-clamp (TEVC) electrophysiology to assess the function and pharmacology of chimeric receptors.

In addition to assessing efficient expression of functional chimeric receptors, we have used site-directed mutagenesis to establish whether chimeric and native receptors gate via a common mechanism. Notably, we examined the structural elements responsible for receptor desensitization, further testing the notion that a desensitization gate, distinct to the activation gate in the ion channel, is responsible for defining a closed channel-state during prolonged exposure to agonist. Whilst pLGIC desensitization arises from the concerted movements of structural elements at the level of the ECD and ECD-TMD interface (Bouzat et al., 2008; Pless and Lynch, 2009a; Wang and Lynch, 2011), recent studies suggest that the ion channel adopts a distinct intermediary conformation in the transition from active-open through desensitized-

closed to the resting-closed state of the receptor (Auerbach and Akk, 1998; Velisetty and Chakrapani, 2012; Miller and Aricescu, 2014; Gielen et al., 2015; Kinde et al., 2015). Structure-function studies have identified residues near an intracellular portal of the ion channel that form the core of a "desensitization gate", inducing a constriction of the pore during prolonged exposure to agonist (Gielen et al., 2015). Despite these recent breakthroughs, the nature of receptor desensitization remains a contentious subject, particularly in assigning structures to the fast and slow desensitized states of the receptor (and the associated conformational transitions).

We have introduced single point mutations into M2 and M3 of chimeric receptors and monitored their effect on receptor desensitization. In cases where mutations rendered the channel non-functional, a well-characterized gain-of-function mutation (at the level of the hydrophobic "activation gate" of the receptor, defined as 9') was introduced in rescue experiments (Chang and Weiss, 1999). Through a combination of mutagenesis studies and pharmacological assessment of non-mutant bearing forms of the chimera, we have been able to establish common structural elements to both receptor activation and modulation, when compared to native $GABA_A$Rs.

3.2. Results

On the basis of comparative alignments of receptor subunits, homology modelling and structure-function data, a chimeric GLIC-$GABA_A$ receptor subunit was designed and generated using standard molecular biology techniques. Structural "mismatches" occurring at the coupling interface (between the prokaryotic ECD and eukaryotic TMD) were identified and mutated (to assess their effect on channel gating). Receptor cDNA was injected in to *Xenopus* oocytes and whole-cell proton activated currents recorded in the two-electrode voltage-clamp configuration. Agonists and allosteric modulators were applied using an in-house gravity flow perfusion system (as described in Materials and Methods) for rapid drug application.

3.2.1. Homology model and schematics

We focused our initial studies on generating a functional chimera between the ECD of GLIC and the TMD of $GABA_A$ receptor α1 subunit. Functional studies of α1-containing $GABA_A$ receptors in recombinant expression systems have revealed a role for residues in the $GABA_A$α1 TMD in coordinating the sensitivtiy to the allosteric modulators, the neurosteroids, and in setting the extent of receptor desensitization (Hosie et al., 2006; Gielen et al., 2015).

In designing a chimeric receptor, an extensive sequence alignment of pentameric ligand-gated ion channels (; previously generated by Dr M. Gielen) was analysed. Existing functional data could be mapped onto known structural elements of the receptors (e.g. TM regions, connecting loops at the gating interface and the large intracellular loop between M3 and M4; *Appendix Fig 3*). Additionally a receptor homology model (using the crystal structure of GLIC: pdb 3EAM as a template) served to guide subsequent mutagenesis at the prokaryotic-eukaryotic interface. The point of ECD-TMD fusion was selected at a site preceding M1 where an arginine residue was identified that is conserved across the pLGIC family, and a glycine-tyrosine motif that is also conserved across many $GABA_A$ subunits (*Fig 3.1* and *Appendix Figure 3*). Expression and trafficking of the chimeric receptor to the cell surface was under the control of the α7 nAChR signal peptide sequence (which has previously been reported to enable efficient expression and export of GLIC to the plasma membrane (Bocquet et al., 2007). While initial studies focused on a simple domain-switch chimeric receptor, structural elements at the coupling-interface (including loop 7; a conserved FPM motif and the M2-M3 linker) were assessed as likely areas where residue mismatches might affect the efficacy of channel gating. It should be noted that for clarity, residue numbering in the ECD and TMD of the receptor is as observed in the native full length receptor (e.g. the domain switch occurs at position GLIC Y194 and continues from $GABA_A$ α1 G223)

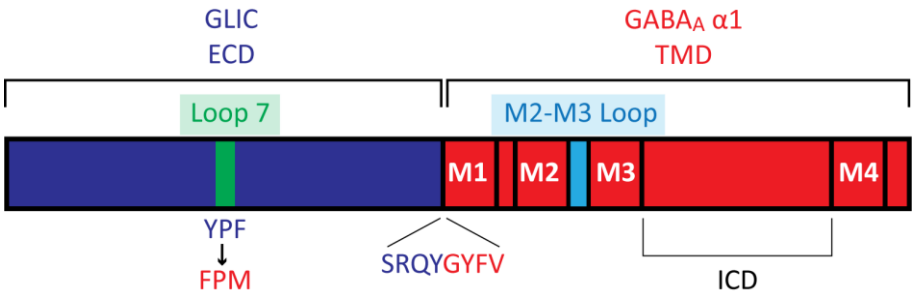

Figure 3.1 - Chimeric GLIC-GABA$_A$R α1 receptor

Schematic representation of GLIC-GABA$_A$R α1 domain chimera. The ECD (blue) is of GLIC and the TMD (red) of the GABA$_A$ α1 receptor subunit. Notable structural elements forming the coupling interface are Loop 7 (Green) and the M2-M3 loop (Blue). The sequence at the point of domain fusion is shown. The large loop between M3 and M4 (forming the ICD) of the GABA$_A$ α1 receptor subunit is not observed in GLIC.

3.2.2. α-Bungarotoxin binding studies

In order to assess the expression, assembly and trafficking of receptors (in HEK293 cells), a mimotope of the binding site for the neurotoxin, α-bungarotoxin (hereafter referred to as bungarotoxin-binding site; BBS (Wilkins et al., 2008) was introduced near the end of the N-terminal. Export of receptors to the surface was monitored in live cells by labelling with an Alexa 555 fluorophore-conjugated α-bungarotoxin (as described in Materials and Methods: *Section 2.4.2*). Given that α7 nAChRs, a distant relative of GLIC, possess an innate bungarotoxin binding site (Li et al., 2011) (coordinated by residues in the ECD) we first assessed toxin-labelling of GLIC lacking a BBS in HEK cells co-transfected with enhanced green fluorescent protein (EGFP). In contrast to HEK cells expressing α7 nAChR-5-HT$_3$ chimeras (*Fig 3.2 A*), innate labelling of GLIC was not observed. Upon introduction of the BBS, robust cell surface labelling of cells expressing ^{BBS}GLIC was observed within 24 hrs of transfection (*Fig 3.2 B*). Labelling of BBS-tagged GLIC-GABA$_A$ receptor α1 chimeric receptors at the cell surface could also be observed, with a peak in labelling approximately 48 hrs after cell transfection (*Fig*

3.2 C). This would suggest that the folding and trafficking process is not as efficient for the chimera when compared to wild type GLIC protein. Throughout this study we have further utilised this mimitope tagging approach to rapidly screen receptors for efficient expression and cell surface export in parallel to functional analyses.

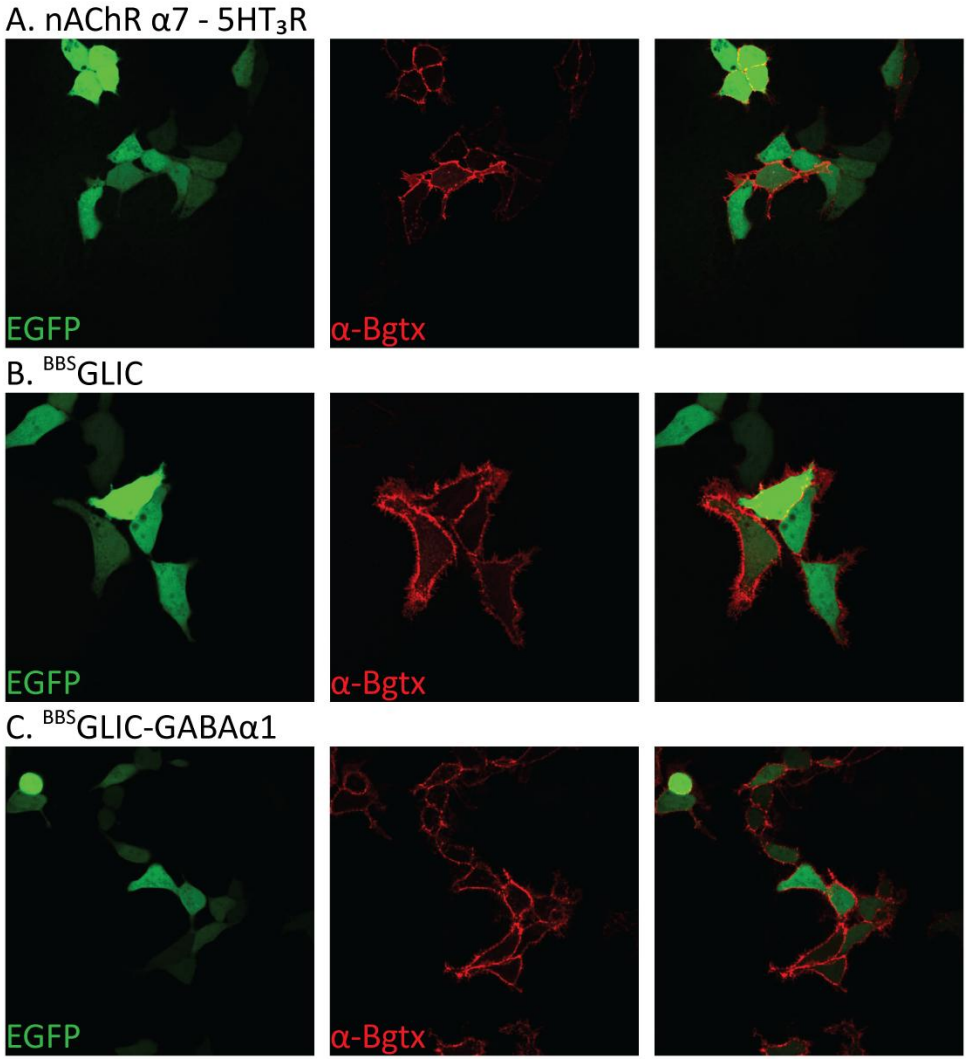

Figure 3.2 - α-Bungartoxin binding to BBS-tagged receptors

Live-cell confocal images of HEK293 cells transfected with the indicated construct following incubation with Alexa555 conjugated α-Bungarotoxin. Left panels: eGFP signal, Centre panels: Alexa555 α-Bungarotoxin, Right panels: merge of two channels. **A.** Untagged nAChR-5-HT_3 receptor chimera **B.** BBS-tagged GLIC **C.** BBS-tagged GLIC-$GABA_AR$ α1 chimera. Following incubation in α-Bungarotoxin, transfected cells were identified by eGFP signal and surface-specific labelling was imaged.

3.2.3. Functional characterisation of proton response of WT-GLIC and GLIC-GABA$_A$R α1 chimera

While α-bungarotoxin labelling studies demonstrate that the GLIC-GABA$_A$R α1 chimera, like GLIC, is expressed at the cell surface, it does not provide information regarding the functional properties of the protein. To determine whether the chimera forms a functional proton-gated ion channel we expressed receptors in *Xenopus* oocytes and measured their electrophysiological properties. *Xenopus* oocytes, rather than HEK293 (or other mammalian cell lines) were preferred for electrophysiological recordings, because we noted that a greater time period was required to obtain robust expression of the chimera in HEK293 cells (determined by imaging). We presumed that the chimeric receptor folding might be less efficient when compared to GLIC. In addition, *Xenopus* oocytes have been used previously for robust expression of "difficult to express" chimeric receptors (e.g. GLIC-GlyR, ELIC-nAChR α7, GABA$_A$ρ1-α1 subunit chimeras; Martínez-Torres et al., 2000; Duret et al., 2011; Tillman et al., 2014). We therefore adopted use of this expression system to assess the functional properties of GLIC-GABA$_A$α1 receptors. Furthermore, oocyte injections and TEVC studies can be carried out rapidly and in a semi-automated manner enabling the study of a number of receptor mutations and truncations.

Two-electrode voltage-clamp studies of *Xenopus* oocytes injected with the chimeric GLIC-GABA$_A$ α1 receptor subunit revealed that, like GLIC (Bocquet et al., 2007), it forms a functional proton gated ion channel (*Fig 3.3)*. In agreement with the fluorescence-imaging experiments with α-Bungarotoxin, maximal current amplitudes evoked decreased extracellular pH for the chimera were observed 48-72 hrs after injection, whilst wild-type (WT) GLIC exhibited large proton-elicited currents within 18-24 hrs of cDNA injection. Current profiles for GLIC and the chimera were distinct to the small proton-elicited currents observed as controls in non-injected oocytes (typically <0.05 μA exhibiting slow onsets to pH 4-5). Furthermore, current profiles of the two proteins exhibited contrasting properties. GLIC is characterized by slow activating currents (following a jump of extracellular pH from pH 7.4 to pH 4), which do not desensitize during prolonged exposure to protons and are rapidly offset by returning to neutral

extracellular pH producing a small inward rebound current (*Fig 3.3 A & B*). In contrast the chimera exhibits comparatively fast onset kinetics, and current decay during exposure to low extracellular pH (*Fig 3.3 A & C*). A rapid recovery of the current response is also observed upon returning to high extracellular pH (low proton concentration). Whilst these properties are reminiscent of wild type (WT) α1-containing $GABA_A$Rs, the time-course of receptor activation and desensitization (when compared at the macroscopic level) is slower for the chimera (*Fig 3.3 A*). Thus the chimera retains the proton-gating properties of GLIC, presumably imparted by the ECD, and approaches the kinetic properties of the $GABA_A$Rs, presumably conferred by the α1 TMD.

In order to characterize the gating and channel properties of the chimera, proton-concentration response and current-voltage relationships were assessed. I-V relationships obtained from voltage-steps (of 10mV) from -60mV to +50mV applied to a pH 5.2 elicited current revealed a marked outward rectification (in a manner similar to that observed for GABA-activated currents of α1β2 $GABA_A$ receptors expressed in oocytes; *Fig 3.3 E*). GLIC, by contrast, exhibits a linear I-V relationship. Currently the ion flux contributing to the observed currents has not been studied further, though one might postulate, that like native $GABA_A$Rs, the chimera forms an anionic, specifically Cl^- selective channel. Ultimately, further studies will confirm this.

Proton-concentration response curves were generated for WT GLIC and the chimera (*Fig 3.3 B-D*). Consistent with previously published results (Bocquet et al., 2007), the threshold for GLIC activation is ~ pH 6, with a pH_{50} (i.e. pH required to activate 50% of the maximal current response) of 5.0 ($[H^+]$ = 1.0 ± 0.15 X 10^{-5} M) and reaches a maximum response at ~pH 4 (*Fig 3.3 B & D*). Contrastingly, the chimera displays threshold proton-gated activity at lower proton-concentrations (pH 7.2) and does not attain a maximal response up to pH 4, presumably non-saturating proton concentrations (*Fig 3.3 C & D*). The observation of GLIC-$GABA_A$R α1 receptor activation at low proton concentrations were also made for another functional chimera formed between GLIC and GlyR α1 (Duret et al., 2011), for which application of the channel blocker picrotoxinin, at pH 8, produced a significant decrease in holding current in chimera expressing oocytes voltage clamped at -60 mV. This would suggest that the

GLIC-GABA$_A$R α1 chimeric receptor might also be similarly allosterically stabilized in an active conformation when compared to WT GLIC.

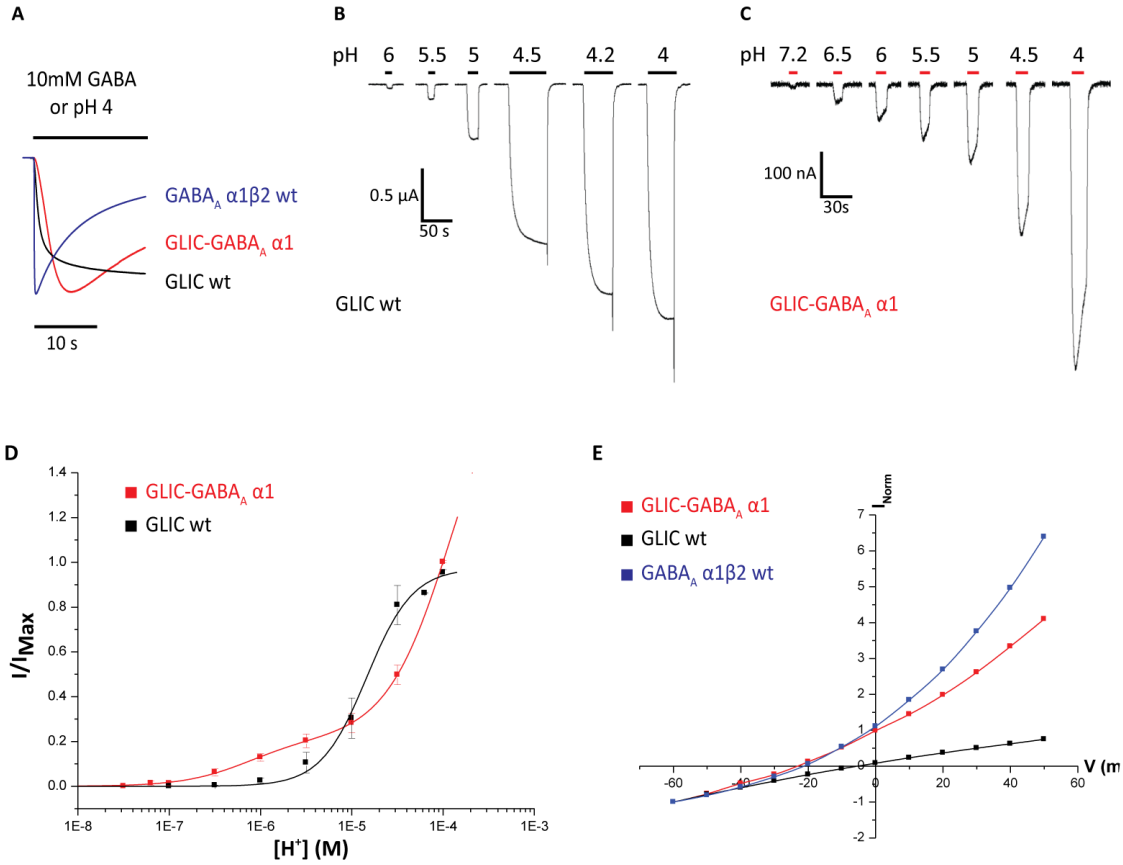

Figure 3.3 - Functional characterisation of proton-gated response at GLIC and GLIC-GABA$_A$R α1 chimera

A. Peak-scaled membrane currents elicited by 10 mM GABA (for α1β2 GABA$_A$R) or pH 4 (for GLIC and the GLIC-GABA$_A$R α1 chimera) showing the activation and desensitization phase of the receptor response. **B** and **C.** Examples of membrane currents recorded from oocytes expressing either GLIC **(B)** or GLIC-GABA$_A$ α1 **(C)** in response to decreasing pH. Horizontal bars indicate the duration of exposure to indicated extracellular pH. **D.** Proton-concentration response curves for GLIC and GLIC-GABA$_A$ α1. Points are mean ± s.d. n = 5-7 oocytes It should be noted that responses at the chimera have been arbitrarily normalized to the response at pH 4 to allow for comparison with the proton response curve of GLIC **E.** Example I-V relationships for α1β2 GABA$_A$R, GLIC and GLIC-GABA$_A$α1. Currents where recorded in response to voltage steps of 10 mV, and normalised to the current at -60 mV (=-1).

In this study, oocytes expressing the GLIC-$GABA_AR$ α1 chimera do not exhibit substantial holding currents at presumed "resting" proton concentrations (~pH 8), nor does picrotoxin application induce changes to the holding current, suggesting our chimera is not spontaneously activating. Monitoring current responses at various proton concentrations jumps (pH 7.5-9.5) using a modified recording solution buffered with tricine (useful pH buffer range 7.4-8.8), rather than MES buffer (useful pH buffer range 5.5-6.7), confirmed GLIC-$GABA_A$ α1 receptor activity at low pH (data not shown). Given that the coupling-interface at the border between the prokaryotic ECD and eukaryotic TMD has not been modified in our chimeric receptor, it might be postulated that the apparent constitutive activity is the result of residue mismatches between critical structural elements responsible for maintaining the receptor in an inactive state under resting conditions.

3.2.4. Analysis of receptor structural mismatch mutations and effect on gating

To ensure that our chimera could be activated and modulated appropriately, without any aberrant behaviour caused by mismatches in critical areas of the receptor that are important to gating, we sought to identify and minimize a number of potential structural mismatches at the interface between the prokaryotic ECD and eukaryotic TMD (*Fig 3.4*). Additionally we assessed the effect of mutating the M3-M4 loop (forming the large ICD of the receptor) on setting the levels of receptor activation and desensitization.

Guided by our homology model (*Fig 3.4 A*) and existing structure-function studies (as reviewed in (Miller and Smart, 2010), loop 7 and M2-M3 loop were identified as potential candidates for mutation at the coupling interface (*Fig 3.4 B & C, and Appendix Figure 3*). Mutation of 11 residues forming the linker between M2 and M3 (*Appendix Figure 3*) to the complementary residues observed in GLIC appeared to almost completely abolish proton-gated current responses (*Fig 3.4 B*). Given the small size of currents for the mutant chimera, it is difficult to distinguish this response from

the endogenous proton response observed in uninjected oocytes. Thus it was unclear if protein expression in the plasma membrane of cells was abolished as a result of disruptive changes to protein folding or due to the chimera adopting non-physiological non-conductive conformations. Notably the M2-M3 loop is crucial for both folding and gating across metazoan members of the Cys-loop receptor superfamily, as well as in GLIC, as revealed by recent crystallographic studies of cross-linked variants or loss-of-function mutants in the M2-M3 loop (Prevost et al., 2012; Gonzalez-Gutierrez et al., 2013).

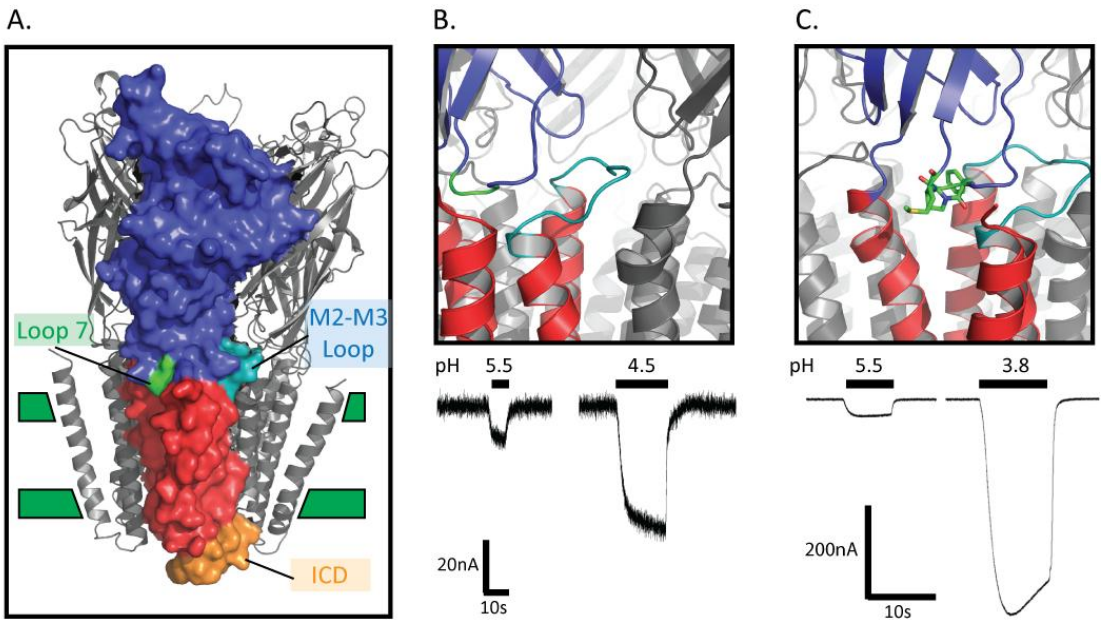

Figure 3.4 - Chimera homology model and functional characterisation of M2-M3 loop and Loop 7 mutants

A. Homology model of the chimera using the crystal structure for GLIC (PDB 3EAM) as a template. Surface rendering of a single subunit is shown and the following regions highlighted; GLIC ECD – blue, $GABA_A$α1 TMD – red, Loop 7 – green, M2-M3 loop – cyan, M3-M4 loop – orange. **B.** M2-M3 loop and proton current evoked for the mutated chimera in which residues in the loop are replaced by those for GLIC. **C.** Loop 7 region, with YPF motif replace by FPM motif from $GABA_A$R α1 subunit, and residues shown in stick representation. Proton evoked current of mutant chimera in oocytes elicited by step to low pH.

Loop 7 formed from connecting strands β6-β7 in the ECD (the characteristic Cys-loop in eukaryotic pLGICs) is another key structural component in communication between the ECD and TMD. Structure-function studies along with recent crystallographic data reveal that loop 7 protrudes down into the TMD where it contacts with M2-M3, the top of M3 and post-M4 (Hibbs and Gouaux, 2011; Althoff et al., 2014; Hassaine et al., 2014; Miller and Aricescu, 2014). We therefore postulated that mutation of the tip of loop 7 to the complementary residues of $GABA_AR$ α1 (Y-P-F > F-P-M) might serve to improve the efficiency of gating of the GLIC-$GABA_AR$ α1 chimera. Unsurprisingly, this relatively conservative mutation (when compared to the M2-M3 loop modification introduced above) did not ablate function of the chimeric receptor (*Fig 3.4 C*), with robust proton-gated responses were observed in *Xenopus* oocytes. While this mutation in loop 7 still enabled the generation of a functional receptor, there was no apparent change to the observed proton-concentration response relationship (i.e. channel gating at low proton concentrations and failure reach to plateau in activation at high concentrations).

3.2.5. Analysis of M3-M4 loop truncation and effect on activation and desensitization

In addition to mutagenesis studies at the coupling interface, the boundary between the prokaryotic ECD and eukaryotic TMD, we assessed both the role of the large ICD, between M3 and M4 TMD helices of the $GABA_A$ α1 subunit, in receptor function and in determining receptor kinetics. A large and variable length M3-M4 loop is a consistent feature across the eukaryotic pLGICs, which, in addition to acting as a scaffold for the binding of accessory proteins, serves to modulate receptor kinetics (potentially through post-translational modifications, e.g. receptor phosphorylation (Moss and Smart, 2001). The discovery of prokaryotic pLGIC homologs, revealed significant evolutionary truncation of the ICD, with short linker segments joining M3 and M4 with no apparent effect on receptor function (Bocquet et al., 2007; Hilf and Dutzler, 2008; Bocquet et al., 2009). Subsequent studies confirmed that the largely removable nature of the ICD extends to eukaryotic pLGICs, with a recent study reporting the generation

of functional 5-HT_3 and $GABA_A$ ρ1 receptors in which the respective M3-M4 loop was replaced with the short linker segment from GLIC (Jansen et al., 2008). Furthermore, recent expression, purification and crystallization studies of eukaryotic receptors and chimeras (including $GluCl_{cryst}$, GABAR $\beta3_{cryst}$ and GLIC-GlyRα1 (Lily) have used constructs lacking the large, structurally unresolved M3-M4 loops (likely to hinder receptor crystallization because of perceived structural flexibility; Hibbs and Gouaux, 2011; Miller and Aricescu, 2014; Moraga-Cid et al., 2015). We therefore assessed the functional amenability of our chimeric receptor to truncation of the M3-M4 loop (~75 amino acids in length), which would likely serve as crucial step in identifying candidate receptors for high-level expression and purification. Furthermore these studies would allow us to further investigate the role of this loop on receptor activation kinetics.

Based upon sequence alignments and existing structural data we designed two chimeric receptors exhibiting truncation of the M3-M4 loop (*Fig 3.5*). In exchange for the stretch of ~ 75 residues observed in $GABA_AR$α1 subunit we included either a short tripeptide, -ATG-, linker (akin to that observed in $GluCl_{cryst}$) or heptapeptide, -SQPARAA-, linker (as observed in GLIC). The point of insertion was positioned so as to not potentially exhibit structural constraints on the M3 and M4 helices (*Fig 3.5 A and Appendix Fig 3*), or displaces residues (particularly at the base of M3) involved in setting the desensitization kinetics of native α1-containing $GABA_A$ receptors.

Live-cell fluorescence imaging experiments using M3-$M4^{tripeptide}$ or M3-$M4^{heptapeptide}$ receptors incorporting a BBS yielded robust cell surface labelling within 24 hrs of cell transfection (*Fig 3.5 B*). The increase in rate of delivery of receptors to the plasma membrane would suggest that the large, unstructured nature of the native ICD likely acts as a hindering factor to overall receptor folding and assembly and subsequent

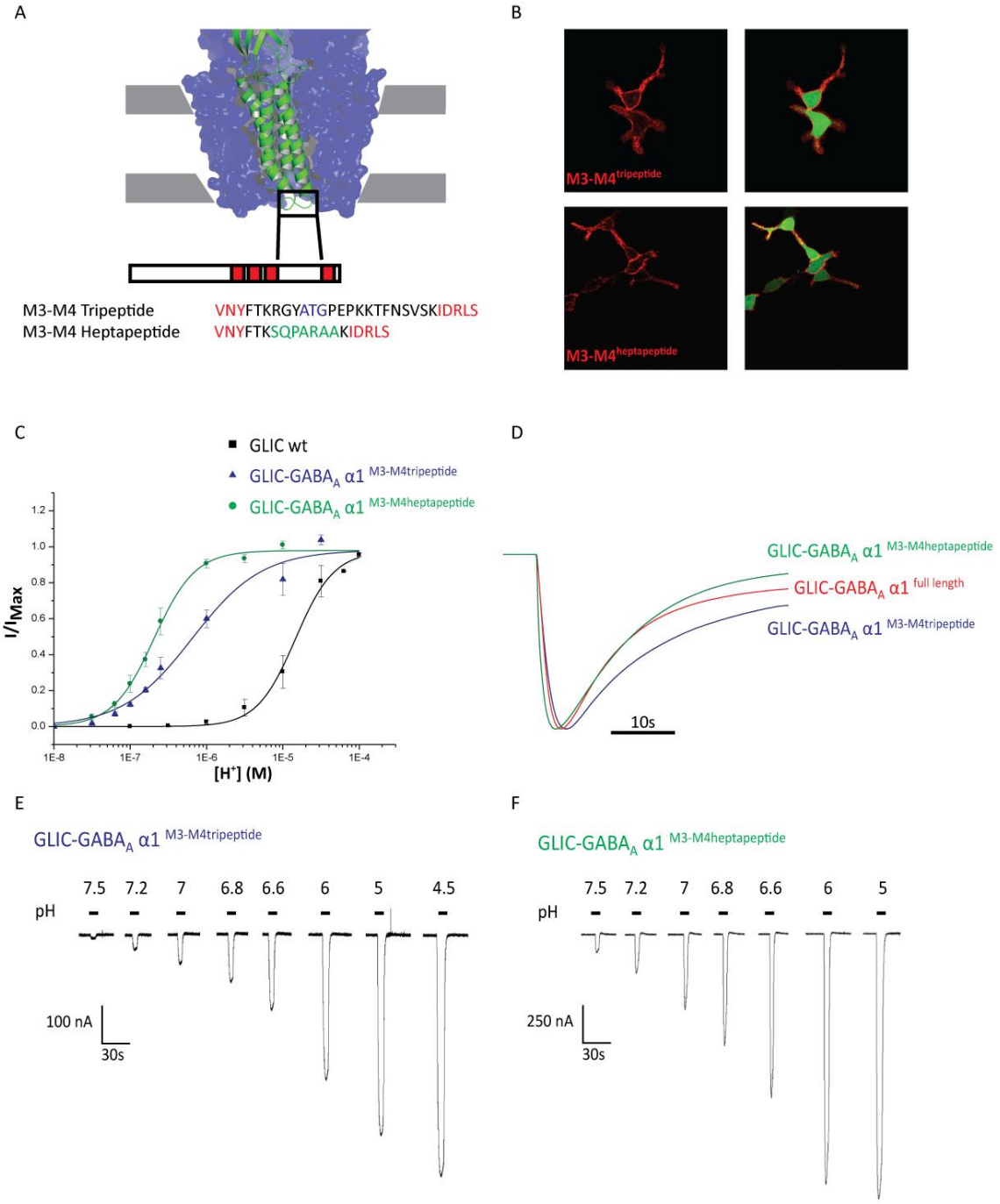

Figure 3.5 - Trafficking and functional characterisation of M3-M4 linker truncations in the chimera.

A. Position of M3-M4 linker in chimera homology model. Below, linear sequence detailing the insertion of the linkers. **B.** α-Bungarotoxin labelling of HEK293 cells transfected with EGFP and BBS-tagged chimeras with tri- or heptapeptide M3-M4 linkers (Alexa 555 α-Bgtx channel red and merge with eGFP). **C.** Proton-concentration response curves for GLIC and M3-M4 linker chimeras. n= 7-8 oocytes **D.** Peak-scaled membrane currents showing activation and decaying phase of proton elicited responses for the indicated receptors. **E.** and **F.** Membrane currents recorded from oocytes expressing M3-M4^{tripeptide}**(E)** or M3-M4^{heptapeptide}**(F)** chimeric recepotrs in response to increasing proton concentrations.

export to the cell surface. Consistent with previous studies deletion of the M3-M4 loop and replacement with either tri- or heptapeptide linkers did not ablate receptor function when analysed electrophysiologically (*Fig 3.5 C-F*). Oocytes expressing either the M3-M4^{tripeptide} or M3-M4^{heptapeptide} GLIC-GABA$_A$R α1 chimera were activated by low external pH within 18-24 hrs of oocyte injection (in accord with the fluorescence-imaging experiments; *Fig 3.5 D*). The nature of the mutation has minimal effect on the apparent activation kinetics of the receptor (*Table 3.1*), whilst having an appreciable effect on entry into desensitization. Deactivation kinetics upon return to extracellular pH 8 were rapid and apparently unaltered.

Evidently replacing the ICD with the heptapeptide linker, in combination with a less conservative conservation of post-M3 and pre-M4 residues (as detailed in linear sequence of *Fig 3.5 A*) gives rise to a receptor which exhibits an increase in rate of desensitization (*Fig 3.5 D*) when compared to replacing the M3-M4 loop with a short tripeptide linker and retention of a greater portion of residues post-M3 and pre-M4. It is also evident that the activation kinetics of the M3-M4^{heptapeptide} chimera is slightly faster, though whether this reflects enhanced receptor gating or an increase in the rate of entrance in to desensitization relative to the rate of receptor activation is unclear.

Whilst there is an apparent effect of the M3-M4 linker on receptor kinetics, we also observed a change in the proton-concentration response curves of the truncated chimeras (*Fig 3.5 C, E & F*). As observed for a chimera in which the large ICD is retained, M3-M4^{tripeptide} and M3-M4^{heptapeptide} chimeras exhibit leftward shifts in the proton-concentration curves when compared to the WT GLIC curve, with proton-gated currents recorded at pH7.5 and with respective pH$_{50}$s of 6.18 ([H^+]=6.49 ± 1.78 x 10^{-7}M) and 6.69 ([H^+]=2.04 ± 0.09 x 10^{-7} M) (*Fig 3.5 C*). Additionally there is a clearer maximum in receptor activation at low pH (high proton concentrations; *Fig 3.5 E & F*). This is most apparent for the M3-M4^{heptapeptide} chimera. It was notable for the M3-M4^{heptapeptide} chimeric receptor that significant holding currents, which could be blocked by the channel blocker picrotoxin, were observed in oocytes maintained at pH 8 when voltage-clamped at-60 mV. This observation along with a leftward shift in the proton-dose response curve is indicative of an increase in the spontaneous activity of

the receptor. This is presumably imparted through structural modifications introduced through altering the length and nature of the M3-M4 loop. These results are consistent with those observed for the GLIC-GlyRα1 chimera which used a linker of similar length and sequence to replace the large M3-M4 loop (~ 75 residues) found in native GlyRα1 (Duret et al., 2011). Whilst the M3-M4^{tripeptide} chimera construct retains proton-gating activity at relatively neutral pH, holding currents at pH 8 were small and similar to those observed with forms of the chimera that retained a full length M3-M4 loop. This presumably reflects greater stability in a non-conducting state under "resting" conditions. It is unclear from concentration-response relationships alone as to whether this M3-M4^{tripeptide} receptor exhibits constitutive basal activity as a result of mismatches in the structural elements at the gating interface or through truncation of the M3-M4 loop.

3.2.6. Functional analysis of desensitization mutations in GLIC-GABA$_A$R α1 M3-M4 linker truncated chimeras

At the macroscopic level two-electrode voltage-clamp recordings of chimeric receptors suggest that through a simple domain switch, we have been able to confer similar activation and gating properties that might be expected for native GABA$_A$Rs (e.g. a faster rate of activation and entrance into a desensitized state when compared to GLIC). To further assess whether the chimera adopts common mechanistic arrangements during channel gating to native GABA$_A$Rs, in particular during receptor desensitization, we used site-directed mutagenesis to study residues at the intracellular end of M2 and M3, recently proposed to form a desensitization gate at the receptor (Gielen et al., 2015). Studies of α1β2(γ2L) GABA$_A$Rs have revealed that introduction of single residue point mutants (altering side chain charge or volume) along the M2/M3 interface is sufficient to dramatically enhance the apparent rate of receptor desensitization. As a result of these functional studies (supported by evidence from recent crystallographic, NMR and DEER spectroscopy data (Miller and Aricescu, 2014; Kinde et al., 2015)), it is now proposed that receptor desensitization is the result of structural rearrangements extending beyond those which occur at the level of ECD and ECD-TMD interface (Gielen et al., 2015).

Having confirmed that deleting the large M3-M4 loop of the chimera does not ablate function, further functional studies were carried out at receptors bearing these truncations (given their potential promise for receptor purification and crystallization strategies, see Chapter 4). Whilst there is an apparent effect of deletion on setting the time course for desensitization, receptor activation kinetics (and crucially, retention of a desensitizing phase) remains largely unchanged.

A question that must, however, be addressed concerns the nature of the structural confirmation this M3-M4 linker adopts when spliced in to the sequence of the GLIC-GABA chimera. Given the point at which we have introduced these linkers (and there positioning in published crystal structures) we might predict that they remain in the cytosolic portion of the linker rather than being incorporated into the α-helices of M3 and/or M4. Thus they would not be expected to impart physical constraints on the helical bundle of the TMD which would drastically alter receptor kinetics.

Mutation of the M2 4' glycine (G258) to alanine, increasing the side chain volume in the GLIC-$GABA_A$ α1 chimera with either M3-M4 linker, is sufficient to increase the rate of desensitization when compared to non-mutant bearing forms of the chimeras (*Fig 3.6 A, B, E & F* and *Table 3.1)*. Further mutation to a bulky hydrophobic valine residue resulted in a loss-of-function for chimeric receptors bearing the M3-$M4^{tripeptide}$ linker whilst currents exhibiting a rapid rate of decay (6-fold increase) were resolvable with chimeric receptors bearing the M3-$M4^{heptapeptide}$ (*Fig 3.6 B, D & F*).

Mutation of -3' valine (251) to isoleucine, another residue profoundly affecting desensitisation in α1β2 $GABA_A$Rs (Gielen et al., 2015) was also sufficient to induce an increase in the rate of receptor desensitization (for both M3-$M4^{tripeptide}$ and M3-$M3^{heptapeptide}$ chimeras), whilst mutation to the bulky aromatic phenylalanine (V251F) did not yield resolvable currents for either chimeric receptor. Peak normalised responses also indicated a shift in the rate of receptor activation, most notable in the more profoundly desensitizing mutants (*Fig 3.6 C & D*). Given the comparatively slow onset kinetics of currents mediated by the chimera (when compared to a $GABA_A$R) this likely represents a rapid entry into desensitization (greater than the rate of activation), manifesting as an increase in apparent current onset.

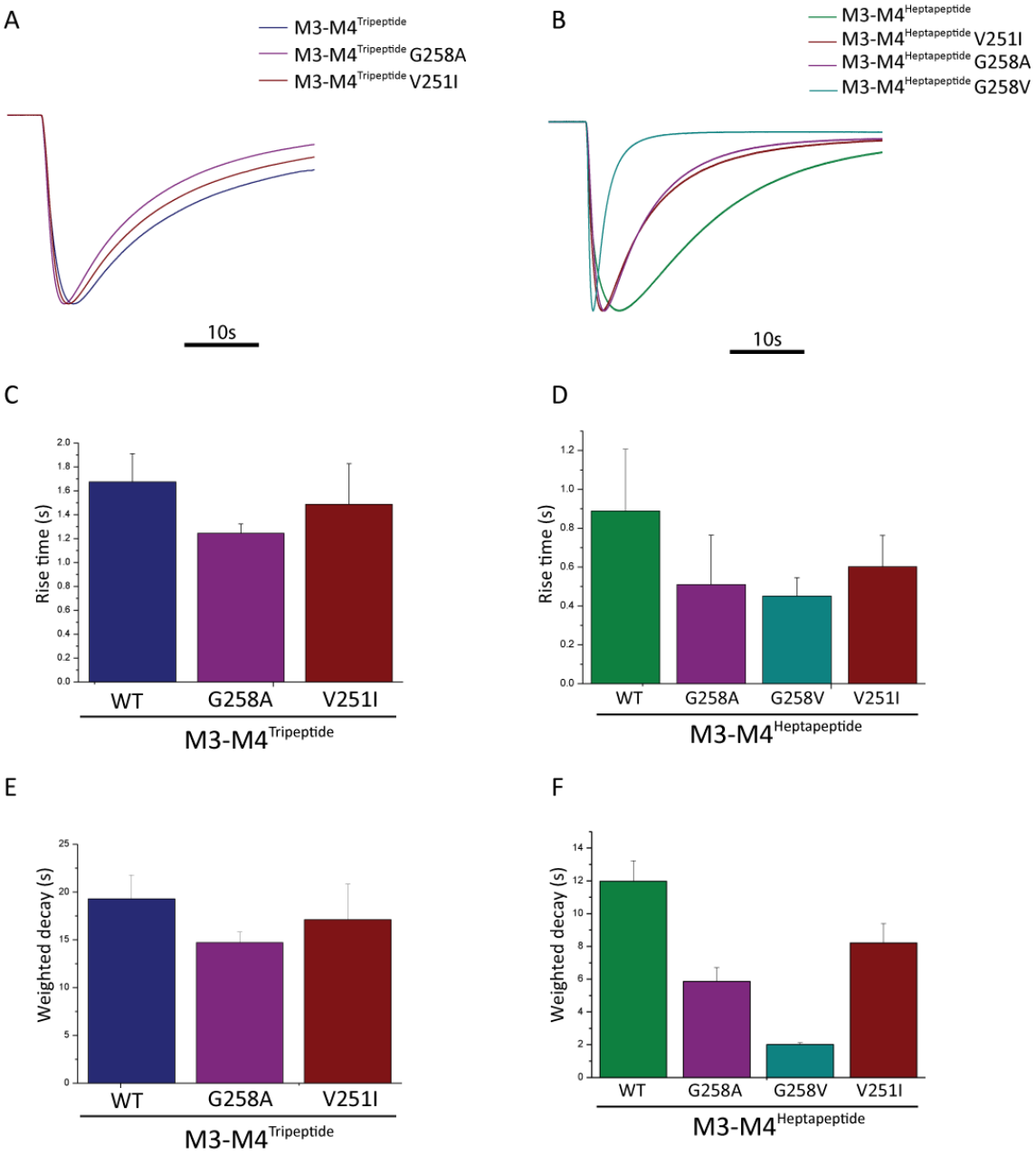

Figure 3.6 - Functional analysis of desensitization mutations at chimeric receptors

Peak scaled membrane currents recorded from oocytes injected with either GLIC-GABAα1$^{M3\text{-}M4tripeptide}$ **(A)** or GLIC-GABAα1$^{M3\text{-}M4heptapeptide}$ **(B)** and indicated TMD mutations upon exposure to low pH. **C**-F**.** Bar charts (mean ± s.d) showing receptor rise times (20-80% activation) and weighted decay time constants for GLIC-GABAα1$^{M3\text{-}M4tripeptide}$ **(C, E)** andGLIC-GABAα1$^{M3\text{-}M4heptapeptide}$ **(D, F)** plus the indicated mutations. n = 3-9 oocytes

In a manner similar to that observed in studies of native $GABA_A$Rs, the selected mutations affected both the rate (and extent) of desensitization for currents mediated by the chimeras. Furthermore systematic mutation at a single site, which increases the rate of desensitization is also apparent on the backbone of the chimeric receptor (e.g. M3-M4^{heptapeptide} G258 (WT; τ_ω 11.9s) < G258A (5.86s) < G258V (2.01s). An unexpected observation was that the extent to which the apparent desensitization profile was affected by the M3-M4 truncation. For example currents exhibiting a rapid decaying phase were resolvable for G258V mutation of GLIC-$GABA_A$α1 M3-M4^{heptapeptide} but not the M3-M4^{tripeptide}. Furthermore in the case of profoundly desensitizing mutants (e.g. V251F) currents could not could be resolved, regardless of the nature of the M3-M4 truncation.

The lack of resolvable currents for profoundly desensitizing mutants, in particular V251F (at -3' position of M2), was maybe not a surprising observation. At α1β2 $GABA_A$Rs, introduction of α1^{V251F} subunits is sufficient to induce a 20-fold increase in the rate of desensitization when compared to its wild type counterpart. Introduction of the equivalent mutation into the β2 (S247F) and co-expression with α1^{V251F} yields receptors with unresolvable currents. As mentioned previously, this likely arises through generating a receptor exhibiting rates of desensitization greater than the rate of ion channel opening. This is also likely to affect homomeric V251F mutant receptors in the present study (i.e. exhibiting mutations at all five -3' positions), which did not generate resolvable currents.

Table 3.1 Weighted decay time constants of desensitization and activation rates for chimeric GLIC-GABA$_A$R α1 receptors bearing 'desensitization mutations'.

Construct	Rise time$_{20\text{-}80\%}$ (s)	τ_ω (s)	n
GLIC-GABA$_A$ α1$^{Full\ length}$	1.77 ± 0.28	11.93 ± 2.22	5
M3-M4^{Tripeptide}	1.67 ± 0.24	19.3 ± 2.46	9
M3-M4^{Tripeptide}G258A	1.24 ± 0.08	14.7 ± 1.11	5
M3-M4^{Tripeptide}V251I	1.49± 0.34	17.1 ± 3.72	3
M3-M4^{Heptapeptide}	0.89 ± 0.32	11.9 ± 1.25	9
M3-M4^{Heptapeptide}G258A	0.51 ± 0.25	5.86 ± 0.84	5
M3-M4^{Heptapeptide}G258V	0.45 ± 0.09	2.01 ± 0.10	5
M3-M4^{Heptapeptide}V251I	0.60 ± 0.16	8.22 ± 1.18	5

τ_ω is the weighted decay time constant for desensitization (calculated from a bi-exponential fit of the decaying phase of currents during prolonged agonist exposure, as detailed in Materials and Methods). It should be emphasized that these number serve to highlight the trend in (increased) rate of desensitization following introduction of various point mutations). Values are means ± s.d and n is the number of cells.

3.2.7. Trafficking and functional rescue of V251F mutant chimera

To determine whether the V251F mutation affects assembly or causes the chimera to adopt a non-conductive state, we used imaging to track cell surface labeling in HEK293 cells and electrophysiological recordings, following introduction of a well characterized gain-of-function mutation at the level of the hydrophobic gate in the pore-lining M2 helix (Leucine-9'-Serine; Chang and Weiss, 1999).

Previous studies have shown that hydrophilic substitution of the conserved 9' leucine in $GABA_AR$ subunits (as for other members of the pLGIC superfamily) results in a profound increase in both agonist sensitivity and spontaneous channel openings (Chang and Weiss, 1999). Given this effect, substitution at the 9' position is often used to rescue the function of apparently non-functional receptors, and in doing so confirm cell surface presence of a receptor exhibiting an expected bias in the gating equilibrium.

We introduced a BBS into GLIC-$GABA_AR$ α1 M3-$M4^{tripeptide}$ V251F chimeras (for cell surface tracking in HEK293 cells) and the L9'S mutation for electrophysiological recordings. Incubation with fluorophore conjugated α-bungarotoxin yielded cell surface labeling of receptors in transfected cells, which would suggest assembly and export to the plasma membrane (*Fig 3.7 C*). Notably we also observed robust surface labeling of receptors at cells expressing both the (electrophysiologically) functional G258A mutant (M3-$M4^{tripeptide}$) chimera and loss-of-function GLIC-$GABA_A$α1 M3-$M4^{tripeptide}$ G258V mutant chimera (*Fig 3.7 A &* B).

Consistent with previous studies of $GABA_ARs$, the M3-$M4^{tripeptide}$ L9'S mutant chimera exhibited spontaneous activity in the absence of agonist (at extracellular solution pH 8), as inferred from a significant increase in the holding current for oocytes clamped at -60 mV (*Fig 3.8 A*). Picrotoxin blocked a proportion of this current, as did the inhibitory neurosteroid pregnenolone sulfate (PS; *Fig 3.8 A*). Application of agonist was able to induce further channel opening, as reflected by an additional inward current following a step to low pH. These results are consistent with the L9'S mutation stabilizing the chimera in one or more open states.

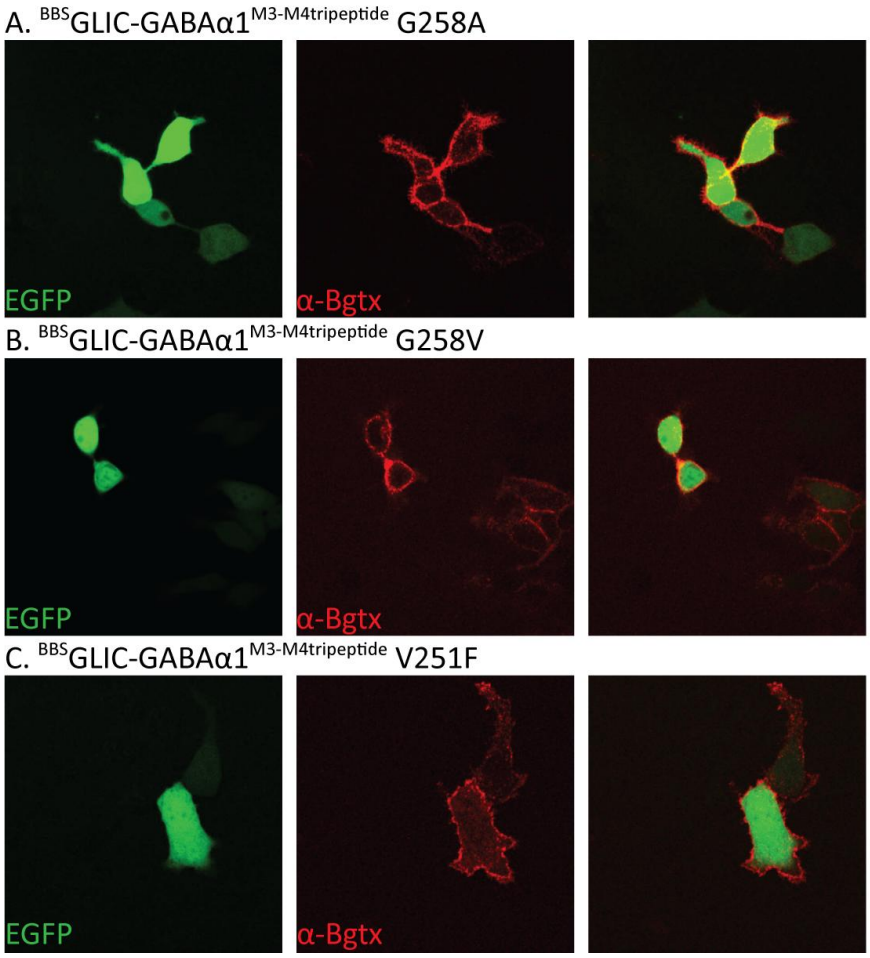

Figure 3.7 - α-Bungarotoxin binding to BBS-tagged desensitization mutant chimeras

Live-cell confocal images of HEK293 cells transfected with the indicated construct following incubation with Alexa555 conjugated α-Bungarotoxin. Left panels: EGFP signal, Centre panels: Alexa555-α-Bungarotoxin staining, Right panels: merge of two channels. **A.** ^{BBS}GLIC-GABA$^{M3\text{-}M4tripeptide}$G258A **B.** ^{BBS}GLIC-GABA$^{M3\text{-}M4tripeptide}$G258A **C.** ^{BBS}GLIC-GABA$^{M3\text{-}M4tripeptide}$G258A. Following incubation in α-Bungarotoxin, transfected cells were identified by EGFP signal and surface-specific labelling imaged.

The L9'S mutation was able to rescue the function of the V251F mutant chimera, with oocytes injected with the double mutant exhibiting currents in response to low pH (*Fig 3.8 B*). This confirms that the V251F mutation has not caused the chimera to form a non-physiological non-conductive state. Additionally, the current traces revealed notable features which might further suggest that the M3-M4^{tripeptide} V251F chimeric

receptor is allosterically stabilized in a distinct gating state. Specifically, spontaneous activity of double mutants was reduced greater than 2 fold when compared to the L9'S mutated chimera. Comparing the spontaneous activity as a percentage of the spontaneous current and the maximal proton response (see Materials and Methods) $\%_{SA}$: L9'S = 71.95 ± 10.4 (n=6) and V251F/L9'S = 30.44 ± 6.93 (n=9).

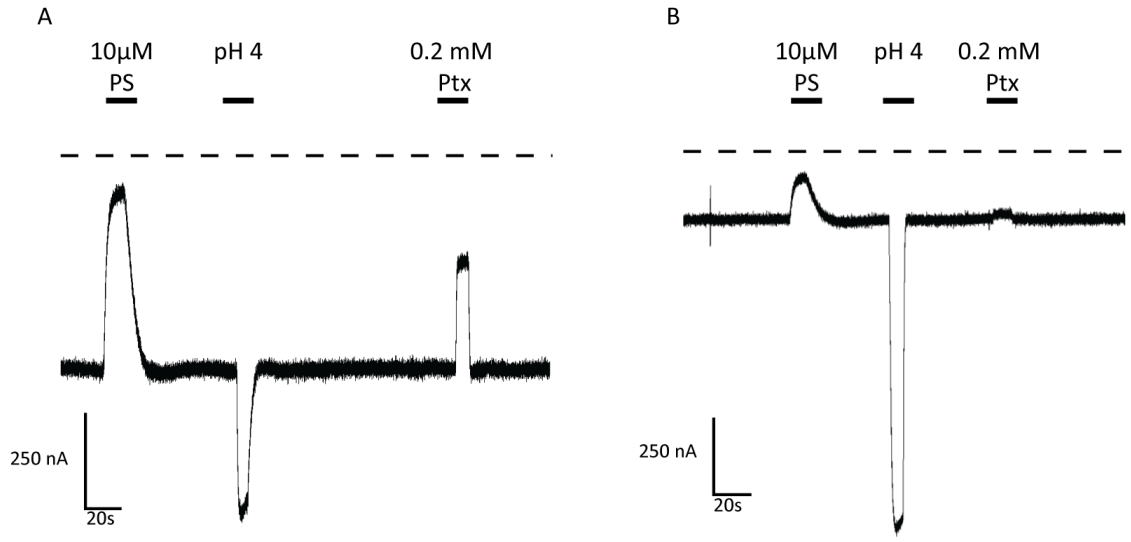

Figure 3.8 - Functional analysis of L9'S rescue of non-functional V251F chimera

Example current responses from **A.** GLIC-GABA$^{M3\text{-}M4tripeptide}$ L9'S receptor and **B.** GLIC-GABA$^{M3\text{-}M4tripeptide}$ L9'S/V251F in oocytes (clamped at -60 mV). Dashed lines represents zero current level, showing spontaneous current at pH 8. Inhibition of spontaneous current by 10 µM pregnenolone sulphate (PS) and 200 µM picrotoxin (Ptx), and further current activation by pH 4.

Furthermore spontaneous currents of the L9'S/V251F receptor were not blocked by picrotoxin (at a concentration shown to reduce a significant portion of the spontaneous current observed in L9'S receptors; *Fig 3.8 B*). By contrast the spontaneous current for the L9'S/V251F and L9'S was reduced by PS (*Fig 3.8 A & B*). Whilst (at the macroscopic level) there was no apparent increase in desensitization of

proton-elicited currents for the L9'S/V251F receptor, the reduction in spontaneous currents and loss of picrotoxin-block are consistent with the notion that the V251F mutation dramatically biases the gating equilibrium constant of the chimera towards a closed-desensitized channel conformation when expressed in *Xenopus* oocytes (and is discussed in greater detail below). Not only does this result further confirm that the mechanisms underlying channel gating, specifically desensitization, are common between native and chimeric $GABA_A$Rs, but also identifies a strong loss-of-function mutant receptor which would serve as an ideal candidate for structural studies of a receptor stabilized in a distinct (presumed desensitized) state.

3.2.8. Neurosteroid potentiation and inhibition of chimeric $GABA_A$ receptors

Having established a channel gating profile for the chimera, revealing a common mechanism for receptor desensitization in comparison to its native $GABA_A$R counterparts, we sought to assess the pharmacological profile of the GLIC-GABA chimera and determine whether key sites for allosteric modulator binding have been retained in the TMD. We focused primarily on the response to the endogenous neurosteroids tetrahydro-deoxycorticosterone (THDOC) and pregnenolone sulphate (PS). These steroids impart distinct and opposite effects, but have both been characterised extensively at α1-containing $GABA_A$Rs; THDOC potentiating activity or directly gating the channel, and PS inhibiting agonist responses. It was hypothesised that within the chimeric receptor, the sites responsible for mediating the binding and effect of these two neurosteroids might be retained and a modulatory effect observed following agonist activation. With regards to the pharmacological profile of GLIC, sensitivity to these two compounds has not been reported. However given that the key residues previously reported to mediate the response to potentiating neurosteroids are not conserved in GLIC, it was expected that distinct responses to steroids would be observed.

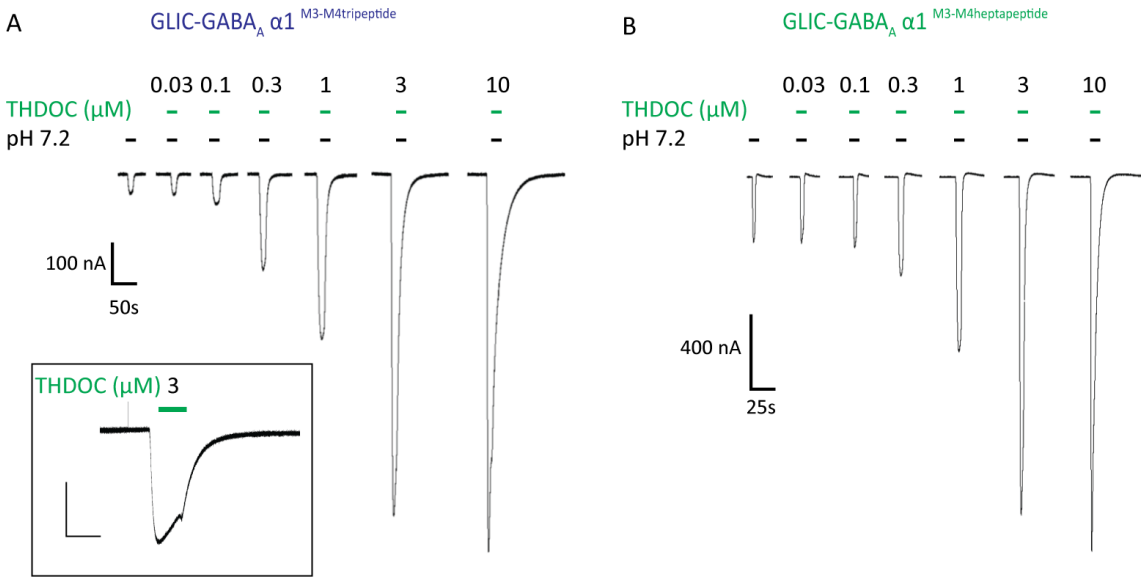

Figure 3.9 - Functional analysis of THDOC potentiation of proton-response

Example current traces of responses induced by pH_{10-20} and their potentiation by increasing concentrations of THDOC in oocytes expressing GLIC-GABA$^{M3\text{-}M4tripeptide}$ (**A**) or GLIC-GABA$^{M3\text{-}M4heptapeptide}$ (**B**). Inset panel in **A** reveals the response induced by 3 μM THDOC in oocytes expressing GLIC-GABA$^{M3\text{-}M4tripeptide}$ at pH 8 (Current calibration bar: 20s/40 nA).

THDOC (across a range of concentrations) was observed to potentiate ~pH_{10-20} elicited currents in oocytes expressing the chimera (*Fig 3.9*). This response was observed for both M3-M4^{tripeptide} and M3-M4^{heptapetide} linker chimeras, exhibiting sensitivities (respective ~EC_{50}s for THDOC; 1.16 ± 0.54 μM and 0.99 ± 0.15 μM, n=5 and 3 respectively) in the high nM-low μM range (*Fig 3.9 A & B*). Unsurprisingly the response recovery is extended at high THDOC concentrations, most likely due to slow washout of the steroid. This response is reminiscent of α1β2γ2 $GABA_A$Rs, though the reported sensitivity is slightly greater in native $GABA_A$Rs (~280 nM in HEK293 cells (Hosie et al., 2006)). The response of WT GLIC to THDOC was distinct in that the receptor was largely insensitive to THDOC (exhibiting a small inhibition of the proton response at high μM THDOC concentrations). These results are consistent with a lack of a THDOC binding site in GLIC, with a critical glutamine (Q241) in M1 of the $GABA_A$ α subunits

replaced by a tryptophan (W213) in GLIC. The binding site for THDOC is however functionally introduced through a domain switch with GLIC by inserting the $GABA_AR$ α1 TMD, as observed by a potentiation of a proton response in the chimera.

Given the constitutive activity observed with the chimera even at resting, neutral pH we cannot yet conclude that a THDOC response observed at pH 8 (*Fig 3.9 A*) represents a true direct activation of the receptor. THDOC could simply be potentiating constitutive channel activity. Moreover, since the direct gating response at the α1β2γ2 containing receptors is presumed to be coordinated by binding of steroid molecule at an interfacial site between alpha and beta subunits (presumably with residues from both subunits responsible for binding (Hosie et al., 2006)), we would not expect direct activation of the GLIC-$GABA_A$α1 chimera where there is a homomeric configuration of α-subunit TMDs.

Whilst potentiating neurosteroids, have been the focus of extensive studies with regard to their mechanism of action, our understanding of how inhibitory neurosteroids bind and antagonize the $GABA_AR$ is less clear. This class of steroids incorporates the sulphated steroids, including pregnenolone sulphate (PS) and dehydropiandrosterone sulphate (DHEAS), and like potentiating steroids are naturally occurring in the CNS (Seljeset et al., 2015). Whole-cell currents elicited by a submaximal proton concentration (~pH_{80}) were recorded from oocytes expressing GLIC-$GABA_A$ α1 chimeras (and GLIC) in the absence or presence of PS (ranging from 100 nM to 30 µM; *Fig 3.9*). Native $GABA_AR$s have previously been shown to be inhibited (in a use dependent manner) at high nM/low µM concentrations of PS, with greater inhibition of steady state currents compared to peak response (Seljeset et al., 2015). Furthermore, this inhibitory response is characterised by promoting the receptor's entry into an apparently desensitized state (Shen et al., 2000; Akk et al., 2008).

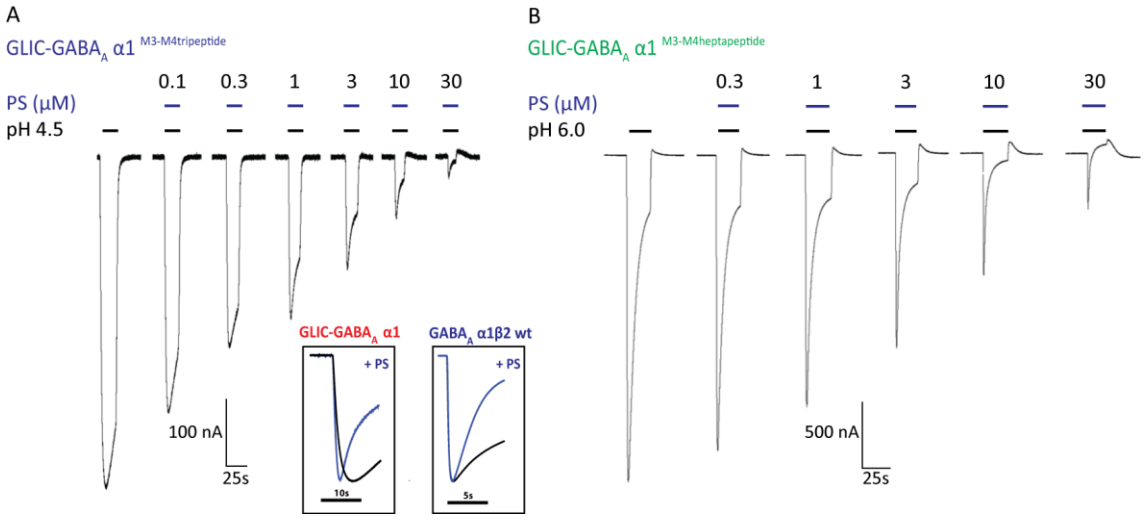

Figure 3.10 - Functional analysis of Pregnenolone Sulphate inhibition of proton-response

Example current traces of ~EC_{80} proton response by increasing concentrations of pregnenolone sulphate (PregS) in oocytes expressing GLIC-GABA$^{M3\text{-}M4tripeptide}$ (**A**) or GLIC-GABA$^{M3\text{-}M4heptapeptide}$ (**B**). Inset in **A** shows enlarged, peak-scaled membrane currents for the pH 4.5 response for the chimera and 10 μM GABA response for α1β2 $GABA_AR$ in the presence or absence of 3 μM PregS.

Whilst not extensively studied, PS exhibited a range of effects at oocytes expressing WT GLIC (depending on the co-applied proton concentration). PS exhibited both weak potentiation and inhibition of the proton activated response. Furthermore the sensitivity of this response to PS (at mid-high μM) was substantially outside of the effective concentration range previously reported for a eukaryotic pLGIC, e.g. α1β2γ2 $GABA_AR$. Given the relatively promiscuous nature of pregnenolone sulphate, which is known to modulate, amongst others, the pLGIC superfamily, iGluRs and TRP channel (Harteneck, 2013), the observation of a low-sensitivity response at GLIC was not surprising.

In contrast to GLIC, introduction of the α1 TMD in the GLIC-GABA chimeras increased the potency of pregnenolone sulphate (*Fig 3.10 A & B*). Chimeric receptors exhibited PS sensitivity in the high nM-low μM concentration range, and in a manner similar to

native $GABA_AR$s this inhibition was characterized by an increase in the desensitization kinetics of the proton response (*Fig 3.10 A Inset*). It is notable that in contrast to the inhibition response observed at a native $GABA_AR$, there was a profound PS mediated depression of the peak proton response (during co-application experiments). This may reflect the slow onset of proton-elicited response, which in the presence of PS is masked by an apparent increase in the rate of entry into a closed-desensitized state. Given that studies were primarily carried out on M3-M4 truncated receptors it would appear that binding and sensitivity of the chimeric receptor to PS was not dependent on structural elements provided by the M3-M4 loop. Whilst we cannot exclude that PS imparts its effect through indirect interaction with the ion channel (i.e. lipid interactions in the bilayer), it is apparent from these studies that structural elements conferred by the $GABA_AR$ α1 TMD are likely to be responsible for the increased sensitivity to PS.

3.2.9. Picrotoxin block of chimera currents

We have focused primarily on the inhibitory effects of PS, a compound for which relatively little is known regarding its mode of action. In addition, the effects of the GABA antagonist picrotoxin at chimeric receptors were also assessed. The antagonistic effects of picrotoxin across members of the pLGIC superfamily has been extensively studied, and it is widely acknowledged that it acts as a channel-blocking agent binding deep within the pore at the -2 to 2' level (Bali and Akabas, 2007). Moreover, recent crystallographic studies of GluCl in complex with picrotoxin provides further weight to this proposed mechanism of action (Hibbs and Gouaux, 2011). In agreement with previous studies, picrotoxin was able to block proton-activated currents through GLIC (*Fig 3.11 B;* Alqazzaz et al., 2011). As might be expected currents through the chimera were also blocked by picrotoxin (*Fig 3.11 A*).

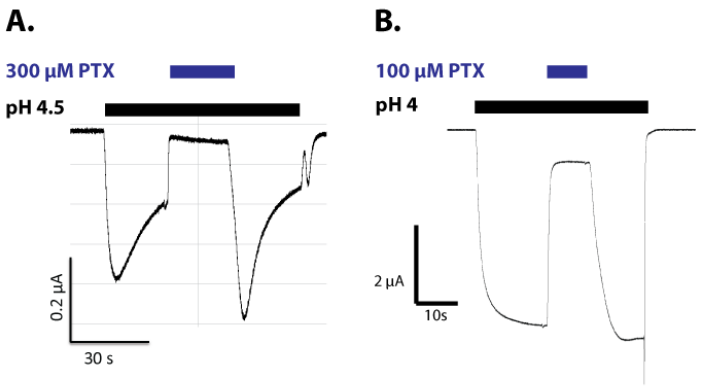

Figure 3.11 - Functional analysis of picrotoxin block of proton-response

Representative membrane current traces showing fast dissociation of picrotoxin (PTX) from oocytes expressing GLIC-GABA$^{M3\text{-}M4tripeptide}$ chimera (**A**) and GLIC (**B**) when activated by a high/saturating concentration of protons. Note the rebound current in **A** after washout of PTX, indicating that PTX is unlikely to bind to a desensitized state of the receptor (Gielen et al., 2015).

3.2.10. Pentobarbital inhibition at α-containing chimeras and potentiation of β-containing chimeras

The pharmacological profile of the chimera (with regards to neurosteroids and picrotoxin) exhibits typical properties that might be expected of a α1-containing $GABA_AR$. In this respect, the chimeric receptor represents a minimal model of an α-containing $GABA_AR$ at the level of the TMD. Therefore, we might also use this receptor to study the effects of other pharmacological agents exhibiting complex mechanisms of actions. General anesthetics (GA) have long been implicated as acting through the $GABA_AR$, however, an understanding of how these compounds act at the molecular level is poorly understood. While a binding site for the intravenous GA propofol has been established at the $GABA_AR$ β subunit (Yip et al., 2013; Franks, 2015), and also at the bacterial homolog GLIC (by co-crystallographic studies; Nury et al., 2011), the mechanism by which barbiturates, including pentobarbital, bind and act are not as clearly defined. Pentobarbital modifies receptor function in three concentration-dependent manners; at low concentrations (<100 µM) channel activity (induced by sub-saturating agonist concentrations) is potentiated, intermediate concentrations

(100µM-1mM) are able to directly activate the receptor, and above 1mM pentobarbital exhibits antagonistic effects, blocking currents through the ion channel (Akk and Steinbach, 2000; Muroi et al., 2009). The mechanisms underlying these distinct modes of action are poorly understood. Given the complex nature of its action, it might seem likely that distinct structural elements, contributed by a combination of subunits, mediate the different functions of pentobarbital at $GABA_A$Rs. Studies to date have revealed that β-subunit homomers can be directly gated by pentobarbital (Davies et al., 1997; Wooltorton et al., 1997). Here we have assessed the pentobarbital response at our GLIC-$GABA_A$ α1 chimera in order to potentially assign a role for the $GABA_A$ α1 TMD in barbiturate binding. It should be noted that studies were carried out on the chimera including the large, native M3-M4 loop of the $GABA_A$ α1 subunit.

The response of WT GLIC and the chimera to a submaximal proton-gating concentration (~pH_{20}) in the absence or presence of pentobarbital (3 µM-1 mM) was recorded in oocytes. Pentobarbital co-application at pH 8 did not induce any effect at WT GLIC receptors or the chimera. Co-application of PB at an extracellular recording pH_{20} proton concentration revealed an inhibitory action of PB at both GLIC and the chimera (IC_{50}s of 113.7 ± 9.4 µM and 272.5 ± 39.5 µM respectively; *Fig 3.12 A & C)*. The concentration ranges over which PB imparts this inhibitory effect is equivalent to the concentrations inducing potentiating-activating responses at α1β2 $GABA_A$Rs (which exhibits an ~EC_{50} of 25.4 ± 12.1 µM, from a fit of 'potentiating' data points). Intriguingly, PB inhibition of proton-gated currents at the chimera were characterised by a transient current increase (or rebound current) upon removal of drug.

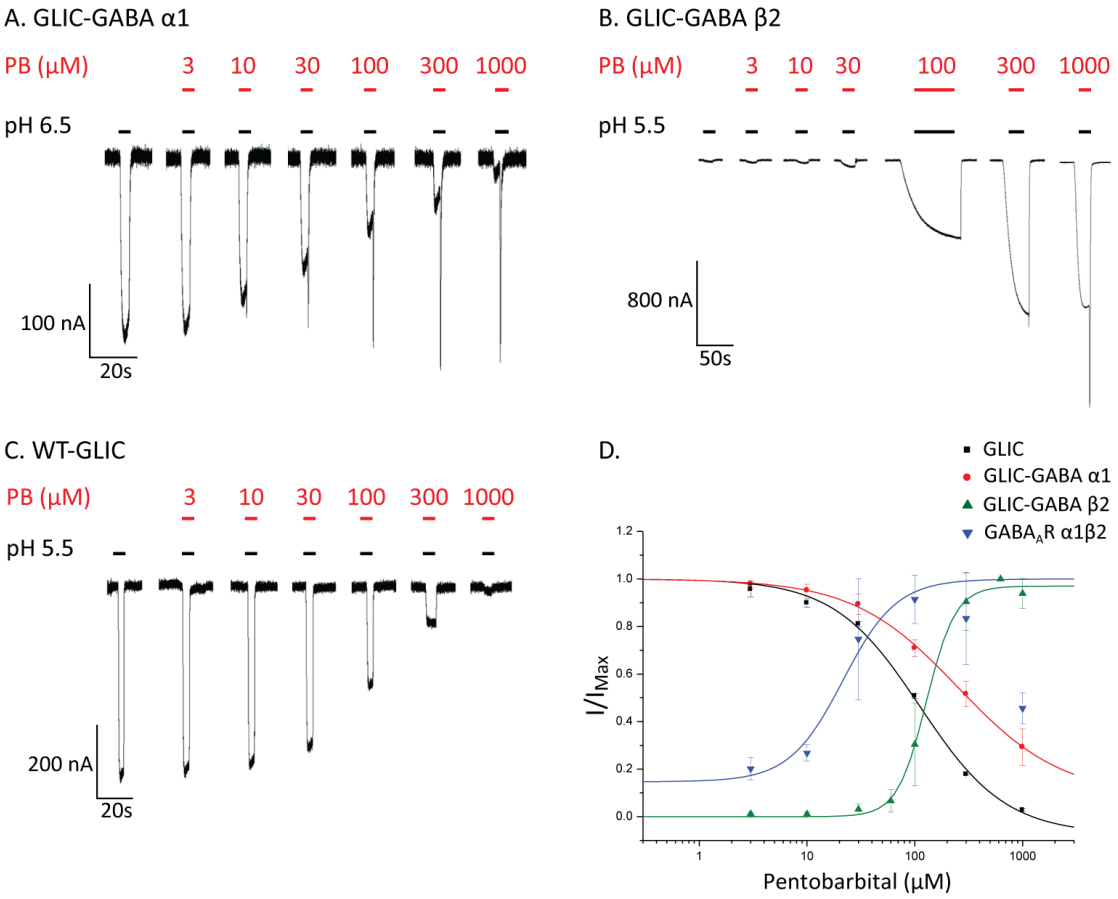

Figure 3.12 - Functional analysis of pentobarbital responses at GLIC and α1 and β2 - GABA$_A$ chimeras.

Example membrane current traces showing the modulatory effect of increasing pentobarbital concentration at an ~pH$_{20}$ proton-gating concentration for GLIC-GABAα1 (**A**), GLIC-GABAβ2 (**B**) and GLIC (**C**). **D**. Pentobarbital concentration response curves at an ~EC/pH$_{20}$ (as shown in A-C) for the indicated GLIC receptor and GLIC-GABA$_A$ chimeras and at 1 μM GABA for oocytes expressing α1β2 GABA$_A$R. Points are mean ± s.d. n = 4 - 8 cells. A concentration response for α1β2 GABA$_A$R data points is fit to 'potentiating' pentobarbital concentrations (3-100 μM) and not those inducing channel block (>100 μM).

This response is consistent with pentobarbital rapidly dissociating from a low affinity, open channel block site (Wooltorton et al., 1997). Rebound currents were not observed for GLIC, though this may reflect the slow kinetics of channel gating observed at this receptor. We cannot conclude from these experiments that an inhibitory

response was mediated through binding of PB to the TMD (for both GLIC and the α1 chimera) and not by the ECD of GLIC, which is common to both receptors. However, given that binding of PB at β-subunits is presumed to be coordinated by parts of M1, M2 and M3 (Amin, 1999) and that other anesthetics have been observed (crystallographically) to bind within the TMD of GLIC (Nury et al., 2011; Sauguet et al., 2013a), it would seem more likely that a (potentially common) inhibitory barbiturate binding site of equivalent affinity is found within the TMD of GLIC and the $GABA_AR$ α1-subunit. It might therefore be concluded that the structural elements critically responsible for the activating effects of PB are contributed by the β-subunit, and not the TMD of the α1-subunit

Based upon previous observations of PB activation of homomeric β-subunit receptors, we reasoned that, if functional, a chimera between the ECD of GLIC and the TMD of the $GABA_A$ β2-subunit might exhibit a contrasting activity profile with respect to the actions of pentobarbital. In a similar manner to that described for the α1 GLIC-$GABA_AR$ α1 chimera, we constructed a domain chimera between the ECD of GLIC and the TMD of the β2 $GABA_AR$ subunit (with no exchange of gating residues at the ECD-TMD interface or truncation of the M3-M4 loop). Tagging these GLIC-$GABA_A$ β2 chimeras with a BBS and expressing them in HEK293 cells revealed robust surface expression with fluorophore conjugated α-Bgtx (*Appendix Figure 4*). When expressed in oocytes, small proton-gated currents were recorded for the GLIC-$GABA_A$ β2 chimera. In contrast to the GLIC-$GABA_A$ α1 chimera this response exhibited slow onset kinetics, and did not decay during prolonged exposure (*Appendix Figure 4*). Given the well characterised proton modulation of $GABA_ARs$, mediated by H267 in TM2 of β2 subunit (Wilkins et al., 2002), it is not immediately clear whether channel gating of the chimera is initiated by proton-sensing at the level of the ECD or if protonation of H267 within the pore is sufficient to induce channel opening.

As for GLIC and GLIC-$GABA_AR$α1 chimera, the proton mediated response of GLIC-$GABA_AR$ β2 was measured in the presence or absence of pentobarbital (ranging from 3 μM to 1 mM). Curiously, application of pentobarbital at pH 8 (presumed resting) did not initiate direct activation of the ion channel. Co-application of pentobarbital at extracellular solutions of low pH evoked currents of increasing magnitude with

increasing concentration of pentobarbital (with an EC_{50} of 142.9 ± 46.5 μM), with a response profile (slow onset) reminiscent of pentobarbital potentiation of agonist induced currents for native $GABA_A$Rs (*Fig 3.12 B & D)*. Furthermore, at higher concentrations of pentobarbital, removal of drug was preceded by a transient increase in current (rebound current)**.** This would suggest that the TMD of the β2-subunit is responsible for contributing residues responsible for coordinating the potentiating effects of pentobarbital, whilst like the α1 TMD, also retaining a low-affinity, open channel block site. From these studies we would infer that structural elements responsible for direct gating are presumably not present on the GLIC-$GABA_A$ β2 chimera. While previously published data demonstrates that barbiturates are able to directly gate receptors formed by full-length β-subunit homomers, it is notable that much of this work has focused on a response at receptors formed of β1 or β3, and to lesser extent, β2-subunits (Cestari et al., 1996; Krishek et al., 1996; Davies et al., 1997; Wooltorton et al., 1997).

3.2.11. Alternative chimeric $GABA_A$ receptors: a GluCl-$GABA_A$ chimera

The study of pentobarbital (presented above) displays the apparently robust nature with which the ECD of the prokaryotic channel GLIC is able to act as a surrogate host for eukaryotic TMDs across the $GABA_A$R subunit family. This is likely to be case for other eukaryotic TMDs of the pLGIC superfamily. Despite the functional nature of these chimeric receptors, and retention of "typical" transmembrane domain based pharmacology of eukaryotic subunits, the kinetics of receptor activation and desensitization are considerably slower than those of its native eukaryotic counterpart. The bacterial channel GLIC is speculated to be responsible for playing a role in bacterial physiology, acting as a proton sensor in the regulation of photosynthesis at the inner membrane of gram-negative *cyanobacteria*. $GABA_A$ receptors on the other hand are critical in mediating fast-inhibition within the CNS. Unsurprisingly therefore, the time-scale with which these receptors are required to activate and impart their effect on membrane potential differs considerably. This is reflected in the response of our

chimera with "$GABA_A$-like" receptor kinetics, whilst retaining the proton-sensing property of GLIC. It is however a "slow" receptor when compared to native $GABA_A$Rs. The α1-chimeras introduced in this study typically activate on a time scale of seconds (in *Xenopus* oocytes). Whilst profoundly faster than GLIC, native $GABA_A$Rs typically activate on the time course of milliseconds (<50 ms in oocytes). This likely reflects the evolutionary separation between the two receptors, and the changes that have occurred at the level of agonist binding, signal transduction and channel gating to generate a more rapid response.

One of the major technical challenges of our functional studies to this point was the need to activate the GLIC-$GABA_A$ chimeras with protons. Repeated and prolonged application of low pH solutions caused additional stress on injected oocytes and could also induce endogenous acid-sensing channel activity which could prove problematic in the analysis of responses to (prolonged) agonist exposure and when screening weakly expressing receptors.

To address this issue and to test the concept that evolution within the pLGIC superfamily allows for large domain switches whilst retaining receptor function, we generated a chimera between the ECD of the glutamate-gated chloride channel (GluCl) α subunit from *C. elegans* and the TMD of the α1 $GABA_A$R subunit (receptors more closely related in evolution). We reasoned that such a chimera, given that the ECD of GluCl is amenable to crystallization (in the presence of Fab fragments), might also be a suitable candidate for high-level expression, purification and crystallization of a receptor bearing the TMD of the $GABA_A$R α1 subunit.

As for GLIC-$GABA_A$ chimeras, the point of domain fusion was at a site pre-M1 (at a conserved arginine residue). Similarly, sequence and structural mismatches at the ECD-TMD interface were not altered. Alignment and analysis of primary sequence reveal greater conservation of residues at the crucial gating interfaces (loop 7, pre-M1, M2-M3 linker, post-M4) between GluCl and the $GABA_A$R α1 subunit, when compared to GLIC.

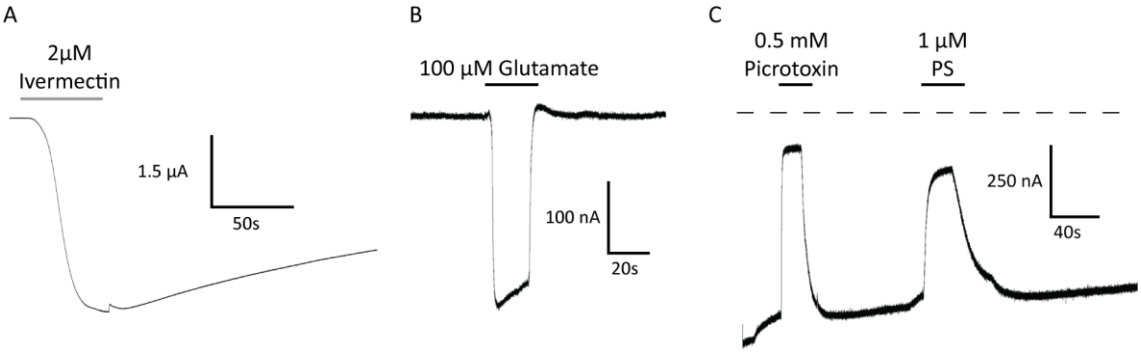

Figure 3.13 - Functional analysis of GluCl$_{cryst}$

A. Membrane currents evoked by 2 μM ivermectin in oocytes expressing GluCl$_{cryst}$. **B.** Following initial activation of GluCl channels with 2 μM ivermectin, application of 100 μM glutamate elicits reversible currents. **C.** Inhibition of ivermectin activated current by 0.5 mM picrotoxin and 1μM pregenolone sulphate (PS). Dotted line indicates zero current level.

The construct used to generate the new chimera was GluCl$_{cryst}$, which is the glutamate-gated chloride channel α subunit with truncations at the N-terminus, M3-M4 loop, and C-terminus, as used in crystallization studies (Hibbs and Gouaux, 2011; Althoff et al., 2014). Consistent with published data on GluCl, ivermectin potently activates GluCl$_{cryst}$ (exhibiting slow current onset and apparently irreversible binding; *Fig 3.13 A*). Following pre-activation with ivermectin, the subsequent application of glutamate resulted in further activation of the receptor, in a reversible manner (*Fig 3.13 B*). As previously observed, pre-activated currents induced by ivermectin are blocked by picrotoxin. Intriguingly and previously unreported, the inhibitory neurosteroid pregnenolone sulphate potently blocked the ivermectin response (*Fig 3.13 C*). Given that current levels return to those comparable with the pre-acitvated state, we might deduce that inhibition mediated by PS is non-competitive and does not displace ivermectin, therefore acting via a distinct binding site.

Expression of chimeric GluCl-GABA$_A$ α1 receptors yielded robust glutamate-activated currents, which were not dependent on prior application of ivermectin (*Fig 3.14*). Indeed application of 2 μM ivermectin alone elicited no response. Glutamate-gated responses exhibited currents with a fast onset of response, which decayed in a

pronounced manner during prolonged application (*Fig 3.14 A*). Current offset upon wash off of the agonist was also fast. The macroscopic kinetics observed for the chimera are distinct to $GluCl_{cryst}$, being more reminiscent of a native α1-containing $GABA_AR$ and notably to a greater extent than those observed for GLIC-GABAA α1 chimeras. Glutamate activated the chimera across a range of concentrations, with concentration-response relationships yielding an EC_{50} of 49.7 ± 7.58 μM (*Fig 3.14 B & C*). The observed glutamate sensitivity is not dissimilar to that observed at full-length GluClα receptors (EC_{50} =7 μM in the presence of ivermectin (Etter et al., 1996)). Given that $GABA_ARs$ are normally insensitive to glutamate, we might conclude that the ECD of GluCl provides the glutamate binding site (consistent with crystallographic data) and that subsequent transduction of the binding response induces chimera channel gating. From this and our previous studies it is clear that an evolutionary conservation of common structural elements exists at the ECD-TMD interface (of pLGIC), which allows for the generation of functional chimeras between two distinct receptors.

Beyond agonist activation of the chimera, we were curious as to whether the pharmacological profile of the chimera and $GluCl_{cryst}$ would exhibit distinct properties with regards to neurosteroids. As previously alluded to, a putative binding site for the inhibitory neurosteroid PS exists at GluClα. At the primary sequence level, residues critical for mediating the effects of potentiating neurosteroids, e.g THDOC, are not conserved between $GABA_AR$ α-subunits and GluCl (Q241 in α1 is a tryptophan at the equivalent position in GluClα). Indeed, application of THDOC (at high nM-low μM concentrations effective at $GABA_ARs$) is not sufficient to induce a response in GluCl, nor does it enhance ivermectin- or ivermectin-glutamate activated currents. This is consistent with GluClα lacking a binding site for THDOC. As for the GLIC-$GABA_AR$ α1 chimera, introduction of the TMD of the $GABA_A$ α1-subunit with GluCl, is sufficient to restore the binding of THDOC, with co-application of THDOC in the presence of an ~EC_{20} concentration of glutamate inducing a potentiation of current (*Fig 3.14 D*). Once again, these results are consistent with an intrasubunit binding site for THDOC being located within the helical bundle of a single α1 subunit TMD. Furthermore, introduction of point mutations known to ablate steroid binding at native $GABA_ARs$ (α1-Q241L/M) exhibited a similar effect at the GluCl-$GABA_AR$ α1 chimera (*Fig 3.14 E*).

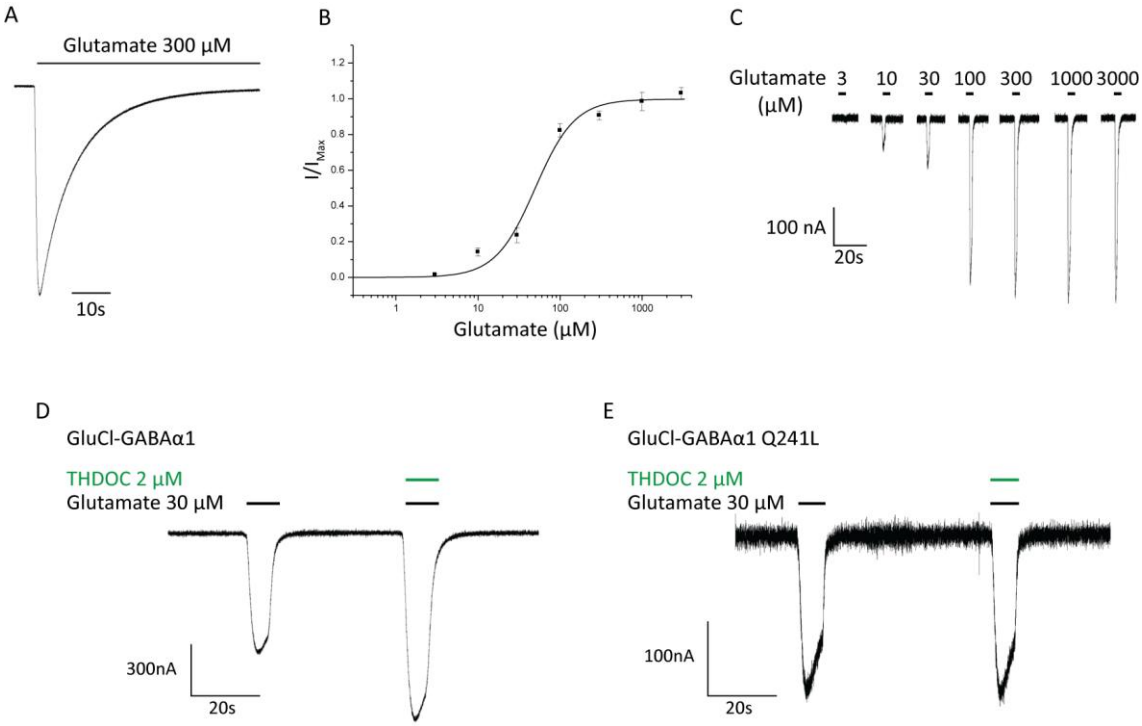

Figure 3.14 - Functional analysis of GluCl-GABA$_A$ α1 chimera

A. Membrane currents showing activation and decay of GluCl-GABA$_A$R α1 chimera (in oocytes) during prolonged exposure to glutamate 300 µM**. B.** Glutamate-concentration response curve for GluCl-GABA$_A$R α1 chimera. Points are mean ± s.d. n = 4 oocytes **C.** Example membrane current responses of occytes expressing the chimera upon exposure to increasing concentrations of glutamate. **D.** Example current traces of response induced by ~EC_{20} glutamate and its potentiation by 2µM THDOC in oocytes expressing GluCl-GABA$_A$R α1 chimera **E.** THDOC mediated potentiation is ablated through introduction of the Q241L mutation into the GluCl-GABA$_A$R α1 chimera.

3.3. Discussion

Previous studies have demonstrated that it is possible to generate functional prokaryotic-eukaryotic chimeras, which exhibit channel gating mechanisms and TMD pharmacological profiles reminiscent of their native receptor counterparts (Duret et

al., 2011; Tillman et al., 2014). Whilst this has been shown for chimeras between GLIC-GlyRα1 and ELIC-nAChR α7, it has not been investigated for receptors incorporating $GABA_AR$ subunit TMDs. Here we have sought to generate functional chimeric receptors between the ECD of GLIC (and later GluCl) and the TMD of $GABA_AR$ α1 (and β2) subunits. The TMD pharmacological profile of chimeric receptors was investigated to determine whether it reflected the TMD of the native receptor subunit. Furthermore, to infer whether common channel gating mechanisms are exhibited by chimeric receptors, particularly with regards to receptor desensitization, point mutations known to confer pronounced desensitizing properties were introduced into the chimeras. Ultimately, these functional studies serve as a starting point in the rationale design of a chimeric receptor that might be suited to high level-expression, purification and atomic resolution structural studies to infer the molecular mechanisms of allosteric modulation and channel gating of $GABA_ARs$.

3.3.1. Evolutionary conserved assembly and gating mechanism revealed by chimeric receptors

An assumption made in the generation of GLIC-$GABA_AR$ α1 chimera (as introduced in this study) was that the receptor would form on obligate homomer. $GABA_AR$ α1 subunits are unable to form functional homomeric receptors at the cell surface, requiring association with at least a β-subunit for export from the ER (Connolly et al., 1996; Taylor et al., 1999; 2000). Despite this, a functional chimera between the ECD of $GABA_AR$ ρ1 and the TMD of $GABA_AR$ α1 has been previously reported, suggesting that the α1 TMD is capable of forming a homo-pentameric arrangement (Martínez-Torres et al., 2000). Similarly, we have observed that the presence of a receptor ECD capable of folding and homo-oligomerizing, e.g. GLIC, is sufficient to constrain the TMD of α1 in to a functional homopentameric assembly. This result is consistent with extensive studies showing that crucial interactions in the ECD (at subunit interfaces) play an integral role in determining receptor assembly (Connolly et al., 1996; Taylor et al., 1999). Moreover, the isolated ECD of GLIC is capable of oligomerizing (independent of

the TMD), though loops that would normally form the ECD-TMD interface are largely disordered (Nury et al., 2010). In summation, it is not immediately clear as to whether the ECD and TMD fold and assemble independently; though the most reasonable hypothesis would suggest folding and assembly of TM spanning helices forming the ion channel is followed by assembly of the ECD domain in to a pentameric arrangement and subsequent trafficking to the cell surface. On this basis, it is apparent that interactions at the interface of $GABA_A$ α1 ECDs are energetically unfavourable and prevent stable homo-oligomerization.

For all the functional chimeras generated in this study we can draw a number of conclusions regarding the structural integrity of the individually incorporated domains and the ECD-TMD interface.

i) The ECD of GLIC is intact and forms the likely site of a proton-sensing site capable of transducing a binding signal to the TMD. Whilst the work of Wang et al (2012) proposes a role for protonation of H235 in channel activation, in this study replacing the TMD of GLIC with that of the $GABA_AR$ α1 subunit removes histidine residues in the TMD that might act as potential proton-sensors. The chimera is functionally activated in response to protons, as was the case in the previously reported GLIC-GlyRα1 chimera. This would be consistent with the proton-sensing capacity being provided by the ECD of GLIC rather than the TMD. Similar conclusions can be drawn for chimeras incorporating the ECD of GluCl. The glutamate binding site at GluClα is well established through crystallographic studies (Hibbs and Gouaux, 2011); with glutamate binding at the classical neurotransmitter binding site capped by loop C. Our results of a glutamate-gated response through the channel of a GluCl-$GABA_AR$ α1 chimera would confirm that the ECD is structurally intact when fused to alternative TMDs.

We must make more cautious conclusions in the case of the GLIC-GABA β2 chimera with regards to channel activation. This is due largely to previous observations regarding both proton modulation of $GABA_AR$ receptors (mediated by the β(2) subunit) and channel gating mechanisms in homomeric β-subunit receptors. For a long time, the consensus view has been that GABA could not gate β-subunit homomers, whilst allosteric compounds including anaesthetics, pentobarbital and propofol, could induce

direct channel gating (Krishek et al., 1996; Wooltorton et al., 1997). Moreover, in the case of homomeric β3 receptors, spontaneous activity was reported. It might therefore be concluded that the homomeric β-receptor lacks one or both of the elements responsible for binding GABA or transduction of a binding signal from the ECD to the TMD. From our studies, when compared to the GLIC-$GABA_AR$ α1 chimera, proton gating of the chimeric receptor incorporating the β2 subunit via a proton-sensor in the ECD is not immediately apparent. The presence of a previously reported proton modulation site, His267, in M2 of the β2 subunit may in fact be responsible for any proton-mediated effects (as observed for the proton-dependent pentobarbital response reported in this study; Wilkins et al., 2002). It should be noted however that recent crystallographic studies, of a $GABA_Aβ3$-homomer, has further confounded views of agonist binding and action at β3-homomers (Miller and Aricescu, 2014). Despite previous reports suggesting these receptors are insensitive to GABA, an X-ray structure reveals binding of a previously unreported agonist benzamidine at the classical neurotransmitter-binding site which is capable of gating the receptor (and also observed in electrophysiological recordings; Miller and Aricescu, 2014). This would suggest β3 homomers are presumably capable of binding agonist and gating in the "normal manner" established across the pLGIC superfamily.

ii) The ECD-TMD interface forms a structure that is part of the signal pathway initiaing receptor gating. As initially proposed by Duret et al, following studies of the GLIC-GlyRα1, the work presented here is in accordance with the principle that underlying gating at the ECD-TMD interface is the interaction of surfaces with complementary shapes (Duret et al., 2011). This concept is supported by the array of functional pLGIC chimeras previously reported; GLIC-GlyRα1, ELIC-nAChR, α7 nAChR-5HT3 and the GLIC-$GABA_AR$ α1 and GluCl-$GABA_AR$ α1 chimeras reported in this study (Eiselé et al., 1993; Duret et al., 2011; Tillman et al., 2014). The extent to which elements at the ECD-TMD have been mutated (either for correct folding or improved receptor kinetics) varies in each of these studies. In the grand scheme though, minimal modifications are required to generate a functional receptor. The altered (often unfavourable) receptor kinetics observed for many of these chimeric receptors likely represent (at an atomic level) the disruption of specific and complex intra- and intersubunit interactions at the coupling

interface (contributed by loops2 and 7, pre-M1, M2-M3 linker, and post-M4), which are normally responsible in setting the efficacy of receptor gating at native pLGICs (Miller and Smart, 2010; Smart and Paoletti, 2012). This work goes some way to confirm these observations, and ultimately highlights the evolutionary conservation of a common gating mechanism.

iii) This study provides strong evidence that the TMD of $GABA_AR$ α1 forms an intact ion channel. Though single channel conductance and ionic selectivity have not been determined, it is likely that the TMD forms an intact channel (with I-V relationships revealing a marked outward rectification of proton-elicited currents, reminiscent to the I-V relationship observed for GABA-gated currents through α1β2 receptors). Furthermore, pharmacological profiling revealed that picrotoxin blocked the chimera, in a manner consistent with it binding deep within the pore of the channel (Bali and Akabas, 2007; Hibbs and Gouaux, 2011). Whilst this does not necessarily confirm an expected organisation of individual TMDs as a four alpha-helical bundle, the potentiating effect of the endogenous THDOC at the chimera provides the strongest evidence of structural intactness in the TMD. An established binding model for potentiating neurosteroids shows the steroid molecule to be coordinated within an aqueous intrasubunit cavity, spanning between a glutamine (Q241) in the lower half of M1 and residues in the upper half of M4 (asparagine and tyrosine residues of the α subunit; Hosie et al., 2006). This cavity, and consequently steroid response, would presumably only be retained within a structurally intact TMD. The high-affinity steroid response of the chimera, contributed by the α1 TMD would provide further support to this model of steroid binding at $GABA_ARs$.

3.3.2. A common mechanism for receptor desensitization

Desensitization of receptors during prolonged agonist exposure is a common phenomenon across the pLGIC superfamily, and plays a critical role in shaping receptor response and, at the wider level, neural network activity. Single channel recordings of

nAChRs reveal that receptors transition from an active (open channel state) to an inactive (closed channel) through two distinct phases of desensitization exhibiting fast and slow kinetics (Sakmann et al., 1980). Whilst mutagenesis studies (Bouzat et al., 2008; Wang and Lynch, 2011) and EPR spectroscopy studies (of solubilized and reconstituted GLIC; Dellisanti et al., 2013) have implicated the role of structures within the ECD and at the ECD-TMD interface in determining receptor desensitization, recent structure-function studies of native $GABA_A$Rs suggest that desensitization is characterised by constriction of the ion channel by a physical "desensitization gate". Residues at the interface of the lower-halves of M2 and M3 are likely to undergo rearrangement in forming this structure (Gielen et al., 2015). Recent crystallographic and NMR studies have added further weight to this theory (Miller and Aricescu, 2014; Kinde et al., 2015).

Using our chimeric receptor as a model for $GABA_A$R channel gating, we sought to determine whether they exhibit a common mechanism for desensitization. Consistent with previous studies (Gielen et al., 2015), a number of systematic mutations of 4' glycine and -3' valine in M2 (of the α1 TMD) had a pronounced effect on the desensitization of the chimera. It should be noted these mutations were introduced in to receptors bearing truncations of the M3-M4 loop, which have been shown in this study and in the work of Papke and Grosman on GlyRα1, to affect the kinetics of entry into desensitized states (potentially through post-translational modulation; Papke and Grosman, 2014). Given that both these studies were carried out on receptors lacking the large M3-M4 loop would suggest that this domain does not have a direct effect on desensitization. From this we might conclude that our studies of chimeric receptors exhibiting desensitization mutations, but lacking the large ICD, are a representative model of a receptor in a desensitized state at the level of the channel.

An intriguing finding of this study was the apparent loss of picrotoxin sensitivity on a chimeric receptor bearing a profound desensitization mutation (conferring loss of function), valine 251 to phenylalanine (in M2 of α1). It was possible to rescue function of this receptor through introduction of a well-characterised gain-of-function mutation at the 9' position of M2, leucine 9' serine (Chang and Weiss, 1999). Whilst (at the macroscopic level) spontaneous currents of L9'S mutant alone were sensitive to block

by picrotoxin, double L9'S/V251F mutants exhibited smaller spontaneous activity and were less sensitive to picrotoxin. Given that a desensitization gate is thought to physically overlap the picrotoxin-binding site (Gielen et al., 2015), it might be deduced that a receptor allosterically stabilized in a desensitized state (i.e. where the pore is constricted at the intracellular end) would occlude the binding of picrotoxin and thus explain the observations made in this study. This theory is complicated firstly by the observation of spontaneous activity, and therefore ion flux through a channel proposed to be allosterically stabilized in a desensitized (and thus non-conducting) state. Secondly, what are the resultant effects of introducing a second mutation in the M2 helix (at the level of the "activation" gate) on the pore profile and orientation of pore-lining residues, particularly near the desensitization gate?

We might be able to make a rationale case that the double mutant has no, or minimal effect on pore residues and overall profile in the active state. This is based upon recent crystallographic studies of gating mutants in GLIC (which manifest themselves as loss-of-function in electrophysiological experiments). Whilst single mutants were crystallized in the "locally-closed" conformation, Gonzalez-Gutierrez and Grosman were able to solve the structure of a double mutant (bearing the equivalent 9' rescue mutant described here) at low pH (Gonzalez-Gutierrez et al., 2013). The structure of this receptor was identical to that of the WT open- channel conformation and thus presumably receptors respond to low pH and gate in a normal manner. We might therefore conclude that in our electrophysiological experiments, V251F/L9'S receptors are expressed in a partially desensitized (low-conductance) state under resting conditions, but are able to gate in response to agonist (high proton) as normal. While these data go some way to confirm that the non-functional V251F receptor is fixed in a desensitized state, high-resolution structural studies will ultimately be needed to provide greater detail.

3.3.3. Pregnenolone sulphate inhibition is characterised by increased desensitization

When compared to the potentiating neurosteroids, the role(s) of inhibitory endogenous steroids in the CNS and their mechanism of action at $GABA_ARs$ is largely

unknown. However, a member of this steroidal subclass, pregenolone sulphate, can also modulate other members of the pLGIC superfamily, iGluRs, including NMDARs as well as members of the Transient Receptor Potential (TRP) channel family (Harteneck, 2013). Never the less, given the affinity with which these steroids apparently bind and impart their effect at $GABA_A$Rs it remains a relevant goal to identify the determinants of an inhibitory steroid-binding site. This would shed light on the role of these compounds in GABAergic inhibition at the neuronal level.

Intriguingly, the presence of the TMD of the α1 $GABA_A$R was sufficient to dramatically enhance chimeric receptor inhibition by PS compared to the variable, low-sensitivity effect observed at WT GLIC. Furthermore this inhibition mimicked the response observed at native $GABA_A$Rs, with an apparent increase in the rate of entry in to the desensitized state (Akk et al., 2001; Eisenman et al., 2003). Given the comparatively slow onset kinetics of the chimera, in comparison to native $GABA_A$Rs and the complicated kinetic profile of PS block (Seljeset et al., 2015), the nature of this inhibitory response cannot be fully deduced.

It might seem reasonable to assume that a binding site for PS has been incorporated in to the chimera through the addition of the α1 TMD. However, with no consensus view regarding a binding model of PS at $GABA_A$Rs, this does not discount GLIC retaining a low-affinity binding site that is merely masked by the slow (non-desensitizing) response of this receptor when compared to both chimeric and native $GABA_A$Rs. Furthermore, previous studies have identified a role for the 2’ residue in the M2 of α1 (V256) in the signal transduction of a PS binding response (Wang et al., 2006; 2007). Mutation to a polar serine residue is sufficient to reduce PS sensitivity 30-fold at α1β2γ2 $GABA_A$Rs (Wang et al., 2006). Given that GLIC exhibits a similar polar residue, threonine, at this 2’ position might simply indicate that the lack of a transduction element at this position is responsible for the weak PS response.

However, we have observed for the first time high-affinity PS binding at GluCl, which further confounds the picture. PS was able to inhibit an ivermectin activated channel response. Given that GluCl, like GLIC, exhibits a polar (threonine) residue at 2’ in the M2 lining helix, it is difficult to deduce whether a mechanism of PS binding and/or

transduction at pLGICs does indeed involve a common role for the 2' M2 residue. The nature of PS inhibition not only at $GABA_ARs$, but also other members of the pLGIC superfamily, is a complex one, and may not even involve direct interaction with the protein (potentially acting through modulation of the surrounding lipid environment). Ultimately high-resolution structural studies are again likely to provide the clearest evidence regarding the determinants of a PS binding site. Later in this study we describe attempts to co-crystallize the bacterial homolog, ELIC, in the presence of PS in order to identify its binding site (Chapter 6).

3.3.4. Pentobarbital acts differentially at structurally distinct chimeric receptors

We have shown in this study that the inhibitory and potentiating effects of the barbiturate, pentobarbital, can be separated by the presence of either an α1 or β2 TMD (in a "GLIC based" chimera). At native $GABA_ARs$ pentobarbital exhibits potentiating, activating and inhibitory effects. Previous studies have suggested a role for residues in M1, M2 and M3 of β-subunits in forming the binding sites for pentobarbital. Indeed one study observed that introduction of M3 of β2 subunit in to ρ1 $GABA_ARs$, was sufficient to impart sensitivity to pentobarbital (Amin, 1999). In line with these observations, we show that the $GABA_AR$ β2 TMD is able to impart binding of pentobarbital necessary for the potentiating effects of this anaesthetic on a chimeric receptor. In contrast, the TMD of the α1 appears to play no role in the potentiating (and presumably activating) effects of pentobarbital. This conclusion is drawn from the assumption that binding is mediated by individual subunits within the heteromeric arrangement observed in native $GABA_ARs$ (which we cannot easily study in our chimeric receptor model). This however is unlikely to be the case for receptor heteromers, with photolabeling studies of anesthetic barbiturate analogs reveal binding at α-β and β-γ subunit interfaces (Chiara et al., 2013; Jayakar et al., 2015). Notably both the β2 and α1 TMD chimeras retain low-affinity pentobarbital channel-blocking sites. A site responsible for the antagonistic effects of pentobarbital has not yet been identified, however previous single channel studies argue for both a single

low-affinity channel-blocking site as well as two or more sites for potentiation and activation (Rho et al., 1996; Akk and Steinbach, 2000).

The bacterial homolog GLIC appeared to retain an inhibitory site for pentobarbital. This result is consistent with the inhibitory effect observed for other normally positive modulatory anesthetics, including propofol, desflurane and bromoform, at GLIC and nAChRs (Violet et al., 1997; Weng et al., 2010; Sauguet et al., 2013a). In the case of the former, co-crystallographic studies have revealed a number of GA binding sites at the level of the TMD (Sauguet et al., 2014a). Moreover, screens of a range of $GABA_AR$ modulators at the bacterial homolog ELIC revealed that PB application at 1 mM had no effect on this bacterial channel (Spurny et al., 2012). The inhibitory response we observed in this study therefore appears to be specific (with an IC_{50} = ~110 μM), comparable to concentrations of PB known to induce a response at $GABA_ARs$ *in vivo*. We have addressed this observation in mutagenesis and co-crystallization studies to further assess the mechanism of action of pentobarbital at GLIC (Chapter 5).

3.3.5. GLIC (and GluCl)-$GABA_AR$ chimeras are strong candidates for expression and purification trials

Crucially, through these functional studies we have shown the capacity to generate chimeras between the ECD of GLIC or GluCl and the TMD of $GABA_AR$ subunits (principally that of α1). These receptors retain the important TMD pharmacological and functional properties, such as desensitization, that is expected at native heteropentameric $GABA_A$ receptors. More over, truncation of this receptor in the region of the large M3-M4 loop does not ablate receptor function. This is likely to be important for structural studies, and validates the receptor chimeras introduced in this chapter as strong candidates for expression and purification trials (as addressed in Chapter 4).

3.4. Conclusions

The ECDs of GLIC and GluCl are capable of acting as surrogate hosts for $GABA_AR$ TMDs.

Receptor truncations in the M3-M4 loop are likely to prove essential for high-level expression, purification and crystallization of receptors and do not alter chimeric receptor function.

GLIC-$GABA_AR$ α1 chimeras exhibit a mechanism of desensitization similar to that for native $GABA_ARs$.

GLIC and GluCl chimeras containing the α1 TMD are functionally gated by protons and glutamate respectively, and exhibit TMD pharmacology (with respect to neurosteroids) that is typical of α1-containing $GABA_ARs$.

The differential effects of pentobarbital are mediated by residues contributed by different $GABA_ARs$ TMDs.

A binding site for barbiturates may be conserved in the bacterial homolog GLIC.

Chapter 4: Expression, purification and crystallization of chimeric $GABA_A$ receptors

4.1. Introduction

In this chapter, the amenability of chimeric GLIC-GABA receptors to high-level expression and purification was assessed in two recombinant expression systems; bacteria and insect cells (the latter under baculoviral infection). This step is a critical one on the path to receptor crystallization for high-resolution structural studies.

The low number of membrane protein structures deposited in the PDB epitomizes the challenge of membrane protein structural biology. Whilst membrane proteins constitute at least 30% of the genome, and an even greater proportion of known drug targets, they comprise less than 3% of the PDB (~2,450 of 111,000 structures in August 2015). This "poor showing" when compared to soluble proteins is a reflection of the difficulties that arise at each stage in the path from project conception through to successful crystallization and structure determination (Carpenter et al., 2008). Essential experimental techniques to be addressed include, but are not limited to; choosing an appropriate expression system, identifying stabilizing detergents, purification strategy, crystallization method, diffraction data collection strategy and model building. Whilst general protocols exist (Newby et al., 2009), and serve as a strong starting point, each membrane protein is different and critically dependent on it's preferred lipidic environment for stable expression. Subsequently the rules for purification of a protein are often non-transferable, even between similar proteins, and thus reliant on substantial experimental optimization. Unsurprisingly, significant steps have been taken to allow experimental variables to be rationalized in a high throughput manner both at the level of pre-crystallization screening (e.g. Fluorescence Size Exclusion Chromatography (FSEC; Kawate and Gouaux, 2006; Hattori et al., 2012)) and in protein crystallization trials (Carpenter et al., 2008; Parker and Newstead, 2012).

Members of the pLGIC family have proved particularly challenging to study at high-resolution, and only in the past few years have a number of pioneering studies allowed for a gradual expansion of our understanding of how these receptors function at the atomic level (reviewed by Cecchini and Changeux, 2014). High-resolution studies of full-length receptors are often hindered by the presence of a large ICD of 70-200 residues, observed across metazoan receptors (Smart and Paoletti, 2012; Stokes et al., 2015). This domain is typically excluded during construct design and functional screening, and thus will likely prove elusive to crystallographic structure determination (in the context of the full length receptor). Recent structural studies of the mouse $5HT_3R$ do however prove an exception to the rule (Hassaine et al., 2014) Never-the-less, the remaining domains, the ECD and TMD, are the site of action of orthosteric ligands and allosteric modulators (as introduced in Chapter 1), and the coupling interface between domains critical in mediating receptor activation and also the site of pathological mutations (Smart and Paoletti, 2012). Thus the wealth of knowledge that can be gained from studying these truncated receptors is considerable.

The modular nature of pLGICs, as emphasized by our functional studies in Chapter 3, highlights a new approach to structural studies. By generating domain chimeras with receptors previously expressed to high yield and crystallized, we can begin to use studies of individual eukaryotic domains, e.g. $GABA_AR$ TMD, to advance our understanding of allosteric modulation and channel gating. This approach circumvents some of the inherent problems of studying full-length eukaryotic receptors. For example; post-translational modification (e.g. glycosylation) of the ECD acts in both receptor assembly and activity regulation (Dellisanti et al., 2007; Miller and Aricescu, 2014), but introduces heterogeneity at the level of purified receptors that prevents energetically-favoured crystal contacts from forming. Chimeric receptors bearing the ECD of prokaryotic homologs will not exhibit such sites, and presumably be more amenable to purification to homogeneity and crystallization. Whilst we might predict that the exposed regions of pLGICs are most likely to form points of contact in the crystal form, identifying specific atomic interactions is more difficult. Exploring the use of chimeras with previously crystallized domains might allow for rationale prediction of crystal packing contacts and increased likelihood of generating well-ordered crystals.

The principal aim of this study was to use crystallographic approaches for structure determination of chimeric receptors. As introduced previously, this is rate limited by the ability to purify large quantities of protein and generate strongly diffracting crystals. Recent advances in electron cryo-microscopy (cryo-EM; discussed briefly in *Appendix Primer 1*) reveal a rival method for structure determination, obviating some of the challenges inherent to X-ray crystallography (Cheng, 2015; Cheng et al., 2015). In seminal studies, cryo-EM was used in determining the structures of TRP channel members (TRPV1 and TRPA1; Liao et al., 2013; Cao et al., 2013b; Paulsen et al., 2015). While significant advances in sample preparation, electron detection and imaging allowed (near) atomic resolution structures to be generated, TRP channels at 300-400 kDA were considered to be at the lower molecular size limit for structure determination by cryo-EM, even though the inherent four-fold symmetry of TRP channels assisted model-building and overall resolution. However the rapid and continual development of direct electron detectors and image processing software is likely to make cryo-EM accessible to the study of smaller membrane proteins, including pLGICS (typically 150-300 kDa in size). We might therefore reason that purified chimeric receptor preparations could provide the starting material for multiple structural techniques (e.g. X-ray crystallography and cryo-EM).

4.2. Results

4.2.1. Identifying an expression system capable of generating appreciable yield of chimeric receptor: Bacterial expression

Using the GLIC-$GABA_AR$ α1 chimera introduced in Chapter 3, our first challenge was to identify a recombinant expression system capable of generating stable receptors in sufficient quantity for downstream processing. The prokaryotic receptor GLIC is strongly expressed in bacterial cells as an N-terminal fusion construct with Maltose-Binding Protein (MBP) (*Fig 4.1 A*). Therefore, we reasoned that a chimera exhibiting the ECD of GLIC and the TMD of the $GABA_AR$ α1 subunit would be similarly expressed

in *E. coli*, assembled as a pentamer and targeted to the periplasmic membrane when expressed as a MBP-fusion construct.

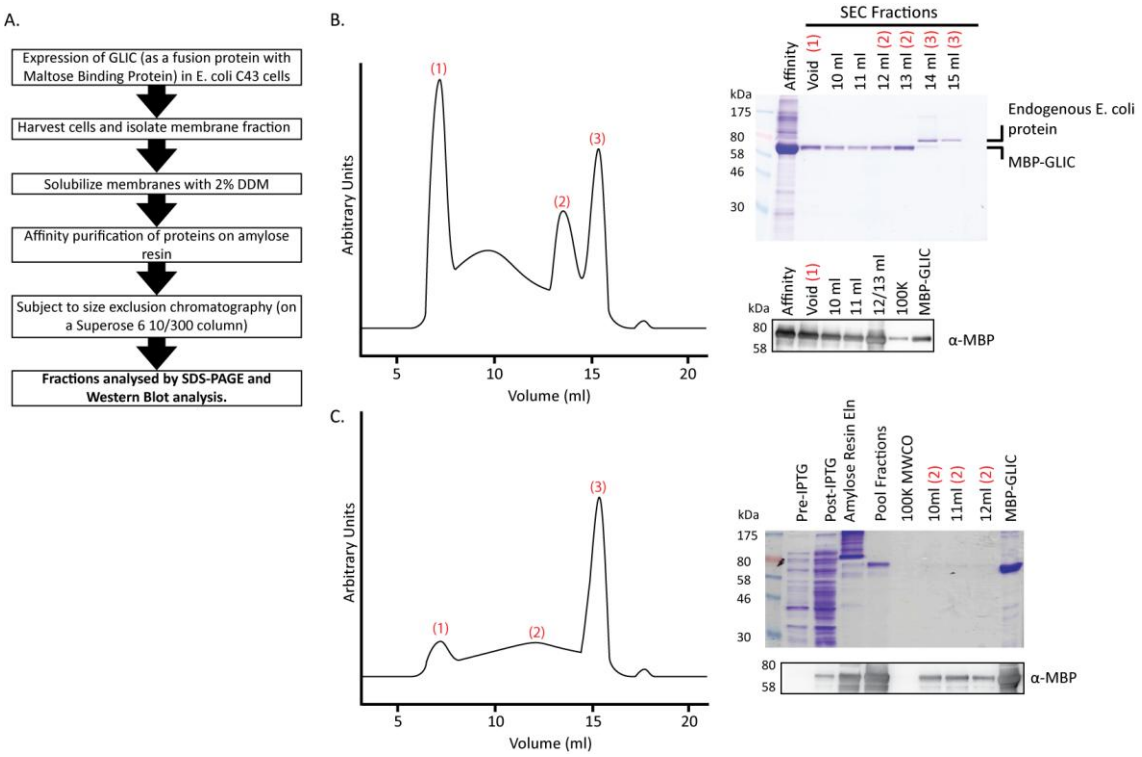

Figure 4.1 - Bacterial expression of MBP-GLIC and chimeric MBP-GLIC-GABA$_A$R β2

A. Workflow for bacterial expression of MBP-GLIC (and chimera), receptor purification and analysis. **B.** Representative size-exclusion profile of MBP-GLIC following solubilization in DDM and purification on amylose resin. Peaks correspond to large aggregates (in the column void) (1), pentameric MBP-GLIC (2) and endogenous porin protein (3). Coomassie-blue stain and western blot analysis of peak fractions is shown on the right, revealing migration of MBP-GLIC as a band of ~70 kDa. **C**. Representative size-exclusion profile of MBP-GLIC-GABA β2 following solubilization in DDM and purification on amylose resin. Peaks correspond to void (1), aggregate of MBP-GLIC (2) and endogenous porin protein (3). Coomassie-blue stain and western blot analysis of peak fractions are shown right, revealing migration of MBP-GLIC-GABA β2 as a band of ~70 kDa and likely degradation product of lower mass.

Consistent with previous studies, we also found that the fusion protein of MBP-GLIC is well expressed in the C43 strain of *E. coli* (Bocquet et al., 2007; 2009). GLIC receptors form a stable pentamer (as well as higher order aggregates) when solubilized in n-Dodecyl-β-D-maltopyranoside (DDM) and purified on an amylose resin. This is apparent from size exclusion chromatography (SEC) where prominent peaks corresponding to larger aggregates (which elute in the column void volume, ~8 ml) and pentameric MBP-GLIC (~13ml elution volume) are observed (*Fig 4.1 B*). SDS PAGE and coomassie blue-stain (and western blot) confirm that these peaks correspond to MBP-GLIC, with material from peaks migrating as a single, homogenous band of ~70 kDa. The third peak component observed in SEC experiments corresponds to an endogenously expressed porin-family member, which binds with high affinity to the amylose resin. At a volume of ~15 ml this elutes in a clearly defined, symmetrical peak, which can be separated from MBP-GLIC (as assessed by SDS-PAGE analysis of peak fractions; *Fig 4.1 B*). Later in this study (Chapter 5) we show how purified MBP-GLIC can be used in further purification strategies, yielding cleaved WT-GLIC (for receptor crystallization trials).

We speculated that GLIC-$GABA_AR$ chimeras might be similarly expressed in *E. coli* (as a fusion protein with MBP). However, subsequent attempts to express chimeric MBP-GLIC-$GABA_A$ α1 chimeras (lacking the large M3-M4 loop) proved unsuccessful. During screening we noticed poor bacterial cell growth following induction of expression, which would suggest that chimera constructs showed increased cell toxicity when compared to wild MBP-GLIC. Possibly this was due to recombinantly expressed proteins being misfolded and forming inclusion body aggregates (though this was not assessed further).This indicated that bacteria are unlikely to be suitable for production of chimeras containing eukaryotic elements, such as the α1 subunit TMD, which probably require a more complex membranous environment for stable expression. Indeed the composition of a eukaryotic membrane differs profoundly from that of the bacterial inner (and outer) membranes, crucially lacking lipids including cholesterol known to interact with and stabilize eukaryotic pLGICs (Hénin et al., 2014; Barrantes, 2015). Further receptor mutations may have improved the expression of the GLIC-

$GABA_AR$ α1 chimera in bacteria. However, the maximum yield achievable was unlikely to be conducive for crystallization trials.

Our only minor success in bacterial expression screens was for a truncated GLIC-$GABA_AR$ β2 chimera (introduced in chapter 3). This was expressed as a fusion protein with MBP and lacking the large M3-M4 loop. Affinity purification on amylose resin, following DDM solubilization of isolated membranes, revealed a faint band of the expected mass for monomeric receptor subunit when assessed by SDS PAGE and coomassie stain (and confirmed by western blot analysis with an α-MBP antibody) (*Fig 4.1 C*). The receptor yield is considerably lower than that of WT GLIC. A lower mass band (exhibiting immuno-reactivity) would suggest that a C-terminally degraded species is also purified. Size exclusion chromatography (of affinity-purified proteins) shows a poorly defined peak spanning a significant volume of the column. Analysis of material from this peak suggests that it corresponds to the chimeric receptor (*Fig 4.1 C*). In contrast to WT-MBP-GLIC, the profile of this peak is unlikely to correspond to a pentameric form of the protein and most likely represents receptor in an aggregated or high-order oligomeric state. At this stage we did not optimize the expression and purification of chimeric receptors from *E. coli*.

4.2.2. Identifying an expression system capable of generating appreciable yield of chimeric receptor: Baculovirus-insect cell expression

In order to improve expression and purification of our chimeric receptor we next considered use of a higher eukaryotic cell line for protein production. Insect cells, and more specifically the baculovirus-insect cell expression system, has been successfully used for the production of eukaryotic ion channels for structural studies, including the rat AMPAR GluA2, *C. Elegans* glutamate-gated chloride channel ($GluCl_{cryst}$) and zebrafish $P2X_4$ receptors (Sobolevsky et al., 2009; Hibbs and Gouaux, 2011; Hattori and Gouaux, 2012). Given that insect cells, unlike stably expressing mammalian cell lines, e.g. HEK293, can be grown easily in suspension with no-atmospheric control, establishing an insect cell line for protein expression is not as costly or time-consuming. We therefore chose to test expression and purification of chimeric

receptors by baculoviral infection of *Spodoptera frugiperda* Sf9 insect cells, using established protocols (Trowitzsch et al., 2010) (*Fig 4.2*).

Initial expression studies with regards to construct design were guided by functional experiments (as detailed in Chapter 3) and focused on GLIC-$GABA_AR$ α1 chimeras. Our initial rationale for construct design and purification was also guided by the existing data for crystallized pLGICs (GLIC, ELIC and $GluCL_{cryst}$) and the wider field of eukaryotic ion channels and membrane proteins.

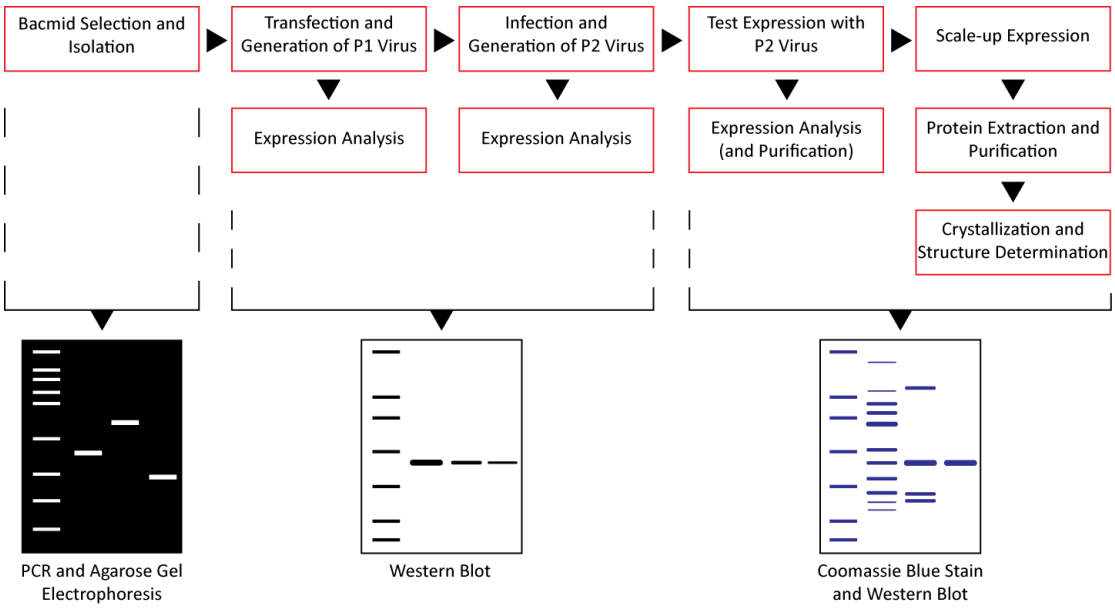

Figure 4.2 - Workflow for pre-crystallization screening of chimera constructs by baculovirus-insect cell expression system

Receptor chimera candidates identified in functional experiments (Chapter 3) were subcloned in to vectors for insect cell expression. Stage 1: PCR reaction analysis by DNA gel electrophoresis was used to confirm gene transposition in to a baculovirus shuttle vector (bacmid). Stage 2: Purified bacmid DNA was used in transfection and recombinant virus generation. Subsequent rounds of viral amplification were used to increase the viral titre. Protein expression and viral titrewasthen assessed by SDS PAGE and coomassie blue-stain and/or western blotting. Stage 3: Expression of stable pentameric receptors was assessed in scale-up experiments prior to large-scale expression, purification and crystallization.

As previously discussed, the large intracellular loop linking M3 and M4, forming the ICD of eukaryotic pLGICs, is likely to hinder high-level receptor expression, purification and subsequent crystallization. In Chapter 3 we developed two M3-M4 truncated variants of the chimera, defined as: M3-M4^{tripeptide} and M3-M4^{heptapeptide}. Both exhibited similar proton gating properties and TMD pharmacology for a GLIC-GABA$_A$R α1 chimera. Here we focused on constructs bearing the M3-M4^{tripeptide} linker for high-level expression. For clarity we have refined this construct as GLIC-GABA$_A$R α1$^{\Delta ICD}$ (where $^{\Delta ICD}$ represents truncation of the M3-M4 loop by the "tripeptide" linker).The decision to focus on this chimera was principally due to its previous successful incorporation into a homologous receptor, GluCl$_{cryst}$, for expression in Sf9 cells and successful crystallization (Hibbs and Gouaux, 2011; Althoff et al., 2014). Additionally we chose this construct on the basis that a shorter linker (replacing the ICD) might impart greater structural rigidity on the TMD and thus facilitate crystallization. In line with recent structural developments in the pLGIC field, occurring during the time-course of this study (namely structures for the GABA$_A$ β3 homomer and GLIC-GlyR α1, LiLy; Miller and Aricescu, 2014; Moraga-Cid et al., 2015), we have begun to assess in greater depth the effects of the M3-M4 linker mutation on receptor expression and purification. Interestingly both of the aforementioned studies use the heptapeptide linker sequence from GLIC.

In addition to truncating the M3-M4 loop (ΔICD), preliminary purification experiments were of a construct bearing a second truncation, of 13 amino acids at the C-terminus (post-M4) of the receptor (*Fig 4.4 A*); we define this additional truncation as 'ΔCt'. As before, this was guided by the requirement of a similar truncation for expression, purification and crystallization of GluCl$_{cryst}$. For purification of chimeric receptors by immobilized-metal affinity chromatography, a C-terminal octa-Histidine tag was introduced using standard molecular biology techniques. This chimera was still activated by protons and functionally indistinguishable from a receptor that retained this stretch of residues at the C-terminus of the receptor (data not shown).

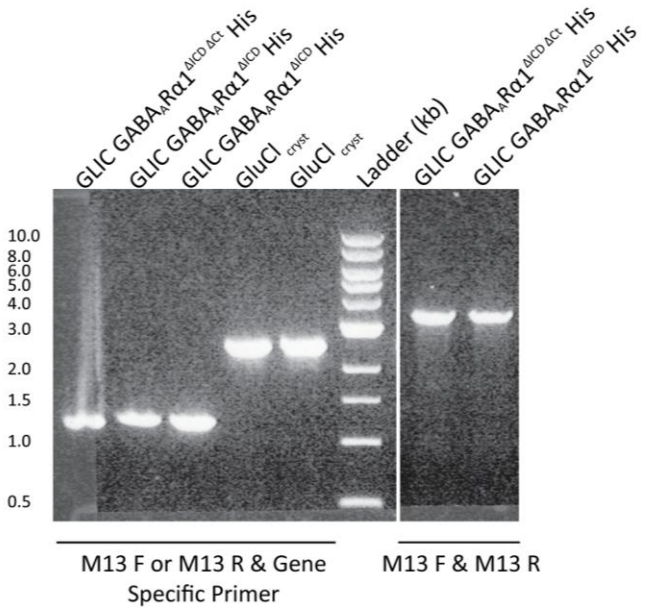

Figure 4.3 - PCR and DNA gel electrophoretic analysis confirms transposition of receptor chimera genes in to bacmid DNA.

DNA gel electrophoresis of PCR products amplified from recombinant bacmids containing the indicated receptor genes. PCRs were carried out with either gene specific primers (e.g. annealing at a site located in the nucleotide sequence of the GLIC ECD) in combination with M13 F/R primers (as described in Materials and Methods), yielding fragments of ~1.2 or ~2.5 kilobases (kb), or M13 F and R primers. For latter primer combinations a PCR product of 2.3 kb + size of insert was expected for successful transposition. Chimeric receptors containing the tripeptide M3-M4 linker and His-tag are defined as GLIC-GABA$_A$R α1$^{\Delta ICD}$His and with the additional C-terminal truncation as GLIC-GABA$_A$R α1$^{\Delta ICD\ \Delta Ct}$His. GluCl$_{cryst}$ is the construct used in previously published crystallization studies (Hibbs and Gouaux, 2011).

Following design and generation, the receptor chimera geneswere integrated into the baculovirus (AcMNPV) genome and propogated in *E. coli*. PCR analysis of "bacmid DNA" was used for analysis of successful transposition. Using primers annealing at sites unique to the gene-of-interest (i.e.chimeric receptors) we were able to confirm successful incorporation of our receptors into the baculovirus genome in preparation for preliminary screens of receptor expression in cultured insect cells (*Fig 4.3*).

4.2.3. Determination of expression levels of chimera in virally transduced insect cells

In preliminary experiments, the expression of the chimeric receptor containing the M3-M4 tripeptide linker, C-terminal truncation (of 13 residues) and C-terminal octa-Histidine tag, GLIC-$GABA_AR$ $\alpha1^{\Delta ICD\Delta Ct}$His, was assessed in whole insect cell extracts following transfection; first round of virus amplification (infection with $P1_{virus}$ and generation of $P2_{virus}$); and after a test expression using high titre virus($P2_{virus}$). SDS PAGE (under reducing conditions) and western blot analysis against the receptor His-tag was carried out (*Fig 4.4*). A band of ~38 kDa corresponding to the chimeric receptor was observed at all stages of virus generation/amplification. As might be expected, signal intensity increased progressively from cells taken following the initial virus generation ($P1_{virus}$) through to expression with high titer virus ($P2_{virus}$ Test Exp) (*Fig 4.4 B*). Using a high-titer $P2_{virus}$ we next determined the time-course of receptor expression (again by western blotting of crude cell extracts). Western blotting allowed the detection of nanogram amounts of protein and thus enabled protein expression to be assessed from small amounts of starting material (typical biomass from ~1 x 10^6 cells). Receptor expression was only apparent after 28 hrs and reached an apparent plateau in expression levels between 44 and 72 hrs (*Fig 4.4 C*). Initial screening of expression in insect cell shows appreciable production of the chimeric receptor, which contrasted with our expression studies in *E. coli*.

Using $P2_{virus}$, we next carried out experiments to determine the efficiency of receptor extraction (following detergent solubilization of membranes) and purification (*Fig 4.4 D & E*). The membrane fraction was isolated, and proteins extracted using DDM and His-tagged chimeras then purified by Immobilized Metal Affinity Chromatography (IMAC) using a Co^{2+} resin. Coomassie blue-stain of SDS PAGE gels of material from elution fractions from IMAC experiments revealed a prominent band of ~38 kDa, presumably corresponding to our His-tagged chimera. Without further purification steps, minor-contaminating bands were also observed (*Fig 4.4 D*).

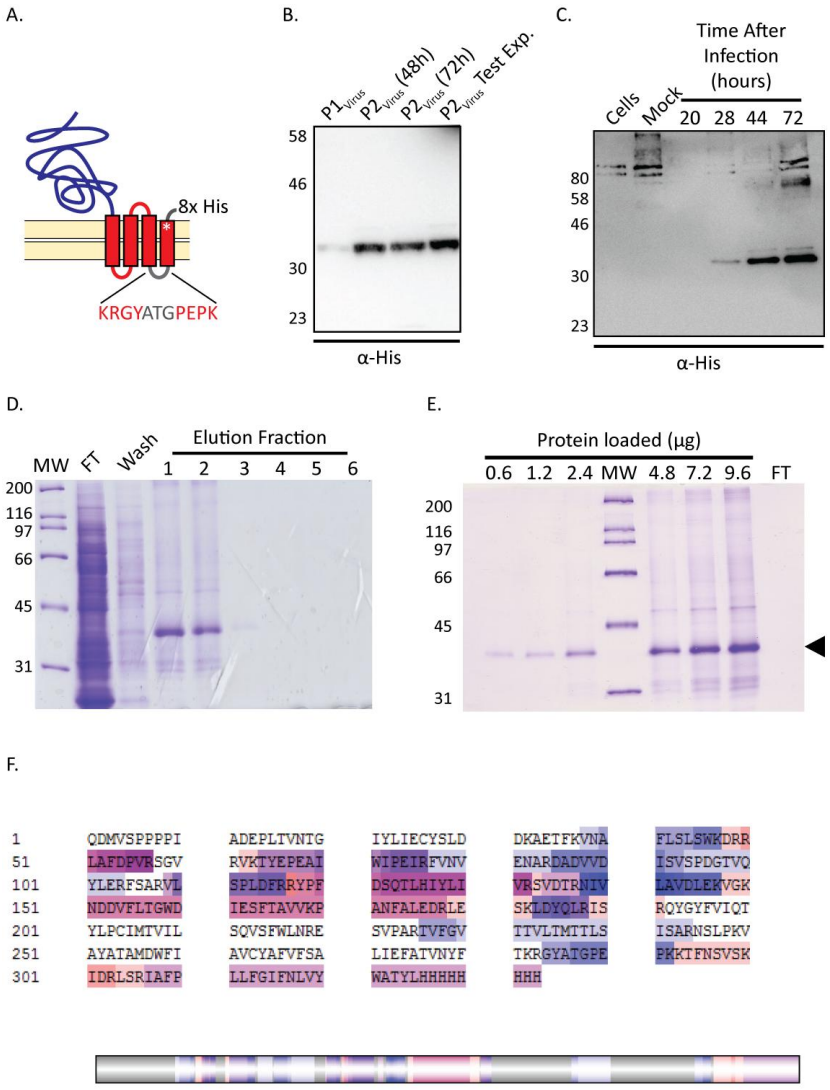

Figure 4.4 - Preliminary screening of GLIC-GABA$_A$R α1$^{\Delta IC\ D\Delta Ct}$His chimera: viral amplification, protein expression and purification

A. Schematic representation of receptor construct; ECD of GLIC (blue) and TMD of GABA$_A$ α1 (red). M3-M4 loop is truncated (ΔICD) and replaced by tripeptide linker ($^{\Delta ICD}$; linker sequence and insertion site shown), C-terminus truncation of 13 residues ($^{\Delta Ct}$; asterisk) and octa-histidine tag (8x His; for affinity purification). **B.** Western blot analysis with α-His antibody shows chimera expression during P1$_{virus}$ and P2$_{virus}$ generation. **C.** Time-course analysis of protein expression (using P2$_{virus}$) reveals plateau peak between 44 and 72 hrs. **D.** and **E.** Protein-expression (using P2$_{virus}$), solubilization and affinity purification using Co^{2+}resin, followed by SDS PAGE and coomassie blue stain reveals a band of the expected size for reduced-monomeric chimera receptor subunit. Loading increasing amounts reveals affinity purified-protein to be relatively pure. Band (shown by arrowhead was excised) for mass spectrometry (MS) and peptide-mapping analysis. **F.** Colour map of the 56 peptide fragments (on receptor chimera primary sequence) identified by MS analysis. Peptide coverage equates to 64.6% of the sequence.

To confirm that the major band (of ~38 kDa) was not a contaminant, we excised gel bands for tryptic-digest of proteins and mass spectrometric analysis of peptide fragments. Mapping of 56 peptide fragments was sufficient to give 64.6% primary sequence coverage (*Fig 4.4 F*), and provide convincing evidence that the chimera is the major species purified on Co^{2+}resin. Though this was encouraging, further purification of affinity-purified material on a size-exclusion column revealed that this material does not exist in a single homogenous state. Presumably the receptor is unstable as a pentamer in DDM-micelles.

Whist we cannot discount that alternative detergents are capable of stabilizing this truncated variant of the GLIC-$GABA_A$R α1 chimera, we were curious as to whether exclusion of the C-terminal residues was responsible for destabilizing the chimera in detergent micelles (*Fig 4.5 A*). Furthermore, we reasoned that by re-introducing the 13 post-M4 residues, access to the preceding octa-Histidine tag in affinity chromatography steps would be improved, potentially increasing receptor recovery.

SDS PAGE-coomassie stain and western blot analysis of crude extracts from virally-infected cells revealed that a receptor including the full C-terminal sequence (GLIC-$GABA_A$R $\alpha1^{\Delta ICD}$His) was expressed at equivalent levels to that bearing the C-terminal truncation (ΔCt). As expected, this receptor migrated as a band of marginally greater mass, ~39 kDa (*Fig 4.5 B*). Using biomass from increased culture volume as our starting material, cell membranes were isolated and detergent solubilized with DDM. Following affinity-purification to recover His-tagged chimera, size-exclusion chromatography was used to further purify and assess the relative homogeneity of the sample (*Fig 4.5 D*). When loaded on to a Superose 6 10/300 column, affinity purified material elutes as two major species. Large aggregates eluted in the void volume (~8 ml) of the column, whilst a second broad peak was observed, bearing a shoulder at ~15 ml (previously not observed for the $^{\Delta Ct}$ construct). We reasoned that the latter shoulder corresponds to the expected elution volume of the pentameric form of our protein (*Fig 4.5 C*). Indeed, when material from peak fractions was separated by SDS PAGE and stained, a band of expected mass for the chimera was observed, and was even more prominent in material taken from the fraction corresponding to an elution volume of 15 ml (*Fig 4.5 D*). Given that the shoulder is not the major species it is difficult to draw firm

conclusions regarding the oligomeric state of our protein in detergent-micelles. We might speculate that it is principally expressed as an unstable pentamer which is in dynamic-equilibrium with higher-order oligomers. On this basis the latter state is favoured and the pentamer is poorly resolved by SEC.

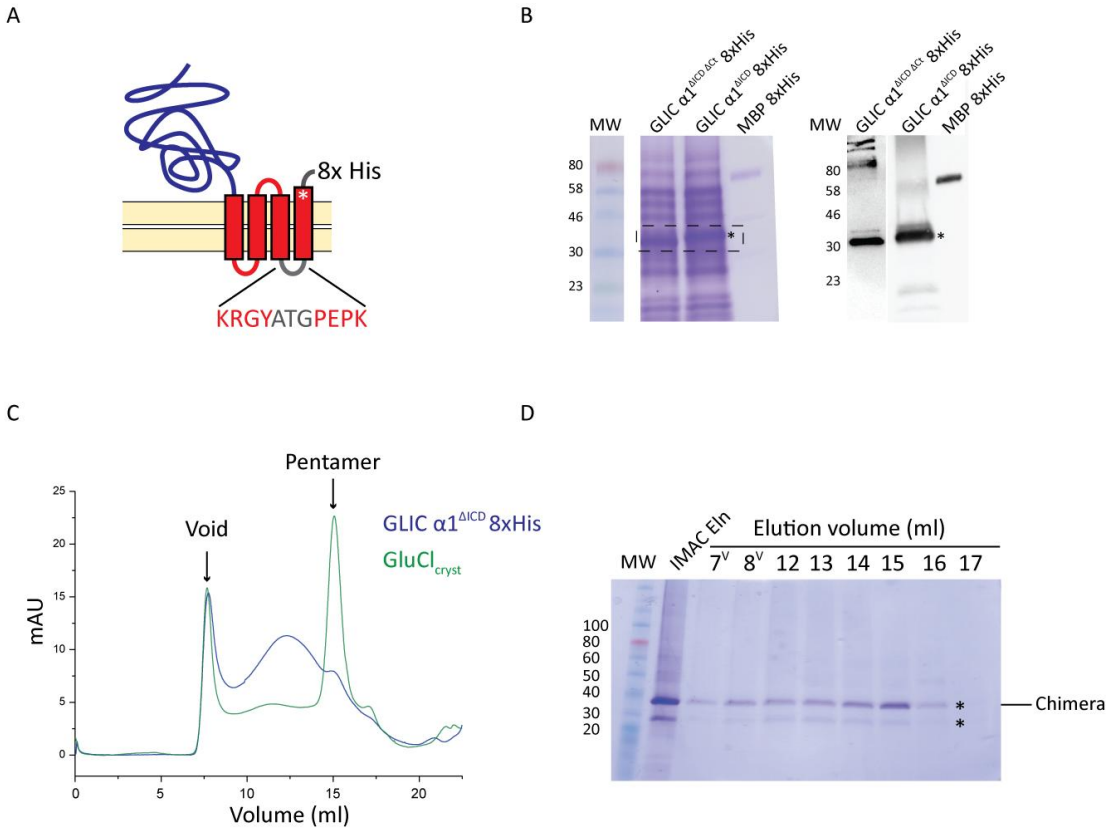

Figure 4.5 - Preliminary screening of GLIC-GABA$_A$R α1$^{\Delta ICD}$His protein expression and purification

A. Schematic representation of receptor construct; Receptor as in Fig 4.4A however the C-terminus of is no longer truncated (asterisk) **B.** Coomassie blue-stained SDS PAGE andwestern blot analysis with α-His antibody shows chimera expression level is unaltered by inclusion of 13 residues at the C-terminus (post-M4). Asterisks indicate band corresponding to chimera. Soluble MBP-His was a positive control (in α-His blots). **C.** SEC profileof DDM-solubilized chimera (blue trace) following purification on Co^{2+} resin. Indicated peaks correspond to void volume and a shoulder at elution volume of ~15 ml likely to be pentameric protein. A sharp symmetrical peak for a pentameric receptor, $GluCl_{cryst}$ in DDM (overlay green trace) is observed at ~15 ml elution volume. **D.** Coomassie blue-stained SDS PAGE analysis of affinity-purified receptor (IMAC Eln) and SEC fractions. Prominent band of ~38 kDa clear during affinity purification and from SEC fractions. Notably a second lower mass band also present (asterisks) throughout, potentially contributed by degraded receptor subunit.

To validate this important result, before being used as a starting point from which to optimize detergent stabilization of this receptor construct, we first needed to confirm that the observed shoulder was likely to represent the pentameric form of the chimera. One might expect a homologous pLGIC protein (of similar structure and mass), in complex with DDM, to exhibit an elution profile to be expected for the pentameric chimera. We therefore expressed and purified $GluCl_{cryst}$ in DDM using previously reported methods (Hibbs and Gouaux, 2011). Affinity-purified proteins eluted in two peaks (when loaded on to a gel filtration column). Large-aggregates elute in the column void volume, whilst the major species exists as a well defined symmetrical peak, with a retention volume of ~15 ml (*Fig 4.5 C*). SDS PAGE (under reducing-conditions) and coomassie stain revealed that material from this peak migrates as single band of ~35 kDa (likely corresponding to the monomeric-$GluCl_{cryst}$ subunit). Given that $GluCl_{cryst}$ is known to exist as a pentamer in DDM, we used this result as a benchmark for assessing the generation of stable detergent-solubilized pentameric chimeras.

4.2.4. Small-scale detergent-screening of "wild type" GLIC-GABA α1 chimeras

Having identified a receptor-construct (*Fig 4.5 A*) from which to optimize detergent stabilization, we sought to generate a procedure for screening many detergents on their ability to efficiently extract receptor protein. Identifying a detergent capable of extracting an appreciable yield of receptor, whilst retaining stability, is critical in ion channel purification and subsequent crystallization. Using high-throughput screening of detergents by FSEC or small-scale purification paired with SEC-MALS (Multi-Angle Light Scattering) has greatly assisted various studies in successfully purifying ion channels for crystallography. However, without access to such resources (in the initial stages of this study), we were only able to determine the efficiency of detergent extraction (using small culture volumes) and not the monodispersity of solubilized receptors. Consequently, to assess the purity, homogeneity and stability of detergent-

solubilized receptors, we used standard purification approaches (IMAC followed by SEC).

In order to screen a panel of detergents (often in combination with cholesterol hemisuccinate (CHS); a cholesterol "mimic" which has been found to dramatically enhance the stability of many membrane proteins in detergent micelles) we developed a micro-purification approach originally used in screening GPCR samples prior to large-scale production (*Fig 4.6 A*). The procedure is summarized in greater depth in Material and Methods (*Section 2.6.3*). We used the harsh, ionic detergent Fos-Choline 12 (FC-12; in which only a few bacterial membrane proteins are capable of maintaining structural integrity) as a gauge of total protein extracted. Since FC-12 is equally capable of extracting both folded and misfolded protein, we can use it to provide estimation (when compared with other detergents) of the relative ratio of correctly folded: misfolded protein. By contrast to FC-12, mild-detergents, including DDM, are much less efficient at solubilizing misfolded protein (Thomas and Tate, 2014).

Crude membranes were prepared from insect cell pellets and split in to equal aliquots (~5ml biomass/condition) for detergent extraction and purification; the panel used (*Fig 4.*6 A) ranged from mild (e.g. DM), to so-called crystallization detergents (e.g. Maltose Neopentyl Glycols, MNGs), and harsh-ionic detergents (e.g. FC-12; full list of detergent names are in Materials and Methods *Table 2.7*). FC-12 extraction confirmed strong expression of the chimera, and its purification on Co^{2+} resin, with a dense band observed at the expected mass of the (monomeric) chimera subunit (*Fig 4.6 B*). Solubilization in DDM yields a largely homogenous band (migrating at ~39kDa), though of reduced intensity when compared to that for FC-12.

Assuming that equal sized populations of receptors were present in DDM and FC-12 samples, this would suggest that while a proportion of expressed receptors might be misfolded, the mild detergent DDM is capable of extracting ~50% of expressed receptors in a (presumably) correctly folded state. This appreciable yield is consistent with our previous results (*Fig 4.5 C and D*), though we know from SEC experiments that much of this purified material represents receptors in a non-pentameric, aggregated state (*Fig 4.5 C and D*).

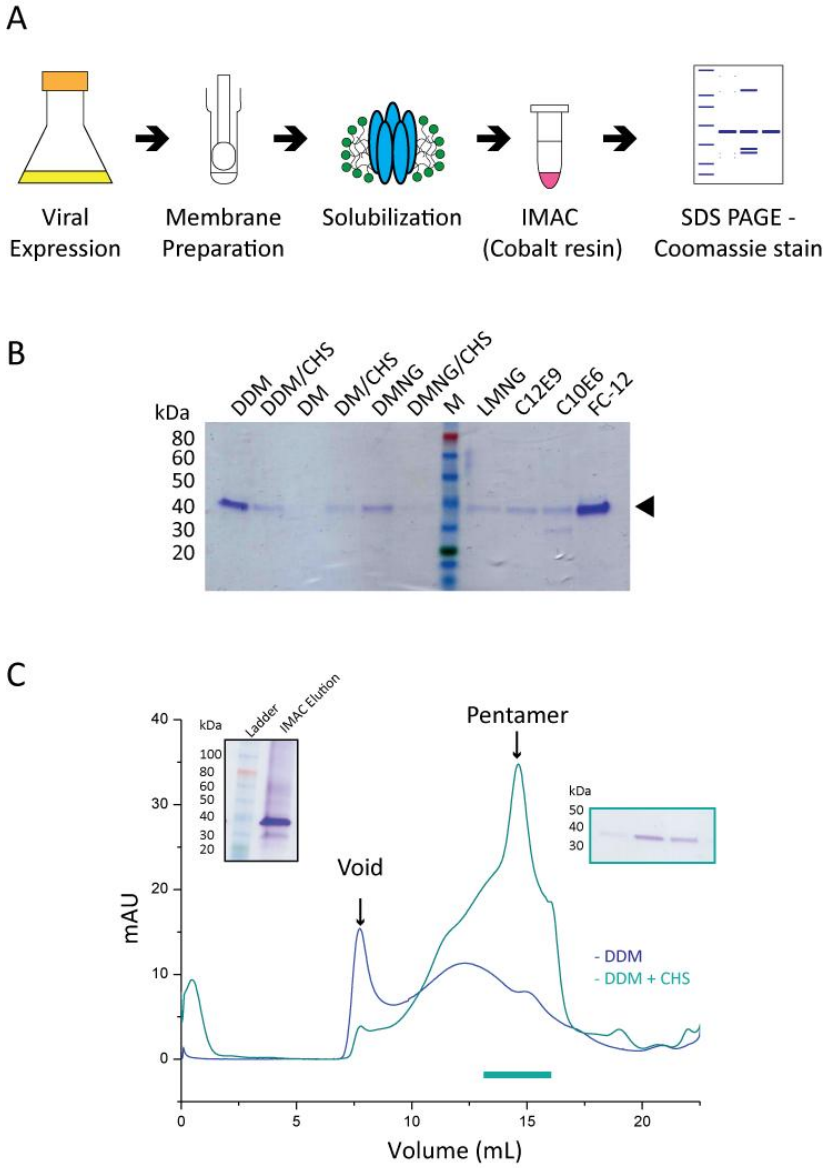

Figure 4.6 - Small-scale detergent screening of GLIC-GABA$_A$R α1$^{\Delta ICD}$His and analytical scale protein purification

A. Small-scale workflow for detergent screening. Viral-infected insect cells are harvested and crude membranes prepared by homogenization and high-salt wash, before solubilization in one of a panel of detergents. Solubilized material is incubated with TALON Co^{2+}resin and His-tagged receptors recovered by affinity purification before analysis by SDS-PAGE. **B.**Coomassie blue-stained SDS PAGE of affinity purified chimera following detergent screening.. Arrowhead denotes prominent band of ~39 kDa corresponding to monomeric chimera subunit. **C.**Receptor solubilized in DDM +/- CHS was affinity purified and further purified by SEC. CHS (cyan trace) is able to further stabilize the presumed pentameric form (elution volume of ~15 ml) of the chimera in DDM micelles. SDS PAGE and coomassie blue-stain analysis of affinity purified receptor **(Inset, left)** and of material from peak fractions (delineated by horizonetal cyan bar), which runs as homogenous band of ~39 kDa **(Inset, right)**.

Faint bands were also (most notably) observed for DDM/CHS, DMNG, LMNG and $C_{12}E_9$. Extraction in $C_{10}E_6$ showed two prominent bands (of ~39 and 30 kDa), potentially due to a smaller degradation product (*Fig 4.6 B*). Whilst the lane for DM/CHS shows a faint band (of expected mass), the shortened alkyl-chain (C_{10}) of DM when compared to DDM (C_{12}) is unlikely to have favourable, stabilizing effects in initial receptor solubilization. We cannot rule out that the additional presence of CHS will not compensate for this destabilizing effect.

Given our previous studies with DDM, we were curious to assess the additional stabilizing effects of CHS on chimeric receptors. Scaling up our preparations, starting with biomass from a ~250 ml culture, we solubilized the membrane fraction with DDM/CHS, and recovered solubilized receptors by affinity-chromatography as previously described. Surprisingly, the addition of CHS was sufficient to dramatically enhance the stability of the presumed pentameric form of the chimera (by SEC), with a clear symmetrical peak at ~15 ml (material from peak fractions showing a band of expected mass when analyzed by coomassie blue-stain; *Fig 4.6 C*). This peak, however, is incorporated within a broader species eluting over a larger volume of the gel filtration column (between 10-16 ml), and thus presumably the detergent-CHS-receptor complex exists in multiple oligomeric or aggregation states. Further experiments are required to determine whether DDM and other detergents (with CHS) identified in small-scale screens are capable of stabilizing the GLIC-$GABA_AR$ $\alpha1^{\Delta ICD}$His chimera.

4.2.5. Small-scale detergent-screening of "desensitization mutant" GLIC-$GABA_AR\alpha1$ chimeras

In parallel to screening detergents for stabilizing properties, we were keen to explore an alternative avenue of receptor stabilization by modifying the conformational state of the channel. This strategy has been adopted in a number of studies to facilitate both purification and crystallization of membrane proteins (in distinct states). Most widely

used in the GPCR field, in an approach termed conformational thermostabilization, genetic engineering of a membrane protein is often capable of imparting stabilizing properties that would not be possible to achieve purely by detergent optimization (Warne et al., 2008; 2009). We therefore postulated that engineering point mutations into our chimera that alter the gating equilibrium would potentially assist expression and purification of a stable pentameric receptor. Given that the active state of the receptor is likely to be thermodynamically unfavorable, we focused on desensitization mutants, which would shift the gating equilibrium towards a distinct closed channel conformation. During preliminary experiments, there was a lack of high-resolution structural information for pLGICs in a desensitized state, and thus we speculated that studies of chimeric receptors bearing such mutations might assist in uncovering the molecular mechanisms for desensitization.

Both functional and non-functional desensitization mutants (introduced in Chapter 3) were engineered in to M2 of the GLIC-$GABA_AR$ $\alpha1^{\Delta ICD}$His chimera (non-functional mutants were presumed to be trapped in a desensitized state). Additionally we introduced the mutations N307S/V in to M3, which were identified as having a profound effect on native $GABA_AR$ desensitization (Gielen et al., 2015). Small-scale purification and extraction screens were carried out to identify strongly expressing candidate receptors (*Fig 4.7 A & B)*. Most of the mutant receptors were expressed (and purified following extraction in DDM or FC-12) to equivalent or greater levels than the "wild-type" chimera, with bands observed at ~39 kDa by SDS PAGE-coomassie stain analysis. This was most notable for G258A (*Fig 4.7 A)* and V251F (*Fig 4.7 B*) mutants. Moreover, the apparent ratio of correctly folded to misfolded protein was greater for desensitization mutants (as determined from an equivalent or stronger band intensity for DDM versus FC-12 extraction). This is most obvious for receptor bearing the G258A (4' M2) mutation. These results should however be viewed cautiously; typically multiple constructs/detergent conditions are screened per experiment, and whilst starting material is split equally between samples, there is no further normalization of (total) protein loaded onto the gel. SDS-PAGE analysis does however provide a "rough" assessment of extraction-purification efficiency and viral-titre (in a manner that is less time consuming or error prone when compared to western blot analysis).

In choosing candidate mutants for further detergent screening and analytical scale-up experiments, we focused on those exhibiting most pronounced (non-) functional effects (and thus stabilized in a distinct conformation). We therefore focused initially on the V251F α1 subunit mutation. The V251F (-3' M2) mutant is electrophysiologically non-functional in *Xenopus* oocytes (*Chapter 3*), but is expressed at the cell surface (as determined by rescue experiments and fluorescent imaging). Small-scale screening in insect cells shows strong expression and purification (of a largely correctly folded population) of receptors. Expanded small-scale detergent screening reveals that the receptor is efficiently extracted by DDM and DMNG and to lesser extent by DDM/CHS, LMNG and $C_{12}E_9$.

In preliminary analytical scale-up experiments (starting from increased biomass) we chose to detergent extract mutant receptors in DDM with CHS. Given the profound effect of CHS in stabilizing the apparent pentameric form of non-mutant bearing chimera, we postulated that it would likely have a beneficial stabilizing effect on mutant receptors. It should be noted that later in the purification, during SEC, we excluded CHS. Following affinity purification of solubilized protein, we further purified material by size-exclusion (*Fig 4.7 C*). Mutant receptors eluted predominantly in a single monodisperse peak at a (column) volume of ~15ml; the expected elution volume of a pentameric form of the receptor. A minor peak corresponding to the void volume, and small "shouldering peaks" to the major elution species were observed, though to a lesser extent than observed for the non-mutant chimera. Reassuringly, SDS-PAGE and coomassie stain revealed that material from the major peak fractions migrates as a single homogenous band, and would suggest that the receptor is of high-purity. Ultimately, this encouraging result provided us with a starting point, a stable receptor, from which we could begin to optimize large-scale expression and purification for further structural studies.

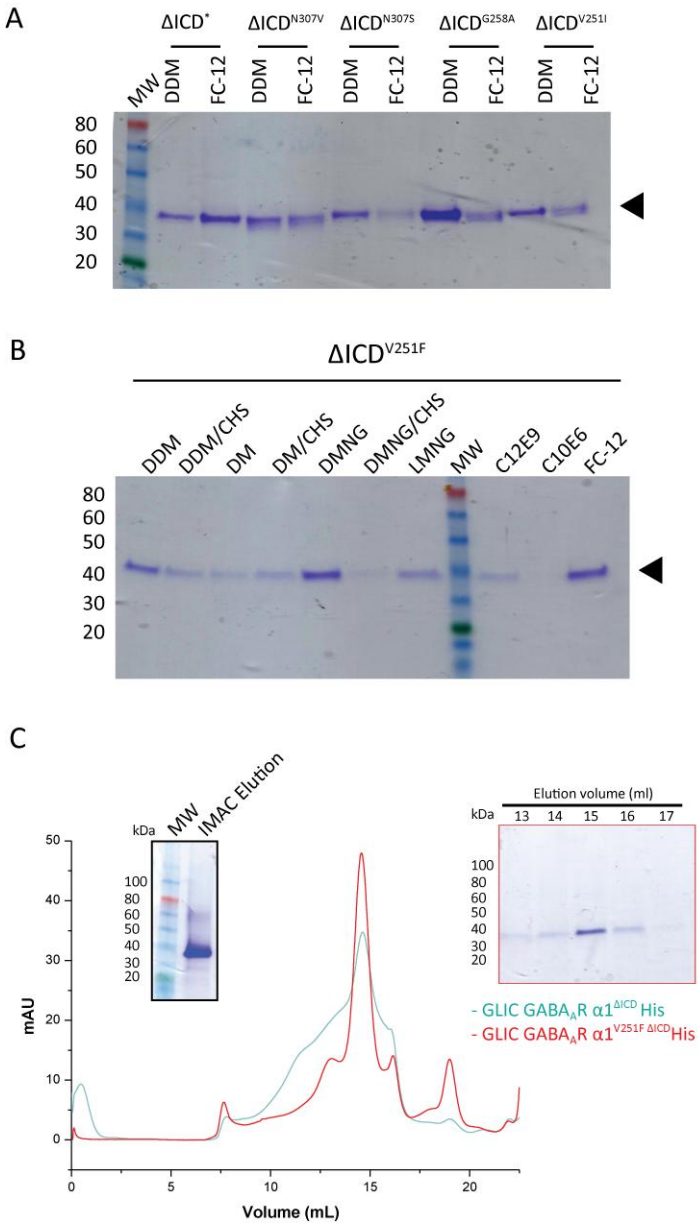

Figure 4.7 - Small-scale detergent screening of desensitization mutant GLIC-GABA$_A$R α1$^{\Delta ICD}$His and analytical scale protein purification of GLIC-GABA$_A$R α1$^{V251F\ \Delta ICD}$His

A.Coomassie-blue stained SDS PAGE of affinity purified mutant chimera following detergent screening with DDM or FC-12. The chimera (ΔICD is GLIC-GABA$_A$R α1$^{\Delta ICD}$His) without or with desensitization mutations and detergents used in the solubilization are shown above each lane. Arrowhead denotes a prominent band at ~39 kDa corresponding to monomeric chimera subunit. **B.**Coomassie-blue stained SDS PAGE of affinity purified V251F mutant chimera following expanded detergent screening. **C.**Stabilizing effects of V251F mutation assessed by size exclusion chromatography. Receptor solubilized in DDM/CHS was affinity purified and further purified by SEC (in DDM). The V251F mutation (red trace) dramatically enhances presumed pentameric form (elution volume of ~15 ml) of the chimera in DDM micelles. SDS PAGE analysis of affinity purified receptor **(Inset, left)** and of material from peak elution fractions, which runs as homogenous band of ~39 kDa **(Inset, right)**.

4.2.6. Preparative scale purification of a "desensitization mutant" GLIC-GABA$_A$Rα1$^{V251F\Delta ICD}$His chimera

Having established that a chimera bearing the V251F mutation exists in a largely monodisperse state in DDM (with CHS), we began to prepare sufficient quantity of the receptor for crystallization trials. After optimization of "scale-up" experiments, we were consistently able to express and purify appreciable yields of pure receptor (0.2-0.3 mg/L). Gel filtration profiles of purified receptor reveal that the predominant pentameric peak and minor shouldering peaks observed in preliminary purifications are not in dynamic equilibrium (and thus, critically, the receptor pentamer forms a stable complex in detergent; *Fig 4.8 A*). For crystallization and further experiments, peak fractions were collected, pooled and concentrated using 100 kDa molecular weight cut-off (MWCO) ultra centrifugal filter devices. Theoretically, these devices should exclude "free" detergent micelles (typically ~70 kDa for DDM), however, it has been reported that even with appropriate molecular weight cut-off, detergent concentration typically increases two-fold. In initial purification experiments we observed that for final gel filtration steps, the exclusion of CHS had no detrimental effect on receptor stability (presumably sufficient levels of CHS are incorporated into and retained in detergent micelles following initial solubilization). Later studies suggest that it is might be beneficial, when extracting receptors in DDM, to also include CHS during the final purification steps.

4.2.7. Sequence and oligomeric analysis of GLIC-GABA$_A$Rα1$^{V251f\,\Delta ICD}$His using mass spectrometric techniques

As for the previous purifications, it was important to ensure that the purified material corresponded to our chimeric receptor. SDS PAGE and coomassie stain (and additionally western blotting; data not shown) consistently revealed that peak fraction migrated as a single, homogenous band of the expected mass for the receptor subunit (under reducing conditions). Reassuringly, band excision and in-gel tryptic digest for mass spectrometric analysis generated sufficient peptides for coverage of greater than 50% of the primary sequence (*Fig 4.8 B*).

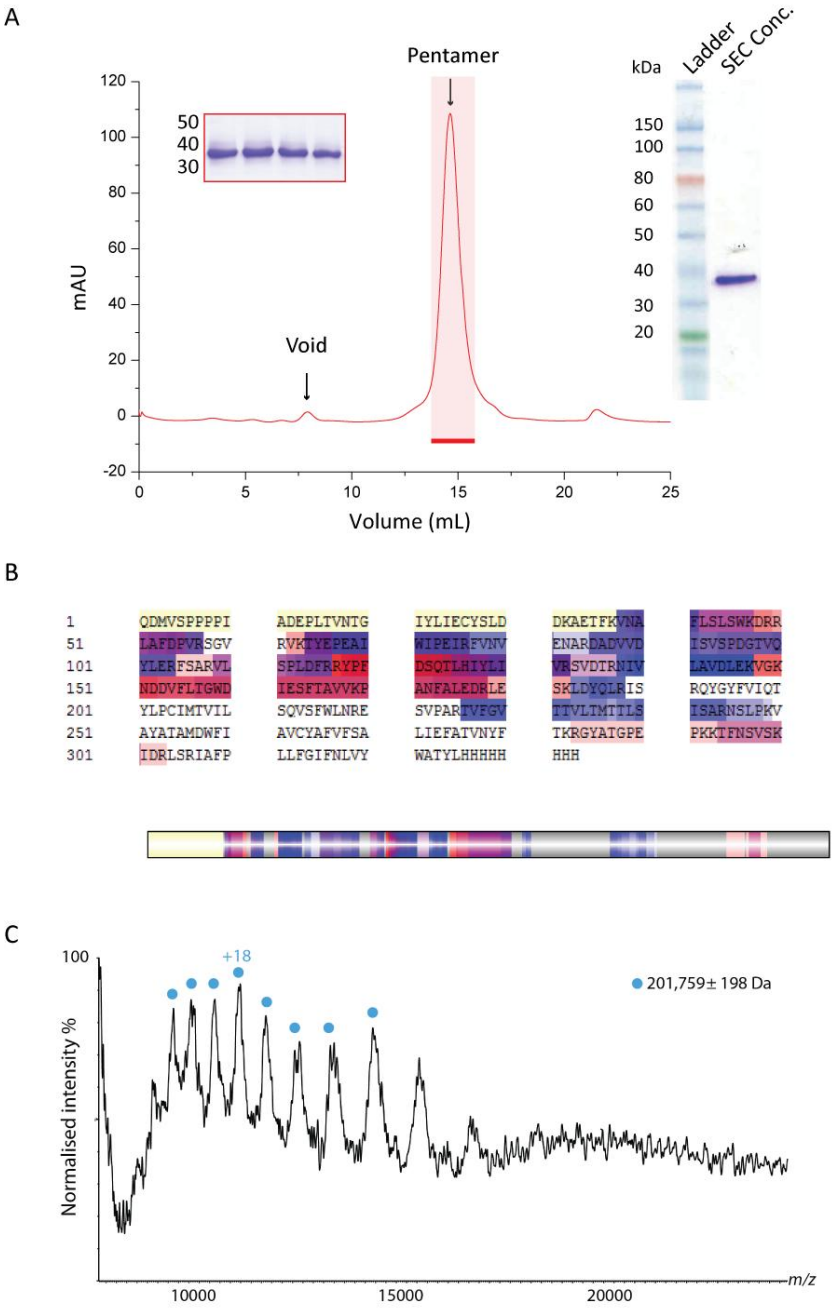

Figure 4.8 - Preparative-scale purification of V251F mutant of GLIC-GABA$_A$R α1$^{\Delta ICD}$His, sequence and oligomerization analysis by mass spectrometric techniques

A.Size exlusion chromatography profile of purified GLIC-GABA$_A$R α1$^{V251F\ \Delta ICD}$His(Extracted: DDM/CHS & SEC: DDM). Major peak of pentameric receptor-detergent complex is shaded red, and was pooled for concentration. **Inset, left:** Coomassie-blue stain/SDS PAGE of material from peak fractions, which was pooled and concentrated. **Inset, right;** Final purified receptor runs as a homogenous single band by SDS PAGE (under reducing conditions). **B.** Colour map of the peptide fragments (on receptor chimera primary sequence) identified by MS analysis (following gel band excision and tryptic digest). **C.** Mass spectra of V251F chimera (from native MS experiments) following collision-induced release of detergent. Blue circles denote charge states used to calculate experimental mass of 201.6 kDa.

Though the gel filtration profile of the mutant chimera is consistent with that of a receptor in a pentameric form (5 subunits totaling ~200 kDa in mass) in complex with detergent molecules (being of comparable elution volume to two homologous channels purified in DDM; $GluCl_{cryst}$ (*Fig 4.5 C*) and cleaved WT-GLIC, introduced in *Chapter 5*), we wanted to assign a definitive oligomeric state to the purified material. Typically, size-exclusion molecular weight standards are used in comparative experiments of elution volume to infer the mass of a purified protein. A caveat to these experiments is that mass standards are typically soluble proteins and will not experience the same effects that detergent-association has on a membrane protein (i.e. altering their hydrodynamic radius). An effect of this is to alter the interaction of membrane protein-detergent complexes with the gel-filtration matrix and subsequent retention time and elution volume.

To obviate the qualitative low-resolution data that SEC provides, we used native mass spectrometry to determine with precision the oligomeric state of the chimera complex. Native mass spectrometry (though technically challenging) can provide accurate assessment of membrane protein complex composition, as well as small molecule and lipid binding. With regards to protein complex composition (and mass), native mass spectrometry provides greater accuracy in calculating mass when compared to more widely adopted techniques including analytical ultracentrifugation. In preliminary experiments carried out by Adam Cryar and Kostas Thalassinos (UCL ISMB), mass spectra were generated for the intact chimera receptor complex following introduction in to the gas phase and release of detergent molecules (*Fig 4.8 C*). Using a series of charge states (observed in the mass spectrum) an experimental mass was calculated. The experimental mass of 201.76 kDa is greater than the theoretical mass of 198.73 kDa by 3.03 kDa, but would demonstrate unequivocally that the chimera does indeed form a pentamer (in DDM). The additional mass may represent bound lipids (present in the insect cell membrane) or detergent/CHS molecules (from purification) that are not released by gas phase collisions.

4.2.8. Preliminary screening of crystallization of GLIC-GABA$_A$R α1$^{V251F\ \Delta ICD}$His receptors

The mutant chimera purified in DDM/CHS (solubilization) and DDM (SEC) was taken forward to crystallization screening. The initial assumption was that crystallization conditions previously reported for WT-GLIC would also allow for crystal formation of the chimera. Presumably, crystal growth would exhibit similar packing contacts primarily between copies of the ECD; a common domain between GLIC and the chimera. However, membrane protein crystallization rarely follows such predictable rules, and often proteins of similar structure require completely different and unique crystallization conditions. In parallel to screening previously published "GLIC crystal growth" conditions we used sparse matrix screening of crystallization conditions in order to identify new buffer compositions, which might yield protein crystals. Whilst we were able to generate an appreciable amount of purified protein, limitations of starting culture volume and final yield meant that a single purification was often only sufficient for setting three or four 96 well-format crystallization plates (using drop sizes of 200 nl; 1:1 protein: reservoir or 150 nl 2:1 protein: reservoir). Full details of crystallization procedures and screens are given in Material and Methods.

Initial screens identified only 3 conditions capable of supporting crystal growth. Of these conditions; two allowed for reproducible crystal growth whilst one was not reproducible (*Table 4.1*). Whether this highlights preparation-to-preparation variability in the purification process is unclear. Reproduction of crystal growth was tested by means of a grid screen around the initial "crystal hit" (as detailed in Methods *Section 2.7.3*). Curiously one of the "hits" was of conditions used previously in the crystallization of WT GLIC. Whilst GLIC robustly forms large parallelepiped (a prism with parallelogram faces) or plate-shaped crystals (see Chapter 5), chimeric receptors formed showers or clusters of small needle-type crystals (typically <50 µm in the longest axis; *Table 4.1*). This size of crystal is not amenable to analysis using "in-house" X-ray sources and CCD detectors. Further optimization allowed for generation of larger rod shaped crystals (by vapour diffusion in hanging drops). However, screening of crystals by synchrotron-radiation source revealed these were detergent based, and not protein crystals; a commonly observed problem in membrane protein crystallization.

The remaining crystal growth "hit" was a peculiar one, on account of its buffer and precipitant composition. Growth was supported in MOPS (3-(*N*-morpholino) propanesulfonic acid) buffer (pH 7-8) with small quantities of a high molecular weight Poly(ethylene) glycol (PEG-8000). Small cuboidal crystals (<30 µm) appeared 1-2 days after setting drops (*Table 4.1*). The lack of further salt solution addition to support crystal growth was surprising as was the use of a large molecular weight PEG (when low MW PEGS, e.g. PEG 400, have typically proved more successful for α-helical membrane protein crystallization; Carpenter et al., 2008; Parker and Newstead, 2012). Of greater interest was that crystals formed at pH 7-8. Given that the chimeric receptor is proton gated, the pH of a crystallization condition likely influences the receptor conformation (as shown by Sauguet et al., 2014b). Whilst GLIC robustly crystallizes at low pH (in open and locally closed-conformations; Bocquet et al., 2009; Hilf and Dutzler, 2009; Sauguet et al., 2014b), growth at neutral pH in resting conformations has proven more elusive. It was therefore encouraging that chimera crystal growth could be supported at neutral pH.

Given the small size of crystals, they were best suited to diffraction charactertisation by microfocus beamline (tunable to a beam size of 10 µm x 10 µm). Chimera crystals diffracted maximally to ~25 Å, revealing diffraction spots consistent with crystals formed from protein. This served as a starting point from which to further optimize crystal growth. However, subsequent additive screening with detergents (Detergent Screening HT Hampton) and compounds known to improve membrane protein crystallization (MemAdvantage^{TM}, Molecular Dimensions) failed to improve crystal growth or diffraction. Given this outcome, we chose to re-assess our protein purification procedures prior to crystallization.

4.2.9. Refined purification and crystallization screens for GLIC-GABA$_A$R α1$^{V251F\ \Delta ICD}$His

To this stage, protein extraction and purification had been carried out in DDM (with CHS). Our initial choice of detergent had been influenced by previous use within the

pLGIC channel field (GLIC and $GluCl_{cryst}$ were both purified in DDM for crystallization). Furthermore, solubilization by alkyl maltopyranosides had accounted for more than half of successful membrane protein crystallizations, with DDM the most commonly used (Parker and Newstead, 2012). However, the latter trend is drawn from studies of all membrane proteins and we cannot easily assume that a single detergent, DDM, will yield crystals that diffract to high resolution for all pLGICs. Given that the starting sample for crystallization drop is protein and associated detergent, it is inherent that the choice of detergent will have a vital role in crystallization success. We therefore re-assessed the choice of detergent (and cholesterol) in which our chimeric receptor was purified.

Preliminary small screens had identified efficient extraction of protein by DMNG. DMNG is a member of a new class of detergent amphiphiles, maltose neopentyl glycols (MNGs) that have been shown to exhibit favorable stabilizing and crystallization properties when compared to conventional detergents (Chae et al., 2010). Preliminary scale-up experiments showed that the extraction efficiency of the chimera from insect membranes by DMNG was lower than anticipated. Given this, we used an alternative strategy to assess chimera stability and crystallization in DMNG, through introduction of a detergent exchange step during the latter stages of purification. This exchange approach has been proven beneficial in the successful crystallization of other ion channels (a bacterial voltage-gated sodium channel, NavM and an NMDAR; Bagnéris et al., 2013; Lee et al., 2014). DDM/CHS solubilized chimera was bound to Co^{2+}resin and washed extensively with buffer comprising DMNG/CHS, prior to elution and final purification by SEC in buffer supplemented with DMNG (once again CHS was excluded in the belief it might hinder crystallization). Purified receptors elute in a largely monodisperse state, as a symmetrical peak of expected elution volume (*Appendix Fig 5B*). In addition to a peak corresponding to the column void volume, a smaller defined shouldering peak was observed. However, “re-running” fractions of the major peak revealed that the presumed pentameric species (retaining a symmetrical peak eluting at ~14.5 ml) was not in dynamic equilibrium with this higher mass species. The protein was concentrated and crystallization trials carried out as previously described.

Crystallization screens yielded three new conditions capable of supporting crystal growth (two of which were similar to those previously reported for GLIC; *Table 4.2*).

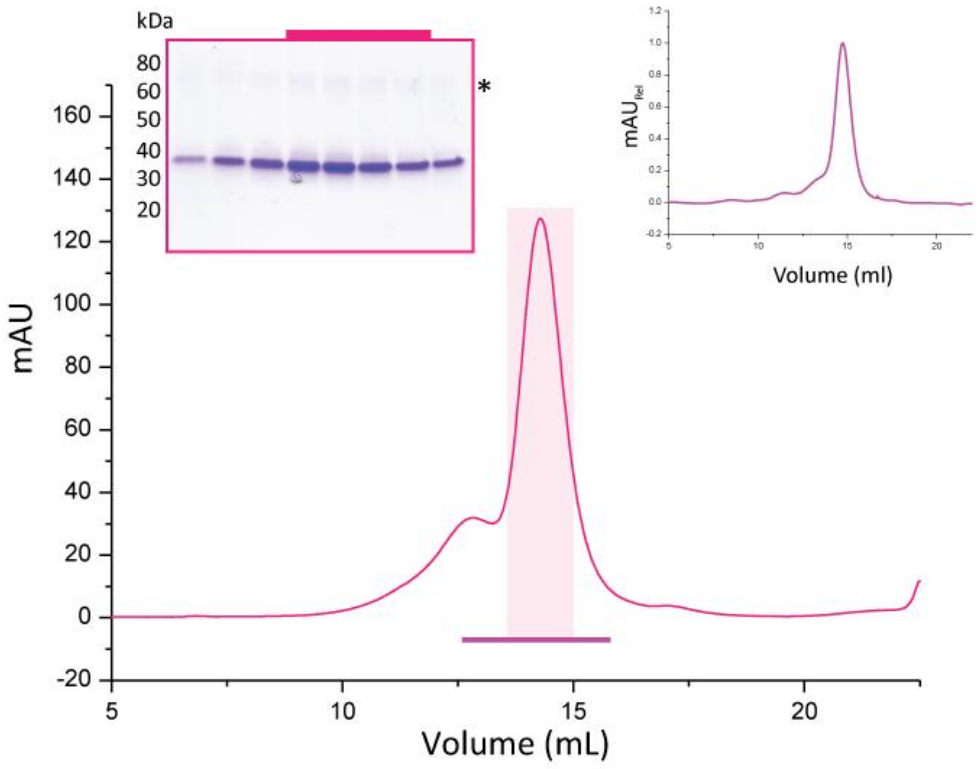

Figure 4.9 - Preparative-scale purification of GLIC-GABA$_A$R α1$^{V251F\ \Delta ICD}$His following detergent exchange in to DMNG/CHS.

A.SEC profile of purified GLIC-GABAα1^{V251F} (Extracted: DDM/CHS & exchanged in to DMNG/CHS). Major peak of pentameric receptor-detergent complex is shaded pink, and was pooled for sample concentration. **Inset, left:** Coomassie-blue stain/SDS PAGE of material from peak fractions (horizontal bar below SEC trace), Peak fractions (solid bar above gel and shaded section of SEC trace) were pooled and concentrated. Asterisk at high MW indicates SDS-resistant dimer of chimera subunits. **Inset, right;** Final purified receptor runs as a symmetrical monodisperse peak following storage 4°C for 48 hrs.

Table 4.1 Crystallization of GLIC-GABA$_A$Rα1$^{V251F\ \Delta ICD}$His (DDM/CHS)

Condition	Drop Composition	Further screening	No. condition screened	Crystal properties	Max Diffraction
MemGold2 G4	0.1M MOPS pH 7.0 9% PEG 8000 16°C/SD	4°C growth Detergent HT Screen Neurosteroids Lipid	~400	20 x 20 x 10 µm 	20-30Å
GLIC (Nury et al., 2011)	0.1M NaAc pH4.5 11-16% PEG 4000 375-450 mM NaSCN	Detergent HT Screen	~200	<10µm 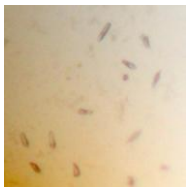	N/A
MemStart/ Sys E3	0.1M NaCit pH4.5 30% PEG400 0.1M NaCl 0.1M $MgCl_2$	16°C Broad Screen	96	N/A	N/A

Table 4.2 Crystallization of GLIC-GABA$_A$Rα1$^{V251F\ \Delta ICD}$His (DMNG/CHS)

Condition	Drop Composition	Further screening	No. conditions screened	Crystal properties	Max Diffraction
MemGold H4	0.1M NaCit pH3.5 28% PEG 400 0.2M $LiSO_4$	4°C growth Mem-Advantage	~300	50 x 20 x 20 µm 	15-20Å
MemGold2 E9	0.1M NaAc pH4.0 16% PEG 4000 0.2M $(NH_4)_2SO_4$	4°C growth Mem-Advantage	~300	100 x 20 x 20 µm 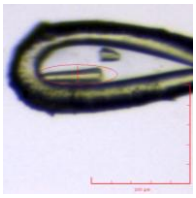	9-15Å
MemGold2 F5	0.1M NaCit pH3.5 16% PEG 4000 0.34M $(NH_4)_2SO_4$	Broad Screens	~200	80 x 20 x 20 µm 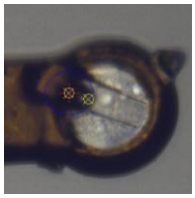	15-20Å

Crystals were typically rod shaped, and exhibit increased size (in longest axis) when compared to those grown from chimera purified in DDM/CHS. Furthermore, crystallization was only observed in drops buffered to low pH (presumably channel activating proton concentrations). One condition (MemGold-2 H4) was capable of supporting the growth of two distinct crystal forms; rod/needle or tetragonal crystals. Intriguingly, screening crystal diffraction revealed diffraction to ~15-20 Å of the latter tetragonal form, whilst rods/needles did not diffract (*Table 4.2*). This would suggest distinct properties regarding the order of receptor packing in the two crystal forms.

Encouragingly, the other two crystallization conditions also revealed protein diffraction following broad grid screens of "crystallization reproducibility" (maximally diffracting to ~15-20Å; *Table 4.2*). Initial efforts to carry out additive screening proved unsuccessful (additional chemicals having apparently detrimental effects on crystal growth).

In parallel to optimizing crystallization of receptors in DMNG by grid screens (from initial conditions), we also assessed the effect of including CHS (at 0.001%) in final size-exclusion purification steps. Unsurprisingly, given the stabilizing qualities of CHS, receptors purified in a largely monodisperse state, showing no elution of aggregated material (column void volume) and substantial reduction in the previously observed shouldering peak (*Fig 4.9*). Material from the symmetrical peak at ~14.5 ml retained its elution profile in subsequent chromatographic analysis (following storage at 4°C for 48 hrs) and ran as a homogenous band by SDS-PAGE and coomassiee stain (a faint higher mass band corresponding to an SDS-resistant dimer can be observed).

Crystallization of receptors under the 3 newly identified conditions was reproducible in grid screens. Furthermore, crystals grown in MemGold-2 E9 were of an increased size (50-100 µm in longest axis) and preliminary diffraction assessment revealed an improvement in maximal diffraction to ~11Å (*Table 4.2*). In order to fully characterize crystals we used a microfocus beamline (for improved crystal alignment relative to beam centre, beam intensity and for assessment of diffraction in various parts of the crystal).

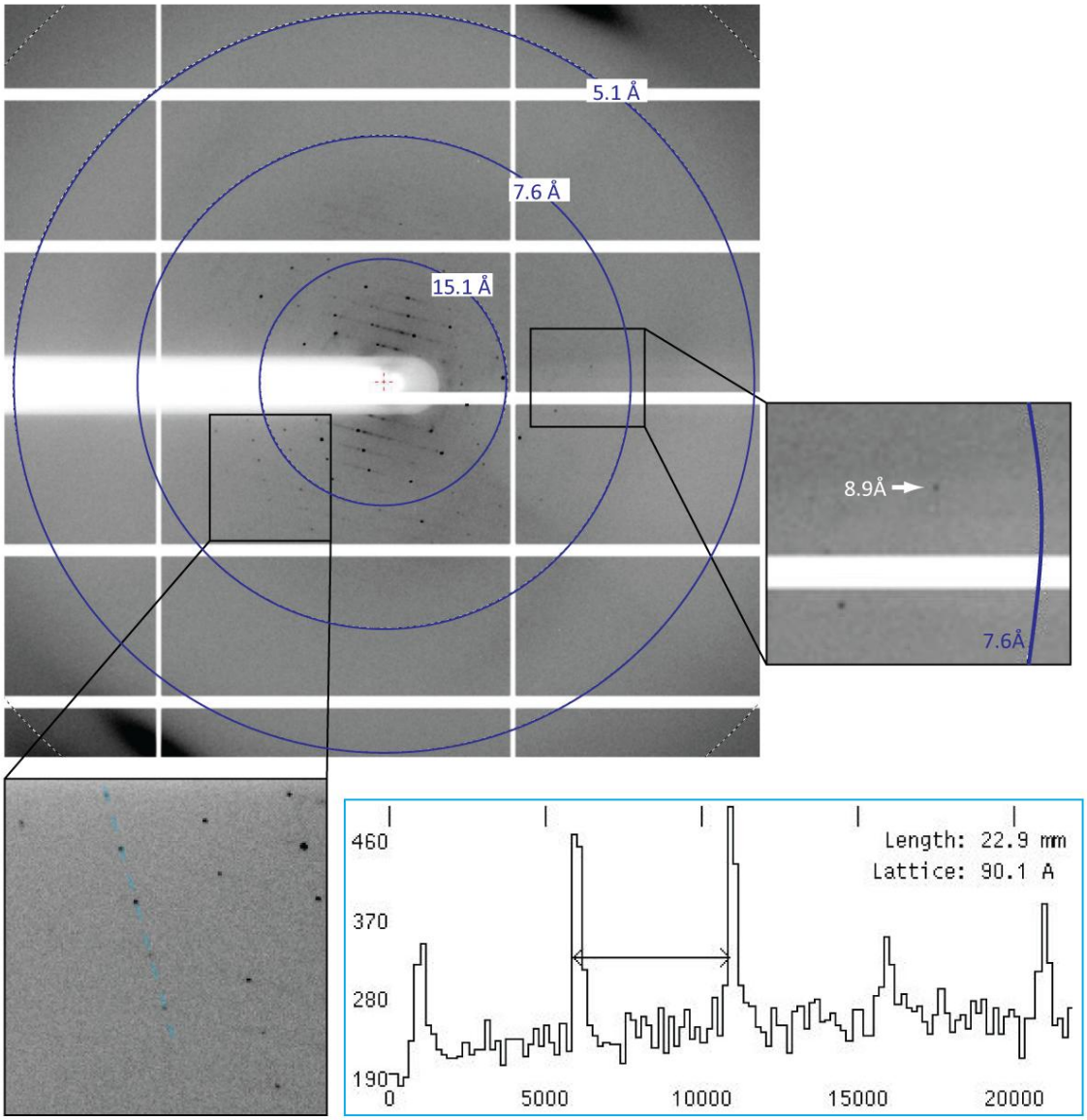

Figure 4.10 - X-ray diffraction pattern for crystals of GLIC-GABA$_A$R α1$^{V251F\ \Delta ICD}$His: DMNG-CHS complex by microfocus beamline.

X-ray diffraction pattern (0.5° oscillation range) for a crystal of GLIC-GABAα1^{V251F} in the presence of DMNG and CHS (by microfocus beamline, ESRF ID23-2). Resolution rings at ~15Å and 7.6Å are shown as blue circles and a faint diffraction spot near the resolution limit (of 8.9Å) is highlighted by a box **right**. **Lower panel** is a magnified section of the diffraction pattern and shows a section through a series of diffraction spots. A plot of intensity through these spots reveals ordered spacing of peaks in the diffraction pattern (and presumably in the crystal lattice).

By microfocus (beamline ID23-2, ESRF), using grid scans to align crystals, chimera crystals diffracted maximally to 8.9Å and showed well-ordered crystal lattice (*Fig 4.10*). Despite this improvement, crystals exhibited anisotropic diffraction (a possible consequence of disproportionate growth along one axis). Consequently, and due to limited diffraction resolution, we have been unable to assign a three-dimensional space group to these crystals. A final point of note is that crystallization of the chimeric receptor in MemGold-2 E9 and MemGold-2 F5 (following grid screen optimization) has supported the growth of two distinct crystal forms; typically 2D plate-form and rod-shaped crystals. Further efforts are underway to fully characterize the different diffraction properties of both crystal types.

4.2.10. Thermal stability assays to determine the effect of detergents on the chimera

Whilst the generation of crystals diffracting to beyond 10Å represents an appreciable achievement, we were ultimately no closer to our goal of producing a high-resolution structure for the $GABA_AR$ α1 TMD. We therefore sought to take a rational high throughput approach to screening detergents during the pre- and early-crystallization stages. Pre-crystallization screening provides information that can guide both purification and crystallization. One such technique (developed by Alexandrov et al., 2008) harnesses the fluorescent signal generated following covalent modification of Cys residues by a thiol specific fluorochrome, N-[4-(7-diethylamino-4-methyl-3-coumarinyl)phenyl]maleimide(CPM), that occurs upon temperature induced protein unfolding (*Fig 4.11 A*). The thermal stability of a purified membrane protein in a range of detergents and small molecules can then be assessed rapidly and efficiently, providing information that might assist in optimizing final purification steps and crystallization. One of the major advantages of the CPM assay is that it requires very little material, less than 5 μg of protein (per sample), which is important where protein yield is a limiting factor.

A major limitation of this assay is that it requires Cys residues to be located within the transmembrane core of the target protein. We postulated that this might not be problematic for our chimeric receptor. Sequence analysis and homology modeling reveals three Cys-residues per subunit (15 per pentamer). One lies within the GLIC ECD, and is buried within the quaternary structure at the subunit-subunit interface, and two are in the TMD of α1 subunits, within the helical bundle in M1 and M3 (possibly forming a stabilizing disulphide bridge). The latter Cys-residues form strong candidate reporters of thermal-induced under folding, suited to the CPM assay.

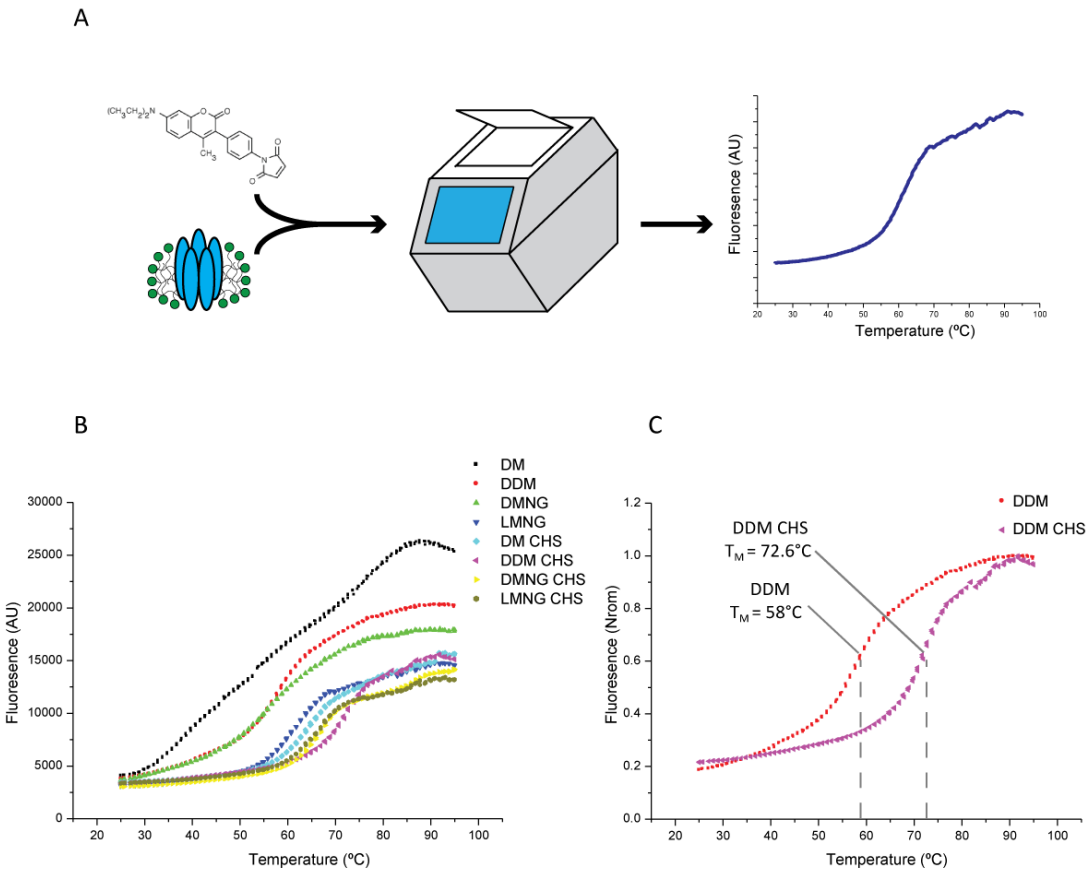

Figure 4.11 - Effect of detergents on GLIC-GABA$_A$R α1$^{V251\ F\Delta ICD}$His thermal stability

A. Purified chimera-detergent complex is mixed in various detergents and with CPM reagent. Fluorescence is monitored during temperature ramp in RT-qPCR apparatus, and a melting curve generated. **B.** Melting curves for mild alky-maltoside and MNG detergents. **C.** Fluorescence normalized melting curves for receptor in DDM and DDM/CHS shows shift in melting transition. A Boltzmann equation fit of the data was used to generate a T_m for DDM (T_m = 58°C) and DDM/CHS (T_m = 72.6°C), revealing a 14.6°C shift in T_m upon addition of CHS.

CPM assays were carried out in a 96 well plate format, with a RT-qPCR machine to monitor fluorescence over a ramp in temperature from 25°C to 95°C (1°C increments). The V251F-mutant chimera (purified in DMNG/CHS) was mixed with a range of detergents and CPM reagent and a melting temperature (T_m) calculated (*Fig 4.11 A*). The raw data (*Fig 4.11 B and Appendix Fig 6)* for a panel of detergents screened shows considerable variability in the maximum fluorescence intensity (representing the end of the unfolding process*)*.

Since an equal amount of protein was used per sample, this is not easily explained by varying amounts of receptor in starting sample. It is more likely to represent the ability or inability of a detergent to protect the protein from both unfolding and aggregation. For the purpose of our study we have assessed the shape and slope of curve (representative of the unfolding transition) to calculate a T_m (*Table 4.3*). As might be expected, harsh destabilizing detergents including OM and LDAO have a melting transition occurring at relatively low temperatures and reach a high maximum fluorescence intensity (presumably providing little protection to unfolding). CHS is able to improve stability, as implied by a shift in the melting transition. Of the Cymal family of detergents, only Cymal 7 in combination with CHS exhibits a melting curve and T_m comparable to that of the favoured mild detergents (e.g. alky maltopyranosides and maltose neopentyl glycols; *Table 4.3* and *Appendix Fig 6*).

Assessing the results for commonly used mild detergents revealed a number of intriguing observations. Consistent with results inferred from our SEC experiments and initial crystallization, CHS has a dramatic effect on the stability of the chimera, inducing a rightward shift in the melting transition curve (and thus increase in T_m) for all detergents tested (*Fig 4.11 B and* Table 4.3). This is most apparent for DDM, with a 14.6°C increase in melting temperature (*Fig 4.11 C*). It should be noted that in crystallization screens of DDM purified chimera, we omitted CHS at the final purification stage. The results from CPM assays would suggest that this might in fact have had a destabilizing effect, affecting crystal formation. Unsurprisingly the shorter alkyl-chain of DM has a destabilizing effect, however addition of CHS dramatically alters the onset of melting transition and reduction in fluorescence intensity of the upper plateau.

Table 4.3 Thermal stability of GLIC-GABA$_A$R α1$^{V251F\ \Delta ICD}$His in various detergents assessed by CPM Assay

	Melting Temperature/T_m(°C)	
Detergent	**-CHS**	**+CHS**
DM	46.6	64.3
UDM	51.5	68.8
DDM	58.0	72.6
DMNG	55.6	66.9
LMNG	61.9	67.1
OGNG	47.0	67
OM	32.3	57.3
LDAO	37.4	47.9
$C_{12}E_8$	53.2	58.7
Cymal 6	43.5	63.0
Cymal 7	55.0	66.4

A Boltzmann equation was used to fit the fluorescence data and generate T_m values. Raw data (Appendix Figure 6) were visually inspected during the data fits to ensure that the calculated T_m represent a "true" melting transition (and not of potential experimental artifact which might be observed at >80°C). Note: each fluorescence data point at 1°C temperature increments was recorded 3 times and then averaged.

DMNG exhibited similar results to DDM, with a pronounced rightward shift in the melting transition curve. This result is consistent with gel filtration experiments (showing reduced aggregation and increase in the proportion pentameric species) and improved diffraction of crystals grown for receptor purified in DMNG/CHS versus DMNG alone (during final SEC purification step). Surprisingly, LMNG (; the conventional detergents for comparison are UDM and DDM) gave similar thermal stability results in the presence and absence of CHS, providing a similar T_m to its shorter chain

counterpart, DMNG (with the inclusion CHS). These assays thus allow for rapid ranking of detergents, based on their ability to stabilize the chimera, and provide a rationale for specific detergent exchange steps prior to crystallization. Immediately it is clear that maltopyranosides and maltose neopentyl glycols are more stabilizing, and that this is further improved by the addition of CHS (*Fig 4.11 B*). This is in agreement with the development of our purification (and crystallization) procedure, where we have empirically selected DDM and then DMNG/CHS for receptor purification.

4.2.11. Negative-stain electron microscopy of GLIC-GABA$_A$R α1$^{V251F\Delta ICD}$His

Whilst CPM assays clearly provide a rapid screen for ranking detergents based upon thermostabilizing properties, it does not provide clear information regarding aggregation state of the chimeric receptor. Direct visualization of the channel complex by electron microscopy provides low-resolution structural information and, crucially, reveals the propensity for aggregation. Furthermore, as alluded to above and in Chapter 6, cryo-EM is rapidly developing as a rival technique to X-ray crystallography for structure determination (Cheng, 2015; Cheng et al., 2015). Since the chimeric receptors generated for crystallization are likely to also be suitable for structural analyses by EM, we were keen to assess both the quality of our purified receptor preparations and their preferential orientations by negative-stain EM.

Negative-stain EM images of chimera in DMNG/CHS were collected by Dan Clare (Birkbeck, University of London) on a Tecnai T10 at 44,000x magnification (*Fig 4.12*). The sample was largely monodisperse, with single receptor particles observed across all sections of the carbon-coated grid (with only few clusters of “receptor-doublets”). This is consistent with the monodisperse state of the protein by SEC (*Fig 4.12 A & B*). As anticipated, EM revealed, for the first time, that the receptor purified in DMNG/CHS exists as an intact (pentameric) channel. Particles clearly resembled rosettes (of subunits around a central pore), reminiscent of a pentameric pLGIC. With regards to particle orientation, the sample is largely homogeneous, with receptors apparently adsorbing to the carbon film in a preferential “end-on” orientation (i.e., observing the

channel in a plane view from above or below). Despite this, closer visual inspection of collected images reveal protein in multiple distinct orientations, most likely assigned to receptors in "side-on" or "tilted" orientations (*Fig 4.12 C*). Preliminary studies reveal that occupation of receptor particles in "side-on" orientations may be by dependent upon the surface charge of EM grids (following poly-lysine treatment). The orientation of protein particles bears substantial importance with regards to high-resolution cryo-EM studies, and negative-stain will serve as a vital tool in screening specimen preparation in further studies.

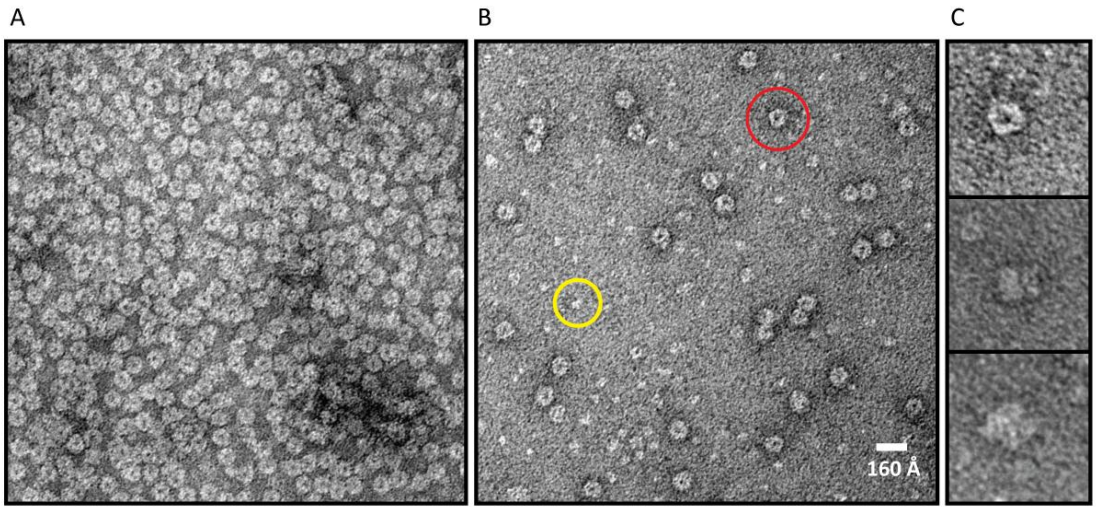

Figure 4.12 - Negative-stain EM of GLIC-GABA$_A$R α1$^{V251F\ \Delta ICD}$His following detergent exchange in to DMNG/CHS.

A. Negative-stain EM images of purified V251F chimera (in DMNG/CHS) at high concentration. **B.** Negative-stain EM images of purified V251F chimera following ten-fold dilution. In both cases receptor was applied to an EM grid covered in a continuous carbon film and stained with uranyl acetate. Receptors typically adsorb to the carbon film in an "end-on" orientation (red circle, B, is a representative end view of receptor particle). Free detergent-CHS micelles are highlighted by yellow circle. **C.** Panels show magnified selection of receptor orientations (Top; end view. Centre and lower panels show side or tilt views, acquired with poly-lysine coated EM grids).

A notable observation from preliminary negative-stain EM studies was the presence of additional small background particles in chimera preparations (*Fig 4.12 B*). Given that grids were prepared using material previously stored at -80°C (following flash freezing in liquid nitrogen) we were concerned that this might represent protein degradation (potentially dissociated subunits). However from the high $T_m$observed in CPM assays and EM images of grids prepared at higher protein concentrations, this seemed unlikely. Negative stain images of gel filtration buffer alone (including DMNG/CHS at the relevant concentration used in final SEC step) revealed a similar dispersion of small particles. Whilst this buffer was not prepared fresh on the day of imaging, we might be confident from this observation that the chimera is not undergoing degradation, and observed particles most likely represent DMNG/CHS micelles. It might therefore be concluded that during final purification, free detergent-cholesterol-micelles are formed and carried over into the final receptor preparation (*Fig 4.12 B*). Such events would not be apparent from SEC monitored by UV detection alone, but would be revealed by SEC-MALS (Multi-Angle Light Scattering) which provides a measure of the ratio of free detergent micelle: protein detergent complex in a sample. The observation of free detergent micelles in a sample taken forward to crystallization might also explain the limited diffraction observed in X-ray crystallography experiments of the chimera. Detergent molecules not associated in a protein complex are likely to hinder crystal-packing formation. In addressing this issue we might potentially reduce the concentration of detergent and CHS used in the final chromatographic stages of purification.

4.3. Discussion

After establishing that a functional chimeric pLGIC between the ECD of GLIC and TMD of $GABA_AR$ can be formed that retains the typical $GABA_AR$ α1 subunit TMD pharmacology and gating mechanism, in this chapter we sought to assess its suitability for high level expression and purification for X-ray crystallography. At the start of this study, high-resolution structures of pLGICs (and the associated purification strategies)

existed only for GLIC, ELIC and GluCl (Hilf and Dutzler, 2008; Bocquet et al., 2009; Hilf and Dutzler, 2009; Hibbs and Gouaux, 2011). Of these receptors, GLIC and ELIC are of prokaryotic origin. Information on how to purify and solve the structure of a eukaryotic pLGICs was distinctly lacking. Having established early on that bacterial expression of our chimera was not possible, we had to draw on techniques and methods from across the membrane protein field to guide development of a purification strategy. During this time, a number of groups have successfully purified and crystallized full-length WT and chimeric pLGICs. The results of these studies have provided support for our empirically derived protocol, as well as new ideas, which we have incorporated into our study.

4.3.1. Receptor chimeras require a "sophisticated" membrane environment for stable expression

We reasoned, as others before, that a receptor chimera between prokaryotic and eukaryotic domains would be amenable to high level expression in bacteria. Whilst this has been possible in chimeras incorporating significant prokaryotic components (e.g. expression of the mammalian Kir3.1 potassium channel in *E. coli* required 75% of the TM pore to be replaced with the prokaryotic Kir equivalent; Nishida et al., 2007), for pLGIC domain switch chimeras this has yet to achieved. Indeed the structure of the GLIC-GlyRα1 chimera (which formed the rational basis for this study) was recently solved, using receptor purified from *Drosophilia* Schneider 2 (S2) cells, after finding that this chimeric receptor was refractory to expression in bacteria (Moraga-Cid et al., 2015). In our study we also found that a domain chimera with GLIC (GLIC-$GABA_AR$ α1) was poorly expressed in bacteria, yet expressed strongly and stably in the confines of a more sophisticated membrane environment provided by a higher order eukaryotic cell line (in this case Sf9 insect cells). Moreover, recently solved structures for human GABA β3 and mouse 5-HT_3homomeric receptors used material expressed and purified from stable eukaryotic HEK293 cell lines (Hassaine et al., 2013; 2014; Miller and Aricescu, 2014). Whilst these latter studies would suggest that a cell line of mammalian

lineage is essential for stable full-length receptor expression, more recent structural studies of zebrafish GlyR α1 and human GlyR α3 receptors have revealed that Sf9 cells are capable of supporting expression of correctly assembled receptors for detergent extraction and purification (Du et al., 2015; Huang et al., 2015). It is therefore apparent that Sf9 cells exhibit a plasma membrane that provides the lipid components that are broadly essential for stable expression of pLGICs, and more importantly, of our chimeric receptor.

4.3.2. A combination of genetic engineering and detergent stabilization are required for receptor purification

Insect cells provide a folding/assembly pathway and plasma membrane capable of expressing chimeric receptor proteins; however for crystallization, receptors must be extracted from these membranes and incorporated into detergent micelles as a stable pentameric complex. Although further studies need to be carried out to address stability in a wider panel of detergents, we have thus far found that commonly used mild-detergents (including DDM and DMNG) in combination with cholesterol hemisuccinate (CHS) are not completely sufficient to completely stabilize the "wild-type" chimera. Notably, CHS dramatically enhances receptor stability on detergent micelles. This is consistent with the notion that pLGICs, and $GABA_A$Rs in particular, are inherently dependent on cholesterol in maintaining structure and function under physiological conditions (Hénin et al., 2014). The enhanced stability in CHS was reminiscent of the GPCR adenosine A_{2A}receptor, in which binding of CHS at peripheral site(s) stabilized DDM-solubilized receptor for crystallization and structure solution (Jaakola et al., 2008). Studies of the GABA β3 homomer by Miller and Ariscescu (2014) subsequently validated our use of CHS during extraction and purification. Here stable purification of a closely related receptor was enhanced by the addition of CHS, allowing for eventual structure determination. The authors were apparently unable to observe or assign electron density to CHS (if directly bound), so the precise mechanism by which it stabilizes the β3 receptor remains unknown.

Where detergent solution alone is insufficient to stabilize a membrane protein, an alternative approach of genetic engineering to generate a thermostabilized protein has proved beneficial. Once again we drew inspiration from the GPCR field. Extensive work on the β_1-adrenergic and adenosine A_{2a} receptors has used alanine-scanning mutagenesis to identify thermostabilising mutations capable (in combination with agonists and antagonists) of allowing for successful receptor crystallization of receptors in distinct conformations (Warne et al., 2008; Lebon et al., 2011). In a similar vein we reasoned that incorporating gating mutants (desensitization mutations, see Chapter 3) into our chimera might bias the gating equilibrium such that a receptor could be trapped in a distinct conformation. If these represent inactive or closed channel states, then this might exhibit greater stability. Indeed introduction of the profound desensitization mutation, V251F in M2 helices of α1 subunits, was sufficient to dramatically improve the stability of the pentameric form of the chimera, allowing for eventual receptor purification and crystallization. This approach has been successfully applied to prokaryotic pLGICs. Gating mutants in the M2-M3 loop of GLIC, though electrophyiologically non-functional, could be crystallized to reveal receptors in a locally-closed conformation (Gonzalez-Gutierrez et al., 2013). Furthermore this approach proved essential in recent crystallographic studies of heterotetrameric NMDA receptors from *Xenopus laevis*, in which introduction of known desensitization mutations (from AMPARs) allowed for channel stabilization in detergent micelles and successful crystallization (Lee et al., 2014).

Equally one can rationalize at a functional level whether a receptor is likely to be amenable to expression, extraction and purification in detergent micelles. Thus far, chimeric receptors exhibiting a basal level of constitutive or spontaneous activity at neutral pH (as observed for non-mutant bearing receptors when assessed by electrophysiology) are not easily stabilized in detergent micelles. This might represent a potential toxicity effect when overexpressed in insect cells with receptor aggregation in the cell membrane (prior to detergent extraction). Whether extensive screening of detergents in the presence of cholesterol derivatives (e.g. CHS) and allosteric antagonists (e.g. pregnenolone sulfate) is sufficient to dampen this constitutive “noise”

and stabilize the receptor in detergent micelles for further structural studies remains to be seen.

4.3.3. Chimeric receptors yield weakly diffracting crystals

Thus far we have been unable to generate crystals that diffract to sufficiently high-resolution for structural determination. Whilst it is achievable, the extensive amount of screening (both crystal growth and diffraction) that is required reveals that this task is far from trivial. Recent crystallographic studies of GLIC at neutral pH revealed that only 1 in 1000 crystals diffracted strongly enough (Sauguet et al., 2014b). Furthermore, even with extensive screening and high-overall resolution, the structure of the GLIC-GlyR α1 chimera is poorly defined at the level of the eukaryotic TMD (Moraga-Cid et al., 2015). In both cases this likely reflects instability of packed receptors within the crystal form. Indeed high crystallographic B-factors, particularly in the case of LiLy, reveal substantial uncertainity in the position of atoms in the lower half of the GlyRα1 TMD (in the crystal form). Moreover a number of side chains (and some residues) in this region could not confidently be built. We might reason that this represents an inherent change in the stability of the protein that arises from, and reflects the effects of truncation of the M3-M4 loop which is nevertheless essential for purification and crystallization. Indeed whilst we have adopted an “alternative truncation strategy”, using a short tripeptide linker and more conservative truncation of post-M3 and pre-M4 regions, it is possible that our inability to grow strongly diffracting crystals, so far, results from the disruptive effects of loop truncation on allowing stable crystal packing contacts to form.

While one might reason that flexible loops (namely between M2-M3 and M3-M4) are likely candidates for preventing growth of well-ordered and strongly diffracting crystals, it is equally possible that the detergent in the sample is the limiting factor. Evidently in a sample composed of receptor protein and associated detergent, both constituent parts need to work harmoniously in order to generate well-ordered

crystals. Poor choice of detergent results in a protein of low thermal stability, increasing the likelihood of aggregation and thus hampering further structural studies. Here we have empirically identified a combination of detergent (DMNG) and cholesterol derivative (CHS) exhibiting high thermal stability and capable of generating diffracting crystals (maximally to 8.9Å). The choice of DMNG is pertinent; since their conception, maltose neopentyl glycols (MNG) amphiphiles are becoming more widely used in membrane protein structural studies (Chae et al., 2010). Moreover purification and successful crystallization of the closely related homopentameric GABAβ3, was also achieved through using DMNG and CHS.

So why have we not been able to generate strongly diffracting crystals? Momentarily ignoring construct design and modifications; preliminary negative-stain EM studies might have revealed a potential "detergent issue". While EM images revealed characteristic rosette shaped particles of the intact pentameric receptor, and were largely monodisperse (with little clustering), images at reduced protein concentration revealed a background containing smaller distinct particles. These were also present in the final purification buffer (from SEC) and probably represent an accumulation of free detergent-CHS micelles. The detrimental effects of enriching detergent in a protein sample have been well documented with regards to crystallization and often result in the phenomenon of phase separation (Newby et al., 2009). Detergent enrichment typically occurs during SEC and protein concentration steps, and can hamper both optimization and reproducibility of crystal growth. We must therefore carry out further assessment of detergent content (using SEC-MALS) and optimization in the final stages of sample preparation prior to crystallization to reveal whether the mutant V251F chimera when purified in DMNG/CHS, can be used to generate crystals which diffract even further.

4.3.4. Is structure solution by crystallography the clear path forward?

Ultimately we have yet to fully address the question of chimera crystallization from all potential avenues. Techniques including crystal seeding, *in situ* diffraction screening, crystal dehydration and crystallization in the Lipid Cubic Phase (Cherezov, 2011) have

all proven beneficial in various crystallographic studies of membrane proteins and should be addressed for their potential application to this project. However, successful crystallization is rarely a guaranteed result. It might therefore prove essential to address our question by alternative approaches. Single particle cryo-EM has developed at a rapid pace in recent years, and now stands as a rival method to X-ray crystallography for high-resolution structure determination; particularly for difficult proteins that are refractory to crystallization. For membrane proteins, structures of γ-Secretase at 3.4 Å and more significantly GlyR α1 at 3.8-3.9Å in complex with strychnine and ivermectin (Du et al., 2015; Bai et al., 2015b) reveal that this technique is becoming increasingly amenable to protein complexes of small size (<200 kDa). In parallel to studies of ELIC (in Chapter 6), we have begun to screen sample preparation of our chimeric receptor for single particle EM studies and hope to further assess the use of this technique for structure determination.

4.4. Conclusions

GLIC-GABA chimeras are poorly expressed in bacteria, but can be expressed to high-level in Sf9 insect cells using baculoviral-infection

Non-mutant chimeras are unstable in detergent micelles in the presence of a stabilizing lipid, cholesterol hemisuccinate.

A single desensitization mutation in M2 of α1, V251F, is sufficient to dramatically stabilize the chimera in detergent micelles.

Negative-stain EM reveals the chimera forms an intact pentameric channel.

Purified chimeric GLIC-$GABA_AR$ α1 receptors are capable of generating protein crystals with a maximal diffraction limit so far of 8.9Å.

Chapter 5: Binding of the barbiturate Pentobarbital to the prokaryotic pLGIC GLIC

5.1. Introduction

Previously in this study we introduced preliminary data describing allosteric potentiation and inhibition of different classes of pLGICs by the barbiturate pentobarbital. Surprisingly, we found that at clinically relevant concentrations, pentobarbital was able to inhibit proton-activated currents at the prokaryotic pLGIC GLIC (Chapter 3). The functional effects of this drug have been reported across both cationic and anionic pLGICs, and the mechanism of action extensively studied using electrophysiological and photo-labelling binding studies (Muroi et al., 2009; Hamouda et al., 2014a; Jayakar et al., 2015). Given the obvious structural similarity between eukaryotic Cys-loop receptors and their prokaryotic counterparts, we were keen to determine whether an evolutionarily conserved pentobarbital binding site exists in GLIC. Using X-ray crystallography, we sought to identify at high-resolution a three-dimensional binding site for this barbiturate anaesthetic.

Barbiturates, including pentobarbital, have been used clinically owing to their anaesthetic, sedative, anxiolytic and anticonvulsant properties (López-Muñoz et al., 2005). However following the development of safer therapeutics (e.g. benzodiazepines) also with lower tolerance levels and fewer withdrawal symptoms, the clinical application of barbiturates is less commonplace. The functional effects of these compounds are well known and it is principally considered that they act by modulating the activity of members of the pLGIC superfamily, and more specifically via $GABA_A$ receptors (Krasowski et al., 2002) As introduced previously, they are known to bind at and allosterically modulate $GABA_A$ receptor activity in three distinct, concentration-dependent manners; potentiating (at 10-100 µM), activating (<1 mM) and blocking (>1 mM) channel function (Akk and Steinbach, 2000; Muroi et al., 2009). In terms of clinically relevant concentrations of pentobarbital required for general anesthesia in mammals, this is estimated to be in the range of ~ 50 µM (Franks and Lieb, 1994).

The role of residues in $GABA_AR$ β-subunits has long been implicated in coordinating drug binding (largely on the basis of functional studies of β-subunit receptor homomers; Amin, 1999). As might be expected in the confines of a physiologically relevant receptor subunit combination (αβγ), the mechanism of action is likely to be more complex and binding orientated through intersubunit (residue) interactions. Indeed, photolabeling studies with photoreactive barbiturate analogs postulate that binding at distinct interfacial sites formed between γ-β and β-α subunits are responsible for mediating the positive and negative allosteric modulatory effects of barbiturates at $GABA_ARs$ (Chiara et al., 2013; Jayakar et al., 2015).

While $GABA_A$receptors form the primary site of activity, it is also well established that barbiturates are non-selective with regards to binding at eukaryotic pLGICs. Of the pLGIC super family members, excitatory currents through neuronal and muscle nAChRs have been observed to be blocked at clinically relevant drug concentrations (Hamouda et al., 2014a). Such observations would go some way to explaining the side effects that are observed following treatment with high drug concentrations. Once again studies with photolabeling barbiturate analogs (in muscle nAChRs) have suggested mechanisms for drug binding in cationic pLGICs: by binding at an ion channel pore site in the nAChR in a desensitized state; or a γ-α interfacial site in resting nAChR forms (Hamouda et al., 2014b). With regards to the wider family of general anaesthetics, it has been observed that in contrast to their properties at anionic-$GABA_ARs$, compounds including propofol and halothane display negative allosteric effects at cationic pLGICs, such as nAChRs (Violet et al., 1997).

Evidently, the non-selective manner in which these compounds act is not an easy one to decipher, with distinct sites likely to exist at cationic and anionic channels. The use of recently identified prokaryotic pLGIC homologues in high-resolution studies of anesthetic binding has begun to shed new light on this subject. X-ray crystallographic structures of the (cationic) channel GLIC have now been solved in complex with either propofol, desflurane or bromoform (Nury et al., 2011; Sauguet et al., 2013a). Whilst these compounds display inhibitory effects at GLIC (in a manner reminiscent of their effects at nAChRs; Weng et al., 2010), the modulatory sites identified (particularly an

intersubunit site) overlap with residues shown to mediate positive modulatory responses at anionic pLGICs such as $GABA_A$Rs and GlyRs (Nury et al., 2011; Sauguet et al., 2014a). We were therefore keen to ascertain whether a barbiturate binding site in GLIC could be identified using crystallographic approaches and subsequently determine if such a site is compatible/comparable with those observed in either its cationic or anionic evolutionary counterparts.

5.2. Results

5.2.1. Proton-gated response of GLIC (and GA mutants) is inhibited by pentobarbital

As detailed in chapter 3, pH_{20} proton-activated currents at GLIC are inhibited by pentobarbital at clinically relevant concentrations, exhibiting an IC_{50} of ~113 ± 9.4 µM (*Fig 5.2 A & B*). We first wanted to determine if residues which had previously been shown to coordinate the binding of propofol and desflurane at GLIC were also implicated in mediating a pentobarbital response (*Fig 5.1 A & B*). Co-crystallization studies reveal that propofol and desflurane occupy an intrasubunit cavity at the extracellular side of the receptor TMD and thus accessible from the lipid bilayer (Nury et al., 2011). Residues from M1, M2, M3 and M4 (of the TMD) as well as the β6-β7 strand (of the ECD) form this binding pocket, with critical contributions from, I202 (M1), V242 (M2) and T255 (M3) (*Fig 5.1 B*). Nury et al., performed site-directed mutagenesis at these three positions and electrophysiological studies of GLIC to emphasize the importance of these residues in mediating propofol and desflurane inhibition. A mutation at T255 (to a neutral non-polar alanine) was sufficient to induce a differential 10-fold shift in the inhibition curves for both propofol (to lower concentrations, i.e. propofol is more potent) and desflurane (to higher concentrations, i.e. desflurane is now less potent).

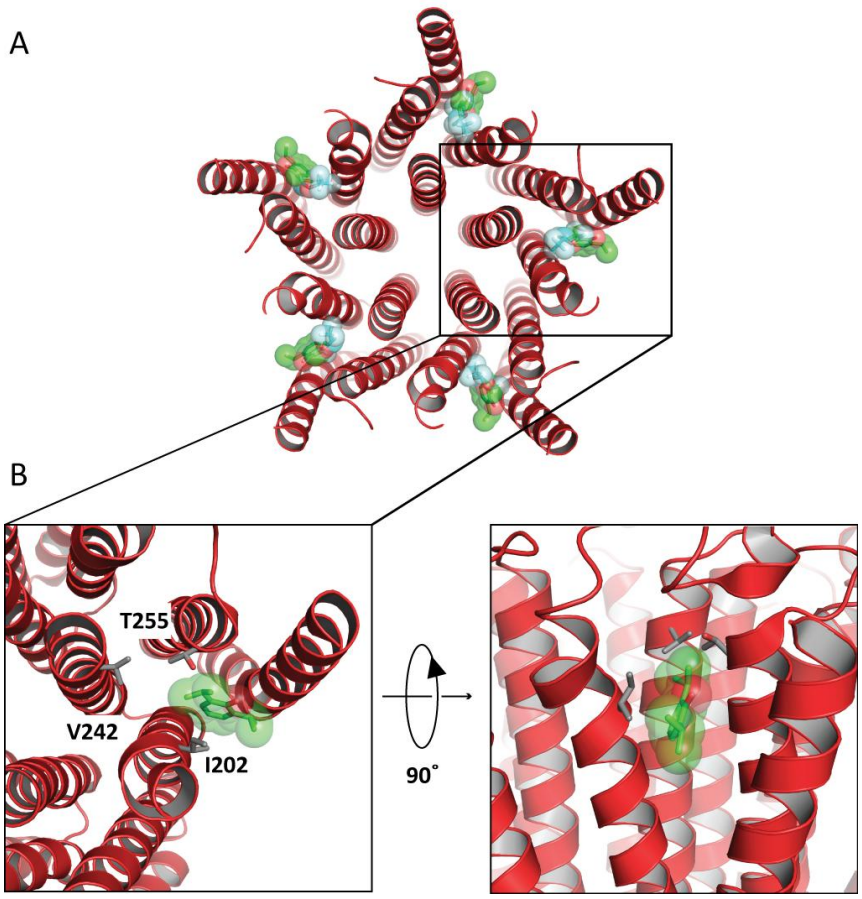

Figure 5.1 - An intrasubunit anaesthetic (propofol and desflurane) binding site at GLIC

A. The pentameric arrangement of subunits at the TMD illustrates the orientation of M1 – M4 α-helices and the location of propofol (green) and desflurane (pale blue) are shown in stick and space filling-representation at each subunit-subunit interface. **B.** Close up of the propofol binding site (Nury et al., 2011) viewed from the extracellular side (left panel) and from the plane of the membrane (right panel). Residues contributing to ligand binding are shown in stick from.

We initially speculated that should pentobarbital be acting via a common binding site (to propofol and desflurane) then identical mutations at GLIC might alter the pentobarbital-inhibition curve. In electrophysiological experiments (carried out in oocytes) a previously reported gain-of-function (with regards to proton gating of GLIC) was observed for receptors bearing the T255A and I202Y mutation. This manifests as an increase in the holding current of oocytes expressing the mutant receptors (even in

pH 8 extracellular solution) and a leftward shift of the proton-concentration response curve (towards lower proton concentrations).

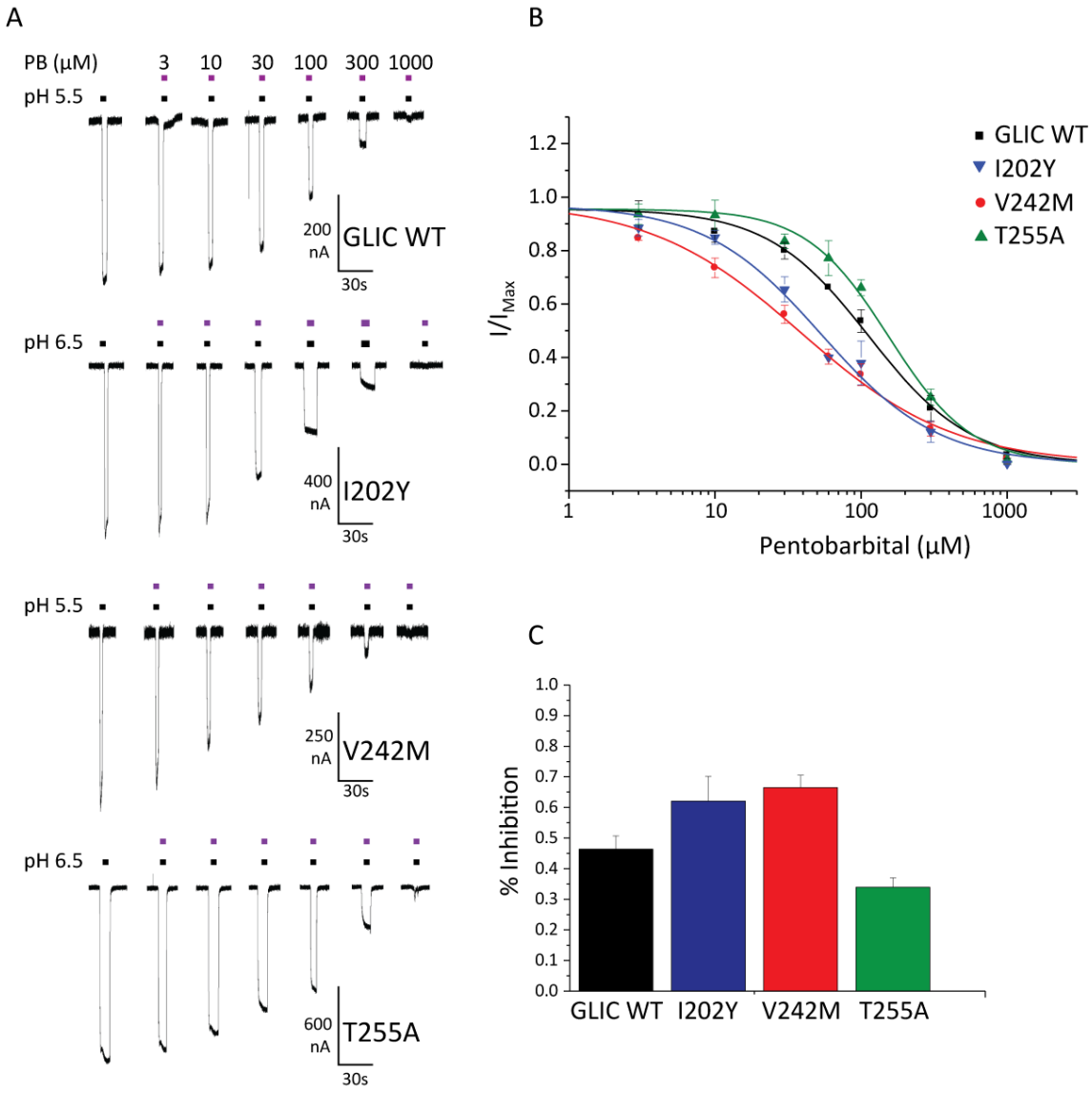

Figure 5.2 - Pentobarbital inhibits proton-gated currents at GLIC by binding at a distinct site to other general anaesthetics.

A. Examples of membrane currents recorded from oocytes expressing GLIC or the indicated GLIC mutant. Currents are evoked at ~pH_{20} in the absence or presence of indicated concentration of pentobarbital (PB). GLIC I202Y and T255A exhibit gain-of-function and were recorded in a bath solution of pH 8 (rather than pH 7.4). **B.**Pentobarbital inhibition-concentration response curves for GLIC WT and the indicated mutants (normalised to the proton activated current in the absence of drug). Points are means ± s.d from n= 4-6 oocytes. **C.**Inhibition of pH_{20} proton gated response by co-application of 100 µM pentobarbital to WT and mutant GLIC receptors.

As in previously published GLIC-propofol/desflurane studies, the pentobarbital-inhibition curve was constructed at pH_{20} (i.e. the pH/proton concentration eliciting a 1/5 maximal response; *Fig 5.2 A and B*). None of the three mutations had substantial effect on the pentobarbital inhibition curve (*Fig 5.2B*). I202Y and V242M mutation induced an approximate twofold shift towards lower pentobarbital concentrations (exhibiting respective IC_{50}s of 53.6 ± 7.38 and 39.1 ± 4.98 μM) whilst T255A reduced apparent sensitivity to pentobarbital (with an IC_{50} of 155.7 ± 14.6 μM). Given that in previous studies T255A and V242M mutations induced much larger (10-fold) shifts in propofol and desflurane IC_{50}s, the lack of an equivalent effect on pentobarbital in this study would suggest that residues forming an intrasubunit anaesthetic site in GLIC are unlikely to be involved in coordinating pentobarbital binding. Presumably, therefore, pentobarbital binds at a distinct site in GLIC.

5.2.2. GLIC can be expressed and purified from bacterial cells for co-crystallization

In light of these observations and to investigate the structural basis for pentobarbital binding to and inhibition of GLIC, we sought to co-crystallize GLIC in complex with pentobarbital for X-ray diffraction and structure determination.

As introduced in the previous chapter, a well-established bacterial expression and purification procedure already exists for GLIC (Bocquet et al., 2007), allowing for milligram quantities of a MBP-fusion protein to be purified following detergent extraction (in DDM). This fusion protein acts as a stabilizing “stepping-stone” in the generation of the mature protein. Evidently, for crystallographic studies, the large soluble MBP-portion of the fusion protein will likely be refractory to the formation of well-ordered receptor protein crystals for X-ray diffraction. Consequently MBP is proteolytically cleaved from the mature GLIC protomer, yielding a stable pentameric GLIC-detergent complex that is further purified by SEC for crystallization trials (see full details in the Materials and Methods).

Using published protocols as a starting point, we carried out large-scale expression of MBP-GLIC for DDM-detergent extraction and receptor purification. In contrast to the procedure introduced in Chapter 4, we used IMAC to recover solubilised-receptors on a Co^{2+} resin. We used this approach, rather than purification on amylose resin, to exclude the undesirable purification of a strongly expressed endogenous porin-protein. We were consistently able to purify 5-10 mg of fusion protein, which was relatively pure (and free of contaminating proteins) when assessed by SDS-PAGE and coomassie blue-stain (*Fig 5.3*). Following cleavage of the MBP-fusion protein in-solution and "reverse IMAC purification" to remove the cleaved His-MBP, analysis by SDS PAGE revealed two distinct bands (free of contaminating products) of ~30 and 40 kDa in mass. The 40 kDa corresponding to the GST-PreScission protease and ~30 kDa band to the monomeric mature GLIC subunit (*Fig 5.3)*. Further purification by SEC allowed the pentameric GLIC protein-DDM complex to be isolated from the protease. As observed for chimeric $GABA_ARs$ and $GluCl_{cryst}$, GLIC elutes as a clearly defined symmetrical peak at ~15 ml (*Fig 5.3*) The protease elutes as a shouldering peak at ~17 ml and can be cleanly separated from the pentameric GLIC (as determined by assessing SEC fractions by SDS PAGE and coomassie blue stain). Peak fractions of the $GLIC(_{pentamer})$-DDM complex from SEC could then be pooled and concentrated (to 5-10 mg/ml) for preliminary co-crystallization studies with pentobarbital.

5.2.3. GLIC crystallization strategies

Having established a procedure for generating substantial quantities of purified GLIC (in DDM), we began to screen for the crystallization of receptors in complex with pentobarbital. In contrast to our efforts to crystallize receptor chimeras, well-defined crystallization conditions have already been extensively reported for GLIC (Bocquet et al., 2009; Nury et al., 2011).

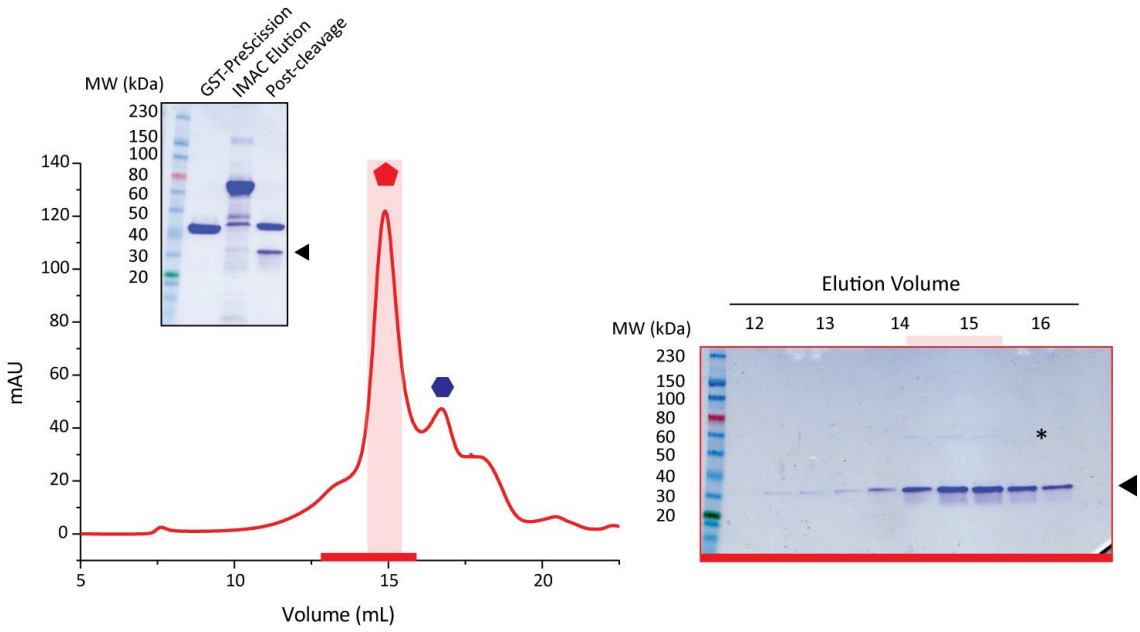

Figure 5.3 - GLIC forms a stable pentameric complex in DDM

SEC profile of (proteolytically) cleaved-GLIC (in DDM). Major peak corresponding to mature pentameric GLIC is indicated by red pentagon and the minor peak, indicated by blue hexagon, GST-PreScission. Inset left; SDS PAGE of purified PreScission protease, IMAC elution and following cleavage reaction. Black arrowhead indicates migration of monomeric cleaved GLIC. Right panel; SDS PAGE of SEC fractions (volumes are indicated by the horizontal red bar below the SEC trace). Peak shaded portion of SEC represents those fractions pooled and concentrated for crystallization.

The most favoured conditions are typically those involving buffering at low pH (high proton concentrations) favouring receptor crystallization in an active-open channel conformation (Bocquet et al., 2009; Hilf and Dutzler, 2009). Recent studies have however shown that crystallization of GLIC is possible at neutral pH, trapping the receptor in an inactive-closed channel state (Sauguet et al., 2014b). Previous co-crystallization studies with general anaesthetics, alcohols and channel blockers have favoured the former condition; binding ligand to an active-channel complex at low pH (Nury et al., 2011; Sauguet et al., 2013a). It should also be noted that the binding of drugs to distinct sites in GLIC crystals has been manipulated using mutant receptors (as

was the case in identifying intra- and inter-subunit sites for the anaesthetic bromoform and alcohol ethanol in a "sensitized" F14'A mutant GLIC protein; Sauguet et al., 2013a).

Using conditions that allowed for successful crystallization of GLIC in complex with propofol and desflurane (PEG 4000, NaSCN and Na-Acetate pH 4), we were able to replicate robust crystal growth in the absence and following incubation of protein solution with an excess of pentobarbital (5 mM). Crystal growth was observed in both sitting and hanging drops (by vapour diffusion), typically forming plate shaped (*Fig 5.5*) or needle crystals. Whilst crystals exhibited favourable sizes for diffraction studies in at least one dimension (> 50 µm), they were largely two-dimensional. Additionally we were able to grow small rectangular cuboid crystals (< 50 µm in the longest dimension). Using a microfocus beamline (I24 at Diamond Light Source) we subjected our crystals to X-ray diffraction characterisation.

We observed limited diffraction of needle shaped crystals (10-20 Å), whilst a number of small cuboidal and plate crystals revealed diffraction approaching and extending beyond 5 Å (maximally to 4.3 Å; *Fig 5.4*). We were unable however to collect complete data sets at this higher resolution due to radiation damage. Though the resolution limit of these crystals (*Fig 5.4*) would be insufficient to build an atomic model of GLIC and it would prove difficult to confidently assign density to a bound ligand. Nevertheless we were able to observe differences in diffraction quality of plate- and cuboidal-shaped crystals. Whilst both showed equivalent maximal diffraction, the former, unsurprisingly, exhibited anisotropic diffraction. We were able to assess and tentatively assign a three-dimensional space group to GLIC crystals grown in the presence of pentobarbital; typically C2 or $P2_12_12_1$ crystal forms, as previously reported for GLIC grown under similar conditions.

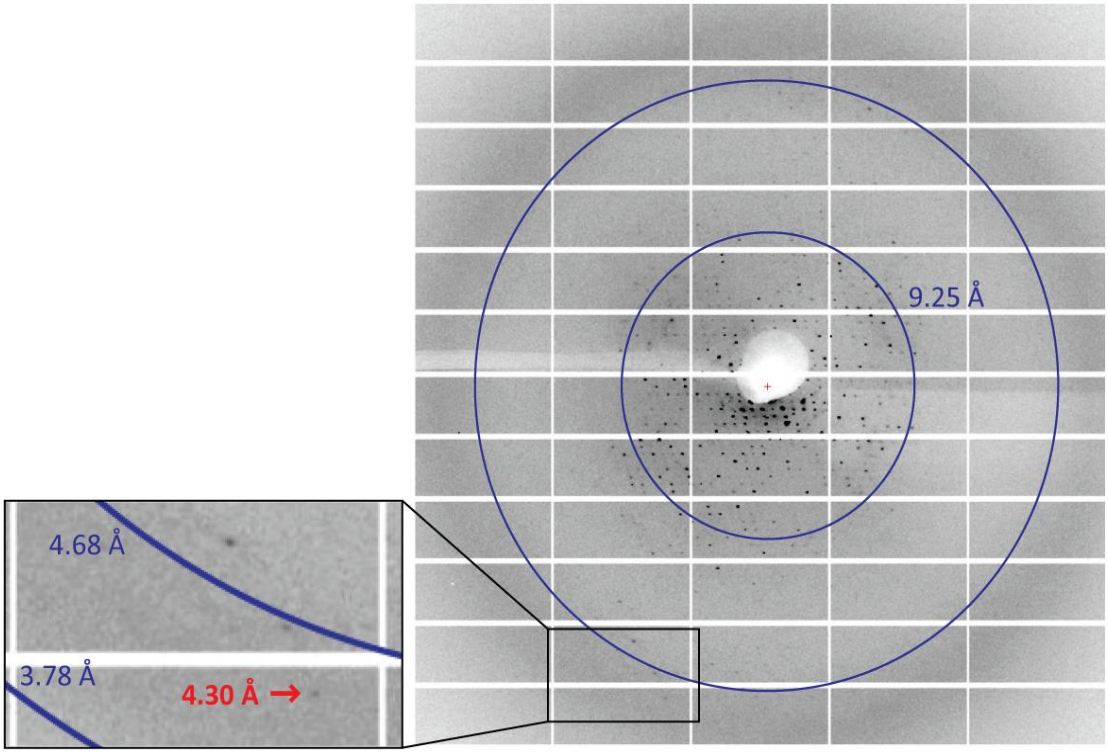

Figure 5.4 - X-ray diffraction pattern for co-crystals of GLIC and Pentobarbital

X-ray diffraction pattern (0.2° oscillation range) from a crystal of GLIC in the presence of DDM (by microfocus beamline, DLS I24). Resolution rings in the main panel at 9.25Å and 4.68Å are shown as blue circles. Left panel, is a magnified section showing diffraction spots diffraction limit, ~4.30 Å (resolution rings at 3.78Å and 4.68Å are shown as blue circle). The data set collected for this crystal was indexed with a space group of $P2_1P2_1P2_1$.

5.2.4. Optimizing the diffraction limit

Whilst the general conditions for crystal growth for GLIC are now well established, it is evident that crystal growth and cryo-protection requires substantial optimization. To date, the large proportion of crystallographic studies of GLIC have been carried out by only a few groups (Hilf and Dutzler, 2009; Gonzalez-Gutierrez et al., 2013; Sauguet et al., 2014b). Published experimental procedures often only provide limited detail regarding the nuances of crystal preparation. Despite this a number of factors are

apparently critical for the formation of crystals that diffract to high resolution. Namely, protein crystallization should be facilitated by using “crystal seeds”, allowing for robust growth of large three-dimensional crystals (Sauguet et al., 2014b). Crystal dehydration, before cryo-protection, improves the diffraction quality and limit. Despite this a large number of crystals must be screened for diffraction before identifying the small number capable of generating atomic resolution datasets (Sauguet et al., 2014b; Moraga-Cid et al., 2015).

We therefore sought to optimize and improve the growth of GLIC crystals exhibiting increased size in all three dimensions. By testing two well-established seeding techniques, we were able to identify a strategy for generating large parallelepiped crystals (that would otherwise form 2D plate-shaped crystals under normal conditions; *Fig 5.5*). Small crystals bearing favourable shape and proportionate growth (in each dimension) could be grown by the streak-seeding approach (with crystal nucleation and growth occurring along the “streak line” (*Fig 5.5*). Given the small size of crystals it is likely that they would only be amenable to diffraction screening and data collection on (synchrotron X-ray source) microfocus beamlines. By contrast, a “micro-seeding” approach, using seeds from crushed crystals allowed for growth of large three-dimensional crystals. Plate shaped crystals of GLIC were harvested and crushed to form a ”seed slurry” and used to establish fresh crystallization drops. Using this approach we were able to manipulate (and reduce) spontaneous nucleation, allowing for crystal growth from seeds. This reduced the number of crystals, while enabling growth to larger sizes (*Fig 5.5*). Using this robust crystallization technique, we could further explore co-crystallization through a number of strategies, including soaking of large crystals in drug solution and crystal seeding in to drug-containing drops.

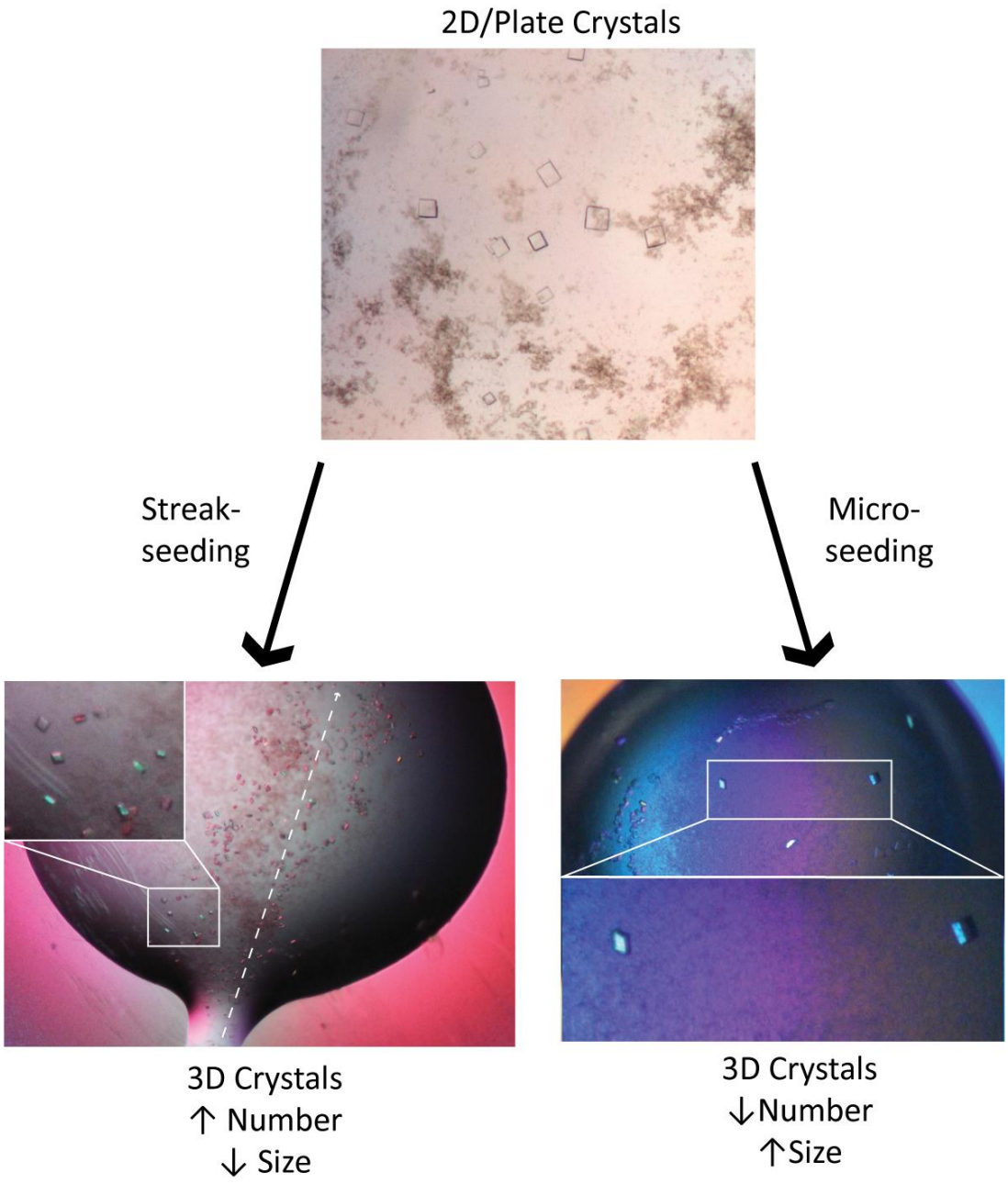

Figure 5.5 - Crystal growth optimization by seeding

Initial crystal growth screens yielded an excess of 2D plate crystals. Using a seed stock (of crushed plate crystals) “streak-seeding” and “micro-seeding” were used to generate three-dimensional crystals of GLIC. Inset panels show magnified images of three dimensional parallelepiped crystals. More details can be found in the Materials and Methods.

5.2.5. A brominated-analog of PB exhibits inhibitory effects with similar affinity

In addition to techniques to improve crystal growth, we were keen to address a potential problem commonly observed in crystallographic studies of ligand binding proteins. It is often the case that assigning electron density to a bound ligand and confidently determining orientation proves problematic particularly if specific structural features of the ligand are poorly represented in electron density maps. These efforts are further hampered if the protein of interest provides only limited diffraction (as is often the case for membrane proteins). In order to ensure that ligand docking results might be more conclusive, it is possible to use the anomalous X-ray scattering of specific atoms (e.g. Br) to allow for their definitive identification in electron density maps (Spurny et al., 2013; Bagnéris et al., 2014). Drug-derivative compounds bearing selenium and bromine atoms have proven particularly useful in anomalously assigning density to small bound molecules, and in determining their orientation. Indeed in studies of anaesthetics (bromoform), alcohol (bromo-ethanol) and channel blockers (bromolidocaine) binding at GLIC, brominated-drug derivatives have been employed and used to determine the binding sites (Hilf et al., 2010; Sauguet et al., 2013a). It is however important to note that the use of such compounds does not obviate the necessity of collecting high-resolution (< 4 Å) data sets.

We identified a commercially available structurally analogous compound that could serve as a pentobarbital derivative; 5-(2-Bromo-ethyl)-5-ethyl-pyrimidine-2,4,6-trione (hereafter referred to as S97617). Significantly, this compound contains a bromine atom and presumably would be more easily identified in electron density maps (as anomalous density peaks). Like pentobarbital, the compound, S97617, is derived from barbituric acid, but instead of ethyl and 1-methybutyl groups at position 5 on the pyrimidine ring of pentobarbital, it has 2-bromo-ethyl and ethyl R^1 and R^2 groups (*Fig 5.6 A*). In order to justify using S97617 in co-crystallization studies, it was first necessary to confirm that its actions resembled that of pentobarbital at both GLIC and native $GABA_AR$ subunit compositions. Reassuringly, the brominated compound was able to directly gate α1β2 $GABA_A$ receptors (expressed in *Xenopus* oocytes; *Fig 5.6B*). Furthermore, (pH_{20}) proton-gated currents in GLIC were inhibited by S97617 with an

IC_{50} of 157.1 ± 25.8 µM (*Fig 5.6A*). In both cases the results were reminiscent of those observed for pentobarbital, over a similar concentration range. This would suggest that this compound is likely to be acting at both GLIC and α1β2 $GABA_A$Rs in a similar manner to pentobarbital and presumably via a common binding site. We have not, at this stage, tested the sensitivity of GLIC-anaesthetic mutants, I202Y, V242M and T255A, to S97617.

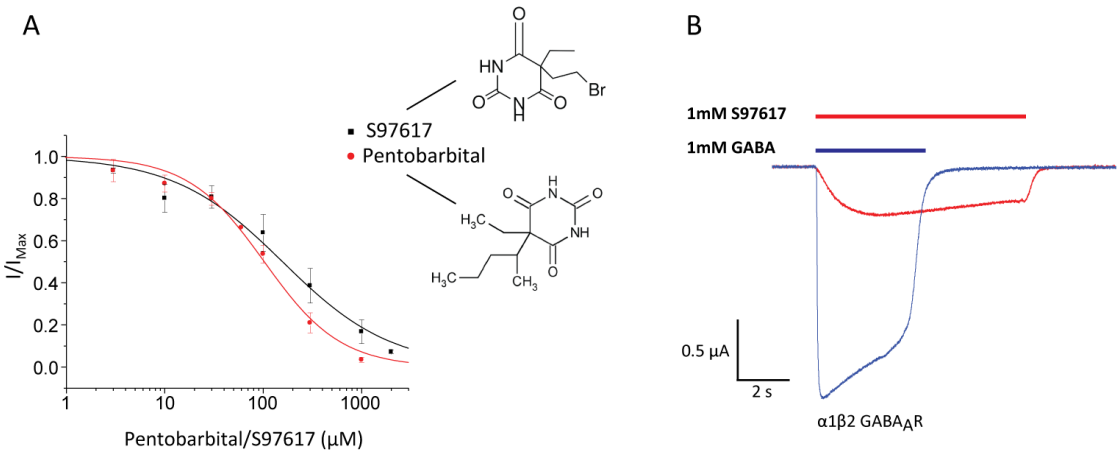

Figure 5.6 - Brominated derivative of pentobarbital inhibits proton-gated currents at GLIC and activates α1β2 $GABA_A$Rs

A. Comparison of pentobarbital and S97617 and inhibition-concentration response curves for GLIC WT (activated by pH_{20} proton concentrations). Points are mean ± s.d and n=6 oocytes. **B.** Comparison of membrane currents evoked by application of 1mM GABA or 1mM S97617 from oocytes injected with α1β2 $GABA_A$Rs.

5.2.6. Crystal structure of GLIC at 3.3 Å

Having identified a brominated compound that exhibits pentobarbital like properties, we sought to co-crystallize GLIC in the presence of S97617. In parallel, crystals grown in the presence of pentobarbital were also screened for improved diffraction. We used

the seeding techniques described above to grow large crystals in the presence of drugs, or native crystals that were soaked in drug before cryo-protection. Extensive screening of crystals yielded a single crystal grown in S97617 that diffracted sufficiently to generate a complete data set at 3.2 Å. It should be noted at this early stage that data was not collected at an X-ray absorption optimized to bromine (0.92 Å).

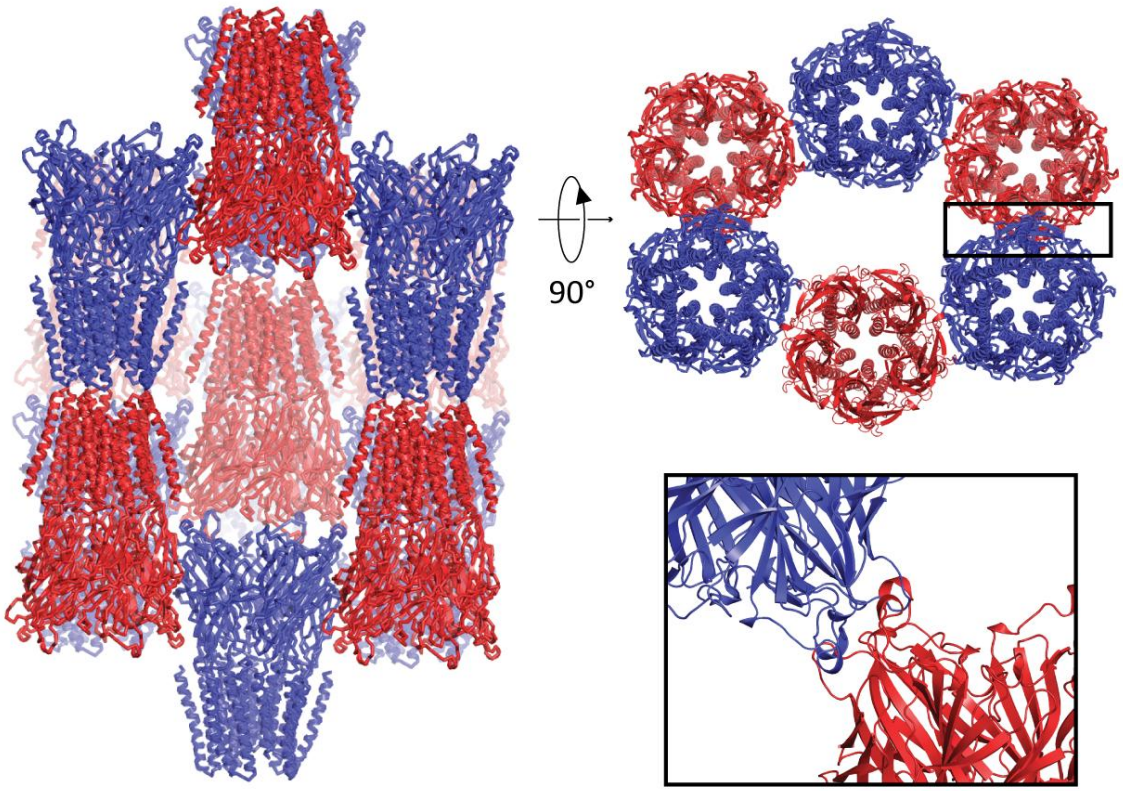

Figure 5.7 - C2-type crystal packing of GLIC

Two views of GLIC crystal packing showing rotation around the indicated axis. Molecules are depicted as red or blue cartoons depending on their orientation. The box insert in the right panel indicates a crystal packing contact between residues in the ECD, which is magnified in the panel bottom right.

As previously detailed, the crystal was grown at pH 4 and allowed for structure solution for GLIC at ~ 3.2Å. The structure of GLIC in the brominated pentobarbital (hereafter referred to as $GLIC^{BrPB}$) was solved by molecular replacement using the 2.4 Å

GLIC structure (PDB 4HFI; Sauguet et al., 2013b) as a search probe and yielding a robust solution (see Materials and Methods *Sections 2.7.8 & 9* for more details of structure solution and data interpretation). An initial round of automated model building and structure refinement was carried out using the Phenix AutoBuild function for initial assessment of the quality of the electron density map, and for the identification of anomalous peaks in the electron density maps (Terwilliger et al., 2008).

The crystals belong to the C2 space group (with one pentamer in the asymmetric unit). With regards to the space group and unit cell dimensions, the $GLIC^{BrPB}$ crystal presented here is isomorphous to 41 of the 45 crystal structures for GLIC reported in the PDB. Unsurprisingly, the analysis of crystal packing reveals common contacting regions as identified in other GLIC data sets (*Fig 5.7*). The major contacts are formed between the ECDs of neighbouring pentamers (at two points) and the exposed loops at the base of the TMD. The second of the two ECD contacting points shows an increased degree of structural flexibility in the crystal form (*Fig 5.7*; as indicated by the high B-factor in this region with respect to the rest of the protein *Fig 5.8*).

The overall architecture of $GLIC^{BrPB}$ is identical to that of the native form, $GLIC^{native}$ (i.e. grown in the absence of ligand, e.g. PDB 4HFI; Sauguet et al., 2013b). As for $GLIC^{native}$, the structure presented here exhibits structural rigidity in the TMD and the core of the β-sandwich of the ECD (as indicated by B-factors for this crystal, 73.7 $Å^2$), with increased flexibility in the exposed loops of the ECD (*Fig 5.8* A). The structure of $GLIC^{BrPB}$ was very similar to $GLIC^{native}$ with a α-carbon (C_α) root mean square deviation (RMSD) of 0.267Å over the entire pentamer (by global alignment of all 5 chains; *Fig 5.8 B*). This is further confirmed when individual TMD and ECD elements are structurally aligned (to $GLIC^{native}$) with C_α-RMSD in ECD of 0.214Å and in the TMD of 0.260Å (*Fig 5.8 C* & *Appendix Table 4*). Small fluctuations in residue side-chain position are observed in more flexible regions of the protein. This would suggest that structurally, if bound in the crystal form, S97617 does not shunt GLIC into a state distinct from the previously reported open channel structure. This is consistent with previous studies of GLIC in complex with general anaesthetics that bind to receptor in the open form, without altering global architecture (when compared to the native/apo form). Moreover, using

global and individual domain structural alignments with GLIC in locally closed (LC) and resting forms revealed that the structure presented here ($GLIC^{BrPB}$) is comparable only to the open form of $GLIC^{native}$ (*Appendix Figure 7* and *Appendix Table 4*).

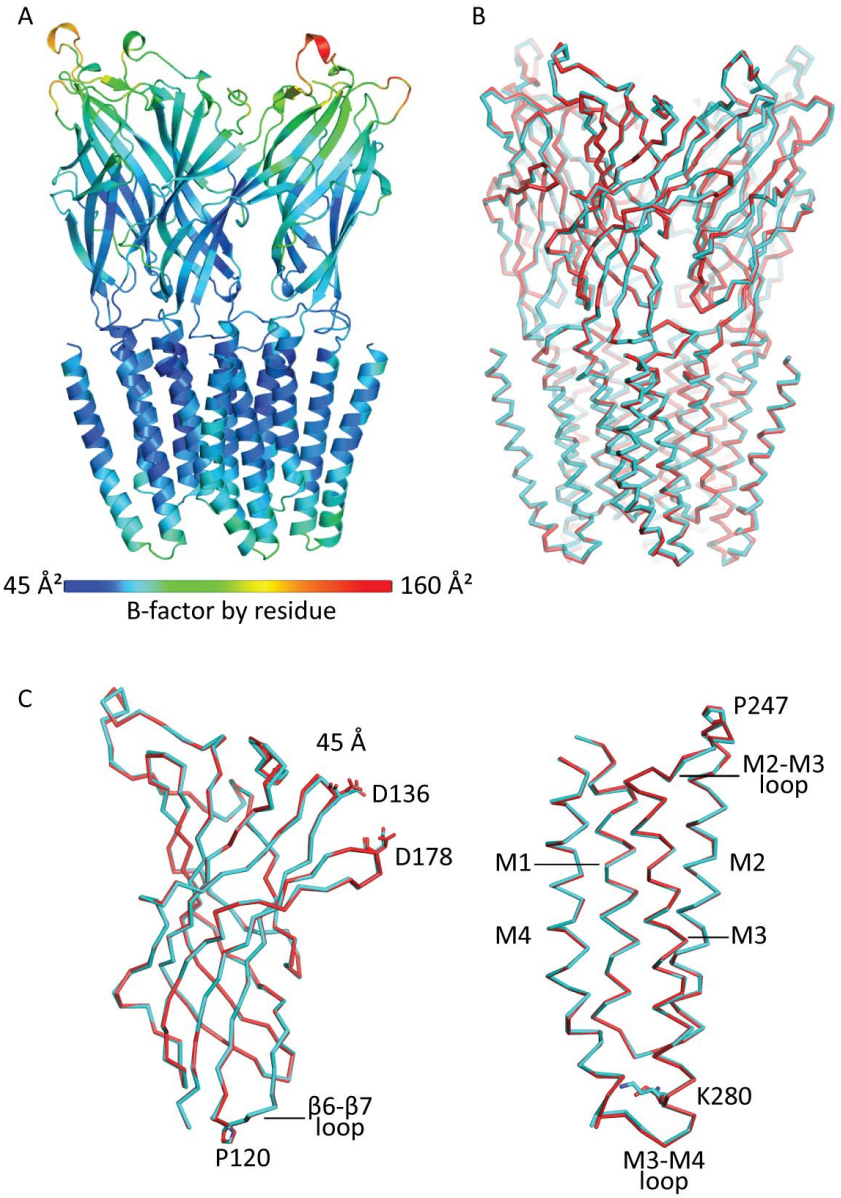

Figure 5.8 - Global architecture of GLIC grown in Bromo-PB is isomorphous to that of GLIC grown under "normal" conditions

A. $GLIC^{BrPB}$ shown in cartoon-respresentation and colored by B-factor **B.** $GLIC^{BrPB}$ (red) pentamer aligned to $GLIC^{native}$ (cyan, PDB 4HFI) and shown as a ribbon arrangement. In both **A** and **B** the proximal two subunits are omitted for clarity. **C.** Individual alignments of $GLIC^{BrPB}$ and $GLIC^{native}$ ECD (left) and TMD (right). Key structural regions are labelled as are residues showing varying degrees of side-chain fluctuation.

Analysing the electron density maps for $GLIC^{BrPB}$ was necessary to assess the quality of the structure solution and to identify peaks in density that could be attributed to non-protein elements (*Fig 5.9 and 5.10*). Electron density maps were of sufficient quality that we could confidently reconstruct the entire peptide backbone and build residue side-chains for much of the model (*Fig 5.9*). At the global level, assessment of electron density maps reveals that the peptide backbone satisfies the previously reported open-active form of GLIC with no ambiguity. This was notably evident at the level of the TMD (where we might expect pentobarbital to bind, as discussed below). Electron density maps show that side chain positions of pore-lining M2 residues is in agreement with those in the open-channel state. Moreover electron density tightly surrounds the modelled orientation of the residue side-chains in the M2-M3 loop and β6-β7 loop (the critical signal transduction elements at the ECD-TMD interface); notably for Tyr-Pro-Phe resdues at the tip of β6-β7 loop and aromatic residues of the M2-M3 loop (involved in stacking interactions at the interface; *Fig 5.9*). As expected, in regions of the protein exhibiting increased flexibility in the crystal form defining side-chain orientation was not possible.

Having assessed the quality of the electron density maps for the protein main chains, we reasoned that it might be possible to identify additional peaks in electron density and difference maps that might be assigned to bound ligands. At the limited resolution of $GLIC^{BrPB}$ this was likely to prove challenging, particularly in terms of defining molecular orientation. While we crystallized GLIC in the presence of a brominated-derivative of pentobarbital, diffraction data was not collected at the peak wavelength for bromine (0.919 Å). This would ultimately hamper efforts to identify bound drug from the anomalous scattering of bromine (which is considered a "weak scatterer" even under optimized experimental conditions"). Indeed generation of an anomalous map did not reveal appreciable peaks above the background signal. Subsequently we would have to rely on strong signals in difference density maps (contoured at +5σ) to determine if S97616 was bound *in situ*.

Difference density maps were contoured at 5σ and assessed for strong positive peaks (*Appendix Fig 8*). Visual inspection of results revealed residual electron density in the pore (and positive peaks in difference maps at ~6 σ) (Fig 5.10A). This corresponds to a

"detergent plug" (formed of 6 detergent molecules) strongly observed across structures of active-open GLIC.

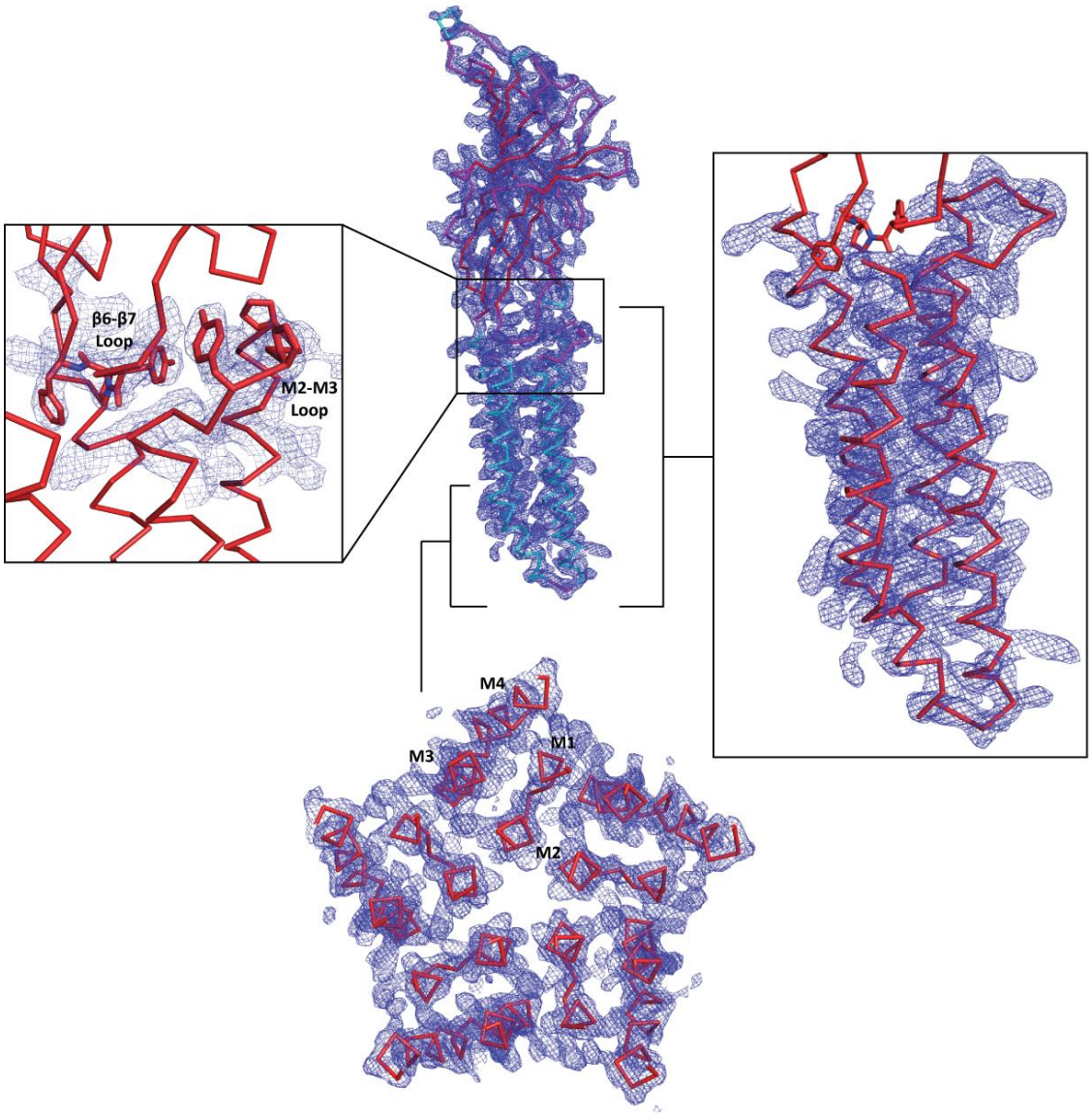

Figure 5.9 - Quality of electron density maps for GLIC

A single subunit in C_α-traceribbon representation is coloured by secondary structure (red; β-strands, cyan; α-helices and pink; loops) and blue map representing 2mF_o-D$F_c$electron density map contoured at a level of 1σ. Panel left; C_α-trace of the M2-M3 loop and β6-β7 loop and electron density map (as in central panel). A number of residues are shown in stick representation to emphasize surrounding electron density. Panel right; C_α-trace of a single TMD region and electron density map. Bottom panel; The pentameric arrangement of subunits at the level of the TMD illustrates the orientation of the M1 – M4 helices (in ribbon representation) and electron density map (as in the central panel).

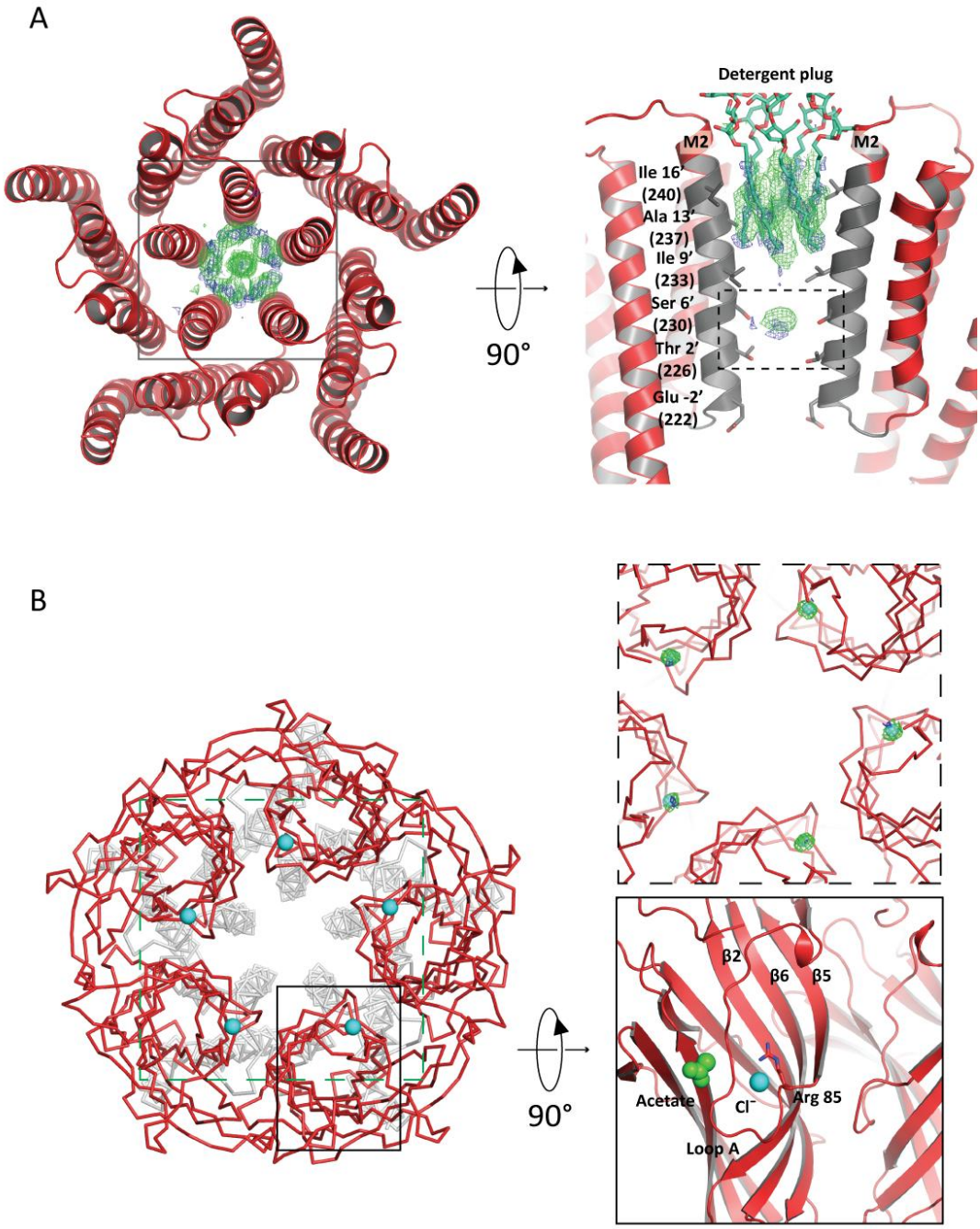

Figure 5.10 - Modelling bounds ions, positioning of (partial) detergent molecules and observed density at 6' Serine level

A. Detergent density (2mF_o-D$F_c$electron density, blue, and F_o-F_c difference density maps, green, contoured at 1.5 σ and 5σ, respectively) in the pore of GLIC^{BrPB} and superposition of detergents (in stick representation). M2 lining residues are shown as sticks and labelled for one subunit. The black dashed box highlights the ambiguous density at the level of the 6' Serine residue. **B.** Location of chloride ions (shown in space-fill) in the ECD of GLIC^{BrPB} is shown for pentameric arrangement of subunits. The green-dashed box is magnified in the top right panel and shows electron density maps as in A. Lower right panel black panel) is a magnified view of the chloride binding site and inter-subunit acetate site in the ECD shown rotated around the axis as indicated). Anions are shown in space-filling representation.

Density is apparent for the aliphatic chain of DDM molecules and not for the maltoside moiety (*Fig 5.10 A* and *Appendix Figure 8*). These molecules form a 6 detergent bundle; a pentagonal arrangement with a further detergent molecule orientated centrally. In initial structural studies of GLIC it was perceived that the central detergent was positioned with the maltoside moiety facing inwards (and the remaining five pointing outward; Bocquet et al., 2009). However, more recent structures at higher resolution (assisted by use of selenium-derived DDM) provide unequivocal evidence that this central detergent also points outwards (Sauguet et al., 2013b). For visualization purposes we have superimposed 5 detergent molecules from $GLIC^{native}$ (PDB 4HFI), including the maltoside head groups for reference (which were modelled in previous structures). Reassuringly, we see a clear overlap in electron density in our maps and the positioning of the detergents aliphatic tails (*Fig 5.10 B*).

Beyond the observation of electron density in the pore of $GLIC^{BrPB}$ we observed the presence of strong peaks in all five subunits (ranging from 5.5 to 7.9 σ) at a vestibular site in the ECD within loop A (*Fig 5.10 B* and *Appendix Fig 8*). This site overlaps with the location of bounds anions, chloride or bromide ions, observed in previous data sets (Sauguet et al., 2013b; Fourati et al., 2015). Given the strong positive peaks in difference maps (and the presence of NaCl in purification buffers) we can assign and model a chloride ion at this site (*Fig 5.10 B*). We favour a chloride ion (as bromine was only included in the crystal drop in form of the compound S97616) though we cannot exclude that a bromide ion may be generated by hydrolysis of the "bromo-pentobarbital" molecule. Regardless of identity, it is likely that the anion is coordinated in a position through interactions with residues of the β5 strand and loop A, within a positively charged pocket. Three further positive peaks in the difference density map (at 6.9 – 7.9 σ) were identified at equivalent positions at three of the five subunit interfaces. This site is located below C-loop (the characteristic agonist binding site across pLGICs) in a cavity wedged between the adjacent subunits. This position was equivalent to a previously identified intersubunit acetate binding site (Fourati et al., 2015). Given that acetate was present in the crystallization drop (at 100 mM) and on the basis of the agreement between our density maps and previous observations, we could confidently model the position of an acetate molecule at 3 positions (*Fig 5.10 B*).

The remaining peak in electron density (contributed presumably by non-protein elements) is more difficult to interpret. Residual electron density and a positive peak in the difference map were observed at 7.2 σ in the pore, below the detergent plug, at the level of the Ser 6' (M2) residue (*Fig 5.10 A*). There are three potential hypotheses regarding the elements responsible for this density, which in the context of this study are discussed in detail below.

5.3. Discussion

In this chapter we sought to build upon the previous observation that the (cationic) prokaryotic pLGIC GLIC is inhibited by the barbiturate, pentobarbital, at clinically relevant concentrations. Given the amenability of this receptor to X-ray crystallographic studies, we used co-crystallization of GLIC in the presence of pentobarbital or a brominated-derivative to identify the molecular determinants of drug binding.

5.3.1. Pentobarbital binds at an inhibitory site distinct to that identified for propofol and desflurane

Since their identification and crystallization, GLIC and ELIC have been used as models to identify binding sites for a range of pharmacological agents (recently reviewed in Sauguet et al., 2014a). Most notably, the structures of GLIC in complex with the general anaesthetics propofol, desflurane and bromoform have been solved at atomic resolution, identifying both intra- and inter-subunit binding sites; the latter site likely to be conserved from prokaryotic to eukaryotic pLGICs (Nury et al., 2011; Sauguet et al., 2013a). However, to date, no high resolution structure exits for a receptor structure in complex with anaesthetic barbiturates. Given that barbiturates, including pentobarbital, likely target and act at pLGICs (principally $GABA_ARs$), we reasoned that an inhibitory barbiturate binding site at GLIC (as for previous studies of anaesthetic binding) might be conserved in eukaryotic pLGICs.

Electrophysiological studies of GLIC revealed that propofol, desflurane and bromoform inhibit proton-gated currents. Subsequent crystallographic studies revealed overlapping binding of these compounds primarily within an intrasubunit cavity formed at the extracellular side of the TMD (Weng et al., 2010; Nury et al., 2011). Hydrophobic residues lining this cavity are likely to be responsible for ligand recognition and coordinating binding through van der Waals interactions. Notably these compounds bound receptor in the open channel form, and thus a mechanism for how an anaesthetic promotes channel closure is not immediately apparent.

Through mutagenesis of residues lining the intrasubunit cavity (namely I202, V242 and T255), we found that the inhibitory response to pentobarbital was unlikely to be coordinated through binding at a site overlapping with that of the aforementioned anaesthetics. Unlike the substantial effects observed in functional studies of propofol inhibition at mutant GLIC receptors, we observed little effect on pentobarbital binding and inhibition of GLIC. Whilst some of these mutations also imparted basal gain-of-function effects, we can reasonably assume non-overlapping sites on the basis of our mutagenesis studies. Also high resolution structural analysis of anaesthetic binding (e.g. propofol, halothane) at soluble surrogate binding proteins of known structure, such as human serum albumin and apoferretin, reveal that binding relies on van der Waals rather than polar interactions (Bhattacharya et al., 2000; Vedula et al., 2009). This is consistent with the nature of residues lining the intrasubunit cavity in GLIC. By comparison, pentobarbital has both a distinct aromatic ring structure and increased overall polarity compared to these other classes of anaesthetics. In crystallographic studies of barbiturate binding to apoferretin, somewhat surprisingly these compounds were found to bind at a cavity overlapping with that observed for other anaesthetics, with binding now relying on polar interactions (with further contributions from van der Waals interactions; Oakley et al., 2012). Whilst the binding site at this surrogate protein, apoferretin, evidently exhibits a degree of versatility in anaesthetic binding, this would appear not to be the case for GLIC as shown in our functional mutagenesis studies.

A further point to note comes from crystallographic studies of mutant GLIC (F14'A) and wild-type ELIC receptors in complex with bromoform (Spurny et al., 2013; Sauguet et al., 2013a). The F14'A mutation imparts ethanol-sensitivity to the GLIC receptor, as well as reversing the direction of the response to bromoform (potentiating rather than inhibitory). In mutant GLIC, bromoform now occupies a second, inter-subunit, TMD binding site. Intriguingly, this site directly overlaps with residues known to regulate allosteric modulation to anaesthetics in eukaryotic plGICs (namely GlyRs and $GABA_A$Rs). While binding of pentobarbital by an inter-subunit site would be in accord with the results of photolabeling studies (with photoreactive barbiturate analogs) carried out on native $GABA_A$Rs, that identified labelled M1 and M3 residues at γ-β and β-α interfaces (Jayakar et al., 2015), ultimately in GLIC, bromoform binding is still coordinated by largely hydrophobic contacts. It should be noted that this inter-subunit site is however lined by an increased number of polar residues (when compared to the intra-subunit site). Moreover, an alternative inter-subunit bromoform binding site in ELIC has also been observed from X-ray crystallography (where bromoform again exhibited inhibitory effects in functional experiments; Spurny et al., 2013). Formed by a pocket at the intracellular side of the TMD, this site is lined by hydrophobic and aromatic residues. As for intra-subunit binding sites in GLIC, the non-polar nature of this site would presumably not energetically favour barbiturate binding. We have not explored further using mutagenesis whether an inter-subunit site is responsible for barbiturate binding in GLIC.

5.3.2. Pentobarbital binds to 'activated' GLIC without affecting global GLIC structure

In our studies we attempted to use crystallographic approaches to identify a barbiturate binding site in GLIC. Whilst we addressed pentobarbital binding, in our efforts to optimize crystallography conditions, we also used a commercially available brominated-derivative of pentobarbital (S97617). In addition to exhibiting identical effects to pentobarbital (inhibition of proton-mediated currents), we also observed a direct activation of α1β2 $GABA_A$Rs in a manner reminiscent of pentobarbital. To our knowledge the functional effects of this compound, particularly at members of the pLGIC superfamily have not yet been reported.

While we were able to grow crystals in the presence of both pentobarbital and S97617, we were only able to identify a single crystal (grown in complex with S97617) capable of generating sufficiently high-resolution structural data (by X-ray diffraction). As alluded to earlier, we did not collect diffraction data at the X-ray absorption edge of bromine (in order to assist localization of this atom in electron density maps). Given this and the difficulty of definitively identifying and assigning drug density at the maximum diffraction resolution generated (~3.2 Å) we cannot confidently confirm whether or not S97617 is present in the atomic model of GLIC presented here. However, fluorescence scans of weakly diffracting $GLIC^{BrPB}$ (> 5Å) revealed a weak-bromine specific signal in our sample. At current it is unclear whether this is bound to protein-elements within the crystal or present as a result of soaking the crystals in a cryo-protectant solution containing the drug (prior to "freezing" in liquid nitrogen).

The only non-protein elements that we have been able to confidently assign in our model are the aliphatic tails of DDM detergent molecules in the receptor pore, as well as chloride and acetate ions (binding to the ECD below the agonist binding C-loop). The detergent molecules in the pore are likely to arise as a result of purification and crystallization procedures, being of no functional significance (Bocquet et al., 2009). However, a functional role for ion (acetate and chloride) binding in the case of GLIC remains unclear. Also the presence of chloride ions in the homopentameric human $GABA_A$ β3 receptor structure, in a spatially equivalent position in the ECD might suggest a role in receptor assembly and stabilization (Miller and Aricescu, 2014; Fourati et al., 2015). With regards to a role for chloride coordination, it is notable that kainate receptors (of the ionotropic glutamate receptor family) require monovalent anions (and cations) for dimer stabilization in the ligand binding domain (Plested and Mayer, 2007; Plested et al., 2008; Vijayan et al., 2009). This serves to maintain normal receptor activity. It will thus be of interest to further study the role of anion binding in the ECD of pLGICs.

Beside these non-protein elements, ambiguous electron density (apparent also as a strong positive peak in difference density maps) was observed lower in the pore

beneath the detergent molecule density at the level of the Ser 6' M2 residues.This density can be interpreted in three ways:

The first is to speculatively assign this density to bound drug, S97617.This would be consistent with computational studies that suggest general anaesthetics can occupy multiple pore (block) sites with micromolar affinities in GLIC (LeBard et al., 2012). One of these sites notably is at the level of the 6' and 9' M2 residues. However, while we cannot confirm that the resolution of the map is insufficient to display full density for the bound drug, ultimately the shape of the electron density does not adequately fit with the contours of S97617. Indeed the only pose in which the drug could be orientated with respect to the observed density in our maps would be with the pyrimidine ring of the barbituric acid moiety perpendicular to the transmembrane helices. Moreover there is no apparent density for the R^1, ethyl and R^2, 1-methybutyl, groups present at position 5 on the pyrimidine ring. Consequently we could not define the orientation of S97617, but assume that it occupies a channel site in the open-form of GLIC. Generating data with positive anomalous signal for the bromine atom would be essential to confirm the presence and precise location of the bound drug.

The second interpretation would be that in contrast to the consensus view of detergent molecule orientation in the pore, the central detergent molecule can indeed reside in a "downward" facing orientation (Bocquet et al., 2009). On this basis, the maltoside moiety would be positioned approximately at the level of the 6' serine, and could account for the residual density (as modelled in the first crystal structures of GLIC).

Finally, a recent study of ion permeation in GLIC, favoured the argument that a self-stabilized pentagon of water molecules is located at the 6' position. This was based upon a high-resolution (2.4Å) structure of GLIC and was corroborated through further crystallographic studies with Selenium-derived DDM (as introduced previously) to discount the second interpretation involving detergent orientation (Sauguet et al., 2013b). This third interpretation and its applicability to explain similarly observed densities in a range of GLIC-open channel structures (essentially isomorphous to that

presented here) appears like the most likely candidate for contributing to electron density.

Our own co-crystallographic studies have thus far been unable to generate a high-resolution structure of a pLGIC in the presence of a barbiturate. However, with our collaborators (Marc Delarue, Institut Pasteur) we intend to corroborate our functional discoveries through intensive co-crystallization studies of previously reported GLIC "channel variants" in the presence of a range of barbiturates. More specifically, we hope to explore whether pentobarbital binds preferentially to locally-closed forms of GLIC (Prevost et al., 2012). Whilst GLIC crystallization occurs at receptor activating low pH conditions, this receptor structure, in terms of the M2 pore lining helix is roughly equivalent to the GLIC inactive/resting structure (solved at neutral pH; *Appendix Fig 7*) Such studies would therefore allow assessment of stable barbiturate binding to a "resting" inactive form of the receptor (a mechanism that has previously been described in functional studies of barbiturate modulation of nAChRs; Hamouda et al., 2014b).

5.4. Conclusions

Pentobarbital inhibits proton-activated currents in the prokaryotic pLGIC GLIC.

Binding of pentobarbital occurs at a new site and not via the previously identified intra-subunit anaesthetic binding cavity.

A brominated pentobarbital-derivative, S97617, exhibits similar functional properties to pentobarbital.

Crystals of GLIC form in the presence of pentobarbital and S97617.

The crystal structure of GLIC at 3.3 Å generated in this study does not allow for the unambiguous identification of a barbiturate binding site, but confirms features previously reported for GLIC channels in an open conformation (in C2 space group crystal form).

Chapter 6: A multi-disciplinary structural approach to assessing Pregnenolone Sulphate binding at the prokaryotic receptor ELIC

6.1. Introduction

In functional studies of $GABA_A$ receptor chimera pharmacology we emphasised the role that the α1 TMD plays in receptor sensitivity to the inhibitory neurosteroid pregnenolone sulphate (PS; Chapter 3). In these studies we observed that in contrast to GLIC, a GLIC-$GABA_AR$ chimera exhibited profound inhibition at micromolar concentrations of PS, in a manner reminiscent of native α1β2 $GABA_ARs$. While the effects of this inhibitory class of steroids (often typified by the presence of a sulphate-group) have been extensively studied at $GABA_A$ receptors (reviewed in Seljeset et al., 2015), its binding site and a mechanism of action remain unknown.

Of interest, these compounds are quite promiscuous (Harteneck, 2013). In addition to the effects imparted at $GABA_ARs$, sulphonated-steroids (including PS and DHEAS) have been shown to have functional effects at other pLGIC family members inhibiting GlyRs (and, as shown in chapter 3, the *C. elegans* GluClα receptor; Fodor et al., 2006). Moreover, PS has been shown to induce ligand-dependent potentiation of NMDARs (Wu et al., 1991; Malayev et al., 2002) and activating effects at Transient Receptor Potential (TRP) channels (Wagner et al., 2008). Regardless of its apparent non-selective nature, PS is one of the most abundant neurosteroids in the brain (Robel and Baulieu, 1994) and is being assessed for its efficacy in treating cognitive and behavioural disorders in mental disorders (Smith et al., 2014). Critical to its therapeutic application will be a more detailed understanding of the mechanism by which it acts at pLGICs, particularly the $GABA_AR$, with new findings potentially assisting rational-based drug design around the sulphonated-steroid backbone.

In this chapter, we have identified an agonist-dependent inhibition of the prokaryotic pLGIC ELIC. As in the previous chapter, and without access to an abundance of high-resolution structural models of eukaryotic receptors, we have used ELIC (for which

there are well-characterised purification and crystallization protocols) as a surrogate model of a eukaryotic pLGICs (Hilf and Dutzler, 2008) for studying the mechanism of binding and action of an inhibitory neurosteroid. In addressing this question we have developed a multi-disciplinary experimental approach using native mass spectrometry, X-ray crystallography and cryo-electron microscopy.

Inhibitory steroids, including PS and DHEAS, are major brain 'inhibitory' neurosteroids, formed during cholesterol metabolism via the precursor pregnenolone (*Fig 6.1*) (Compagnone and Mellon, 2000). In a manner distinct to the potentiating neurosteroids, these compounds impart non-competitive antagonist effects at $GABA_ARs$ (Shen et al., 2000; Akk et al., 2001). The two aforementioned examples, PS and DHEAS, are structurally distinct to the potentiating neurosteroids by the presence of a sulphate group at the C3 position of the steroidal A-ring (*Fig 6.1;* Gibbs et al., 2006). Surprisingly however, this distinctive substituent is not critical to the inhibitory response (with previous studies showing that similar compounds lacking a charged group at this position also inhibit $GABA_A$ receptor function; Wang et al., 2002).

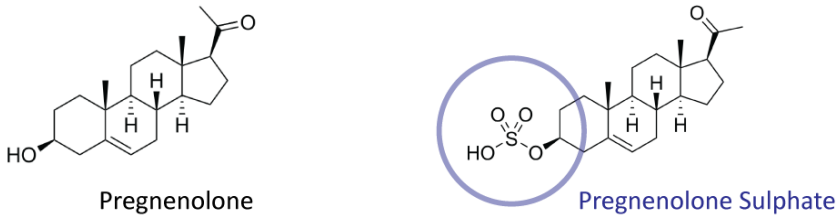

Figure 6.1 - Chemical structures of pregnenolone and pregnenolone sulphate

Chemical structures of pregnenolone (potentiating) and pregnenolone sulfate (inhibitory) are shown. The charged sulphate group of PS at C3 of the A ring is highlighted by a blue circle.

Besides the differential effects imparted by the compound's structure, many functional studies have sought to understand the mechanism of action of inhibitory steroids at $GABA_ARs$, by identifying a receptor binding site. Electrophysiological studies of

neurosteroid-mutant $GABA_A$ receptors (at the critical binding Q241 and transduction W245 M1 residues) reveal that the inhibitory steroid PS is unlikely to act through binding at an overlapping site to that suggested for the potentiating steroids (Majewska et al., 1990; Park-Chung et al., 1999; Akk et al., 2008). Indeed in our studies of chimeric $GABA_A$ α1 TMD receptors this was also apparent (Chapter 3). Additional studies have focused on the role of the $GABA_AR$ α subunit M2 2' residue in inhibitory steroid sensitivity (Akk et al., 2001; Wang et al., 2006; 2007). Whilst mutation of the α1 2' valine (256) to serine was sufficient to reduce sensitivity 30-fold (Wang et al., 2006), the lack of voltage sensitivity in the inhibition caused by this sulphated neurosteroid does not fit with the properties of a charged compound acting as a (presumed) channel blocker (Akk et al., 2001; Eisenman et al., 2003). Further comparative structure-function studies using the invertebrate GABA receptor orthologue, UNC-49 (from *C. elegans*) have suggested a role for α subunit M1 residues. Residues at the extracellular end of M1 in UNC-49C were found to have a dramatic effect on PS sensitivity (in studies of chimeric receptors formed from UNC-49B with the more sensitive UNC-49C; Wardell et al., 2006; Twede et al., 2007). Given the likely location of these residues and their proximity to pre-M1 and M2-M3 loops (both critical elements in receptor gating) these appear as potential candidates for binding and/or transducing an inhibitory signal. However studies of the equivalent residue positions in mammalian $GABA_ARs$ (composed of α1β2γ2) did not indicate a similar conserved role for M1 residues in mediating the inhibitory (sulphated) steroid response (Baker et al., 2010).

Evidently, the manner in which inhibitory steroids act at pLGICs, and the $GABA_A$ receptor in particular is complex. As discussed briefly in Chapter 3, the inhibitory steroid PS may show preferential binding to distinct kinetic states of the receptor and seems to impart its inhibitory effect by promoting entrance of the receptor into the desensitized state (Akk et al., 2001; Eisenman et al., 2003). Moreover, it is not implausible that this class of steroids imparts its effects through localised interactions with the lipid-bilayer encasing the receptor (Sooksawate and Simmonds, 2001).

In order to address the question of how inhibitory steroids act at the molecular level we were keen to take advantage of the apparent promiscuity in the pLGIC family for PS. As for studies of anaesthetic binding at GLIC, it might be that binding of PS at a homologous receptor is via a site that is conserved through evolution and thus relevant to the $GABA_AR$. Whilst GLIC exhibits relative insensitivity to PS, we found that ivermectin activated currents at $GluCl(\alpha1)_{cryst}$ were inhibited by micromolar concentrations of PS. Though previously crystallized, and thus a strong starting model for high-resolution structural analysis of allosteric modulation by PS, crystallographic studies of the GluCl receptor are hampered by the necessity of including Fab antibody fragments to obtain atomic resolution data (Hibbs and Gouaux, 2011; Althoff et al., 2014). The response of the prokaryotic pLGIC ELIC to PS has not been reported, and thus we were keen to determine whether this receptor (which intriguingly is GABA-gated) also exhibits sensitivity to steroidal inhibition. By virtue of its amenability to receptor purification and crystallization, high-resolution studies of ELIC have identified binding sites for a number of inhibitory ligands; divalent cations, the anaesthetic bromoform and also the novel Alzheimers' medication memantine (the binding sites of which are summarised in *Fig 6.2;* Hilf and Dutzler, 2008; Zimmermann et al., 2012; Spurny et al., 2013; Ulens et al., 2014).

We have used electrophysiology to screen ELIC for inhibition by PS for follow-up studies using biochemical and structural biology approaches (with purified receptor) for the identification of potential inhibitory steroid binding sites. We reason that by using mass spectrometry, X-ray crystallography and cryo-EM, this would enable a complementary approach to studies of a drug that seems to impart distinct effects in a receptor, particularly dependent on the receptor's kinetic state.

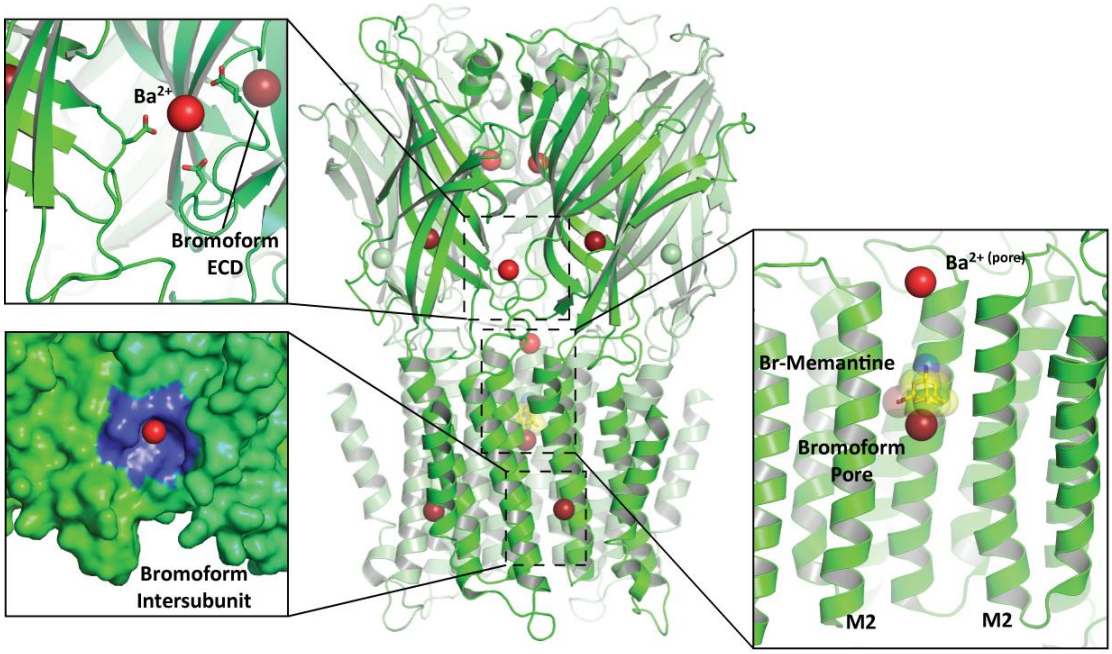

Figure 6.2 - Inhibitory ligand binding sites at the prokaryotic pLGIC ELIC

The overall structure for ELIC in complex with Ba^{2+} (red sphere; PDB 2yn6) is shown (central, left top and right panel). Ligand bound structures for ELIC-Bromoform and ELIC-Bromo-memantine were aligned and ligands (space fill representations) superimposed on to the ELIC-Ba^{2+} structure for comparison. Panel left top; A binding site for divalent ions (responsible for mediating inhibition) was identified through barium binding (red sphere centre) in the ECD below the ligand-binding pocket (at subunit interfaces), co-ordinated by the side chains of acidic amino acids. Note bromoform molecule in foreground, binding at ECD site. Panel right; close up view of the channel pore (proximal two subunits are removed for clarity) revealing additional barium ion binding site at the extracellular end of the channel as well as overlapping bromoform and bromo-memantine pore block sites (~16' in M2). Panel left bottom; shows an intersubunit binding site for bromoform molecules formed from a cavity at the intracellular end of the TMD.

6.2. Results

6.2.1. GABA-gated currents are inhibited by Pregnenolone Sulphate

A previously published screen reported the effects of range of $GABA_A$ receptor modulators at ELIC, but did not assess the sensitivity of ELIC to a member of the

inhibitory class of steroids (Spurny et al., 2012). Of the compounds screened, alphaxalone (used at 100 µM in electrophysiological recordings) was the only steroid tested of similar chemical structure to the inhibitory steroids and this failed to exhibit notable positive or negative allosteric modulatory effects (normally it will potentiate at native $GABA_A$Rs).

To assess the sensitivity of ELIC to PS, we used TEVC electrophysiology with injected oocytes and recorded agonist-induced currents in the presence or absence of PS. GABA has been identified as an agonist of ELIC, binding at the orthosteric binding site (as determined from crystallographic studies; Spurny et al., 2012). It should be noted that divalent cations were included in the recording solution, despite previous observations that divalent cations allosterically regulate ELIC in a negative manner (Zimmermann et al., 2012). This is most likely to be through ion coordination at a binding site in the outer rim of the extracellular domain (between adjacent subunits of ELIC; *Fig 6.2*). Whilst divalent cations (principally Ca^{2+} and Mg^{2+}) in the recording solution are likely to affect ELIC activation by GABA, we reasoned that they were unlikely to alter the sensitivity to PS through binding at a competing site (with PS presumably modulating at the level of the TMD). Moreover, in absence of divalent cations, ELIC activation is dramatically slowed (only reaching peak amplitude in the order of minutes) and apparently non-desensitizing during prolonged exposure, making experimental recordings difficult. When divalent ions are included in the recording solution ELIC activates rapidly upon exposure to GABA, and this response desensitizes during prolonged exposure (*Fig 6.3 A*). Deactivation is relatively fast upon agonist removal. Given that this response is most akin to that observed at a $GABA_A$ receptor we maintained these recording conditions for PS sensitivity experiments.

After pre-incubation of oocytes in PS and co-application of 30 mM GABA we observed a dramatic reduction in the peak current amplitude, which increased with micromolar concentrations of PS (*Fig 6.3 A and B*). At 100 µM PS there was near complete inhibition of current (*Fig 6.3 A & B*). Even at high concentrations, the wash-out of steroid is not notably slowed following removal of GABA/PS. In separate experiments we also observed inhibition to a similar extent (at 100 µM PS) following ELIC activation by an alternative orthosteric agonist, propylamine (data not shown). For both agonists,

activation is not dependent on the presence of divalent cations in recording solution. For purposes of gauging the relative sensitivity of ELIC to PS, the inhibitory curve sits within the range of 10-100 µM (*Fig 6.3 B*). In this regard there is slight reduction in PS sensitivity when compared to eukaryotic $GABA_A$ receptors (reported values typically in the low micromolar range; Wang et al., 2006; 2007; Sachidanandan and Bera, 2015). This may reflect the notable differences in receptor activation kinetics.

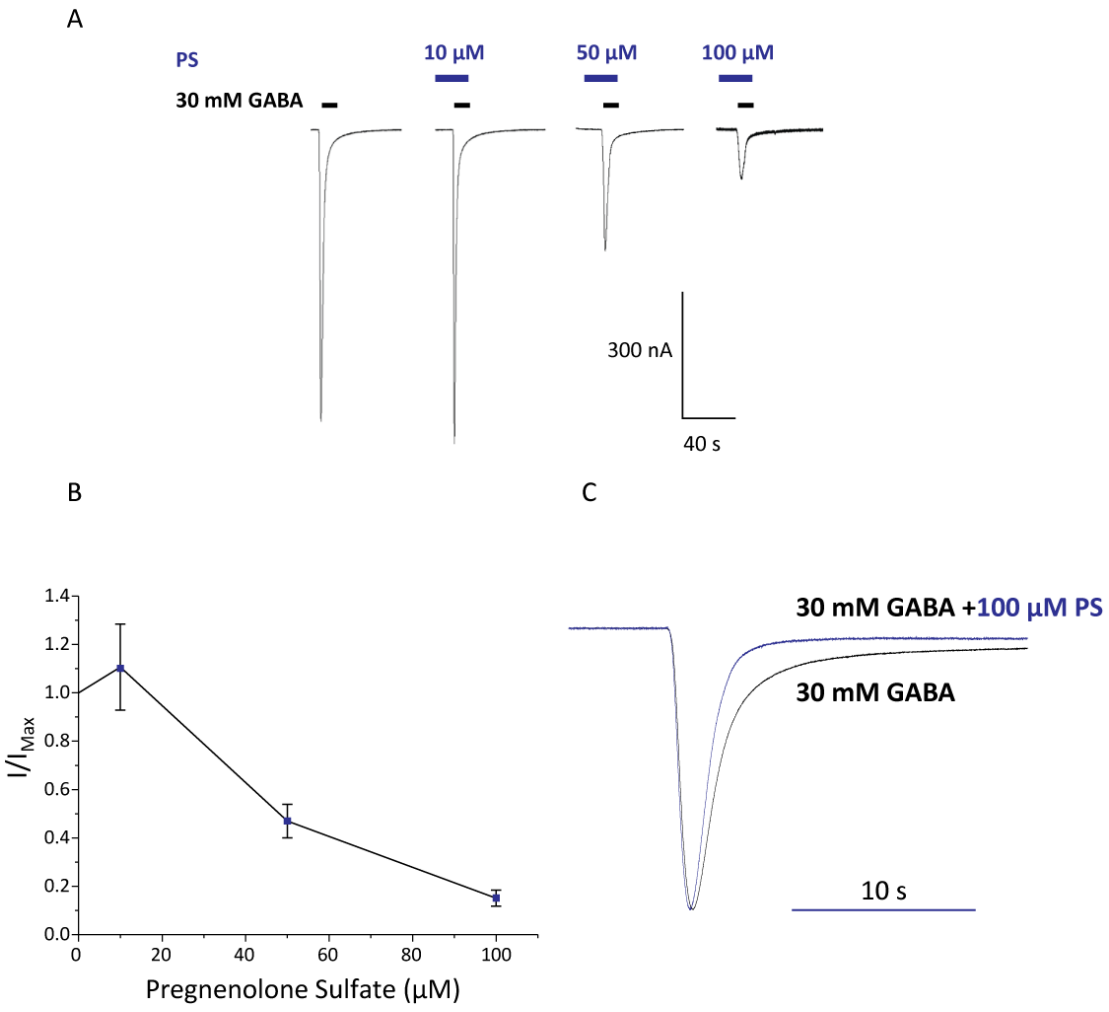

Figure 6.3 - Electrophysiological studies of ELIC inhibition by PS

A. Membrane currents elicited by GABA application recorded from oocytes expressing ELIC in the absence or presence of pregnenolone sulphate (PS). Note oocytes were pre-incubated in PS prior to agonist application. **B.** PS inhibition curve for ELIC for 30 mM GABA response. Points are normalised to a control 30 mM GABA response. Points are mean ± sd from n=4 oocytes. **C.** Peak normalised response of membrane currents recorded from co-application of 30 mM GABA +/- 100 µM PS. Note the faster decay in the presence of PS.

In separate studies we assessed the effects of co-applying agonist and PS on ELIC function. In a manner reminiscent of that observed at $GABA_A$ receptors we observed a reduction in the inhibition of the peak current response, however there was an apparent increase in the rate of current decay during prolonged exposure (*Fig 6.3 C*). It would appear (from the 'pre-incubation' studies; *Fig 6.3 A & B*) that PS is able to bind to the resting state of the receptor, preventing activation upon agonist exposure. In the 'co-application' of agonist and PS (*Fig 6.3 C*), it appears that PS promotes occupancy in the closed-desensitized state (when considered at the macroscopic level). It is difficult to derive the precise kinetic model for PS inhibition of ELIC (and extract a precise PS sensitivity) from electrophysiological recordings carried out thus far. Crucially however, the inhibitory profile observed is not overtly dissimilar to that observed at mammalian $GABA_A$ receptors. Thus a potentially common binding site for PS may have formed early on in evolution. Therefore we used ELIC as a model for structural studies of negative allosteric modulation of a pLGIC by PS.

6.2.2. Biochemical and structural biology approaches

Having established that the prokaryotic receptor ELIC, like metazoan pLGICs including the $GABA_A$ receptor, is inhibited by PS, we sought to establish a structural mechanism for inhibition. We also aimed to determine a three dimensional binding site for PS. In our attempts to do so we employed a range of biochemical and structural biology approaches to corroborate functional findings (*Fig 6.4*). Given the amenability of ELIC to high-level bacterial expression for detergent solubilisation, receptor purification and crystallization we were keen to assess whether we could generate co-crystal complexes of ELIC in the presence of PS (and agonist). Given the restricted nature of the crystal form, particularly for ELIC, in determining receptor structure in distinct gating states (Cecchini and Changeux, 2014), we were concerned that binding and co-crystallization of ELIC with PS may be not be favoured.

To date, in all reported structures of ELIC in the absence and presence of both agonists and allosteric modulators, the channel resides in a profile delineating a closed non-

conductive state (Hilf and Dutzler, 2008; Gonzalez-Gutierrez et al., 2012; Spurny et al., 2012). As to whether this represents the receptor in a closed-inactive or closed-desensitized state is not immediately clear. Given the likely complex kinetic profile of PS inhibition, we were concerned that the propensity for ELIC to crystallize in a single form might restrict either PS binding or in the case of successful neurosteroid binding, that the receptor might not display a structural state truly reflective of one observed in its physiological environment (i.e. in a lipid bilayer). We therefore sought to address the question of structure determination in a manner that would be free of the potential restraints imposed by the crystal form, namely, electron cryo-microscopy (cryo-EM; *Fig 6.4*). As introduced in previous chapters (and *Appendix Primer 1*) this technique allows for direct imaging of solubilised receptor protein (Cheng et al., 2015), and thus is an appealing method for elucidating structures of the same protein in distinct conformations – something that has yet to be truly achieved for ELIC. Given the proven stability and yield of purified ELIC (in detergent micelles), and the potential questions one might address, we reasoned that this might be a perfect candidate receptor for optimizing cryo-EM studies of a pLGIC.

The final approach we have used in our study of PS binding at ELIC is native mass spectrometry (nMS; a technique used in previous chapters to define molecular mass of intact receptor pentamers). This challenging technique, pioneered by Carol Robinson's group, allows for the characterisation of membrane proteins in various oligomeric states devoid of detergent molecules (upon projection into the gas phase) as well as the critical assessment of lipid and small molecule binding in the intact protein complex (Barrera et al., 2009; Laganowsky et al., 2013; 2014). Furthermore, through employing ion-mobility (IM) MS measurements, it is feasible to determine the extent to which bound lipids and molecules enhance resistance to gas phase unfolding, and thus are stabilizing protein structure (Laganowsky et al., 2014). Through generating well resolved mass spectra for protein complexes and their associated charge states, it is possible to identify and then distinguish the binding of lipids and small molecules at interfacial sites (in an oligomeric complex), as 'plugs' in channels or in the bulk lipid bilayer (*Fig 6.4*; Bechara and Robinson, 2015). We reasoned that with sufficient optimization, we might use native (IM-)MS to address questions regarding the direct-

association of PS with the pentameric ELIC complex, or whether PS inhibitory effects occur in a more transitory manner, through interactions at the receptor periphery with the surrounding lipid bilayer.

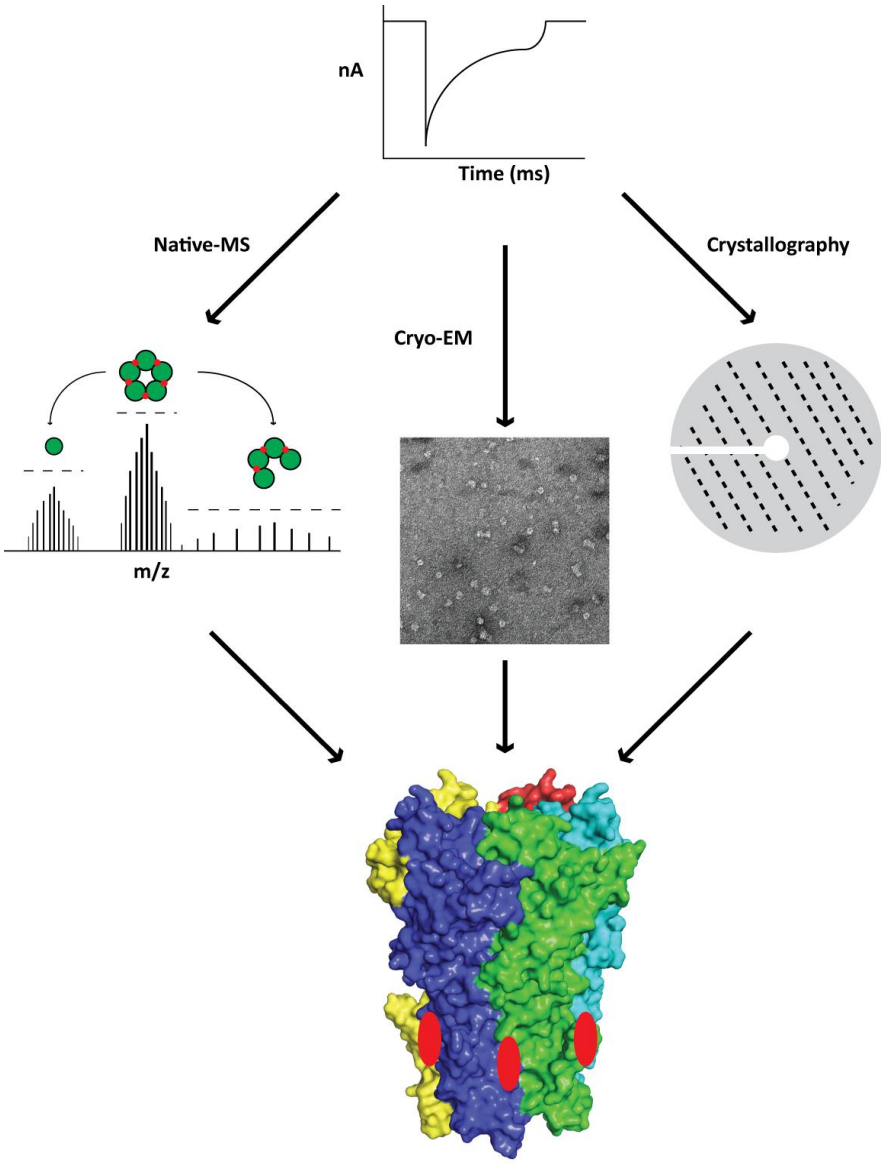

Figure 6.3 - Integration of biochemical and structural biology techniques to address the inhibitory binding site for PS

We will use three techniques to provide structural information for PS binding to ELIC. Native IM-MS of protein complexes can reveal the association of lipids or small molecule with intact protein or distinct oligomers. Here ligand (shown as red circles) binds at subunit interfaces and is associated with pentameric and a 'stripped' tetramer but not with a dissociated monomer of a pLGIC. Cryo-EM and crystallography allow for high resolution structural determination (in the absence or presence of ligands). A successful combination of all techniques allows for molecular determinants of binding and mechanism of action to be defined.

6.2.3. Purification of ELIC

As for its prokaryotic counterpart (GLIC) a well-established procedure exists for high level bacterial expression and purification of ELIC (Hilf and Dutzler, 2008). Once again this takes advantage of the stabilizing properties bestowed by the addition of a soluble MBP-fusion tag (during initial detergent extraction and affinity purification steps). As for GLIC, proteolytic cleavage of the N-terminal (His-) MBP portion of the fusion protein is required for isolation of the mature pentameric ELIC-detergent complex for further structural analyses.

Essentially, as described in the previous chapter for crystallographic studies of GLIC (and as detailed in Materials and Methods), MBP-ELIC was expressed at high-levels in large bacterial cultures. However, for ELIC, detergent extraction and receptor purification was carried out in UDM (a similar maltoside-derived detergent). We were consistently able to purify upwards of 10 mg of fusion protein. This protein was relatively pure and free of contaminating proteins (*Fig 6.5 A*). Moreover, the high stability of the pentameric form of MBP-ELIC in UDM is immediately apparent from SEC, where UDM solubilised material, recovered by IMAC, runs in a monodisperse state (eluting as single symmetrical peak at approximately 12.7 ml; *Fig 6.5 A*). SDS-PAGE and coomassie blue-stain analysis revealed that this peak clearly corresponded to the MBP-ELIC fusion protein (migrating as a single homogenous band of ~ 70 kDa). After solution-cleavage of the MBP-fusion protein, using a dual-tagged (His- and GST-) HRV 3C protease, and "reverse-IMAC purification", the mature-ELIC (in complex with UDM) was obtained. This material is highly stable in the pentameric form as assessed by SEC (*Fig 6.5 B*). Purified receptor material elutes a single symmetrical peak at ~14.8 ml, consistent with the elution profiles of detergent complexed-pentameric GLIC, $GluCl_{cryst}$ and chimeric $GABA_A$Rs. SDS-PAGE confirmed that this peak corresponded to the cleaved ELIC, migrating predominantly as a homogenous band of ~30 kDa. The higher molecular mass bands most likely correspond to SDS-resistant receptor oligomers (*Fig 6.5 B*). Following analysis, the peak fractions were pooled and concentrated depending on their application.

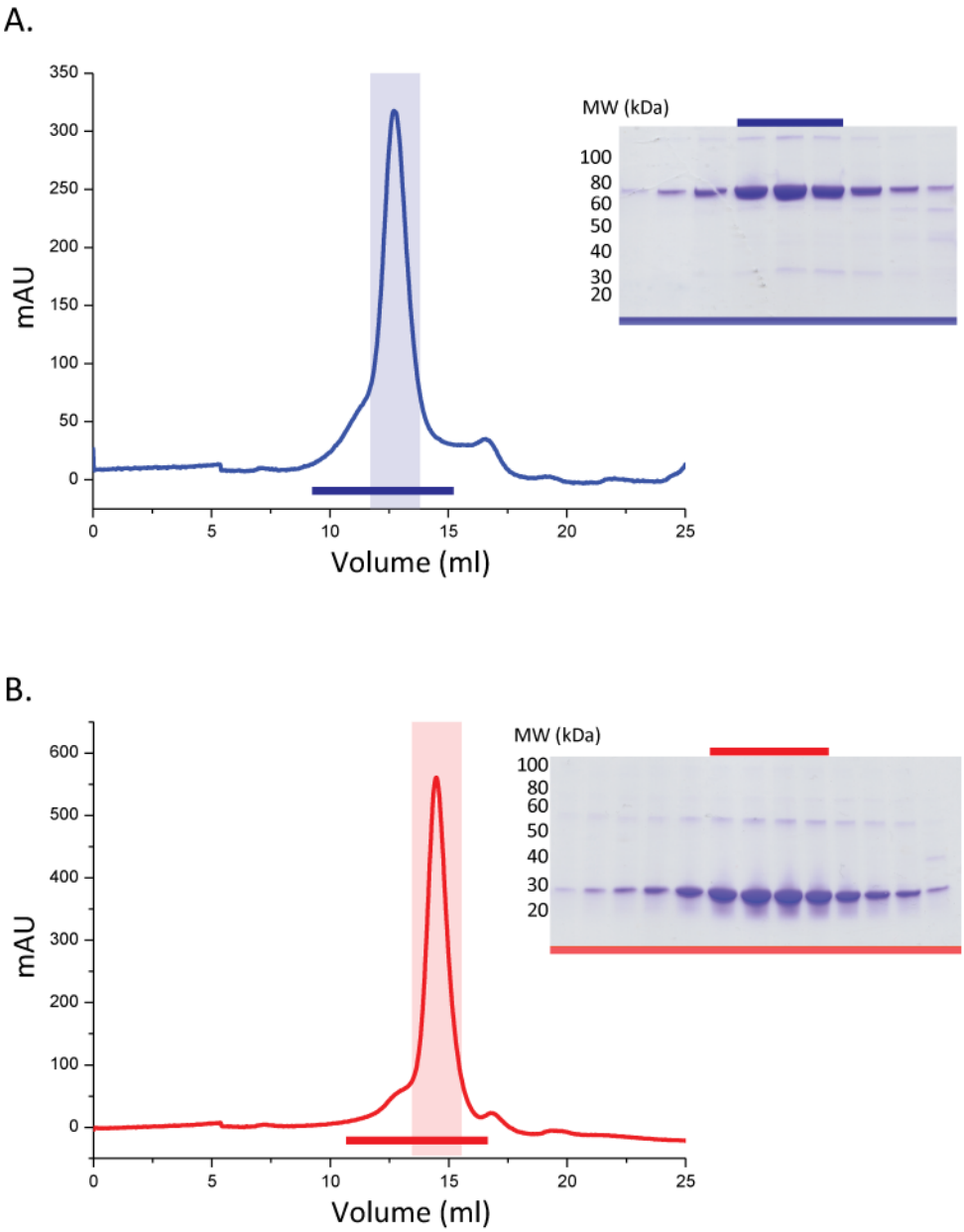

Figure 6.5 - ELIC forms a stable pentameric complex in UDM

A. SEC profiles of uncleaved-MBP-ELIC (in UDM). The pentameric fusion protein purifies in a largely monodisperse state, with the pentameric complex the predominant species (shaded portion). Inset; SDS PAGE of SEC fractions (corresponding to the blue bar below the SEC trace). **B.** SEC profile of (proteolytically) cleaved-ELIC (in UDM). The pentameric complex elutes as a single symmetrical peak (shaded portion was pooled and concentrated for crystallization). Inset shows SDS PAGE of SEC fractions (corresponding to red bar below the trace). Protein migrates largely as a homogeneous band at ~30 kDa.

6.2.4. Crystallization of ELIC in complex with PS (and agonists)

Given the abundance of purified protein that can be isolated (upwards of 2 mg per preparation) and the well-defined crystallization conditions that have been reported for ELIC, we first addressed ELIC crystallization in complex with PS. It is notable that of the 15 crystal structures reported for ELIC, the vast proportion used identical crystallisation conditions (yielding only one crystal form that is not isomorphous to the originally reported apo-form). To address crystallization in an unbiased manner, and introduction of a new ligand for ELIC (PS), we screened crystallization using membrane protein specific-sparse matrix screens (MemStart/Sys, MemGold and MemGold II - introduced in Chapter 4). In all previous crystal structures of ELIC, equilibration of the receptor in lipids prior to crystallization was apparently essential in generating high-resolution diffraction data. We therefore pre-equilibrated our protein samples with one of two phosphatidylcholine phopsholipids, 1,2-dipalmitoyl-*sn*-glycero-3-phosphocholine (DPPC) or 1-palmitoyl-2-oleoyl-sn-glycero-3-phosphocholine (POPC). It should be noted that the lipid molecules associated with the ELIC receptor have not yet been reported in crystallographic data sets, and thus we cannot be sure of the manner in which these lipids interact with and stabilize the protein during crystallization. The protein was subsequently mixed with PS and crystal drops set in the presence or absence of an orthosteric agonist (GABA or propylamine). We reasoned that agonist activation of the receptor in detergent micelles might be necessary for PS occupation of its receptor binding site in the crystal form.

Surprisingly, we found that a large number of conditions supported crystallization (as assessed by results from sparse matrix screening). Unsurprisingly, a condition previously reported to allow for receptor crystallization (and generation of strongly diffracting crystals) was also a crystal growth 'hit' in early trials. ELIC crystals typically formed large rod or extended rectangular prism crystals (>100µm in longest dimension; *Fig 6.6*). Of more than 10 crystallization conditions assessed for (X-ray) diffraction (before further crystal growth optimization) we found that almost all exhibited protein diffraction. Typically crystals diffracted maximally to at least 10Å. For five 'newly identified' conditions, diffraction extended to 5Å, and in the case of two of

these hits, diffraction approached 4Å (one of which is shown in *Fig 6.6*). For these crystals we were able to confidently assign a three-dimensional space group to ELIC crystals grown in the presence of PS. Crystals were of the space group $P2_1$ and in that respect were identical to the majority of previously reported ELIC crystal structures. At this stage crystal quality was insufficient to collect complete data sets at the maximal observed resolution. Whilst it was possible to index and integrate reflections for generation of a low-resolution model (by molecular replacement) it is not possible to identify specific structural features. The α-helices of the TMD are clear as tube-shaped sections of density, and the β-sandwich of the ECD formed a large sheet of density. At this resolution we are unable to assign the receptor to a definitive activation state, or identify bound ligand or model residue side chains.

We chose to focus our initial crystal growth optimization on a small number of newly identified hits (exhibiting strongest diffraction) as well as a previously reported ELIC crystallization condition(Hilf and Dutzler, 2008). Whilst new hits yielded crystal space groups identical to that previously reported, we reason that these were more likely to represent receptor crystallized in a distinct conformation to that observed in previously reported structures. Extensive crystal growth optimization was carried out at three temperatures; 4°C, 16°C and 22°C; under two different vapour diffusion strategies - hanging and sitting drops; in the presence of a combination of antagonist (PS), lipids (DPPC or POPC) and agonist (GABA or propylamine). In agreement with results from the initial screens, crystal growth was reproducible and consistently observed across a number of optimization screens. Assessing the effects of crystal growth optimization in extending the diffraction limit has thus far not yielded further success. Never-the-less, we have still to fully determine the importance of varying crystal cryo-protection prior to diffraction data collection; the effects of small molecule additive screening and the potential use of crystal-seeding (as introduced in chapter 5). Ultimately given the long list of diffracting hits in preliminary screens, identifying those with the greatest potential will be critical.

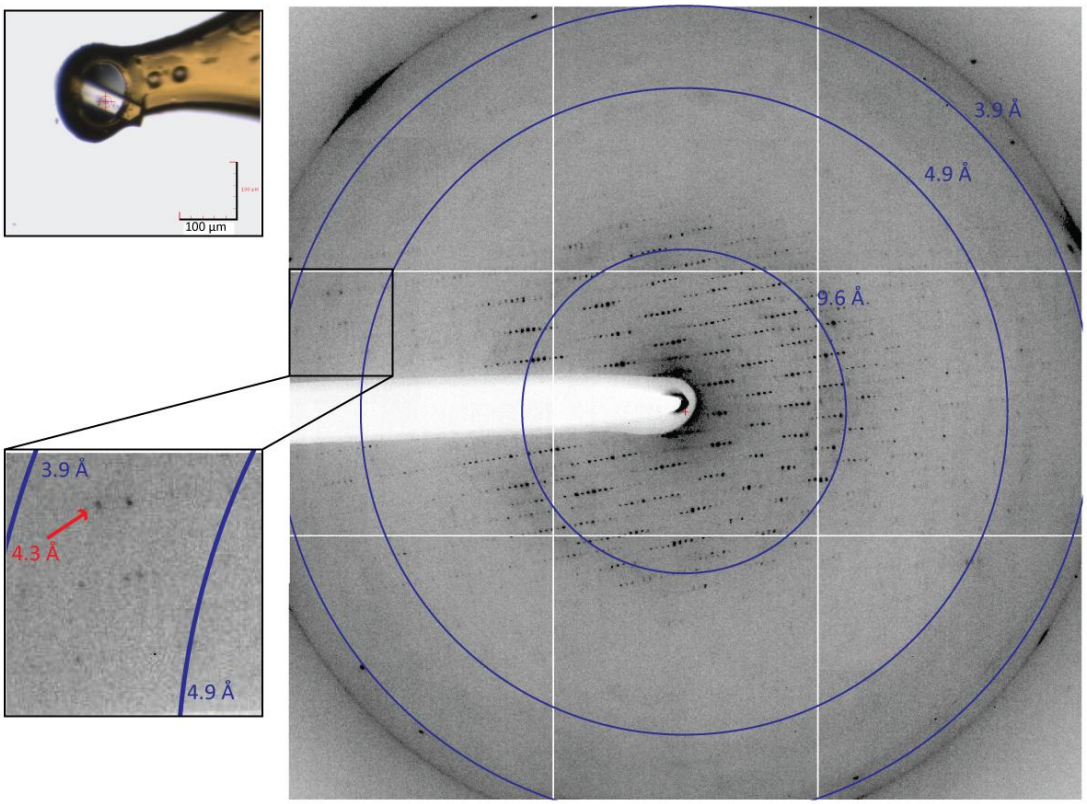

Figure 6.6 - Diffraction pattern for crystal of ELIC

X-ray diffraction pattern (0.5° oscillation range) from a crystal (top left panel) of ELIC grown in the presence of UDM, lipids and PS using microfocus beamline (Soleil Proxima 2). Resolution rings in the main diffraction at 9.6, 4.9 and 3.9Å are shown as blue circles. Lower left panel; magnified section of the diffraction image showing spots near to the diffraction limit, ~4.2 Å (resolution rings of 4.9 and 3.9 Å are shown in inset as blue circles). Data sets were collected for this crystal (though only complete at lower resolution) and indexed successfully as space group $P2_1$.

6.2.5. Electron-microscopy of ELIC

On the basis of the high yields of purified ELIC that could be generated, extensive screening of crystallisation was possible. However, what became clear from our efforts to co-crystallize GLIC (in Chapter 5) and ELIC, is that the bacterial pLGICs homologs should not be viewed as a panacea for rapid progression to high-resolution structural solutions. The addition of larger more complex molecules to the receptor-detergent complex could disrupt the ordered packing that is observed for receptors in their native-apo states. For example, PS is a significantly larger structure compared to

ligands previously crystallised in complex with ELIC and also GLIC. However the large macrocyclic lactone, ivermectin, could be crystallised in complex with GluClα (Hibbs and Gouaux, 2011).

We therefore explored structure determination by using alternative means, namely cryo-EM. The rapid developments in this technique (as described in the *Appendix Primer 1*) make this a highly appealing technique for structure determination at near-atomic resolution, especially for challenging proteins, such integral membrane proteins (Liao et al., 2013; Cheng et al., 2015; Bai et al., 2015a). Moreover this technique no longer requires the production of large amounts of protein or well-ordered crystals. Despite these advantages, cryo-EM has its own set of technical challenges and caveats (Cheng et al., 2015). We attempted to optimize ELIC channel preparation for cryo-EM with a view to allowing data collection for single-particle cryo-EM (and eventual structure determination). We view this not only as an important step in attempting to solve the "in-solution" structure of ELIC, but also in establishing quality sample preparation that might be applied to alternative pLGICs, namely chimeric $GABA_AR$s, for single-particle analysis.

The results of the following section are part of a collaborative project with Dan Kofi-Clare (and Helen Saibil, Birkbeck); who prepared EM grids, collected electron micrographs and carried out initial data analysis. We prepared and optimized protein-detergent complexes for EM and assisted with image acquisition. An overview of experimental procedures and image analysis is provided in the Materials and Methods and Appendix.

ELIC was previously prepared (for X-ray crystallography) in sodium phosphate buffered solution, however this buffer displays unfavourable properties in EM studies causing high background signal. Receptors were therefore exchanged in to Tris-buffer (and UDM) by using SEC prior to EM grid preparation (*Fig 6.7 A*). ELIC retains its stability as a pentameric-detergent complex during this purification step (with SEC profiles displaying a sharp symmetrical peak of identical elution volume to that of the receptor purified in phosphate buffer). SDS PAGE and coomassie-staining revealed no receptor degradation and an extremely high degree of purity (>95%).

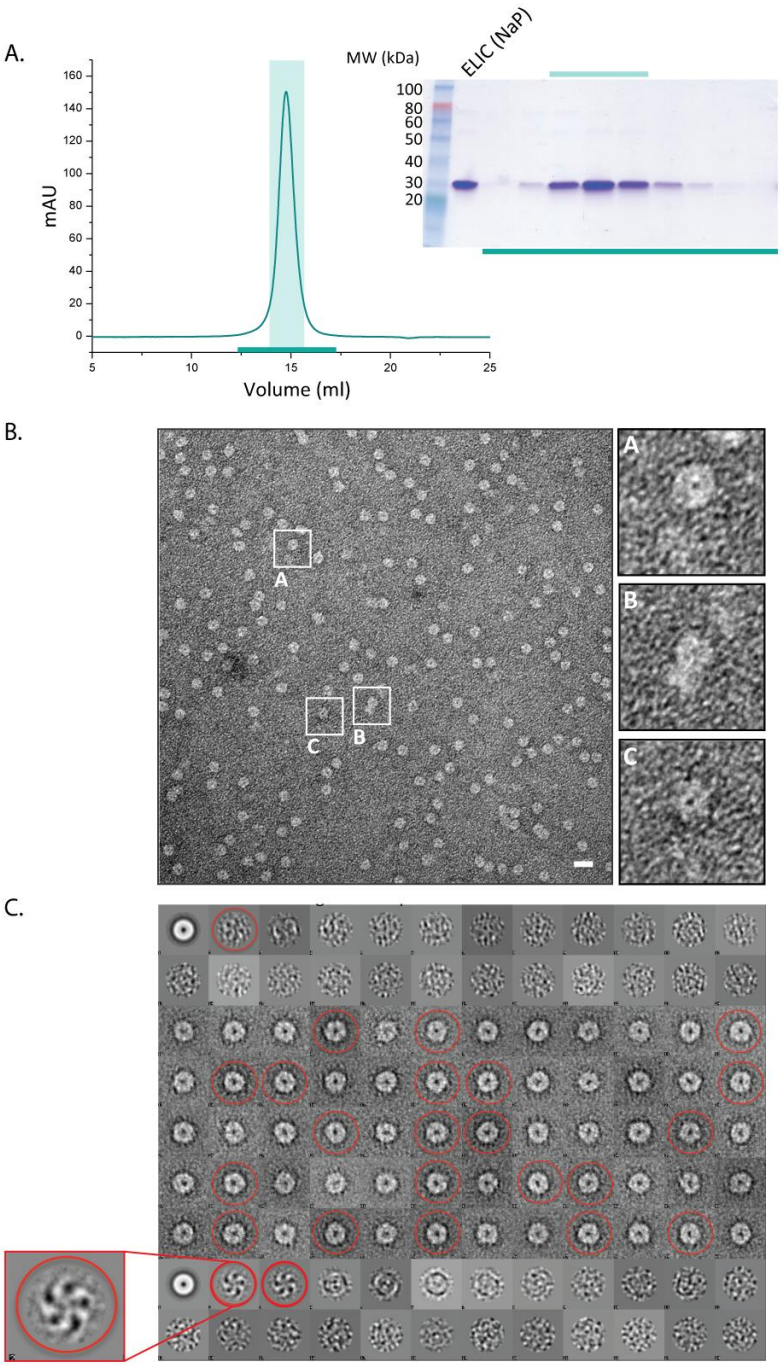

Figure 6.7 - Tris purification, negative stain, symmetry analysis (UDM).

A. SEC profile for ELIC (in UDM) following exchange in to Tris-buffer (fractions corresponding to the shaded section were pooled for EM experiments). Inset shows SDS PAGE analysis of SEC fractions (starting material for buffer exchange is labelled as ELIC (NaP)). **B.** Negative-stain EM images of purified ELIC in UDM. Receptors preferentially adsorb to (continuous) carbon-coated grids in "end view" orientation. Two typical particle "end views" and one "side view" are highlighted by white boxes and shown magnified in side panels (A-C). Scale bar is 160 Å. **C.** Eigen-image analysis reveals five-fold symmetry expected of a pentameric receptor, emphasized in the magnified image (left inset).

We first needed to establish the sample conformation and compositional heterogeneity of ELIC in detergent (i.e. does the receptor form single particles or clusters of intact particles) by using negative-stain EM. Diluted samples of ELIC were applied to (glow discharged) EM grids with a continuous carbon film, stained with uranyl acetate before imaging (on a Tecnai T12 TEM at 67,000x magnification). The high contrast of negative stain micrographs revealed that ELIC forms single receptor particles, with very few imaged grid regions displaying receptor clustering or aggregation (*Fig 6.7 B*). Grids were largely devoid of significant background staining or ambiguous particles, and thus presumably detergent molecules are almost completely incorporated into receptor-micelles complexes. What was apparent in negative-stain micrographs was the propensity for ELIC to adsorb to carbon films in a preferential "end-on" (plan view) orientation (*Fig 6.7 B*). The vast majority of receptor particles can be clearly visualised as prototypical receptor rosettes (formed by the pentameric arrangement of subunits around the central pore) with a diameter of ~80Å (Hassaine et al., 2014). In most micrographs a small number of particles could be visualized in a distinct, presumed, "side-on" orientation. Particles resembling a more rectangular structure, with a central invagination, presumably at the border between receptor ECD and TMD; *Fig 6.7 B)* Whilst providing immediate confirmation of receptor structural integrity, this high degree of sample homogeneity (with regard to receptor orientation) might prove problematic during latter particle picking and image processing for structure calculations.

From the micrographs collected, 1800 particles were picked to confirm that the end-on orientations corresponded to the intact pentameric receptor (*Fig 6.7 C*). Translational centering and alignment of particles and eigen image calculations allowed for generation of class averages. A second round of eigen image calculation using a subset of class averages enabled symmetry analysis of receptor particles. It is clear from image processing and analysis that, as expected for a pLGIC, particles in the "end-on" orientation display five-fold symmetry around the central axis (*Fig 6.7 C*).

While negative stain micrographs display exceptional sample homogeneity (i.e. few receptor clusters), this approach only reveals overall particle shape through negative

contrast. The native structure is likely to be distorted by sample dehydration (Saibil, 2000). Ultimately for structure determination, receptors must be prepared in vitreous ice for single-particle cryo-EM. During this vitrification process the sample is applied to a holey-carbon coated grid and plunged in to a coolant, typically liquid ethane. The result is the generation of a frozen hydrated sample in which native receptors are suspended and structure maintained (though particles now exhibit a lower contrast in the collected images; Saibil, 2000; Milne et al., 2013).

In preliminary sample preparation for cryo-EM we observed few particles suspended in the amorphous ice layer over EM grid holes (*Fig 6.8*). Ideally a high degree of protein should partition into grid holes in random orientations, which is necessary for image collection, particle picking and analysis. What became apparent is that receptor particles adsorbed to the carbon-coated grid, resembling train tracks of particles lined up along grid lines and projecting out in to ice (*Fig 6.8*). On the basis of negative-stain experiments, it is likely that receptors adsorb to the support film preferentially in an "end-on manner". The detrimental effects of the carbon support on image contrast mean that it is not possible to pick particles for image analysis. This phenomenon was consistently observed across grid regions and was independent of the thickness of the amorphous ice generated during sample vitrification. It is notable that these results are reminiscent of those observed in earlier studies of the kainate receptor, GluK2 (Schauder et al., 2013), on conventional holey-carbon supports (receptor adsorbing almost exclusively to carbon in a preferential orientation). For subsequent studies that yielded structures of GluK2 (and GluA2) it was necessary to chemically modify the grids to "drive" receptors into the grid holes (Meyerson et al., 2014a; 2014b).

Assessing various "grid supports" including graphene coated (Russo and Passmore, 2014) and poly-lysine treated grids had no apparent effect on preferential orientation and partitioning of apo-ELIC by negative-stain or cryo-EM. Moreover it appeared that incubation with agonists (GABA or propylamine) in the absence or presence of PS did not alter receptor orientation. We therefore reasoned that potentially the choice of detergent, UDM and its inherent micellar properties might be influencing the orientation which is detrimental for EM imaging (Hauer et al., 2015). Recent studies of

TRP channels and γ-secretase (allowing for eventual structure determination) found that it was essential to exchange detergent solubilised membrane protein in to an amphipathic polymer (amphipols, e.g. A8-35 and PMAL-C8; Liao et al., 2013; Cao et al., 2013b; Paulsen et al., 2015; Bai et al., 2015b). These amphipol surfactants are able to exchange with and substitute for detergents used in membrane protein extraction, whilst maintaining protein stability (Kleinschmidt and Popot, 2014). Moreover they have been found to improve the preparation of membrane proteins in vitreous ice for cryo-EM (Althoff et al., 2011; Liao et al., 2014).

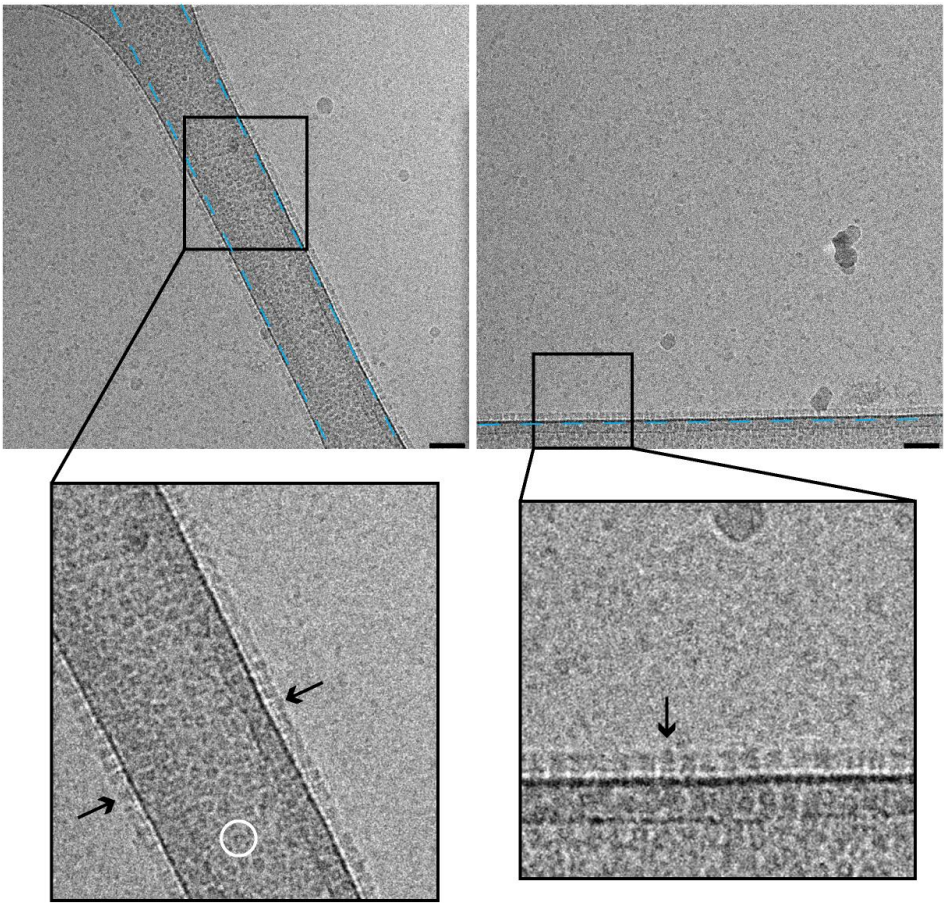

Figure 6.8 - Preliminary cryo-EM of ELIC in UDM

Two representative images of frozen-hydrated ELIC in UDM. Carbon segments of grids are regions of high contrast and are emphasised by dashed blue lines. Electron dense particles can be clearly seen as lines of receptor particles along hole edges and also on top of the carbon grid surface. These are shown in greater details in the magnified regions (lower panels). Receptors lining hole edge protruding into the ice are indicated by arrows and example of particles packed “on top” of the grid by a white circle. Scale bar is 50 nm.

ELIC purified in UDM was mixed at varying ratios of protein to the amphipol A8-35 (ranging from 1:3 to 1:10 protein: A8-35 w/w). During this incubation it is assumed that A8-35 exchanges with UDM in the protein-detergent micelle complex, eventually surrounding the receptor. Following removal of "free-detergent" molecules (with Bio-beads), the ELIC-amphipol complex was isolated by a further SEC purification step (in detergent-free aqueous solution; *Fig 6.9 A*). Receptor mixed with A8-35 at a 1:6 ratio exhibited a SEC profile with clearly defined peaks. The predominant (symmetrical) peak corresponded to the ELIC-amphipol complex, eluting at ~13 ml, and a second minor peak likely corresponded to excess free amphipol. We can infer the former from SDS PAGE analysis of peak fractions; material migrates predominantly as a band of expected mass for the monomeric ELIC receptor subunit; and from the shift in the elution profile of the ELIC-amphipol complex when compared to ELIC-UDM. The ELIC-amphipol complex now elutes earlier from the SEC column, indicative of a complex of greater mass (and potentially hydrodynamic radius) when compared to that of ELIC-UDM. This not surprising given that a single A8-35 molecule is of ~8 kDa (while UDM is ~0.5 kDa). It is not immediately clear how many molecules of A8-35 associate with the pentameric ELIC (of ~185 kDa). It should be noted a small shouldering peak is observed with an elution volume roughly equivalent to the mass of ELIC-UDM (~15.5 ml). Given that material collected from this peak corresponds to ELIC (as assessed by SDS PAGE analysis), it would suggest that this equates to a small portion of ELIC retained in UDM (and not exchanged for amphipol). For negative-stain EM characterization we pooled the peak fractions presumably corresponding to ELIC-amphipol.

Sample heterogeneity was assessed by using negative-stain EM (*Fig 6.9 B and C*). ELIC-A8-35 complexes were applied to carbon-coated grids. Additionally we tested grids which had also been treated with poly-lysine (thereby altering surface charge). Whilst ELIC-A8-35 (like the sample in UDM) does not show a propensity to cluster or aggregate, existing largely as single particles on the carbon support, in contrast to previous observations in UDM, the receptor now displays considerable heterogeneity with respect to particle orientation. The number of receptor particles in an "end on" orientation is now matched by those in other orientations. Particles of extended length and mushroom-shaped were also observed (likely representing particles in "side-on"

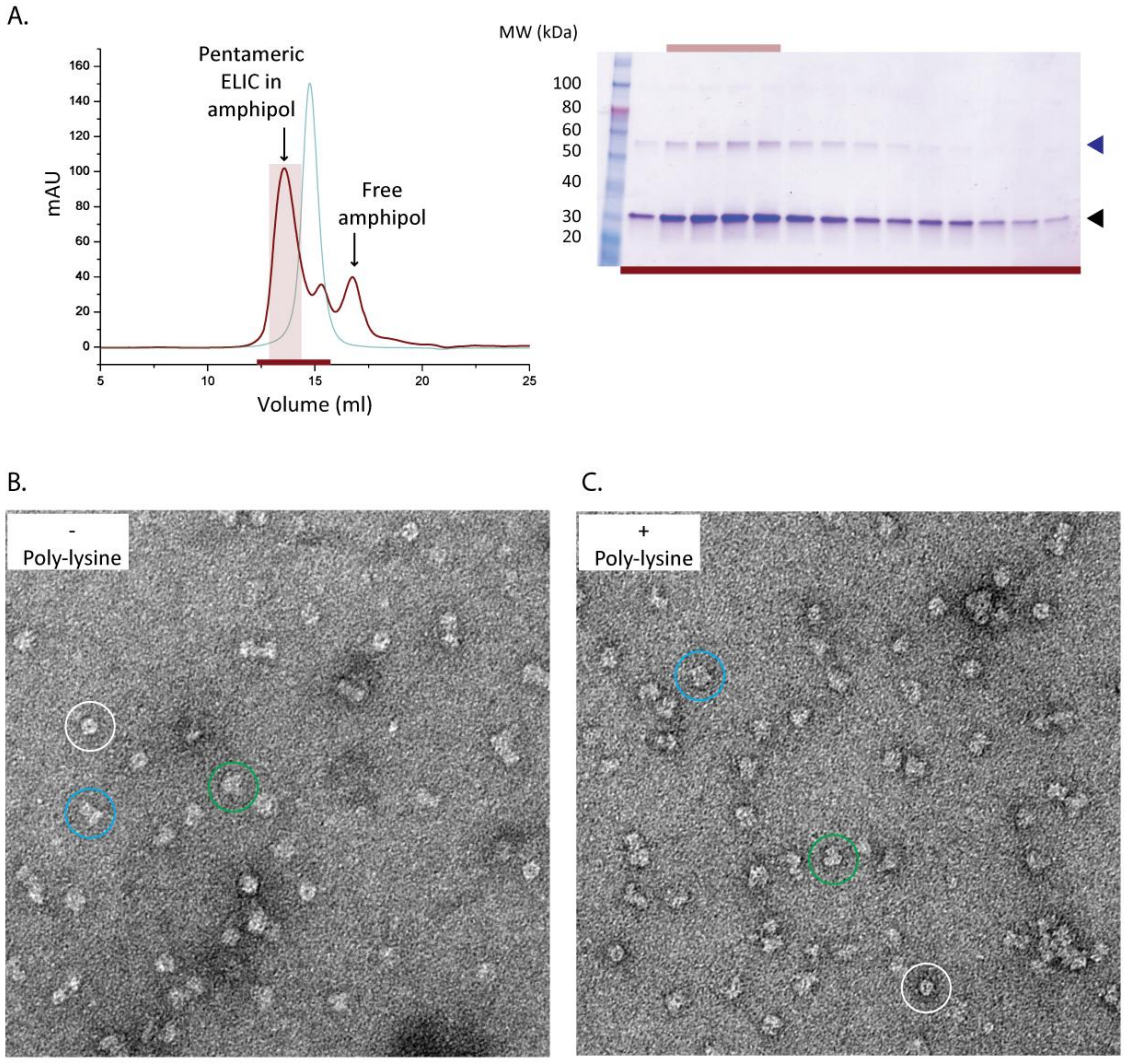

Figure 6.9 - Detergent exchange of ELIC in to amphipol, A8-35, and negative-stain EM

A. SEC profile of ELIC-A8 35 complex (overlaid with ELIC-UDM SEC profile, pale cyan). Pentameric ELIC-amphipol complex elutes at ~13 ml. Fractions from shaded section were pooled for studies. Inset right: peak fractions from SEC (corresponding to the dark red horizontal line in SEC profile) were analysed by SDS PAGE. Monomeric ELIC is indicated by a black arrowhead and detergent resistant dimer by blue arrowhead. **B.** and **C.** Negative-stain EM images of ELIC-A8 35 (on continuous carbon film). Receptor particles appear to occupy multiple random orientations in both the absence and presence of additional poly-lysine coating to EM grids. Three typical orientations are highlighted in both images; “end view” (white circles), “side view” (blue circle) and “tilt angle view” (green view). The tilt angle perspective for ELIC exhibits a “mushroom-like” appearance with extended “stalk”.

and “tilted” orientations). We assumed that effects on particle orientation are as a result of detergent exchange in to amphipol. Additionally we observed that altering the surface charge (through coating grids with poly-lysine) induced further effects on particle orientation (most likely an additive effect of altering surface charge and the nature of surfactant surrounding protein particle; *Fig 6.9C*). Given the large size of amphipol molecules, it is possible that some remaining free amphipols in the sample accumulate to form larger particulates or aggregates that might be of an equivalent size to the protein particle. However given the consistency of purified ELIC samples, and average particle size we are relatively confident that micrographs taken for ELIC–amphipol preparations do indeed represent receptor particles in multiple random orientations.

As before, negative stain EM serves only as a quality control step for sample preparation optimization and generating 2D averages of a set of particles (i.e. “low resolution” sample refinement). For “high resolution” sample refinement we must image vitrified samples by cryo-EM. As in previous cryo-EM experiments, ELIC-amphipol complexes were applied to holey (carbon) EM grids and vitrified by plunging in to liquid ethane. In initial imaging experiments we observed that whilst a significant proportion of protein was adsorbed on to the carbon, there is a large number of protein particles suspended in vitreous ice (partitioned) in the holes of the EM grids (*Fig 6.10 A)*. This contrasts with experiments carried out in UDM at equivalent protein concentrations (typically 2-3 mg/ml). Moreover, generation of tomograms (through reconstruction of 2D tilted images) reveals that the number of particles in the holes is too high at this protein concentration, and would likely complicate particle-picking and analysis. Due to the inherent low contrast of the samples in ice; the need to collect images using a microscope equipped with lower operating acceleration voltages; and the use of indirect detection device (for image recording) it was not immediately apparent whether particles reside in a preferential orientation in vitreous ice. At this stage grids were prepared without further alteration of the surface charge.

Having established a high quality sample preparation for cryo-EM, we collected cryo-EM images using a high power Polara microscope (operating at 200 kV) equipped with

a K2 direct electron detector (*Fig 6.10*). Owing to the improved sample contrast it was possible to assess sample heterogeneity in ice. Once again receptors appeared to be preferentially orientated in the "end-on" view – easily recognised as a ring of electron dense receptor subunits around a central pore. Despite this a number of other particle orientations could also be visualized (though not clearly distinguished by eye alone). We therefore generated 2D class averages from 4,500 particles (picked from 79 images; *Fig 6.10B*). Alignment and 2D classification is a critical step preceding 3D reconstruction and allows one to group the major views present in a data set and also remove 'bad particles' in a data set. Alignment and classification of particles was carried out in the software package RELION (**RE**gularised **LI**kelihood **O**ptimisatio**N;** Scheres, 2012).

2D class averages of images collected with the K2 direct electron detector revealed a number of important factors. Before considering particle orientation one must appreciate the greater detail obtained by "direct detection". "End" views of receptor show clear symmetry, and it is even possible to distinguish gross structural features (the helical bundle of the TMD). "Side views" reveal clear demarcation between the ECD and the TMD, and location of the outer vestibule and pore along the long axis of the receptor (*Fig 6.10 B*). With respects to receptor orientation, there are a number of notable observations. Firstly; the "end-on" view is highly populated when compared to other views (as indicated by the number of classes in which this orientation is observed). Secondly; there are few "bad or junk" classes (in which the nature of the particles is not obvious). Thirdly; an additional class of potentially "tilt" viewed receptor particles is also apparent. Finally, and most striking, is the presence (in initial rounds of alignment and classification) of double complexes resembling an "end view" particle associated with an additional "side view" particle. A second round of alignment and classification confirms this observation.

We are currently further assessing particle classification (in parallel to subtle variations in sample preparation) to determine the amenability of this data set to initial 3D map generation. More crucially we will assess the effect of receptor agonists (GABA and

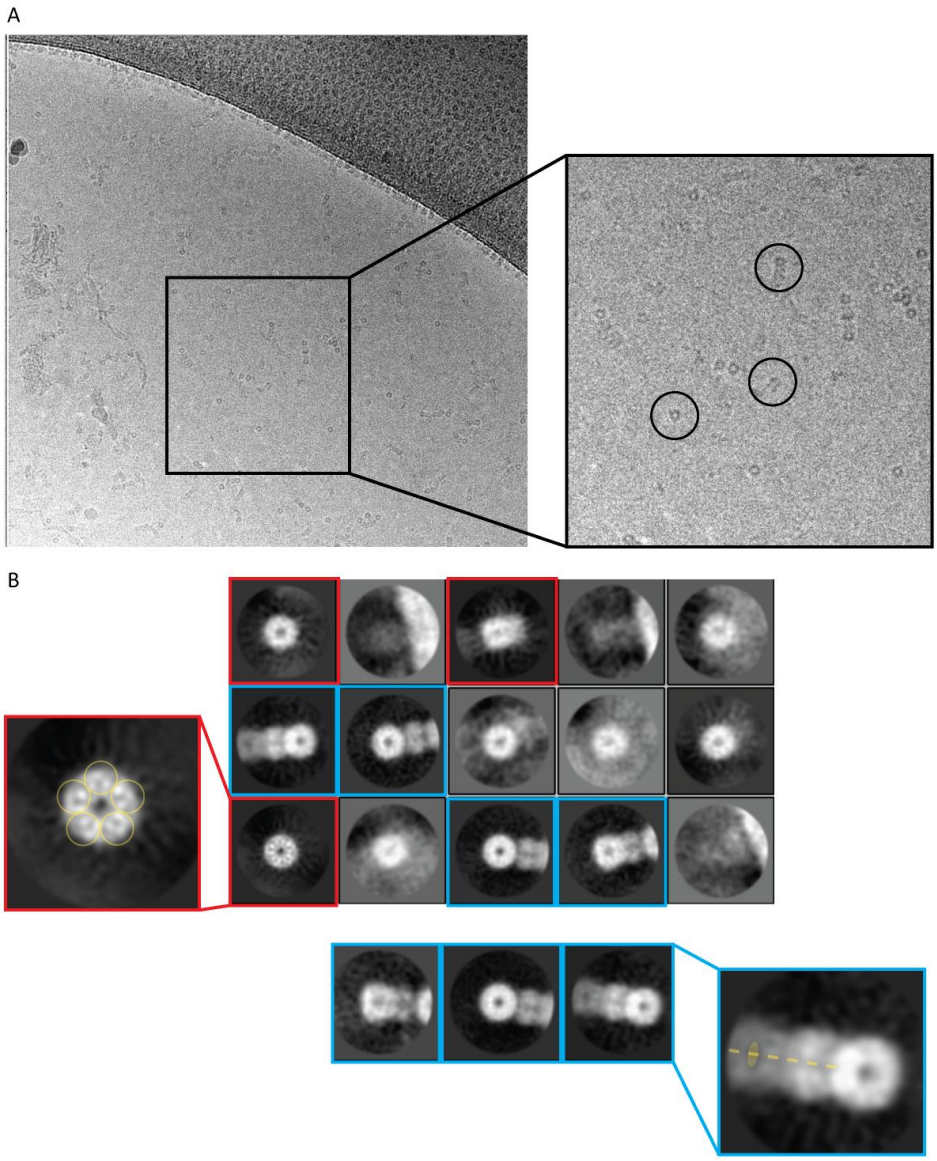

Figure 6.10 - Cryo-EM images of ELIC - A8-35 complex and 2D class average analysis

A. Typical images of frozen hydrated ELIC – A8-35 complex recorded on a Polara microscope (operated at 200 kV) and equipped with a K2 direct detection camera. Particles are visibly lined up along carbon grids and also partitioned in to ice over the grid holes. Right panel shows a magnified region of ice with embedded particles. End on views exhibit strong image contrast. Typical particle orientations are highlighted by black circles. **B**. Representative 2D class averages of ELIC particles (4,500 particles were used for the analysis). Three classes are indicated by red boxes clearly showing "end views" and "tilt views" for ELIC. The left panel shows a magnified end view emphasizing detail detected by K2 camera. The symmetry in the particles is emphasized by overlay of circle representing a pentameric arrangement of receptor subunits. Blue boxes indicate "doublet" particle classes. These were used in a second round of class averaging (shown in the lower panel). Increased detail in the side views is shown in the lower right panel (magnified view). Central pore axis is shown by a dashed yellow line and the location of the water filled ECD vestibule as a yellow oval.

propylamine) in the presence of PS on ELIC receptor orientation and particle picking by cryo-EM. In doing so we may obtain data sets capable of generating 3D models for subsequent structure solution. This would represent a significant step with regards to determining the structures of pLGICs free from the constraints and conformational bias of the crystal form.

6.2.6. Native mass spectrometry of ELIC in UDM

In our integrated biochemical and structural biology approach to addressing PS-mediated inhibition of the prokaryotic pLGIC ELIC, we also used native (ion mobility) mass spectrometry (Uetrecht et al., 2010). By this approach, mass spectra can be obtained for intact membrane protein complexes in the gas phase (stripped of detergent micelles; Barrera et al., 2008). This method, when coupled to ion mobility measurements, can assess the binding strengths and stabilizing effects of small molecules and lipids on the receptor (Laganowsky et al., 2014). Moreover the generation of high resolution spectra and collision induced dissociation of subunits from an oligomeric complex allows for the assessment of oligomeric-state dependent association of small molecules and lipids and their likely location of binding on the receptor (e.g. at subunit interfaces, plugs, or cavities). Given the lipidic-like nature of steroid-derived molecules, we reasoned that native (IM)-MS might also allow for the assessment of steroidal molecule binding at pLGICs, such as that of PS binding at of ELIC.

Given the significant technical challenge, we have carried out MS investigation as part of a collaboration with Kitty Hendriks and Konstantinos Thalassionos at UCL, who acquired and analysed MS data. We prepared protein-detergent complexes for MS and assisted with experimental design and data analysis/interpretation.

For mass spectra generation protein-detergent complexes were ionized by electrospray ionization before introduction into the mass spectrometer. Detergents

are subsequently stripped from the complex by incrementally increasing collisional activation energy following transmission into the quadrapole mass analyzer and acceleration in to a collision cell. A time-of-flight (TOF) mass analyser is used to then separate ions based on their mass: charge ratio (*m/z*) (Laganowsky et al., 2013). For additional IM measurements the drift time of an ion (dependent on size and shape) can be deduced. Experiments presented here were performed on a Synapt G1 (Water) mass spectrometer.

Following substantial optimization, high quality mass spectra were generated for ELIC in UDM (*Fig 6.11)*. Three distinct charge state distributions could be observed, from which experimental mass could be defined for different protein species. The intense distributions of lower *m/z* ratio showed a mass of 37.2 ± 0.013 kDa and likely corresponds (with high confidence) to dissociated monomeric ELIC subunit. Two further distributions of higher *m/z* were recorded. The second distribution was calculated to have a mass of 185.7 ± 0.042 kDa and the third a mass of 148.6 ± 0.046 kDa (*Fig 6.11*). These distributions likely correspond to the pentameric and stripped pentamer, or tetrameric, complexes respectively. In the case of the latter, stripping of a single subunit occurs with increased collision energy, yielding a tetrameric complex. The experimentally derived mass of all species is in strong agreement with calculated theoretical masses and would allow for unequivocal assignment of charge distributions to oligomeric states of ELIC (*Table 6.1*). Given the relatively broad peak corresponding to the pentameric state of ELIC, we might conclude that under these experimental parameters inefficient removal of detergent models is occurring (resulting in poor complex transmission and peak resolution). Nevertheless, the error in determining mass is sufficiently small that we might now be able to assess small molecule binding. However in order to determine (with high confidence) the identity of bound molecules we would need to increase the peak resolution across charge distributions.

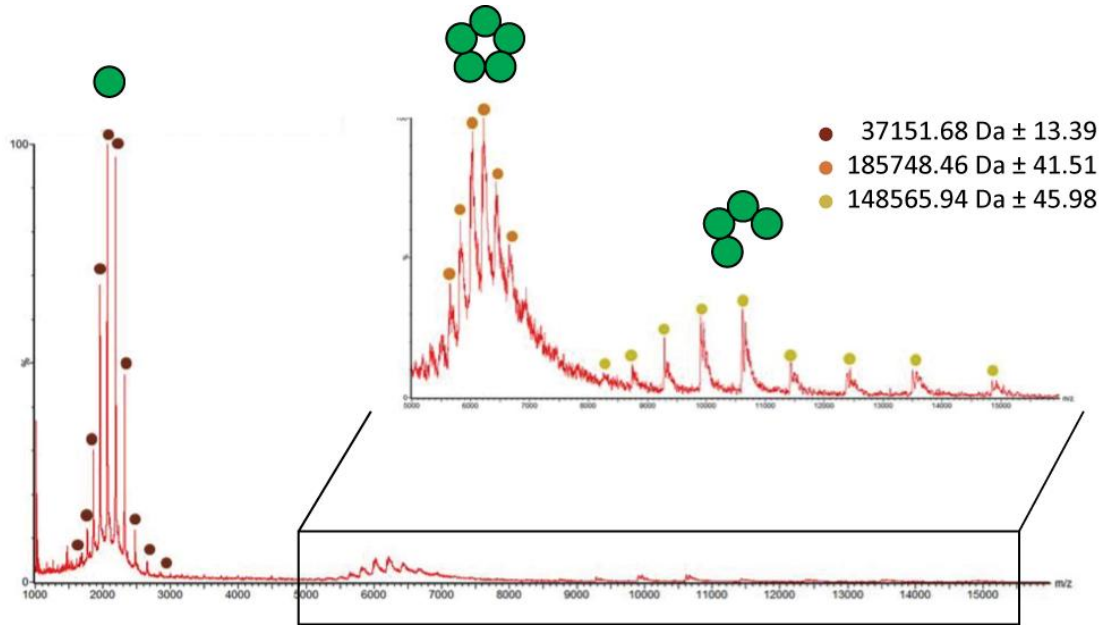

Figure 6.11 - Native mass spectrum of ELIC in UDM

Mass spectrum of ELIC in UDM. Three distinct charge distributions were observed in the spectraum ranging from 1000 to 16000 *m/z* and which following mass analysis equate to monomeric, pentameric and tetrameric ELIC (depicted by green circles above the spectrum). Peaks used to determine masses are shown by red, orange and yellow circles and the calculated mass and error are shown top right. Inset shows magnified view of the spectrum ranging from 5000 to 16000 *m/z*. The first distribution (orange circles) in this region corresponds to the pentameric form of the protein and the second distribution (yellow circles) corresponds to the stripped tetramer.

We therefore carried out MS coupled with IM (IM-MS). Following extensive optimization of mass spectrometer parameters, spectra were generated displaying three clear charge distributions (as observed under the standard experimental conditions described above; *Fig 6.12*). The first distribution was more poorly defined, and peaks of lower intensity compared to those observed under standard conditions. The mass calculated from this distribution of 37.1 ± 0.001 kDa is consistent with this distribution corresponding to a dissociated monomer. The second and third distributions of higher *m/z* exhibited far greater intensity and resolution under IM parameters. The second distribution exhibited a calculated mass of 185.7 ± 0.008 kDa and the third a mass of 148.6 ± 0.005 kDa. When compared to theoretical masses of

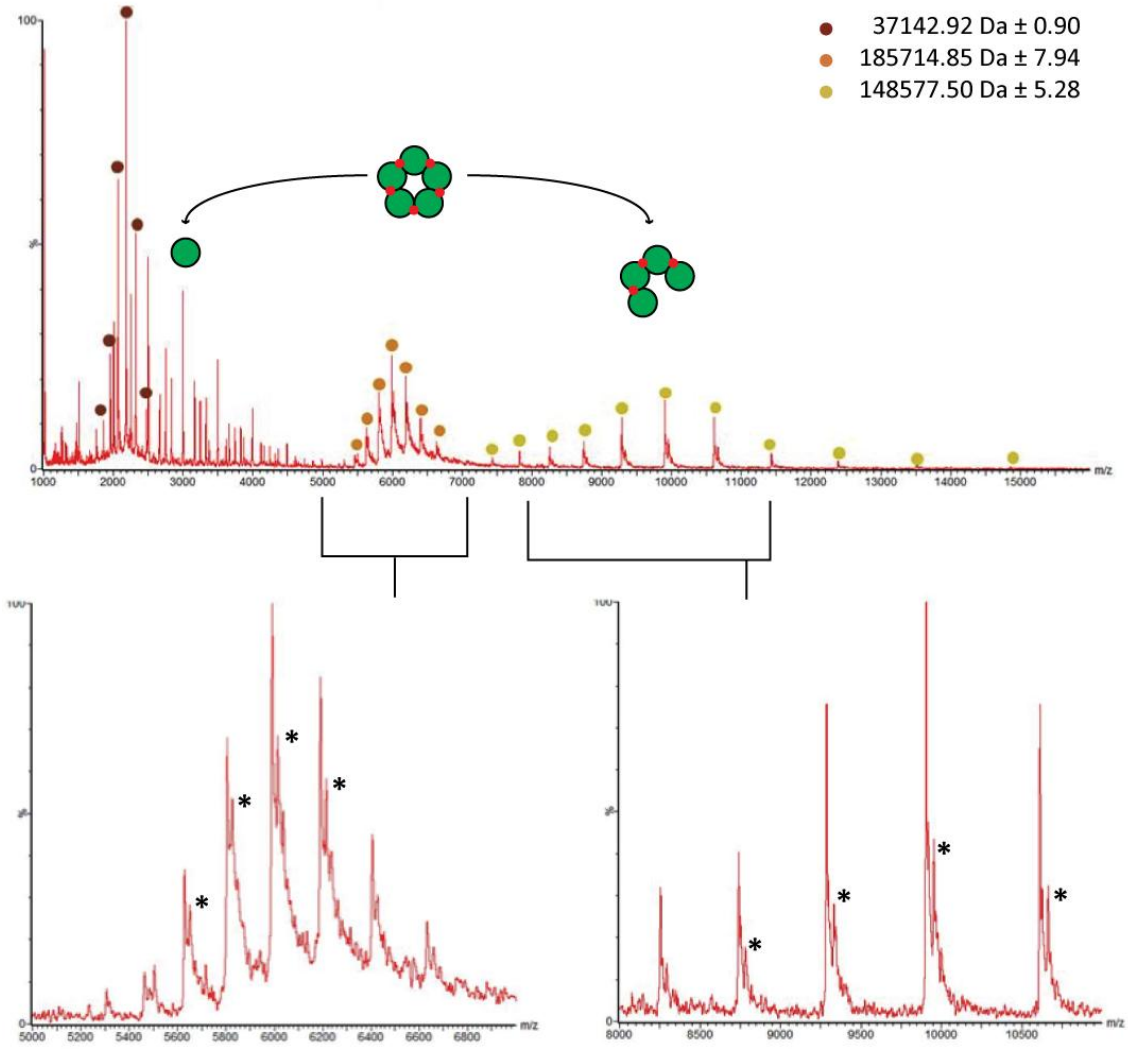

Figure 6.12 - Ion-mobility mass spectrum of ELIC in UDM

IM-Mass spectrum of ELIC in UDM. As before three distinct charge distributions were observed in the spectrum ranging from 1000 to 16000 *m/z* and following mass analysis these equate to monomeric, pentameric and tetrameric ELIC (depicted by green circles above the spectrum, red circles suggest association and location of bound small molecule). Peaks used to determine the masses are shown by red, orange and yellow circles and the calculated mass and error shown top right. Lower panel left; shows a magnified view of the spectrum ranging from 5000 to 7000 *m/z*. This distribution corresponds to the pentameric form of ELIC and exhibits a second set of peaks of higher *m/z value* (indicated by asterisks). High *m/z peak* likely corresponds to protein complexes with associated small molecule. Lower panel right; a magnified view of the spectrum ranging from 8000 to 11000 *m/z*. This distribution corresponds to the stripped tetramer and also exhibits a second set of peaks of higher *m/z* value (also indicated by asterisks).

ELIC, these distributions corresponded to pentameric and stripped pentamer/tetrameric complexes (*Table 6.2*). More intriguingly, for both pentameric and tetrameric charge distributions, we could clearly resolve additional sets of peaks of greater *m/z* values (*Fig 6.12:* indicated by asterisks on expansion of the charge states). Calculation of experimental masses revealed additional values of 721. 49 Da and 707.49 Da for the pentameric and tetrameric states of ELIC respectively (*Table 6.2*). Crucially this additional mass was not observed for the lower mass dissociated monomer.

Given that measurements by IM-MS exhibit greatly improved transmission and resolution of intact oligomeric (principally pentameric) ELIC we can begin to use these experimental parameters as a starting point from which to assess the strength (and location) of small molecule binding, specifically of PS. Moreover we have been able to identify with high confidence an additional mass associated with pentameric and (stripped) tetrameric forms of ELIC. We can tentatively assign this to an endogenous lipid tightly bound at ELIC throughout the extraction and purification (the most likely candidate being phosphatiydlethanolamine, PE, a major *E. coli* lipid of average mass of 719.302 Da). This is to our knowledge the first observation of endogenous lipid binding at ELIC, a phenomenon which was not observed from crystallographic studies. We discuss the potential implications of this below.

Table 6.1 Comparison of theoretical and experimental masses of ELIC in UDM as determined by MS.

Oligomer	Experimental Mass (Da)	Theoretical Mass (Da)	Difference between experimental and theoretical mass (Da)
Monomer	37151.68 ± 13.39	37133.58	18.10
Tetramer	148565.94 ± 45.98	148534.32	31.62
Pentamer	185748.46 ± 41.51	185667.90	80.56

Note: Theoretical mass of tetramer and pentamer calculated from the mass of a monomer

Table 6.2 Comparison of theoretical and experimental masses of ELIC in UDM as determined by IM-MS.

Oligomer	Experimental Mass (Da)	Theoretical Mass (Da)	Difference between experimental and theoretical mass (Da)
Monomer	37142.98 ± 0.9	37133.58	9.34
Tetramer	148557.50 ± 5.28	148534.32	43.18
Tetramer *	149284.99 ± 15.41	148534.32	707.49
Pentamer	185714.85 ± 7.94	185667.90	46.85
Pentamer *	186436.28 ± 32.82	185667.90	721.49

Note: * corresponds to masses calculated from charge states in *Figure 6.12, also denoted* *.

6.3. Discussion

In this chapter we have identified a previously unreported inhibition of the prokaryotic pLGIC ELIC by the sulphonated brain steroid, PS. In efforts to further characterise PS binding and its mechanism of action we have carried out X-ray crystallography, cryo-EM and native IM-MS. Despite each being challenging techniques in their own right, we have made significant progress in preparing high quality samples for the generation of preliminary data. Through combined use and integration of data from each of these techniques we hope to generate a high-resolution unbiased three-dimensional model of allosteric inhibition at a pLGIC.

We are now at a position that we might reasonably implement these techniques for directly assessing PS inhibition. Having not yet generated definitive structural or binding data for PS, we do not feel it is appropriate to speculate on a mechanism of binding and action of PS at ELIC (and other pLGICs). We do however feel it is important to further emphasise the relative merits of the functional, biochemical and structural biology techniques that we have introduced and how they might assist us in advancing our understanding of allosteric modulation at ELIC. Moreover, experimental design in the framework of a combination of techniques is likely to prove beneficial to the study of other receptors, namely the chimeric $GABA_A$ receptors introduced in earlier chapters.

It should initially be noted that further electrophysiological characterisation (beyond the extent of that presented here) is essential in further deciphering the underlying mechanism of PS inhibition at ELIC. While, reassuringly, PS exhibits allosteric-inhibition of agonist activity (as observed for a number of pLGICs, including $GABA_A$Rs), it is not currently clear whether this inhibition is receptor state-dependent. Indeed, a consensus mechanism of PS block at native $GABA_A$Rs is still yet to be reached (Seljeset et al., 2015). It was notable in our recordings that by co-application (and not pre-incubation) of agonist (GABA) and PS, current profiles exhibited an apparent increase in the rate of current decay (in a manner akin to that observed at native $GABA_A$Rs (Akk et al., 2001; Eisenman et al., 2003)). As to whether this represents a PS-mediated

increased occupancy of ELIC in a desensitised state is not fully clear at this stage. With recent NMR and DEER spectroscopy experiments (Kinde et al., 2015) revealing that ELIC is able to exist in multiple resting and desensitized states, it will be intriguing to see if structural studies in the presence of PS will favour occupancy of the receptor in a state distinct to that observed in previous crystallographic studies (Hilf and Dutzler, 2008; Spurny et al., 2012).

While X-ray crystallography and cryo-EM will ultimately provide the greatest details regarding the site for steroid binding, they are reliant on generating strong unambiguous density (or signal) for bound ligand (which can be open to interpretation). In native (IM-) MS we introduced an alternative technique that can provide (lower-resolution) structural information. In line with the lack of consensus view regarding the kinetics of PS block, as to where PS binds (at the level of the receptor) is far from apparent. Whilst the reasonable assumption is that it likely imparts an effect at the level of the TMD, as to whether binding occurs within the channel (Wang et al., 2006), through association with the α-helical bundle, or even at the periphery of the protein (via lipid-protein interactions) is not clear. Given that in each of these scenarios the likely binding strength and number of molecules bound per pentamer will vary significantly, we reason that native IM-MS measurements will allow for unbiased analysis (i.e. studies of native, non-mutant receptor forms) of these variables. Indeed in our own experiments we are able to generate well resolved charge distributions and peaks for pentameric (apo-)ELIC that allow for identification of additional associated mass, likely corresponding to the endogenous *E. coli* lipid PE. The observation of additional mass at both pentameric and (stripped) tetrameric forms, but not dissociated monomers, reveals that this protein-lipid interaction is likely formed at the subunit interface (which would not be present in the monomeric form). Through binding studies with PS we hope to generate similarly well resolved mass spectra for unambiguous assessment of ligand association with pentameric and (gas phase) dissociation complexes.

Of the results presented in this chapter, possibly the most exciting are those for the preparation and preliminary imaging of ELIC by cryo-EM. Whilst it was previously

believed that the “size cut-off” for atomic resolution structure determination by cryo-EM was 300 kDa (Bai et al., 2015a), the rapid development of direct electron detectors and image processing tools is continually challenging this limitation. Indeed a recent structure of γ-secretase membrane protein (of ~170 kDa) at 3.4Å reveals that these cut-off boundaries are already shifting significantly (Bai et al., 2015b). Despite these advances, the starting sample must be prepared in such a manner that it allows for generation of high resolution data. For a membrane protein extracted and purified in detergent this is particularly important. We have been able to clearly show that a prototypical pLGIC, ELIC, is stable in an amphipathic polymer (amphipol) known to show favourable properties in cryo-EM experiments (when compared to traditional detergents). Not only is this ELIC-amphipol complex biochemically stable, but also reveals improved properties in preliminary cryo-EM studies (with 2D class average images already revealing details of receptor architecture). We are keen to now test the size limit of cryo-EM for structure determination of a pLGIC in a non-crystalline environment. To date such a feat has only just been achieved for the GlyR (Du et al., 2015). Moreover, given the quality of sample preparation, we believe this may be transferable across similar proteins and intend to assess the stability of chimeric $GABA_A$Rs in amphipols for cryo-EM.

6.4. Conclusions

Agonist activated currents of ELIC are inhibited by pregnenolone sulphate exhibiting a state-dependent mechanism of action.

Crystals of ELIC can be grown in the presence of pregnenolone sulphate and in the presence of lipids and orthosteric agonists.

Crystals maximally diffract to ~4Å, but do not at current resolution allow for unequivocal structural determination.

ELIC can be detergent exchanged in to the amphipol A8-35, in which it retains biochemical stability and can adopt multiple orientations by negative-stain and cryo-EM.

IM-MS revealed the binding of small, structurally stabilising, molecules to ELIC, which are likely to be an endogenous *E. coli* lipid.

Chapter 7: General Discussion

For many years, pLGICs, and more specifically the $GABA_A$ receptor, proved elusive to high-resolution structural studies. The inherent importance of these receptors in maintaining normal network function and as significant pharmacological targets provides a strong rationale for identifying novel ways to 'open up' the $GABA_A$ receptor family for structural determination. This formed the principal focus of this thesis, which was to explore the use of chimeric $GABA_A$ receptors as a means to study the functional and structural properties of the receptor TMD. On the basis of a previously reported chimera between the ECD of the prokaryotic pLGIC GLIC and TMD of the human GlyR α1 (Duret et al. 2011), we adopted a similar approach by generating a domain chimera between the ECD of GLIC and the TMD of the $GABA_AR$ α1 subunit. By using a surrogate ECD of a receptor (e.g. GLIC) which is amenableto protein crystallization and structure determination, we were keen to determine whether this might allow for crystallization of the $GABA_AR$ α1 TMD. In doing so we could begin to address fundamental questions of how channel gating and allosteric modulation is coordinated at the atomic level.

During the course of this study we have also identified novel interactions of $GABA_AR$ allosteric modulatory compounds with the prokaryotic pLGIC homologs GLIC and ELIC. These have provided the basis for structural studies to elucidate the mechanism of binding at these receptors, with a view to determine the evolutionary significance of a binding site and how these might relate to allosteric modulation of a native $GABA_AR$ subtype.

7.1. The ECD of GLIC can act as a surrogate host for $GABA_AR$ subunit TMDs

As alluded to, it was previously reported that the ECD of GLIC when fused to the TMD of the GlyR α1 subunit (a chimera termed as LiLy) formed a functional proton gated channel, with a receptor 'TMD pharmocology' reminiscent of that of the native α1 GlyR (Duret et al., 2011). In accord with this report, we found that 'GLIC-based' chimeras

with the TMD of the $GABA_AR$ α1 or β2 subunit were capable of forming functional receptors retaining those properties, with regard to receptor kinetics and pharmacology, to be expected of a native $GABA_AR$ (*Chapter 3*). This exciting finding provided the starting point for the principal aim of this study, of expressing and purifying receptor chimeras for crystallization and subsequent structure determination. Ultimately a significant proportion of this study has been committed to identifying the expression and purification conditions which allow for the generation of a stable homopentameric GLIC-GABA chimera for structural studies (*Chapter 4*). This is somewhat unsurprising given that the purification strategies and structures for the homopentameric GABA β3 and LiLy have only recently been reported (Miller and Aricescu., 2014; Moraga-Cid et al., 2015). We expanded our approach and have been able to purify a chimeric receptor, bearing a single point mutation known to profoundly affect receptor desensitization, which allows robust crystal growth and X-ray diffraction to 9 Å.

This crucial finding forms the platform from which to advance our efforts of chimeric receptor crystallization. In doing so we will implement the array of techniques learnt and developed during this study (e.g. CPM fluorescence stability assays) to increase the throughput with which we screen new crystallization conditions. Moreover, we are beginning to address the question of structure determination by alternative approaches, especially cryo-EM, which has seen rapid technical advances in the last few years (Cheng et al., 2015). We believe that these approaches can then be applied to other receptor chimeras, either of alternative 'desensitization' mutants of the GLIC-$GABA_AR$ α1 chimera or a GLIC-$GABA_AR$ β2 chimera for example. Given that studies of full-length native $GABA_AR$ subunits, exhibiting extensive post-translational modifications (e.g. glycosylation), will continue to prove challenging, the use of receptor chimeras is likely to remain an important one for advancing our understanding of $GABA_AR$ structure.

7.2. $GABA_A$ receptor modulators bind at the prokaryotic pLGICs GLIC and ELIC

Although this was not a major focus of this study, we have identified previously unreported inhibitory responses of $GABA_A$R-active compounds at prokaryotic receptor homologs, GLIC and ELIC. The barbiturate, pentobarbital, was observed to inhibit a proton gated response at GLIC, while the inhibitory neurosteroid, pregnenolone sulphate, inhibited GABA-activated currents at ELIC. These observations provided the basis for attempts to determine the respective binding sites using X-ray crystallography (GLIC and ELIC) and cryo-EM (ELIC).

7.2.1. Pentobarbital inhibition of GLIC

With regard to the pentobarbital-inhibition of GLIC, it is unclear as to whether a barbiturate binding site on GLIC is likely to resemble a conserved binding site for these compounds on native $GABA_A$Rs. Given the complex nature of barbiturate modulation of $GABA_A$Rs (Muroi et al., 2009), and on the basis that we only observed inhibition of agonist activity at GLIC, it might be that an identified binding site on GLIC would more likely resemble that of a barbiturate binding site on cationic-pLGICs, e.g. nAChRS. Indeed, barbiturates have previously been reported to block neuronal and muscle nAChRs (Hamouda et al., 2014a). While our efforts to co-crystallize GLIC and pentobarbarbital (or a brominated derivative) yielded high-resolution diffraction data, allowing for structure determination, we were unable to identify a binding site. Ultimately, further efforts, utilizing distinct GLIC-gating mutants (Prevost et al., 2012), might assist in determining the molecular basis of pentobarbital binding. From this, one might begin to determine whether a binding site resembles one conserved at cationic (e.g. nAChRs) or anionic (e.g. $GABA_A$Rs) pLGICs.

7.2.2. Pregnonlone sulphate inhibition of ELIC

During this study we also observed that GABA-activated currents through ELIC receptors were inhibited by the steroid, pregnenolone sulphate (PS) in a manner reminiscent to that observed at native $GABA_AR$s (Seljeset et al., 2015). While we have yet to fully characterize the kinetic properties on this response, we have however begun to address the determinants of binding using a combination of structural approaches; X-ray crystallography, cryo-EM and native ion-mobility mass spectrometry. This integration of techniques, though challenging, will likely provide the most complete picture of how PS binds at and then inhibits receptor activity. During the course of this study, we have been able to optimize each of these methodological approaches for studies of ELIC and now find ourselves in a position to address the underlying basis for PS-mediated inhibition. Of particular note is the study of ELIC by cryo-EM. We have identified conditions that allow for the preparation of EM grids exhibiting ideal dispersion of ELIC receptor particles in vitrified ice with multiple orientations. This sample forms the ideal starting position for high-resolution data collection and structure determination by cryo-EM. Moreover, the application of this approach to the structure determination of pLGICs *per se* is likely to prove a significant one.

References

Adams, J.M., Thomas, P., and Smart, T.G. (2015). Modulation of neurosteroid potentiation by protein kinases at synaptic- and extrasynaptic-type $GABA_A$ receptors. Neuropharmacology *88*, 63–73.

Akk, G., and Steinbach, J.H. (2000). Activation and block of recombinant $GABA_A$ receptors by pentobarbitone: a single-channel study. British Journal of Pharmacology *130*, 249–258.

Akk, G., Bracamontes, J., and Steinbach, J.H. (2001). Pregnenolone sulfate block of $GABA_A$ receptors: mechanism and involvement of a residue in the M2 region of the α subunit. J. Physiol. (Lond.) *532*, 673–684.

Akk, G., Li, P., Bracamontes, J., Reichert, D.E., Covey, D.F., and Steinbach, J.H. (2008). Mutations of the $GABA_A$ receptor α1 subunit M1 domain reveal unexpected complexity for modulation by neuroactive steroids. Mol. Pharmacol. *74*, 614–627.

Alexandrov, A.I., Mileni, M., Chien, E.Y.T., Hanson, M.A., and Stevens, R.C. (2008). Microscale fluorescent thermal stability assay for membrane proteins. Structure/Folding and Design *16*, 351–359.

Alqazzaz, M., Thompson, A.J., Price, K.L., Breitinger, H.-G., and Lummis, S.C.R. (2011). Cys-loop receptor channel blockers also block GLIC. Biophys. J. *101*, 2912–2918.

Althoff, T., Hibbs, R.E., Banerjee, S., and Gouaux, E. (2014). X-ray structures of GluCl in apo states reveal a gating mechanism of Cys-loop receptors. Nature *512*, 333–337.

Althoff, T., Mills, D.J., Popot, J.-L., and Kühlbrandt, W. (2011). Arrangement of electron transport chain components in bovine mitochondrial supercomplex I1III2IV1. Embo J. *30*, 4652–4664.

Amin, J. (1999). A single hydrophobic residue confers barbiturate sensitivity to gamma-aminobutyric acid type C receptor. Mol. Pharmacol. *55*, 411–423.

Amin, J., and Weiss, D.S. (1996). Insights into the activation mechanism of ρ1 GABA receptors obtained by coexpression of wild type and activation-impaired subunits. Proc. Biol. Sci. *263*, 273–282.

Auerbach, A. (2015). Agonist activation of a nicotinic acetylcholine receptor. Neuropharmacology *96*, 150–156.

Auerbach, A., and Akk, G. (1998). Desensitization of mouse nicotinic acetylcholine receptor channels. A two-gate mechanism. J. Gen. Physiol. *112*, 181–197.

Bagnéris, C., Decaen, P.G., Hall, B.A., Naylor, C.E., Clapham, D.E., Kay, C.W.M., and Wallace, B.A. (2013). Role of the C-terminal domain in the structure and function of tetrameric sodium channels. Nature Communications *4*, 2465.

Bagnéris, C., Decaen, P.G., Naylor, C.E., Pryde, D.C., Nobeli, I., Clapham, D.E., and Wallace, B.A. (2014). Prokaryotic NavMs channel as a structural and functional model for eukaryotic sodium channel antagonism. Proc. Natl. Acad. Sci. U.S.a. *111*, 8428–8433.

Bai, X.-C., McMullan, G., and Scheres, S.H.W. (2015a). How cryo-EM is revolutionizing structural biology. Trends Biochem. Sci. *40*, 49–57.

Bai, X.-C., Yan, C., Yang, G., Lu, P., Ma, D., Sun, L., Zhou, R., Scheres, S.H.W., and Shi, Y. (2015b). An atomic structure of human γ-secretase. Nature.

Baker, C., Sturt, B.L., and Bamber, B.A. (2010). Multiple roles for the first transmembrane domain of

$GABA_A$ receptor subunits in neurosteroid modulation and spontaneous channel activity. Neurosci. Lett. *473*, 242–247.

Bali, M., and Akabas, M.H. (2007). The location of a closed channel gate in the $GABA_A$ receptor channel. J. Gen. Physiol. *129*, 145–159.

Barrantes, F.J. (2015). Phylogenetic conservation of protein-lipid motifs in pentameric ligand-gated ion channels. Biochim. Biophys. Acta *1848*, 1796–1805.

Barrera, N.P., Di Bartolo, N., Booth, P.J., and Robinson, C.V. (2008). Micelles protect membrane complexes from solution to vacuum. Science *321*, 243–246.

Barrera, N.P., Isaacson, S.C., Zhou, M., Bavro, V.N., Welch, A., Schaedler, T.A., Seeger, M.A., Miguel, R.N., Korkhov, V.M., van Veen, H.W., et al. (2009). Mass spectrometry of membrane transporters reveals subunit stoichiometry and interactions. Nat. Methods *6*, 585–587.

Beato, M., Groot-Kormelink, P.J., Colquhoun, D., and Sivilotti, L.G. (2004). The activation mechanism of α1 homomeric glycine receptors. Journal of Neuroscience *24*, 895–906.

Bechara, C., and Robinson, C.V. (2015). Different modes of lipid binding to membrane proteins probed by mass spectrometry. J. Am. Chem. Soc. *137*, 5240–5247.

Belelli, D., and Lambert, J.J. (2005). Neurosteroids: endogenous regulators of the $GABA_A$ receptor. Nat. Rev. Neurosci. *6*, 565–575.

Ben-Ari, Y. (2002). Excitatory actions of GABA during development: the nature of the nurture. Nat. Rev. Neurosci. 3(9):728-39.

Ben-Ari, Y., Khalilov, I., Kahle, K.T., and Cherubini, E. (2012). The GABA excitatory/inhibitory shift in brain maturation and neurological disorders. Neuroscientist. 18(5):467-86.

Benson, J.A., Löw, K., Keist, R., Möhler, H., and Rudolph, U. (1998). Pharmacology of recombinant gamma-aminobutyric acidA receptors rendered diazepam-insensitive by point-mutated α-subunits. FEBS Lett. *431*, 400–404.

Bera, A.K., and Akabas, M.H. (2005). Spontaneous thermal motion of the $GABA_A$ receptor M2 channel-lining segments. J. Biol. Chem. *280*, 35506–35512.

Bhattacharya, A.A., Curry, S., and Franks, N.P. (2000). Binding of the general anesthetics propofol and halothane to human serum albumin. High resolution crystal structures. J. Biol. Chem. *275*, 38731–38738.

Bianchi, M.T., and Macdonald, R.L. (2002). Slow phases of $GABA_A$ receptor desensitization: structural determinants and possible relevance for synaptic function. J. Physiol. (Lond.) *544*, 3–18.

Bocquet, N., Nury, H., Baaden, M., Le Poupon, C., Changeux, J.-P., Delarue, M., and Corringer, P.-J. (2009). X-ray structure of a pentameric ligand-gated ion channel in an apparently open conformation. Nature *457*, 111–114.

Bocquet, N., Prado de Carvalho, L., Cartaud, J., Neyton, J., Le Poupon, C., Taly, A., Grutter, T., Changeux, J.-P., and Corringer, P.-J. (2007). A prokaryotic proton-gated ion channel from the nicotinic acetylcholine receptor family. Nature *445*, 116–119.

Bogdanov, Y., Michels, G., Armstrong-Gold, C., Haydon, P.G., Lindstrom, J., Pangalos, M., and Moss, S.J. (2006). Synaptic $GABA_A$ receptors are directly recruited from their extrasynaptic counterparts. Embo J. *25*, 4381–4389.

Bouzat, C., Bartos, M., Corradi, J., and Sine, S.M. (2008). The interface between extracellular and transmembrane domains of homomeric Cys-loop receptors governs open-channel lifetime and rate of

desensitization. Journal of Neuroscience *28*, 7808–7819.

Bouzat, C., Gumilar, F., Spitzmaul, G., Wang, H.-L., Rayes, D., Hansen, S.B., Taylor, P., and Sine, S.M. (2004). Coupling of agonist binding to channel gating in an ACh-binding protein linked to an ion channel. Nature *430*, 896–900.

Braat, S., and Kooy, R.F. (2015). The $GABA_A$ Receptor as a Therapeutic Target for Neurodevelopmental Disorders. Neuron *86*, 1119–1130.

Brejc, K., van Dijk, W.J., Klaassen, R.V., Schuurmans, M., van Der Oost, J., Smit, A.B., and Sixma, T.K. (2001). Crystal structure of an ACh-binding protein reveals the ligand-binding domain of nicotinic receptors. Nature *411*, 269–276.

Brickley, S.G., and Mody, I. (2012). Extrasynaptic $GABA_A$ receptors: their function in the CNS and implications for disease. Neuron *73*, 23–34.

Calimet, N., Simoes, M., Changeux, J.-P., Karplus, M., Taly, A., and Cecchini, M. (2013). A gating mechanism of pentameric ligand-gated ion channels. Proc. Natl. Acad. Sci. U.S.a.

Cao, E., Cordero-Morales, J.F., Liu, B., Qin, F., and Julius, D. (2013a). TRPV1 channels are intrinsically heat sensitive and negatively regulated by phosphoinositide lipids. Neuron *77*, 667–679.

Cao, E., Liao, M., Cheng, Y., and Julius, D. (2013b). TRPV1 structures in distinct conformations reveal activation mechanisms. Nature *504*, 113–118.

Carpenter, E.P., Beis, K., Cameron, A.D., and Iwata, S. (2008). Overcoming the challenges of membrane protein crystallography. Curr. Opin. Struct. Biol. *18*, 581–586.

Carswell, C.L., Hénault, C.M., Murlidaran, S., Therien, J.P.D., Juranka, P.F., Surujballi, J.A., Brannigan, G., and Baenziger, J.E. (2015). Role of the Fourth Transmembrane α Helix in the Allosteric Modulation of Pentameric Ligand-Gated Ion Channels. Structure/Folding and Design *23*, 1655–1664.

Cecchini, M., and Changeux, J.-P. (2014). The nicotinic acetylcholine receptor and its prokaryotic homologues: Structure, conformational transitions & allosteric modulation. Neuropharmacology.

Celie, P.H.N., van Rossum-Fikkert, S.E., van Dijk, W.J., Brejc, K., Smit, A.B., and Sixma, T.K. (2004). Nicotine and carbamylcholine binding to nicotinic acetylcholine receptors as studied in AChBP crystal structures. Neuron *41*, 907–914.

Cestari, I.N., Uchida, I., Li, L., Burt, D., and Yang, J. (1996). The agonistic action of pentobarbital on $GABA_A$ β-subunit homomeric receptors. Neuroreport *7*, 943–947.

Chae, P.S., Rasmussen, S.G.F., Rana, R.R., Gotfryd, K., Chandra, R., Goren, M.A., Kruse, A.C., Nurva, S., Loland, C.J., Pierre, Y., et al. (2010). Maltose-neopentyl glycol (MNG) amphiphiles for solubilization, stabilization and crystallization of membrane proteins. Nat. Methods *7*, 1003–1008.

Chang, Y., and Weiss, D.S. (1998). Substitutions of the highly conserved M2 leucine create spontaneously opening ρ1 gamma-aminobutyric acid receptors. Mol. Pharmacol. *53*, 511–523.

Chang, Y., and Weiss, D.S. (1999). Allosteric activation mechanism of the α1 β2 γ2 gamma-aminobutyric acid type A receptor revealed by mutation of the conserved M2 leucine. Biophys. J. *77*, 2542–2551.

Cheng, Y. (2015). Single-Particle Cryo-EM at Crystallographic Resolution. Cell *161*, 450–457.

Cheng, Y., Grigorieff, N., Penczek, P.A., and Walz, T. (2015). A primer to single-particle cryo-electron microscopy. Cell *161*, 438–449.

Cherezov, V. (2011). Lipidic cubic phase technologies for membrane protein structural studies. Curr.

Opin. Struct. Biol. *21*, 559–566.

Chiara, D.C., Dostalova, Z., Jayakar, S.S., Zhou, X., Miller, K.W., and Cohen, J.B. (2012). Mapping general anesthetic binding site(s) in human α1β3 γ-aminobutyric acid type A receptors with [^{3}H]TDBzl-etomidate, a photoreactive etomidate analogue. Biochemistry *51*, 836–847.

Chiara, D.C., Jayakar, S.S., Zhou, X., Zhang, X., Savechenkov, P.Y., Bruzik, K.S., Miller, K.W., and Cohen, J.B. (2013). Specificity of intersubunit general anesthetic binding sites in the transmembrane domain of the human α1β3γ2 $GABA_A$ receptor. Journal of Biological Chemistry.

Colquhoun, D. (2006). Agonist-activated ion channels. British Journal of Pharmacology *147 Suppl 1*, S17–S26.

Comenencia-Ortiz, E., Moss, S.J., and Davies, P.A. (2014). Phosphorylation of $GABA_A$ receptors influences receptor trafficking and neurosteroid actions. Psychopharmacology (Berl.) *231*, 3453–3465.

Compagnone, N.A., and Mellon, S.H. (2000). Neurosteroids: biosynthesis and function of these novel neuromodulators. Front Neuroendocrinol *21*, 1–56.

Connolly, C.N., Krishek, B.J., McDonald, B.J., Smart, T.G., and Moss, S.J. (1996). Assembly and cell surface expression of heteromeric and homomeric gamma-aminobutyric acid type A receptors. J. Biol. Chem. *271*, 89–96.

Corringer, P.-J., Poitevin, F., Prevost, M.S., Sauguet, L., Delarue, M., and Changeux, J.-P. (2012). Structure and pharmacology of pentameric receptor channels: from bacteria to brain. Structure *20*, 941–956.

Corringer, P.J., Le Novère, N., and Changeux, J.P. (2000). Nicotinic receptors at the amino acid level. Annu. Rev. Pharmacol. Toxicol. *40*, 431–458.

Dacosta, C.J.B., Free, C.R., Corradi, J., Bouzat, C., and Sine, S.M. (2011). Single-channel and structural foundations of neuronal α7 acetylcholine receptor potentiation. Journal of Neuroscience *31*, 13870–13879.

Davies, P.A., Kirkness, E.F., and Hales, T.G. (1997). Modulation by general anaesthetics of rat $GABA_A$ receptors comprised of α1β3 and β3 subunits expressed in human embryonic kidney 293 cells. British Journal of Pharmacology *120*, 899–909.

Dellisanti, C.D., Ghosh, B., Hanson, S.M., Raspanti, J.M., Grant, V.A., Diarra, G.M., Schuh, A.M., Satyshur, K., Klug, C.S., and Czajkowski, C. (2013). Site-directed spin labeling reveals pentameric ligand-gated ion channel gating motions. PLoS Biol. *11*, e1001714.

Dellisanti, C.D., Yao, Y., Stroud, J.C., Wang, Z.-Z., and Chen, L. (2007). Crystal structure of the extracellular domain of nAChR α1 bound to alpha-bungarotoxin at 1.94 A resolution. Nat. Neurosci. *10*, 953–962.

Draguhn, A., Axmacher, N., and Kolbaev, S. (2008). Presynaptic ionotropic GABA receptors. Results Probl Cell Differ *44*, 69–85.

Du, J., Lü, W., Wu, S., Cheng, Y., and Gouaux, E. (2015). Glycine receptor mechanism elucidated by electron cryo-microscopy. Nature.

Duret, G., Van Renterghem, C., Weng, Y., Prevost, M., Moraga-Cid, G., Huon, C., Sonner, J.M., and Corringer, P.-J. (2011). Functional prokaryotic-eukaryotic chimera from the pentameric ligand-gated ion channel family. Proc. Natl. Acad. Sci. U.S.a. *108*, 12143–12148.

Dürr, K.L., Chen, L., Stein, R.A., De Zorzi, R., Folea, I.M., Walz, T., Mchaourab, H.S., and Gouaux, E. (2014). Structure and Dynamics of AMPA Receptor GluA2 in Resting, Pre-Open, and Desensitized States. Cell *158*, 778–792.

Eaton, M., Cao, L., Chen, Z., Franks, N.P., Evers, A.S., and Akk, G. (2015). Mutational Analysis of the Putative High-Affinity Propofol Binding Site in Human β3 Homomeric $GABA_A$ Receptors. Mol. Pharmacol.

Eiselé, J.L., Bertrand, S., Galzi, J.L., Devillers-Thiéry, A., Changeux, J.P., and Bertrand, D. (1993). Chimaeric nicotinic-serotonergic receptor combines distinct ligand binding and channel specificities. Nature *366*, 479–483.

Eisenman, L.N., He, Y., Fields, C., Zorumski, C.F., and Mennerick, S. (2003). Activation-dependent properties of pregnenolone sulfate inhibition of $GABA_A$ receptor-mediated current. J. Physiol. (Lond.) *550*, 679–691.

Emsley, P., Lohkamp, B., Scott, W.G., and Cowtan, K. (2010). Features and development of Coot. Acta Crystallogr. D Biol. Crystallogr. *66*, 486–501.

Eswar, N., Eramian, D., Webb, B., Shen, M.-Y., and Sali, A. (2008). Protein structure modeling with MODELLER. Methods Mol. Biol. *426*, 145–159.

Etter, A., Cully, D.F., Schaeffer, J.M., Liu, K.K., and Arena, J.P. (1996). An amino acid substitution in the pore region of a glutamate-gated chloride channel enables the coupling of ligand binding to channel gating. J. Biol. Chem. *271*, 16035–16039.

Farrant, M., and Nusser, Z. (2005). Variations on an inhibitory theme: phasic and tonic activation of $GABA_A$ receptors. Nat. Rev. Neurosci. *6*, 215–229.

Farrant, M., and Kaila, K. (2007). The cellular, molecular and ionic basis of $GABA_A$ receptor signalling. Prog Brain Res. 160:59-87.

Fisher, J.L., and Macdonald, R.L. (1997). Single channel properties of recombinant $GABA_A$ receptors containing γ2 or δ subtypes expressed with α1 and β3 subtypes in mouse L929 cells. J. Physiol. (Lond.) *505 (Pt 2)*, 283–297.

Fodor, L., Boros, A., Dezso, P., and Maksay, G. (2006). Expression of heteromeric glycine receptor-channels in rat spinal cultures and inhibition by neuroactive steroids. Neurochem. Int. *49*, 577–583.

Fourati, Z., Sauguet, L., and Delarue, M. (2015). Genuine open form of the pentameric ligand-gated ion channel GLIC. Acta Crystallogr. D Biol. Crystallogr. *71*, 454–460.

Franks, N.P., and Lieb, W.R. (1994). Molecular and cellular mechanisms of general anaesthesia. Nature. 367(6464):607-14.

Franks, N.P. (2008). General anaesthesia: from molecular targets to neuronal pathways of sleep and arousal. Nat. Rev. Neurosci. *9*, 370–386.

Franks, N.P. (2015). Structural comparisons of ligand-gated ion channels in open, closed, and desensitized states identify a novel propofol-binding site on mammalian γ-aminobutyric acid type A receptors. Anesthesiology *122*, 787–794.

Geromanos, S.J., Vissers, J.P.C., Silva, J.C., Dorschel, C.A., Li, G.-Z., Gorenstein, M.V., Bateman, R.H., and Langridge, J.I. (2009). The detection, correlation, and comparison of peptide precursor and product ions from data independent LC-MS with data dependant LC-MS/MS. Proteomics *9*, 1683–1695.

Gibbs, T.T., Russek, S.J., and Farb, D.H. (2006). Sulfated steroids as endogenous neuromodulators. Pharmacol. Biochem. Behav. *84*, 555–567.

Gielen, M., Thomas, P., and Smart, T.G. (2015). The desensitization gate of inhibitory Cys-loop receptors. Nature Communications *6*, 6829.

Gielen, M.C., Lumb, M.J., and Smart, T.G. (2012). Benzodiazepines modulate $GABA_A$ receptors by

regulating the preactivation step after GABA binding. Journal of Neuroscience *32*, 5707–5715.

Gill, J.K., Savolainen, M., Young, G.T., Zwart, R., Sher, E., and Millar, N.S. (2011). Agonist activation of α7 nicotinic acetylcholine receptors via an allosteric transmembrane site. Proc. Natl. Acad. Sci. U.S.a. *108*, 5867–5872.

Gonzalez-Gutierrez, G., Cuello, L.G., Nair, S.K., and Grosman, C. (2013). Gating of the proton-gated ion channel from Gloeobacter violaceus at pH 4 as revealed by X-ray crystallography. Proc. Natl. Acad. Sci. U.S.a. *110*, 18716–18721.

Gonzalez-Gutierrez, G., Lukk, T., Agarwal, V., Papke, D., Nair, S.K., and Grosman, C. (2012). Mutations that stabilize the open state of the Erwinia chrisanthemi ligand-gated ion channel fail to change the conformation of the pore domain in crystals. Proc. Natl. Acad. Sci. U.S.a. *109*, 6331–6336.

Hamouda, A.K., Jayakar, S.S., Chiara, D.C., and Cohen, J.B. (2014a). Photoaffinity labeling of nicotinic receptors: diversity of drug binding sites! J. Mol. Neurosci. *53*, 480–486.

Hamouda, A.K., Stewart, D.S., Chiara, D.C., Savechenkov, P.Y., Bruzik, K.S., and Cohen, J.B. (2014b). Identifying barbiturate binding sites in a nicotinic acetylcholine receptor with [3H]allyl m-trifluoromethyldiazirine mephobarbital, a photoreactive barbiturate. Mol. Pharmacol. *85*, 735–746.

Hansen, S.B., Sulzenbacher, G., Huxford, T., Marchot, P., Taylor, P., and Bourne, Y. (2005). Structures of Aplysia AChBP complexes with nicotinic agonists and antagonists reveal distinctive binding interfaces and conformations. Embo J. *24*, 3635–3646.

Hansen, S.B., Wang, H.-L., Taylor, P., and Sine, S.M. (2008). An ion selectivity filter in the extracellular domain of Cys-loop receptors reveals determinants for ion conductance. J. Biol. Chem. *283*, 36066–36070.

Harrison, N.L., and Simmonds, M.A. (1984). Modulation of the GABA receptor complex by a steroid anaesthetic. Brain Res. *323*, 287–292.

Harteneck, C. (2013). Pregnenolone sulfate: from steroid metabolite to TRP channel ligand. Molecules *18*, 12012–12028.

Hassaine, G., Deluz, C., Grasso, L., Wyss, R., Tol, M.B., Hovius, R., Graff, A., Stahlberg, H., Tomizaki, T., Desmyter, A., et al. (2014). X-ray structure of the mouse serotonin 5-HT_3 receptor. Nature.

Hassaine, G., Deluz, C., Li, X.-D., Graff, A., Vogel, H., and Nury, H. (2013). Large scale expression and purification of the mouse 5-HT_3 receptor. Biochim. Biophys. Acta *1828*, 2544–2552.

Hattori, M., and Gouaux, E. (2012). Molecular mechanism of ATP binding and ion channel activation in P2X receptors. Nature *485*, 207–212.

Hattori, M., Hibbs, R.E., and Gouaux, E. (2012). A fluorescence-detection size-exclusion chromatography-based thermostability assay for membrane protein precrystallization screening. Structure *20*, 1293–1299.

Hauer, F., Gerle, C., Fischer, N., Oshima, A., Shinzawa-Itoh, K., Shimada, S., Yokoyama, K., Fujiyoshi, Y., and Stark, H. (2015). GraDeR: Membrane Protein Complex Preparation for Single-Particle Cryo-EM. Structure *23*, 1769–1775.

Hénin, J., Salari, R., Murlidaran, S., and Brannigan, G. (2014). A predicted binding site for cholesterol on the $GABA_A$ receptor. Biophys. J. *106*, 1938–1949.

Hibbs, R.E., and Gouaux, E. (2011). Principles of activation and permeation in an anion-selective Cys-loop receptor. Nature *474*, 54–60.

Hilf, R.J.C., and Dutzler, R. (2008). X-ray structure of a prokaryotic pentameric ligand-gated ion channel. Nature *452*, 375–379.

Hilf, R.J.C., and Dutzler, R. (2009). Structure of a potentially open state of a proton-activated pentameric ligand-gated ion channel. Nature *457*, 115–118.

Hilf, R.J.C., Bertozzi, C., Zimmermann, I., Reiter, A., Trauner, D., and Dutzler, R. (2010). Structural basis of open channel block in a prokaryotic pentameric ligand-gated ion channel. Nat. Struct. Mol. Biol. *17*, 1330–1336.

Hinkle, D.J., and Macdonald, R.L. (2003). Beta subunit phosphorylation selectively increases fast desensitization and prolongs deactivation of α1β1γ2L and α1β3γ2L $GABA_A$ receptor currents. Journal of Neuroscience *23*, 11698–11710.

Hosie, A.M., Clarke, L., da Silva, H., and Smart, T.G. (2009). Conserved site for neurosteroid modulation of $GABA_A$ receptors. Neuropharmacology *56*, 149–154.

Hosie, A.M., Dunne, E.L., Harvey, R.J., and Smart, T.G. (2003). Zinc-mediated inhibition of $GABA_A$ receptors: discrete binding sites underlie subtype specificity. Nat. Neurosci. *6*, 362–369.

Hosie, A.M., Wilkins, M.E., da Silva, H.M.A., and Smart, T.G. (2006). Endogenous neurosteroids regulate $GABA_A$ receptors through two discrete transmembrane sites. Nature *444*, 486–489.

Huang, X., Chen, H., Michelsen, K., Schneider, S., and Shaffer, P.L. (2015). Crystal structure of human glycine receptor-α3 bound to antagonist strychnine. Nature. 52, 277-80.

Hübner, C.A., and Holthoff, K. Anion transport and GABA signaling. (2013). Front. Cell. Neurosci. 7:177.

Jaakola, V.-P., Griffith, M.T., Hanson, M.A., Cherezov, V., Chien, E.Y.T., Lane, J.R., Ijzerman, A.P., and Stevens, R.C. (2008). The 2.6 angstrom crystal structure of a human A2A adenosine receptor bound to an antagonist. Science *322*, 1211–1217.

Jacob, T.C., Moss, S.J., and Jurd, R. (2008). GABA(A) receptor trafficking and its role in the dynamic modulation of neuronal inhibition. Nat. Rev. Neurosci. *9*, 331–343.

Jansen, M., Bali, M., and Akabas, M.H. (2008). Modular design of Cys-loop ligand-gated ion channels: functional 5-HT_3 and GABA ρ1 receptors lacking the large cytoplasmic M3M4 loop. J. Gen. Physiol. *131*, 137–146.

Jayakar, S.S., Dailey, W.P., Eckenhoff, R.G., and Cohen, J.B. (2013). Identification of propofol binding sites in a nicotinic acetylcholine receptor with a photoreactive propofol analog. Journal of Biological Chemistry *288*, 6178–6189.

Jayakar, S.S., Zhou, X., Savechenkov, P.Y., Chiara, D.C., Desai, R., Bruzik, K.S., Miller, K.W., and Cohen, J.B. (2015). Positive and Negative Allosteric Modulation of an α1β3γ2 γ-Aminobutyric acid Type A (GABAA) Receptor by Binding to a Site in the Transmembrane Domain at the γ+-β- Interface. Journal of Biological Chemistry.

Johnston, G.A.R. (2005). $GABA_A$ receptor channel pharmacology. Curr. Pharm. Des. *11*, 1867–1885.

Johnston, G.A.R. (2013). Advantages of an antagonist: bicuculline and other GABA antagonists. British Journal of Pharmacology *169*, 328–336.

Jones, M.V., and Westbrook, G.L. (1995). Desensitized states prolong $GABA_A$ channel responses to brief agonist pulses. Neuron *15*, 181–191.

Kabsch, W. (2010). Integration, scaling, space-group assignment and post-refinement. Acta Crystallogr. D Biol. Crystallogr. *66*, 133–144.

Karakas, E., and Furukawa, H. (2014). Crystal structure of a heterotetrameric NMDA receptor ion channel. Science *344*, 992–997.

KATZ, B., and Miledi, R. (1966). Input-output relation of a single synapse. Nature *212*, 1242–1245.

KATZ, B., and THESLEFF, S. (1957). A study of the desensitization produced by acetylcholine at the motor end-plate. J. Physiol. (Lond.) *138*, 63–80.

Kawate, T., and Gouaux, E. (2006). Fluorescence-detection size-exclusion chromatography for precrystallization screening of integral membrane proteins. Structure *14*, 673–681.

Kelley, S.P., Dunlop, J.I., Kirkness, E.F., Lambert, J.J., and Peters, J.A. (2003). A cytoplasmic region determines single-channel conductance in 5-HT3 receptors. Nature *424*, 321–324.

Kinde, M.N., Chen, Q., Lawless, M.J., Mowrey, D.D., Xu, J., Saxena, S., Xu, Y., and Tang, P. (2015). Conformational Changes Underlying Desensitization of the Pentameric Ligand-Gated Ion Channel ELIC. Structure *23*, 995–1004.

Kittler, J.T., Thomas, P., Tretter, V., Bogdanov, Y.D., Haucke, V., Smart, T.G., and Moss, S.J. (2004). Huntingtin-associated protein 1 regulates inhibitory synaptic transmission by modulating gamma-aminobutyric acid type A receptor membrane trafficking. Proc. Natl. Acad. Sci. U.S.a. *101*, 12736–12741.

Kittler, J.T., Wang, J., Connolly, C.N., Vicini, S., Smart, T.G., and Moss, S.J. (2000). Analysis of GABAA receptor assembly in mammalian cell lines and hippocampal neurons using γ2 subunit green fluorescent protein chimeras. Mol. Cell. Neurosci. *16*, 440–452.

Kleinschmidt, J.H., and Popot, J.-L. (2014). Folding and stability of integral membrane proteins in amphipols. Arch. Biochem. Biophys. *564*, 327–343.

Krasowski, M.D., Hong, X., Hopfinger, A.J., and Harrison, N.L. (2002). 4D-QSAR analysis of a set of propofol analogues: mapping binding sites for an anesthetic phenol on the $GABA_A$ receptor. J. Med. Chem. *45*, 3210–3221.

Krishek, B.J., Moss, S.J., and Smart, T.G. (1996). Homomeric β1 gamma-aminobutyric acid A receptor-ion channels: evaluation of pharmacological and physiological properties. Mol. Pharmacol. *49*, 494–504.

Kumar, J., and Mayer, M.L. (2013). Functional insights from glutamate receptor ion channel structures. Annu. Rev. Physiol. *75*, 313–337.

Labriola, J.M., Pandhare, A., Jansen, M., Blanton, M.P., Corringer, P.-J., and Baenziger, J.E. (2013). Structural sensitivity of a prokaryotic pentameric ligand-gated ion channel to its membrane environment. Journal of Biological Chemistry.

Laganowsky, A., Reading, E., Allison, T.M., Ulmschneider, M.B., Degiacomi, M.T., Baldwin, A.J., and Robinson, C.V. (2014). Membrane proteins bind lipids selectively to modulate their structure and function. Nature *510*, 172–175.

Laganowsky, A., Reading, E., Hopper, J.T.S., and Robinson, C.V. (2013). Mass spectrometry of intact membrane protein complexes. Nat Protoc *8*, 639–651.

Laha, K.T., Ghosh, B., and Czajkowski, C. (2013). Macroscopic Kinetics of Pentameric Ligand Gated Ion Channels: Comparisons between Two Prokaryotic Channels and One Eukaryotic Channel. PLoS ONE *8*, e80322.

Lambert, J.J., Cooper, M.A., Simmons, R.D.J., Weir, C.J., and Belelli, D. (2009). Neurosteroids: endogenous allosteric modulators of $GABA_A$ receptors. Psychoneuroendocrinology *34 Suppl 1*, S48–S58.

Lape, R., Colquhoun, D., and Sivilotti, L.G. (2008). On the nature of partial agonism in the nicotinic

receptor superfamily. Nature *454*, 722–727.

LeBard, D.N., Hénin, J., Eckenhoff, R.G., Klein, M.L., and Brannigan, G. (2012). General anesthetics predicted to block the GLIC pore with micromolar affinity. PLoS Comput. Biol. *8*, e1002532.

Lebon, G., Warne, T., Edwards, P.C., Bennett, K., Langmead, C.J., Leslie, A.G.W., and Tate, C.G. (2011). Agonist-bound adenosine A2A receptor structures reveal common features of GPCR activation. Nature *474*, 521–525.

Lee, C.-H., Lü, W., Michel, J.C., Goehring, A., Du, J., Song, X., and Gouaux, E. (2014). NMDA receptor structures reveal subunit arrangement and pore architecture. Nature *511*, 191–197.

Lee, W.Y., Free, C.R., and Sine, S.M. (2008). Nicotinic receptor interloop proline anchors beta1-beta2 and Cys loops in coupling agonist binding to channel gating. J. Gen. Physiol. *132*, 265–278.

Li, G.-D., Chiara, D.C., Cohen, J.B., and Olsen, R.W. (2009). Neurosteroids allosterically modulate binding of the anesthetic etomidate to gamma-aminobutyric acid type A receptors. J. Biol. Chem. *284*, 11771–11775.

Li, S.-X., Huang, S., Bren, N., Noridomi, K., Dellisanti, C.D., Sine, S.M., and Chen, L. (2011). Ligand-binding domain of an α7-nicotinic receptor chimera and its complex with agonist. Nat. Neurosci. *14*, 1253–1259.

Liao, M., Cao, E., Julius, D., and Cheng, Y. (2013). Structure of the TRPV1 ion channel determined by electron cryo-microscopy. Nature *504*, 107–112.

Liao, M., Cao, E., Julius, D., and Cheng, Y. (2014). Single particle electron cryo-microscopy of a mammalian ion channel. Curr. Opin. Struct. Biol. *27*, 1–7.

López-Muñoz, F., Ucha-Udabe, R., and Alamo, C. (2005). The history of barbiturates a century after their clinical introduction. Neuropsychiatr Dis Treat *1*, 329–343.

Lüscher, B., and Keller, C.A. (2004). Regulation of $GABA_A$ receptor trafficking, channel activity, and functional plasticity of inhibitory synapses. Pharmacol. Ther. *102*, 195–221.

Lüscher, B., Fuchs, T., and Kilpatrick, C.L. (2011). $GABA_A$ receptor trafficking-mediated plasticity of inhibitory synapses. Neuron *70*, 385–409.

Lyford, L.K., Sproul, A.D., Eddins, D., McLaughlin, J.T., and Rosenberg, R.L. (2003). Agonist-induced conformational changes in the extracellular domain of α7 nicotinic acetylcholine receptors. Mol. Pharmacol. *64*, 650–658.

Majewska, M.D., Demirgören, S., and London, E.D. (1990). Binding of pregnenolone sulfate to rat brain membranes suggests multiple sites of steroid action at the $GABA_A$ receptor. Eur. J. Pharmacol. *189*, 307–315.

Malayev, A., Gibbs, T.T., and Farb, D.H. (2002). Inhibition of the NMDA response by pregnenolone sulphate reveals subtype selective modulation of NMDA receptors by sulphated steroids. British Journal of Pharmacology *135*, 901–909.

Martínez-Torres, A., Demuro, A., and Miledi, R. (2000). GABAρ1/$GABA_A$α1 receptor chimeras to study receptor desensitization. Proc. Natl. Acad. Sci. U.S.a. *97*, 3562–3566.

McCoy, A.J., Grosse-Kunstleve, R.W., Adams, P.D., Winn, M.D., Storoni, L.C., and Read, R.J. (2007). Phaser crystallographic software. J Appl Crystallogr *40*, 658–674.

Meyerson, J.R., Kumar, J., Chittori, S., Rao, P., Pierson, J., Bartesaghi, A., Mayer, M.L., and Subramaniam, S. (2014a). Structural mechanism of glutamate receptor activation and desensitization. Nature *514*, 328–334.

Meyerson, J.R., Rao, P., Kumar, J., Chittori, S., Banerjee, S., Pierson, J., Mayer, M.L., and Subramaniam, S. (2014b). Self-assembled monolayers improve protein distribution on holey carbon cryo-EM supports. Sci Rep *4*, 7084.

Mihic, S.J., Ye, Q., Wick, M.J., Koltchine, V.V., Krasowski, M.D., Finn, S.E., Mascia, M.P., Valenzuela, C.F., Hanson, K.K., Greenblatt, E.P., et al. (1997). Sites of alcohol and volatile anaesthetic action on $GABA_A$ and glycine receptors. Nature *389*, 385–389.

Miller, P.S., and Aricescu, A.R. (2014). Crystal structure of a human $GABA_A$ receptor. Nature.

Miller, P.S., and Smart, T.G. (2010). Binding, activation and modulation of Cys-loop receptors. Trends Pharmacol. Sci. *31*, 161–174.

Milne, J.L.S., Borgnia, M.J., Bartesaghi, A., Tran, E.E.H., Earl, L.A., Schauder, D.M., Lengyel, J., Pierson, J., Patwardhan, A., and Subramaniam, S. (2013). Cryo-electron microscopy-a primer for the non-microscopist. Febs J. *280*, 28–45.

Miyazawa, A., Fujiyoshi, Y., and Unwin, N. (2003). Structure and gating mechanism of the acetylcholine receptor pore. Nature *423*, 949–955.

Moraga-Cid, G., Sauguet, L., Huon, C., Malherbe, L., Girard-Blanc, C., Petres, S., Murail, S., Taly, A., Baaden, M., Delarue, M., et al. (2015). Allosteric and hyperekplexic mutant phenotypes investigated on an α1 glycine receptor transmembrane structure. Proc. Natl. Acad. Sci. U.S.a. *112*, 2865–2870.

Moss, S.J., and Smart, T.G. (2001). Constructing inhibitory synapses. Nat. Rev. Neurosci. *2*, 240–250.

Möhler, H. (2006). $GABA_A$ receptor diversity and pharmacology. Cell Tissue Res. *326*, 505–516.

Mukhtasimova, N., Lee, W.Y., Wang, H.-L., and Sine, S.M. (2009). Detection and trapping of intermediate states priming nicotinic receptor channel opening. Nature *459*, 451–454.

Muroi, Y., Theusch, C.M., Czajkowski, C., and Jackson, M.B. (2009). Distinct structural changes in the $GABA_A$ receptor elicited by pentobarbital and GABA. Biophys. J. *96*, 499–509.

Newby, Z.E.R., O'Connell, J.D., Gruswitz, F., Hays, F.A., Harries, W.E.C., Harwood, I.M., Ho, J.D., Lee, J.K., Savage, D.F., Miercke, L.J.W., et al. (2009). A general protocol for the crystallization of membrane proteins for X-ray structural investigation. Nat Protoc *4*, 619–637.

Newell, J.G., McDevitt, R.A., and Czajkowski, C. (2004). Mutation of glutamate 155 of the $GABA_A$ receptor β2 subunit produces a spontaneously open channel: a trigger for channel activation. Journal of Neuroscience *24*, 11226–11235.

Newstead, S., Ferrandon, S., and Iwata, S. (2008). Rationalizing alpha-helical membrane protein crystallization. Protein Sci. *17*, 466–472.

Nicoll, R.A., Malenka, R.C., and Kauer, J.A. (1990). Functional comparison of neurotransmitter receptor subtypes in mammalian central nervous system. Physiol. Rev. 70(2):513-65.

Nishida, M., Cadene, M., Chait, B.T., and MacKinnon, R. (2007). Crystal structure of a Kir3.1-prokaryotic Kir channel chimera. Embo J. *26*, 4005–4015.

Nury, H., Bocquet, N., Le Poupon, C., Raynal, B., Haouz, A., Corringer, P.-J., and Delarue, M. (2010). Crystal structure of the extracellular domain of a bacterial ligand-gated ion channel. J. Mol. Biol. *395*, 1114–1127.

Nury, H., Van Renterghem, C., Weng, Y., Tran, A., Baaden, M., Dufresne, V., Changeux, J.-P., Sonner, J.M., Delarue, M., and Corringer, P.-J. (2011). X-ray structures of general anaesthetics bound to a pentameric ligand-gated ion channel. Nature *469*, 428–431.

Oakley, S., Vedula, L.S., Bu, W., Meng, Q.C., Xi, J., Liu, R., Eckenhoff, R.G., and Loll, P.J. (2012). Recognition of anesthetic barbiturates by a protein binding site: a high resolution structural analysis. PLoS ONE *7*, e32070.

Olsen, R.W., and Sieghart, W. (2008). International Union of Pharmacology. LXX. Subtypes of gamma-aminobutyric acid(A) receptors: classification on the basis of subunit composition, pharmacology, and function. Update. Pharmacol. Rev. *60*, 243–260.

Olsen, R.W., and Sieghart, W. (2009). $GABA_A$ receptors: subtypes provide diversity of function and pharmacology. Neuropharmacology *56*, 141–148.

Olsen, R.W., Li, G.-D., Wallner, M., Trudell, J.R., Bertaccini, E.J., Lindahl, E., Miller, K.W., Alkana, R.L., and Davies, D.L. (2013). Structural Models of Ligand-Gated Ion Channels: Sites of Action for Anesthetics and Ethanol. Alcohol. Clin. Exp. Res.

Papke, D., and Grosman, C. (2014). The role of intracellular linkers in gating and desensitization of human pentameric ligand-gated ion channels. Journal of Neuroscience *34*, 7238–7252.

Papke, D., Gonzalez-Gutierrez, G., and Grosman, C. (2011). Desensitization of neurotransmitter-gated ion channels during high-frequency stimulation: a comparative study of Cys-loop, AMPA and purinergic receptors. J. Physiol. (Lond.) *589*, 1571–1585.

Park-Chung, M., Malayev, A., Purdy, R.H., Gibbs, T.T., and Farb, D.H. (1999). Sulfated and unsulfated steroids modulate gamma-aminobutyric acidA receptor function through distinct sites. Brain Res. *830*, 72–87.

Parker, J.L., and Newstead, S. (2012). Current trends in α-helical membrane protein crystallization: an update. Protein Sci. *21*, 1358–1365.

Paulsen, C.E., Armache, J.-P., Gao, Y., Cheng, Y., and Julius, D. (2015). Structure of the TRPA1 ion channel suggests regulatory mechanisms. Nature *520*, 511–517.

Petrek, M., Otyepka, M., Banás, P., Kosinová, P., Koca, J., and Damborský, J. (2006). CAVER: a new tool to explore routes from protein clefts, pockets and cavities. BMC Bioinformatics *7*, 316.

Pless, S.A., and Lynch, J.W. (2009a). Ligand-specific conformational changes in the alpha1 glycine receptor ligand-binding domain. J. Biol. Chem. *284*, 15847–15856.

Pless, S.A., and Lynch, J.W. (2009b). Magnitude of a conformational change in the glycine receptor beta1-beta2 loop is correlated with agonist efficacy. Journal of Biological Chemistry *284*, 27370–27376.

Plested, A.J.R., and Mayer, M.L. (2007). Structure and mechanism of kainate receptor modulation by anions. Neuron *53*, 829–841.

Plested, A.J.R., Vijayan, R., Biggin, P.C., and Mayer, M.L. (2008). Molecular basis of kainate receptor modulation by sodium. Neuron *58*, 720–735.

Powell, H.R., Johnson, O., and Leslie, A.G.W. (2013). Autoindexing diffraction images with iMosflm. Acta Crystallogr. D Biol. Crystallogr. *69*, 1195–1203.

Prevost, M.S., Delarue-Cochin, S., Marteaux, J., Colas, C., Van Renterghem, C., Blondel, A., Malliavin, T., Corringer, P.-J., and Joseph, D. (2013). Identification of Cinnamic Acid Derivatives As Novel Antagonists of the Prokaryotic Proton-Gated Ion Channel GLIC. J. Med. Chem. *56*, 4619–4630.

Prevost, M.S., Sauguet, L., Nury, H., Van Renterghem, C., Huon, C., Poitevin, F., Baaden, M., Delarue, M., and Corringer, P.-J. (2012). A locally closed conformation of a bacterial pentameric proton-gated ion channel. Nat. Struct. Mol. Biol. *19*, 642–649.

Reddy, D.S. (2010). Neurosteroids: endogenous role in the human brain and therapeutic potentials. Prog. Brain Res. *186*, 113–137.

Reeves, D.C., Jansen, M., Bali, M., Lemster, T., and Akabas, M.H. (2005). A role for the beta 1-beta 2 loop in the gating of 5-HT3 receptors. Journal of Neuroscience *25*, 9358–9366.

Revah, F., Bertrand, D., Galzi, J.L., Devillers-Thiéry, A., Mulle, C., Hussy, N., Bertrand, S., Ballivet, M., and Changeux, J.P. (1991). Mutations in the channel domain alter desensitization of a neuronal nicotinic receptor. Nature *353*, 846–849.

Rho, J.M., Donevan, S.D., and Rogawski, M.A. (1996). Direct activation of $GABA_A$ receptors by barbiturates in cultured rat hippocampal neurons. J. Physiol. (Lond.) *497 (Pt 2)*, 509–522.

Richter, L., de Graaf, C., Sieghart, W., Varagic, Z., Mörzinger, M., de Esch, I.J.P., Ecker, G.F., and Ernst, M. (2012). Diazepam-bound $GABA_A$ receptor models identify new benzodiazepine binding-site ligands. Nat. Chem. Biol. *8*, 455–464.

Robel, P., and Baulieu, E.E. (1994). Neurosteroids Biosynthesis and function. Trends Endocrinol. Metab. *5*, 1–8.

Rudolph, U., and Knoflach, F. (2011). Beyond classical benzodiazepines: novel therapeutic potential of GABAA receptor subtypes. Nat Rev Drug Discov *10*, 685–697.

Rudolph, U., and Möhler, H. (2004). Analysis of $GABA_A$ receptor function and dissection of the pharmacology of benzodiazepines and general anesthetics through mouse genetics. Annu. Rev. Pharmacol. Toxicol. *44*, 475–498.

Rudolph, U., and Möhler, H. (2014). $GABA_A$ receptor subtypes: Therapeutic potential in Down syndrome, affective disorders, schizophrenia, and autism. Annu. Rev. Pharmacol. Toxicol. *54*, 483–507.

Ruiz, A., Campanac, E., Scott, R.S., Rusakov, D.A., and Kullmann, D.M. (2010). Presynaptic $GABA_A$ receptors enhance transmission and LTP induction at hippocampal mossy fiber synapses. Nat. Neurosci. *13*, 431–438.

Russo, C.J., and Passmore, L.A. (2014). Controlling protein adsorption on graphene for cryo-EM using low-energy hydrogen plasmas. Nat. Methods *11*, 649–652.

Sachidanandan, D., and Bera, A.K. (2015). Inhibition of the $GABA_A$ Receptor by Sulfated Neurosteroids: A Mechanistic Comparison Study between Pregnenolone Sulfate and Dehydroepiandrosterone Sulfate. J. Mol. Neurosci. *56*, 868–877.

Saibil, H.R. (2000). Macromolecular structure determination by cryo-electron microscopy. Acta Crystallogr. D Biol. Crystallogr. *56*, 1215–1222.

Sakmann, B., Patlak, J., and Neher, E. (1980). Single acetylcholine-activated channels show burst-kinetics in presence of desensitizing concentrations of agonist. Nature *286*, 71–73.

Sauguet, L., Howard, R.J., Malherbe, L., Lee, U.S., Corringer, P.-J., Adron Harris, R., and Delarue, M. (2013a). Structural basis for potentiation by alcohols and anaesthetics in a ligand-gated ion channel. Nature Communications *4*, 1697.

Sauguet, L., Poitevin, F., Murail, S., Van Renterghem, C., Moraga-Cid, G., Malherbe, L., Thompson, A.W., Koehl, P., Corringer, P.-J., Baaden, M., et al. (2013b). Structural basis for ion permeation mechanism in pentameric ligand-gated ion channels. Embo J.

Sauguet, L., Shahsavar, A., and Delarue, M. (2014a). Crystallographic studies of pharmacological sites in pentameric ligand-gated ion channels. BBA - General Subjects 1–13.

Sauguet, L., Shahsavar, A., Poitevin, F., Huon, C., Menny, A., Nemecz, À., Haouz, A., Changeux, J.-P., Corringer, P.-J., and Delarue, M. (2014b). Crystal structures of a pentameric ligand-gated ion channel provide a mechanism for activation. Proc. Natl. Acad. Sci. U.S.a. *111*, 966–971.

Schauder, D.M., Kuybeda, O., Zhang, J., Klymko, K., Bartesaghi, A., Borgnia, M.J., Mayer, M.L., and Subramaniam, S. (2013). Glutamate receptor desensitization is mediated by changes in quaternary structure of the ligand binding domain. Proc. Natl. Acad. Sci. U.S.a. *110*, 5921–5926.

Scheres, S.H.W. (2012). RELION: implementation of a Bayesian approach to cryo-EM structure determination. J. Struct. Biol. *180*, 519–530.

Seljeset, S., Laverty, D., and Smart, T.G. (2015). Inhibitory neurosteroids and the $GABA_A$ receptor. Adv. Pharmacol. *72*, 165–187.

Shen, W., Mennerick, S., Covey, D.F., and Zorumski, C.F. (2000). Pregnenolone sulfate modulates inhibitory synaptic transmission by enhancing $GABA_A$ receptor desensitization. Journal of Neuroscience *20*, 3571–3579.

Sieghart, W., and Sperk, G. (2002). Subunit composition, distribution and function of $GABA_A$ receptor subtypes. Curr Top Med Chem *2*, 795–816.

Sigel, E., and Steinmann, M.E. (2012) Structure, function, and modulation of $GABA_A$ receptors. J. Biol. Chem. 23;287(48):40224-31.

Smart, T.G., and Paoletti, P. (2012). Synaptic neurotransmitter-gated receptors. Cold Spring Harb Perspect Biol *4*.

Smith, C.C., Gibbs, T.T., and Farb, D.H. (2014). Pregnenolone sulfate as a modulator of synaptic plasticity. Psychopharmacology (Berl.) *231*, 3537–3556.

Sobolevsky, A.I., Rosconi, M.P., and Gouaux, E. (2009). X-ray structure, symmetry and mechanism of an AMPA-subtype glutamate receptor. Nature *462*, 745–756.

Sooksawate, T., and Simmonds, M.A. (2001). Influence of membrane cholesterol on modulation of the $GABA_A$ receptor by neuroactive steroids and other potentiators. British Journal of Pharmacology *134*, 1303–1311.

Spurny, R., Billen, B., Howard, R.J., Brams, M., Debaveye, S., Price, K.L., Weston, D.A., Strelkov, S.V., Tytgat, J., Bertrand, S., et al. (2013). Multi-Site Binding Of A General Anesthetic To The Prokaryotic Pentameric Ligand-Gated Ion Channel ELIC. Journal of Biological Chemistry.

Spurny, R., Ramerstorfer, J., Price, K., Brams, M., Ernst, M., Nury, H., Verheij, M., Legrand, P., Bertrand, D., Bertrand, S., et al. (2012). Pentameric ligand-gated ion channel ELIC is activated by GABA and modulated by benzodiazepines. Proc. Natl. Acad. Sci. U.S.a. *109*, E3028–E3034.

Srinivasan, S., Nichols, C.J., Lawless, G.M., Olsen, R.W., and Tobin, A.J. (1999). Two invariant tryptophans on the alpha1 subunit define domains necessary for $GABA_A$ receptor assembly. J. Biol. Chem. *274*, 26633–26638.

Staley, K.J., and Mody, I. (1992). Shunting of excitatory input to dentate gyrus granule cells by a depolarizing $GABA_A$ receptor-mediated postsynaptic conductance. J. Neurophysiol. 68(1):197-212.

Stokes, C., Treinin, M., and Papke, R.L. (2015). Looking below the surface of nicotinic acetylcholine receptors. Trends Pharmacol. Sci. *36*, 514–523.

Tasneem, A., Iyer, L.M., Jakobsson, E., and Aravind, L. (2005). Identification of the prokaryotic ligand-gated ion channels and their implications for the mechanisms and origins of animal Cys-loop ion channels. Genome Biol. *6*, R4.

Taylor, P.M., Connolly, C.N., Kittler, J.T., Gorrie, G.H., Hosie, A., Smart, T.G., and Moss, S.J. (2000). Identification of residues within $GABA_A$ receptor α subunits that mediate specific assembly with receptor beta subunits. J. Neurosci. *20*, 1297–1306.

Taylor, P.M., Thomas, P., Gorrie, G.H., Connolly, C.N., Smart, T.G., and Moss, S.J. (1999). Identification of amino acid residues within $GABA_A$ receptor beta subunits that mediate both homomeric and heteromeric receptor expression. J. Neurosci. *19*, 6360–6371.

Terwilliger, T.C., Grosse-Kunstleve, R.W., Afonine, P.V., Moriarty, N.W., Zwart, P.H., Hung, L.W., Read, R.J., and Adams, P.D. (2008). Iterative model building, structure refinement and density modification with the PHENIX AutoBuild wizard. Acta Crystallogr. D Biol. Crystallogr. *64*, 61–69.

Thomas, J., and Tate, C.G. (2014). Quality control in eukaryotic membrane protein overproduction. J. Mol. Biol. *426*, 4139–4154.

Thomas, P., Mortensen, M., Hosie, A.M., and Smart, T.G. (2005). Dynamic mobility of functional $GABA_A$ receptors at inhibitory synapses. Nat. Neurosci. *8*, 889–897.

Thompson, A.J., Lester, H.A., and Lummis, S.C.R. (2010). The structural basis of function in Cys-loop receptors. Q. Rev. Biophys. *43*, 449–499.

Tillman, T.S., Seyoum, E., Mowrey, D.D., Xu, Y., and Tang, P. (2014). ELIC-α7 Nicotinic acetylcholine receptor (α7nAChR) chimeras reveal a prominent role of the extracellular-transmembrane domain interface in allosteric modulation. Journal of Biological Chemistry *289*, 13851–13857.

Trowitzsch, S., Bieniossek, C., Nie, Y., Garzoni, F., and Berger, I. (2010). New baculovirus expression tools for recombinant protein complex production. J. Struct. Biol. *172*, 45–54.

Twede, V., Tartaglia, A.L., Covey, D.F., and Bamber, B.A. (2007). The neurosteroids dehydroepiandrosterone sulfate and pregnenolone sulfate inhibit the UNC-49 GABA receptor through a common set of residues. Mol. Pharmacol. *72*, 1322–1329.

Uetrecht, C., Rose, R.J., van Duijn, E., Lorenzen, K., and Heck, A.J.R. (2010). Ion mobility mass spectrometry of proteins and protein assemblies. Chem Soc Rev *39*, 1633–1655.

Ulens, C., Spurny, R., Thompson, A.J., Alqazzaz, M., Debaveye, S., Han, L., Price, K., Villalgordo, J.M., Tresadern, G., Lynch, J.W., et al. (2014). The prokaryote ligand-gated ion channel ELIC captured in a pore blocker-bound conformation by the Alzheimer's disease drug memantine. Structure *22*, 1399–1407.

Unwin, N. (1995). Acetylcholine receptor channel imaged in the open state. Nature *373*, 37–43.

Unwin, N. (2005). Refined structure of the nicotinic acetylcholine receptor at 4A resolution. J. Mol. Biol. *346*, 967–989.

Unwin, N., and Fujiyoshi, Y. (2012). Gating movement of acetylcholine receptor caught by plunge-freezing. J. Mol. Biol. *422*, 617–634.

Van Renterghem, C., Bilbe, G., Moss, S., Smart, T.G., Constanti, A., Brown, D.A., and Barnard, E.A. (1987). GABA receptors induced in Xenopus oocytes by chick brain mRNA: evaluation of TBPS as a use-dependent channel-blocker. Brain Res. *388*, 21–31.

Vedula, L.S., Brannigan, G., Economou, N.J., Xi, J., Hall, M.A., Liu, R., Rossi, M.J., Dailey, W.P., Grasty, K.C., Klein, M.L., et al. (2009). A unitary anesthetic binding site at high resolution. J. Biol. Chem. *284*, 24176–24184.

Velisetty, P., and Chakrapani, S. (2012). Desensitization Mechanism in Prokaryotic Ligand-gated Ion Channel. Journal of Biological Chemistry *287*, 18467–18477.

Vijayan, R., Plested, A.J.R., Mayer, M.L., and Biggin, P.C. (2009). Selectivity and cooperativity of modulatory ions in a neurotransmitter receptor. Biophys. J. *96*, 1751–1760.

Violet, J.M., Downie, D.L., Nakisa, R.C., Lieb, W.R., and Franks, N.P. (1997). Differential sensitivities of mammalian neuronal and muscle nicotinic acetylcholine receptors to general anesthetics. Anesthesiology *86*, 866–874.

Wagner, T.F.J., Loch, S., Lambert, S., Straub, I., Mannebach, S., Mathar, I., Düfer, M., Lis, A., Flockerzi, V., Philipp, S.E., et al. (2008). Transient receptor potential M3 channels are ionotropic steroid receptors in pancreatic beta cells. Nat. Cell Biol. *10*, 1421–1430.

Wang, H.-L., Cheng, X., and Sine, S.M. (2012). Intramembrane proton binding site linked to activation of bacterial pentameric ion channel. Journal of Biological Chemistry *287*, 6482–6489.

Wang, M. (2011). Neurosteroids and GABA-A receptor function. Frontiers in Endocrinology *2*.

Wang, M., He, Y., Eisenman, L.N., Fields, C., Zeng, C.-M., Mathews, J., Benz, A., Fu, T., Zorumski, E., Steinbach, J.H., et al. (2002). 3beta -hydroxypregnane steroids are pregnenolone sulfate-like $GABA_A$ receptor antagonists. Journal of Neuroscience *22*, 3366–3375.

Wang, M.-D., Rahman, M., Zhu, D., and Bäckström, T. (2006). Pregnenolone sulphate and Zn2+ inhibit recombinant rat $GABA_A$ receptor through different channel property. Acta Physiol (Oxf) *188*, 153–162.

Wang, M.-D., Rahman, M., Zhu, D., Johansson, I.-M., and Bäckström, T. (2007). 3β-hydroxysteroids and pregnenolone sulfate inhibit recombinant rat $GABA_A$ receptor through different channel property. Eur. J. Pharmacol. *557*, 124–131.

Wang, Q., and Lynch, J.W. (2011). Activation and desensitization induce distinct conformational changes at the extracellular-transmembrane domain interface of the glycine receptor. Journal of Biological Chemistry *286*, 38814–38824.

Wardell, B., Marik, P.S., Piper, D., Rutar, T., Jorgensen, E.M., and Bamber, B.A. (2006). Residues in the first transmembrane domain of the Caenorhabditis elegans $GABA_A$ receptor confer sensitivity to the neurosteroid pregnenolone sulfate. British Journal of Pharmacology *148*, 162–172.

Warne, T., Serrano-Vega, M.J., Baker, J.G., Moukhametzianov, R., Edwards, P.C., Henderson, R., Leslie, A.G.W., Tate, C.G., and Schertler, G.F.X. (2008). Structure of a β1-adrenergic G-protein-coupled receptor. Nature *454*, 486–491.

Warne, T., Serrano-Vega, M.J., Tate, C.G., and Schertler, G.F.X. (2009). Development and crystallization of a minimal thermostabilised G protein-coupled receptor. Protein Expr. Purif. *65*, 204–213.

Weng, Y., Yang, L., Corringer, P.-J., and Sonner, J.M. (2010). Anesthetic sensitivity of the Gloeobacter violaceus proton-gated ion channel. Anesth. Analg. *110*, 59–63.

Wieland, H.A., Lüddens, H., and Seeburg, P.H. (1992). A single histidine in $GABA_A$ receptors is essential for benzodiazepine agonist binding. J. Biol. Chem. *267*, 1426–1429.

Wilkins, M.E., Hosie, A.M., and Smart, T.G. (2002). Identification of a β subunit TM2 residue mediating proton modulation of GABA type A receptors. J. Neurosci. *22*, 5328–5333.

Wilkins, M.E., Li, X., and Smart, T.G. (2008). Tracking cell surface $GABA_B$ receptors using an alpha-bungarotoxin tag. J. Biol. Chem. *283*, 34745–34752.

Winn, M.D., Ballard, C.C., Cowtan, K.D., Dodson, E.J., Emsley, P., Evans, P.R., Keegan, R.M., Krissinel, E.B., Leslie, A.G.W., McCoy, A., et al. (2011). Overview of the CCP4 suite and current developments. Acta Crystallogr. D Biol. Crystallogr. *67*, 235–242.

Wooltorton, J.R., Moss, S.J., and Smart, T.G. (1997). Pharmacological and physiological characterization of murine homomeric beta3 GABA(A) receptors. Eur. J. Neurosci. *9*, 2225–2235.

Wu, F.S., Gibbs, T.T., and Farb, D.H. (1991). Pregnenolone sulfate: a positive allosteric modulator at the N-methyl-D-aspartate receptor. Mol. Pharmacol. *40*, 333–336.

Yamodo, I.H., Chiara, D.C., Cohen, J.B., and Miller, K.W. (2010). Conformational changes in the nicotinic acetylcholine receptor during gating and desensitization. Biochemistry *49*, 156–165.

Yip, G.M.S., Chen, Z.-W., Edge, C.J., Smith, E.H., Dickinson, R., Hohenester, E., Townsend, R.R., Fuchs, K., Sieghart, W., Evers, A.S., et al. (2013). A propofol binding site on mammalian $GABA_A$ receptors identified by photolabeling. Nat. Chem. Biol. *9*, 715–720.

Zhou, M., Morais-Cabral, J.H., Mann, S., and MacKinnon, R. (2001). Potassium channel receptor site for the inactivation gate and quaternary amine inhibitors. Nature *411*, 657–661.

Zimmermann, I., and Dutzler, R. (2011). Ligand activation of the prokaryotic pentameric ligand-gated ion channel ELIC. PLoS Biol. *9*, e1001101.

Zimmermann, I., Marabelli, A., Bertozzi, C., Sivilotti, L.G., and Dutzler, R. (2012). Inhibition of the prokaryotic pentameric ligand-gated ion channel ELIC by divalent cations. PLoS Biol. *10*, e1001429.

Appendix

Primer 1: Electron cryo-microscopy and single particle analysis

Cryo-EM allows for direct imaging of non-crystalline protein particles. After being developed in the 1970's, the last few years have seen rapid developments in single-particle cryo-EM that make this technique a genuine competitor to X-ray crystallography for high-resolution structure determination (Cheng et al., 2015). This is particularly useful for proteins that are inherently refractory to crystallization, including membrane proteins (e.g. pLGICs). Moreover, by imaging proteins in a near native-state (not necessarily observed in the confines of protein packed into crystal form), cryo-EM allows for potential structure solution of a single protein in multiple conformational states. This has been highlighted by the recent cryo-EM study of the zebrafish α1 Gly receptor, which utilised cryo-EM to generate structures of agonist-, antagonist- and agonist/allosteric modulator-bound receptor (Du et al., 2015).

Below summarises the key steps in sample preparation, imaging and image analysis that enables the generation of a 3D model.

1. Sample Preparation: Purified protein is generated exactly as for protein crystallization trials. The amount of protein required is typically less (on the µg rather than mg scale). Construct design is also similar, with non-essential or highly flexible regions of the protein typically removed (whilst ensuring near-normal receptor function). For membrane proteins, additional detergent exchange may be carried out. Amphipathic polymers, including Amphipol A8-35 and PMAL-C8, have been used to stabilize membrane proteins, improving their qualities for cryo-EM grids when compared with proteins in conventional detergents (Cao et al., 2013a; Liao et al., 2014; Paulsen et al., 2015).

2. Sample characterisation by Negative stain EM: Protein is applied to an EM grid and a heavy metal stain applied (typically uranyl acetate). During this process the protein sample is dried down in a thin layer of the heavy metal salt. The overall shape of the

protein is revealed by negative contrast, though this may be distorted during sample dehydration. Negative stain EM is a critical preliminary step in cryo-EM studies for structure determination, as it provides details of sample heterogeneity. For example, is the protein complex (, e.g. the pentameric assembly of a pLGIC) in the expected stoichiometry and does the sample show undesirable aggregation tendencies? Additionally the orientation of particles can be assessed; is there a preference towards a single or multiple orientations? This will have a bearing on the ability to generate a structure. Samples showing favourable properties by negative stain EM can be prepared for cryo-EM experiments (*Appendix Fig 1*).

3. For cryo-EM the sample is embedded in a layer of vitreous ice (*Appendix Fig 1 A*). This is achieved by applying sample to EM grids that are then rapidly plunged into a coolant with high heat conductivity, such as liquid ethane. While the hydrated frozen protein retains its native structure, the protein-ice contrast is low compared to that observed for negative stain. For this reason, and to maximise contrast, cryo-specimens are prepared on grids with holes in the carbon support film. Ideally the protein particles are distributed in ice over the grid holes for imaging.

4. Samples are imaged in the electron microscope (*Appendix Fig 1 B*). For structure determination (and due to the low protein-ice contrast) images are recorded at high electron energies (200-300 kV). Multiple low exposure images (to minimize the damaging effects of high energy electron exposure) are collected for a number of grid regions containing thousands of particles. The recent developments of direct electron detector device (DDD) cameras (where electrons are detected by silicon sensors instead of less sensitive charge couple device (CCD) cameras) dramatically improves the signal-to-noise ratio in images.

5. From the acquired images single protein particles are selected (i.e. defined within a region of interest). This is performed either manually or in a semi-automated manner (depending on sample quality). At this stage, these images represent the (real) observed 2D projections of particles. In *Appendix Figure 1* C the likely molecular architectures of a pLGIC (rendered in iso-surface form) for these 2D projections are also shown. Thousands (and in some cases millions) of particles are picked for structural analysis.

6. Particles are grouped by computational methods (e.g. by classification algorithms in the software RELION (Scheres, 2012)) based upon variations in particle orientation and structural features. Similar (or related) orientation classes are grouped, forming 2D class averages. We have shown 3 idealised classes for a pLGIC; a side view of the receptor, a top-down plan view of the ECD and bottom-up view of the TMD (*Appendix Fig 1 D*). Ideally a greater range of orientations would be observed for generating a 3D electron density map.

7. From these 2D projections a 3D density map can be recovered by inverse Fourier transformation (*Appendix Fig 1 E &F*). The Fourier transform of each 2D projection is a section through the 3D Fourier transform of the structure. In this case we have represented the 3D transform as two intersecting transform sections, derived from the side view and end-on (TMD) view of our pLGIC (*Appendix Fig 1 E*). This is an over simplification, and realistically once enough 2D sections spanning a complete range of orientations are available, the full 3D transform can be interpolated and an inverse Fourier transformation recovers the 3D density map (*Appendix Fig 1 F*).

8. Initial 3D maps can be further refined and then a structural model built from the electron density maps (as shown for the α1 GlyR, *Appendix Fig 1 F*) and analysed for correct stereochemistry (in a manner similar to that carried out for crystal structure model building and refinement).

Appendix Figure 1 - Structure determination by Cryo-EM

A. After initial sample characterization by negative stain EM, samples are prepared for single particle cryo-EM and structure determination. EM grids can be treated with various substrates to alter the surface charge and force particles into the ice over the grid holes. Plunge freezing in liquid ethane can be semi-automated using robotic plungers. The quality of freezing has substantial effects on the "ice quality" and thickness and subsequent imaging. **B.** An example of a cryo-EM image is shown for ELIC with a number of receptor particles circled. Hypothetical 3D molecular orientations of a pLGIC are shown (EM density maps of the α1 GlyR, contour level arbitrarily adjusted, are used as an example; EMDB-6344, Du et al., 2015) **C.** Note the ring of density around the TMD formed by the detergent shell. **D.** Theoretical 2D projections of a pLGIC for side and end views. **E.** Intersecting sections of side view and end view (TMD) are used to represent the 3D transform. **F.** The EM 3D density map (filtered and sharpened) and model solution (red ribbon representation) for the α1 GlyR is shown in complex with glycine.

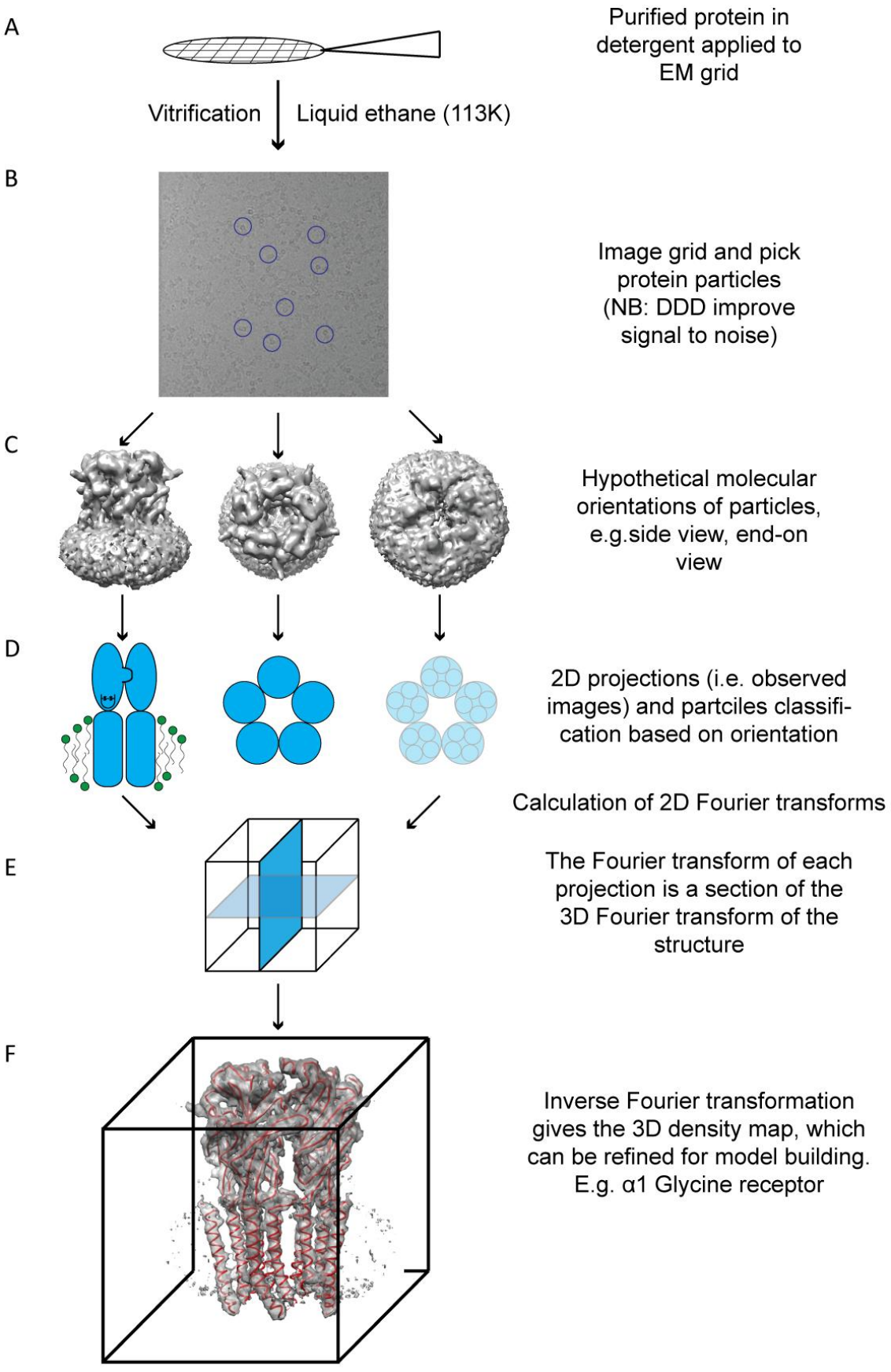
A
Purified protein in detergent applied to EM grid
Vitrification
Liquid ethane (113K)
B
Image grid and pick protein particles (NB: DDD improve signal to noise)
C
Hypothetical molecular orientations of particles, e.g.side view, end-on view
D
2D projections (i.e. observed images) and partciles classification based on orientation
Calculation of 2D Fourier transforms
E
The Fourier transform of each projection is a section of the 3D Fourier transform of the structure
F
Inverse Fourier transformation gives the 3D density map, which can be refined for model building. E.g. α1 Glycine receptor

Primer 2: Mass spectrometry (MS) reveals modes of lipid and small molecule binding to membrane protein complexes.

While it is not intended to describe in depth the procedure of generating native MS data for membrane proteins, it is important to emphasize what can be obtained from high quality mass spectra for detergent solubilized pLGICs. This technique can be used to generate 'images' of how lipids and small molecules (free of additional labels) form non-covalent interactions with ion channels. Lipid stabilization and modulation of pLGICs is important for maintaining normal function, yet is typically restricted to reconstitution studies in proteoliposomes. Such studies do not necessarily provide information regarding the direct interaction and affinity of binding of pLGICs for lipids. In the case of $GABA_A$ receptors it is still far from clear as to the role that lipids play in modulating receptor function.

1. Sample preparation: Mass spectrometry is a highly sensitive technique and while requiring less material than crystallography, samples should still be as pure and homogenous (Laganowsky et al., 2013). A range of detergents is compatible with MS measurements; however, the ability to generate quality mass spectra is somewhat empirical in its derivation and dependent on the choice of detergent. This will also be inherently linked to the stability of the protein of interest in a certain detergent.

2. Instrument parameters: Following ionisation of protein-detergent complexes and transfer into the gas phase, detergent molecules surrounding the pLGIC are removed by thermal agitation (via collisions with inert gas molecules, *Appendix Figure 2*; Bechara and Robinson, 2015). This releases detergent molecules, gradually exposing the transmembrane regions of the protein (*Appendix Figs 2 B & C*). Evidently maintaining the intact protein complex in the native oligomeric state is necessary for experimental mass measurements, and thus fine-tuning instruments parameters is critical. Collision cell energies (i.e. varying the acceleration of ions in to a collision cell containing inert gas) can be varied to gradually eject the membrane complex from the detergent micelles. Here we show that at lower collision energies the pLGIC is trapped in the detergent micelle, yielding broad ill-defined mass spectra (*Appendix Fig 2 A*). Gradual loss of detergent molecules is reflected by an increase in the resolution of the mass spectrum as the detergent is stripped from the pentamer (*Appendix Fig 2B & C*).

At higher energies ejection of detergent molecules yields a high-resolution mass spectrum of the pentameric complex (*Appendix Fig 2 C*). Additionally collision-induced dissociation of the pentameric complex yields highly charged monomers and "stripped" receptor tetramers.

3. Revealing endogenous lipids: Recent structural data suggests that lipid molecules bind at both intra- and intersubunit clefts in pLGICs (Nury et al., 2011; Althoff et al., 2014). For GluClα, the lipid POPC induced a distinct open-like channel conformation when this lipid was added during the crystallization procedure (Althoff et al., 2014). In some cases it is possible that endogenous lipids (from the host cell used for protein over-expression) may remain tightly bound to receptor following detergent extraction. Well-resolved mass spectra of the charged receptor complex should reveal any endogenous lipid binding.

In this example (*Appendix Fig 2 D*) we have two lipid molecules bound to the pentamer at two equivalent subunit interfaces. Expansion of the charge states shows three peaks. Deconvolution of these charge states allows the intact mass of the protein-lipid complex, and stoichiometry of lipid binding to be deduced. The peak with lowest mass/charge (*m/z*) value corresponds to the lipid free pentamer and peaks of increased *m/z* value correspond to a pentamer with one or two bound lipid molecules (*Appendix Fig 2 D*). With well-resolved spectra the mass of lipids can be determined for further analysis. In the example shown, with lipid binding at subunit interfaces, one might expect similar charge distributions across the "stripped" tetramer. On this basis, lipid association with the monomeric pLGIC subunit, lacking an interfacial site, would not be observed. In contrast lipid molecules tightly associated through binding at intrasubunit sites would be associated with charge states for all intact and dissociated complexes.

4. Application to exogenous lipid and small molecule binding: By the principles introduced above, it should be theoretically possible to assess the mechanism of binding of a range of small molecules and lipids (at intrasubunit cavities or subunit interfaces). In doing so, specific binding sensitivities, in particular to different lipid classes, might be established for pLGICs, and the $GABA_A$ receptor in particular.

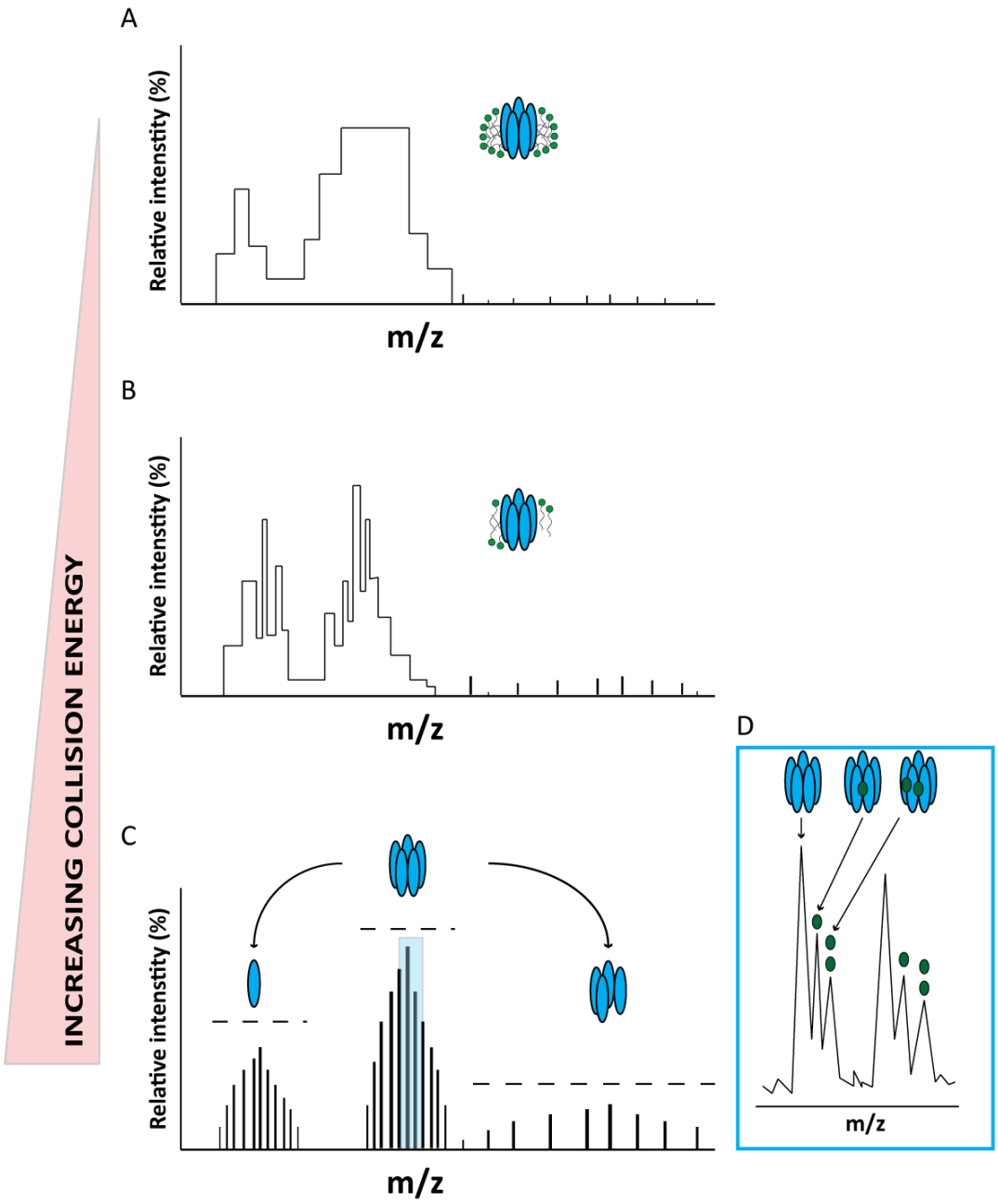

Appendix Figure 2 - MS reveals detergent stripped-pLGIC and endogenous lipid binding

A-C. Increasing collision cell energy strips detergent molecules from a pLGIC. As more detergent molecules are removed, the resolution of the mass spectrum improves (i.e. a narrowing of peaks). At optimal settings (**C**) peaks of charge distributions can be resolved and used for protein mass calculations. At high collision energies (**C**), the pentameric complex is disrupted to yield charged monomeric and "stripped" tetrameric species. Lipid and small molecule binding studies can be carried out on all species. **D.** Expansion across the (blue) highlight charge state reveals additional peaks with greater *m/z* value, which can be quantitatively defined as lipid bound complexes. In this example binding of one or two lipid molecules (green spheres) at equivalent sites is shown.

Appendix Table 1 Details of constructs used in electrophysiology

Construct name	Vector backbone	Vector type	Bacterial resistance	Insert	Tag/Fusion protein
pRK5-GABA$_A$R α1	pRK5	Mammalian	Ampicillin	Mouse GABA$_A$R α1	-
pRK5-GABA$_A$R β2	pRK5	Mammalian	Ampicillin	Mouse GABA$_A$R β2	-
pRK5-GLIC	pRK5	Mammalian	Ampicillin	GLIC (with nAChR α7 signal peptide)	-
pRK5-ELIC	pRK5	Mammalian	Ampicillin	ELIC (with nAChR α7 signal peptide)	-
pRK5-GluClα	pRK5	Mammalian	Ampicillin	*C. elegans* GluClα	8x His (C-terminal on insert)
pRK5-GLIC-GABA$_A$R α1	pRK5	Mammalian	Ampicillin	ECD of GLIC and TMD of GABA$_A$R α1	-
pRK5-^{BBS}GLIC-GABA$_A$R α1	pRK5	Mammalian	Ampicillin	ECD of GLIC and TMD of GABA$_A$R α1	BBS mimotope tag (N-terminal on insert)
pRK5-GLIC-GABA$_A$R α1$^{M3\text{-}M4}$ Tripeptide	pRK5	Mammalian	Ampicillin	ECD of GLIC and TMD of GABA$_A$R α1, ΔICD with tripeptide linker	-
pRK5-GLIC-GABA$_A$R α1$^{M3\text{-}M4}$ Heptapeptide	pRK5	Mammalian	Ampicillin	ECD of GLIC and TMD of GABA$_A$R α1, ΔICD with heptapeptide linker	-
pRK5-GLIC-GABA$_A$R β2	pRK5	Mammalian	Ampicillin	ECD of GLIC and TMD of GABA$_A$R β2	-
pRK5-GluClα-GABA$_A$R α1	pRK5	Mammalian	Ampicillin	ECD of GluClα and TMD of GABA$_A$R α1	-

Appendix Table 2 Details of constructs used in bacterial expression studies

Construct name	Vector backbone	Vector type	Bacterial resistance	Insert	Tag/Fusion protein
pET26-MBP-GLIC	pET26	Bacterial	Kanamycin	GLIC (*Gloeobacter violaceus*)	10x His (N-terminal on MBP) MBP (N-terminal on insert)
pET26-MBP-ELIC	pET26	Bacterial	Kanamycin	ELIC (*Eriwinia chrisanthemi*)	10x His (N-terminal on MBP) MBP (N-terminal on insert)
pET26-MBP-GLIC-$GABA_AR$ α1	pET26	Bacterial	Kanamycin	ECD of GLIC and TMD of $GABA_AR$ α1 ΔICD	10x His (N-terminal on MBP) MBP (N-terminal on insert)
pET26-MBP-GLIC-$GABA_AR$ β2	pET26	Bacterial	Kanamycin	ECD of GLIC and TMD of $GABA_AR$ β2 ΔICD	10x His (N-terminal on MBP) MBP (N-terminal on insert)

Appendix Table 3 Details of constructs used in insect cell expression studies

Construct name	Vector backbone	Vector type	Bacterial resistance	Insert	Tag/Fusion protein
pFB-GluClα	pFastBac	Insect	Ampicillin	*C. elegans* GluClα	8x His (C-terminal on insert)
pFB-GLIC-GABA$_A$R α1$^{\Delta ICD}$ His	pFastBac	Insect	Ampicillin	ECD of GLIC and TMD of GABA$_A$R α1, ΔICD with tripeptide linker	8x His (C-terminal on insert)
pFB-GLIC-GABA$_A$R α1$^{\Delta ICD\ \Delta Ct}$ His	pFastBac	Insect	Ampicillin	ECD of GLIC and TMD of GABA$_A$R α1, ΔICD with tripeptide linker and ΔCt (13 amino acids at C-terminal end of insert)	8x His (C-terminal on insert)
pFB-GLIC-GABA$_A$R α1$^{V251F\Delta ICD}$ His	pFastBac	Insect	Ampicillin	ECD of GLIC and TMD of GABA$_A$R α1, ΔICD with tripeptide linker and ΔCt (13 amino acids at C-terminal end of insert). V251F mutation in M2 of α1	8x His (C-terminal on insert)

Appendix Figure 3 - Alignment of GABA$_A$R α1, GLIC and GLIC-GABA$_A$R α1

Alignment of WT mouse GABA$_A$R α1 (red), WT GLIC (blue) and GLIC-GABA$_A$R α1 chimera. Site of domain fusion is at residue 223 of the GABA$_A$R α1 subunit. α-helices of TMD are highlighted grey. Highlighted positions show residues lining the channel pore (light green); forming loop 7; M2-M3 loop; responsible for neurosteroid (NS) potentiation (teal), transduction (dark green) and activation (yellow); and affecting receptor desensitization (purple).

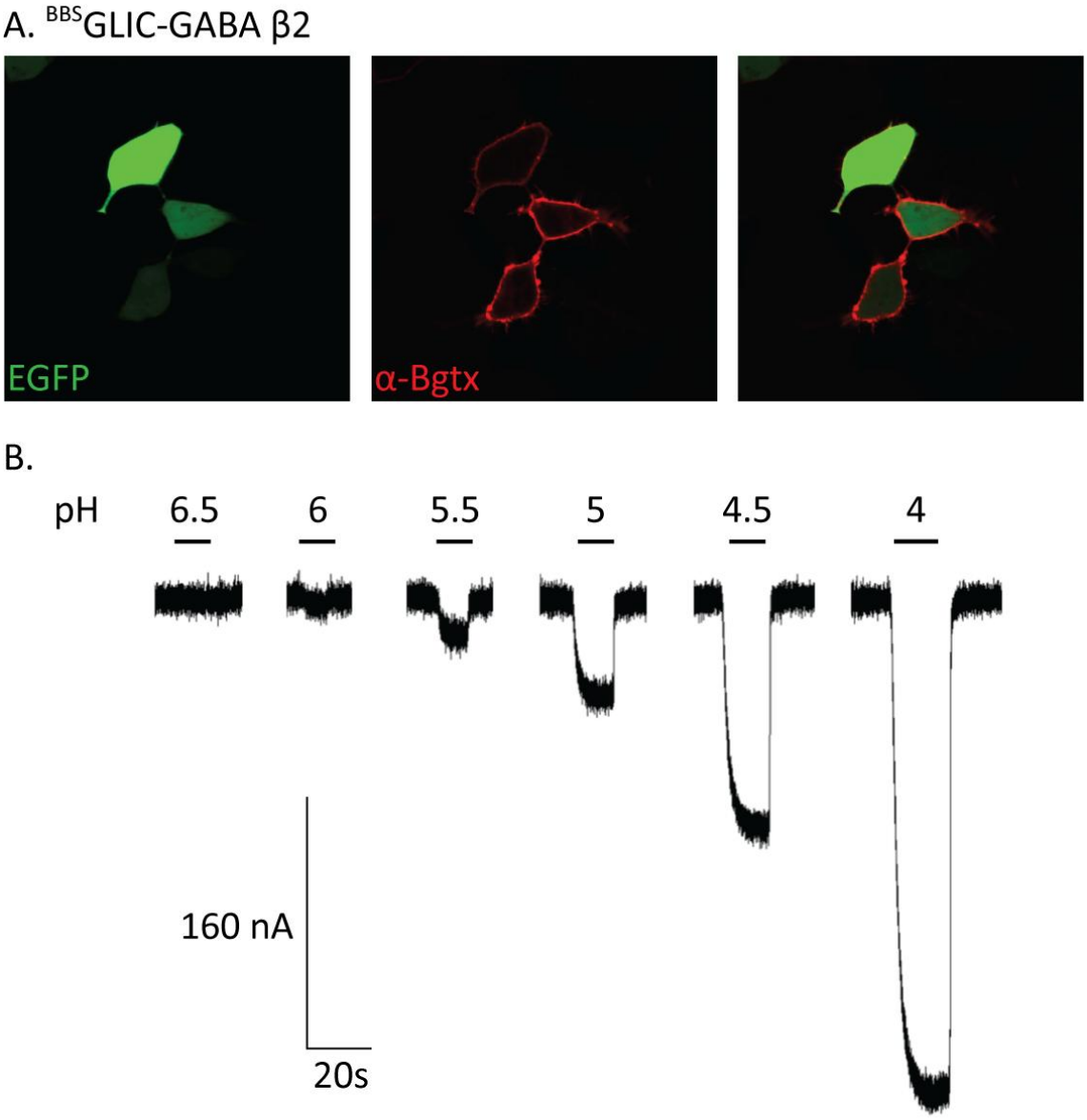

Appendix Figure 4 - Trafficking and functional characterisation of a GLIC-GABA$_A$R β2 chimera.

A. α-Bungarotoxin labelling of HEK293 cells transfected with EGFP and BBS-tagged GLIC-GABA$_A$R β2 chimera (eGFP channel green, Alexa555 α-Bgtx channel red and merge with eGFP). B. Proton-gated currents for the GLIC-GABA$_A$R β2 chimera (when expressed in oocytes). Currents were small and exhibited slow onsets when compared to currents from a GLIC-GABA$_A$R α1 chimera.

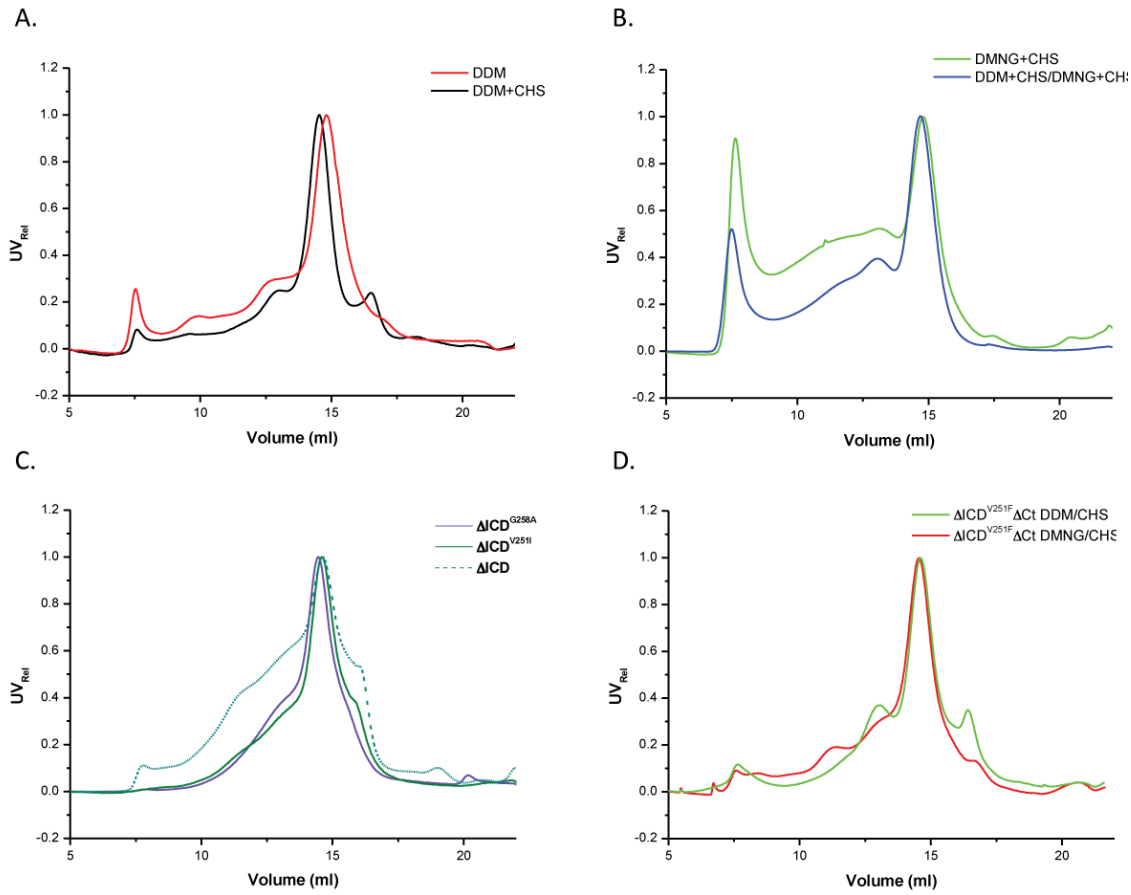

Appendix Figure 5 - SEC profiles of mutant GLIC-GABA$_A$R α1 chimeras following extraction and exchange into various detergents

A. Size exclusion chromatography profile of purified GLIC-GABA$_A$R α1$^{V251F\ \Delta ICD}$His (Extracted: DDM± CHS & SEC: DDM). Major peak of pentameric receptor-detergent complex is at an elution volume of ~14.5 ml. **B.** Size exclusion chromatography profile of purified GLIC-GABA$_A$R α1$^{V251F\ \Delta ICD}$His following extraction in DMNG + CHS (green) or in DDM +CHS and then exchange into DMNG + CHS(blue) and SEC in DMNG (for both). Major peak of pentameric receptor-detergent complex is at an elution volume of ~14.5 ml.**C.** Size exlusion chromatography profile of purified GLIC-GABA$_A$R α1$^{V251I\ or\ G258A\ \Delta ICD}$His (extracted in DDM ± CHS and SEC in DDM) and comparison with 'non-mutant' bearing chimera. Major peak of pentameric receptor-detergent complex is at an elution volume of ~14.5 ml. D. **B.** Size exclusion chromatography profile of purified GLIC-GABA$_A$R α1$^{V251F\ \Delta ICD\Delta Ct}$Hisfollowingextraction inDMNG + CHS (red) or in DDM +CHS (green). SEC was in DDM for both.

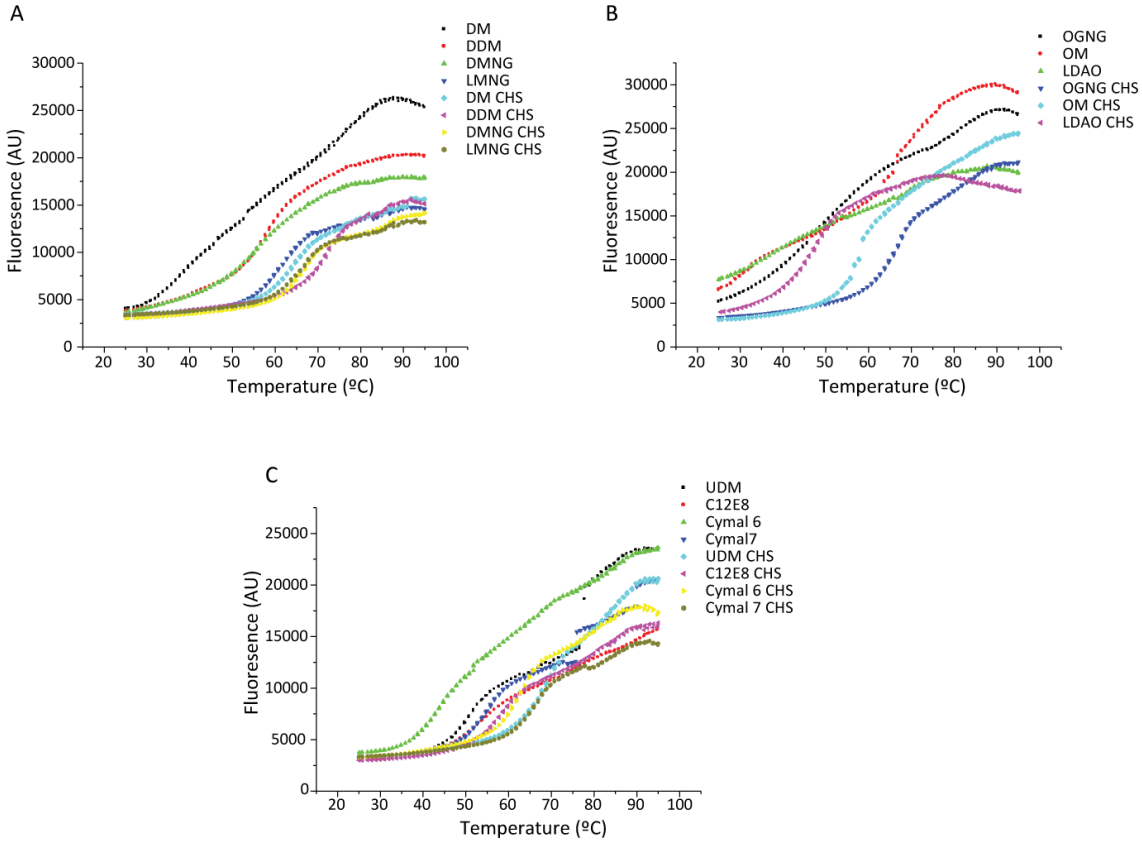

Appendix Figure 6- Effect of detergents and CHS on GLIC-GABA$_A$R α1$^{V251\ F\Delta ICD}$His thermal stability

A. Melting curves for mild alky-maltoside and MNG detergents in the absence or presence of CHS **B.** Melting curves for less mild detergents: amino oxide (LDAO), ocytl glucoside and maltosides in the absence or presence of CHS **C.** Melting curves for an alky-maltoside (UDM), cycloalkylglycosides (Cymal 6 and 7), and the anapoe $C_{12}E_8$ detergent in the absence or presence of CHS.

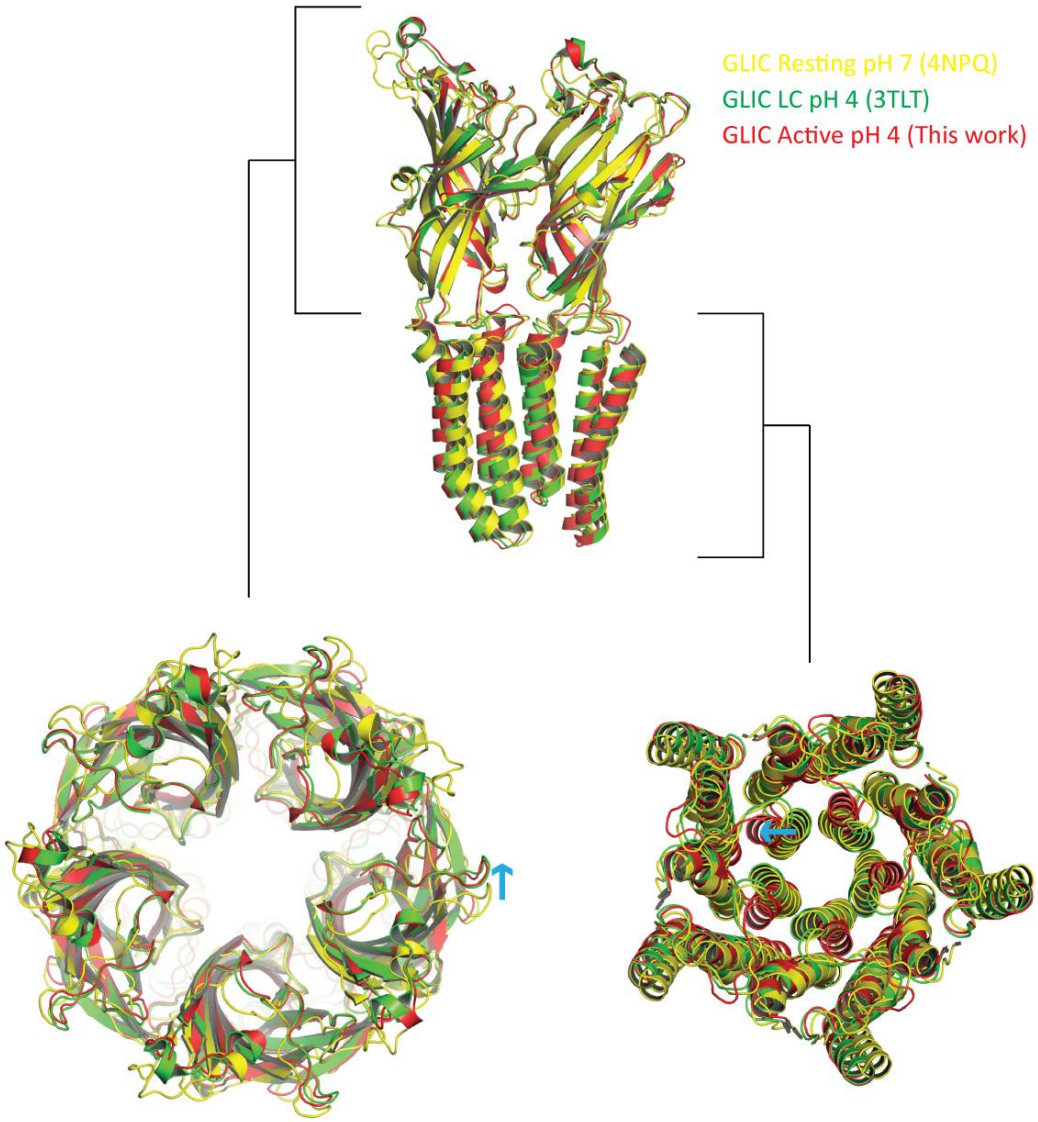

Appendix Figure 7 - Global alignment of activated GLIC^{BrPB} at pH 4 (this study) with locally closed (pH 4) and resting (pH 7) forms

Global alignment of the entire GLIC pentamer for active (red; this study), locally closed (LC; green, PDB 3TLT) and resting (yellow, PDB 4NPQ) forms of GLIC. Active and LC forms were solved at pH 4 while the resting form was solved at neutral pH 7. The top panel shows the alignment of two subunits in a pentamer with the proximal three subunits removed for clarity. Lower panels show pentameric arrangements viewed from the extracellular side at the level of the ECD (left) and TMD (right). The relative transitions from resting to active forms are shown by blue arrows. At the level of the TMD, bending of the upper portion of M2 towards the channel creates an obstruction to ion flow in the resting and LC GLIC form

Appendix Table 4 Structural alignments of GLIC from this study with equivalent regions (pentamer, ECD and TMD) of previously reported GLIC structures solved in distinct states.

Reference structure	Moving structure for alignment (pH & PDB ID)	RMSD of C_α atoms (Å)
$GLIC^{BrPB}$ Pentamer	GLIC Active (pH 4 4HFI) Pentamer	0.267
	GLIC LC (pH 4 3TLT) Pentamer	0.612
	GLIC Resting (pH 7 4NPQ) Pentamer (Chains	2.450

Reference structure	Moving structure for alignment (pH & PDB ID)	RMSD of C_α atoms (Å)
$GLIC^{BrPB}$ ECD	GLIC Active (pH 4 4HFI) ECD	0.214
	GLIC LC (pH 4 3TLT) ECD	0.289
	GLIC Resting (pH 7 4NPQ) ECD (Chains A-E)	0.576

Reference structure	Moving structure for alignment (pH & PDB ID)	RMSD of C_α atoms (Å)
$GLIC^{BrPB}$ TMD	GLIC Active (pH 4 4HFI) TMD	0.260
	GLIC LC (pH 4 3TLT) TMD	0.529
	GLIC Resting (pH 7 4NPQ) TMD (Chains A-E)	0.502

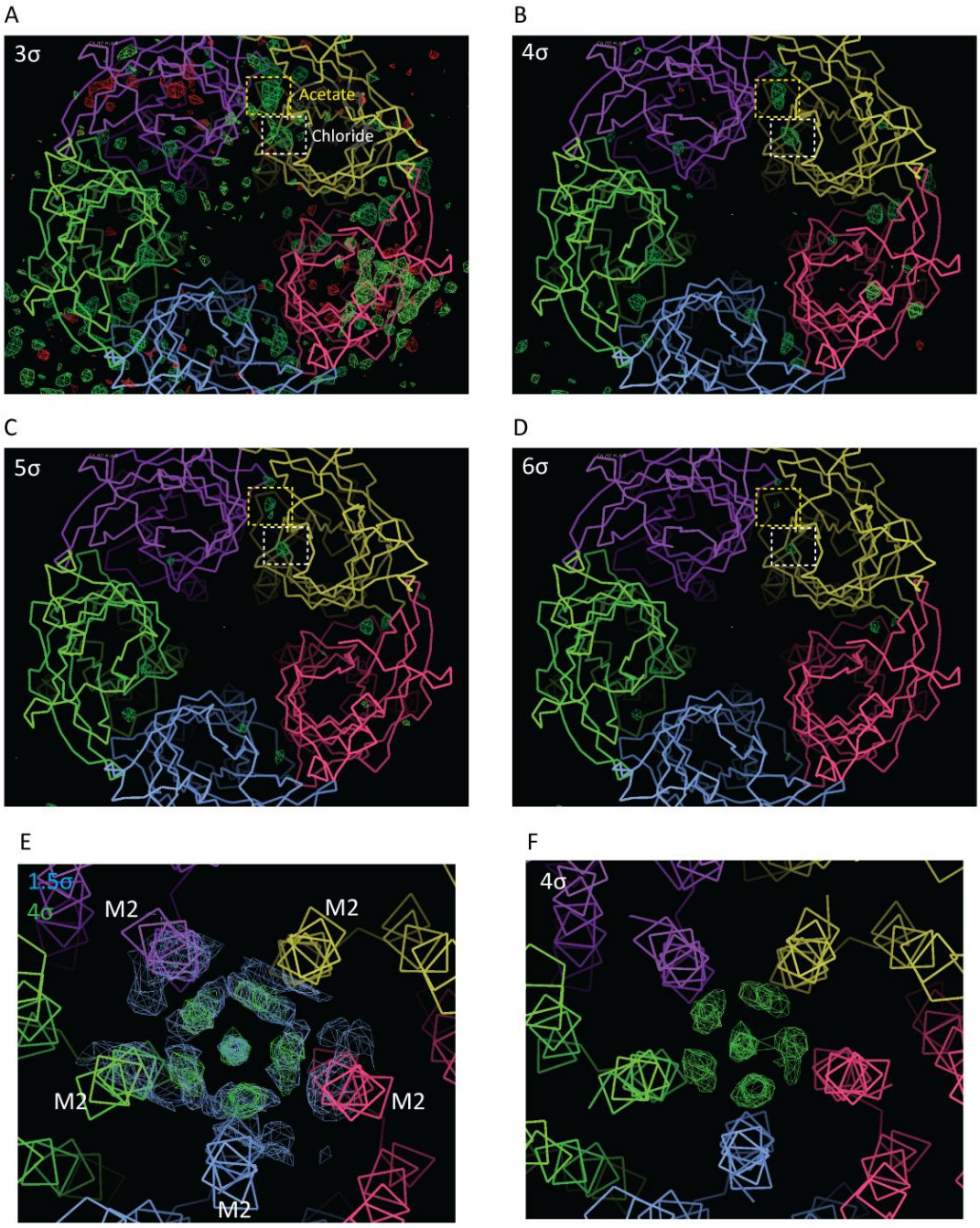

Appendix Figure 8 - Difference density maps at high contouring show the likely presence of bound ions and detergent molecules

A-D. F_o-F_c difference density map for the ECD, green, at increasing contour levels reveal peaks at the sites of previously identified chloride (white box) and acetate ions (yellow box). **E-F.** Peaks in 2mF_o-DF_c electron density, blue, and F_o-F_c difference density maps, reveal presence of detergents in the ion channel pore.